

# Symmetry Pathways in Solid-State NMR

Philip J. Grandinetti, Jason T. Ash, Nicole M. Trease

*Department of Chemistry, The Ohio State University, 120 W. 18<sup>th</sup> Avenue, Columbus, Ohio 43210-1173*

---

**Keywords:** transition pathway, spatial pathway, symmetry pathway, coherence transfer pathway, affine transformation, shear transformation, hypercomplex acquisition, shifted-echo acquisition, solid echo, Jeener-Broekaert echo, Solomon echoes, perturbation theory, irreducible tensors, magic-angle spinning, double rotation, dynamic-angle spinning, multiple-quantum magic-angle spinning, satellite transition magic-angle spinning, spinning sidebands, phase-adjusted spinning sidebands, two-dimensional one-pulse

---

*Progress in Nuclear Magnetic Resonance Spectroscopy,*

Volume 59, Issue 2, August 2011, Pages 121-196.

doi: 10.1016/j.pnmrs.2010.11.003

Received 4 July 2010

Accepted 12 November 2010

Available Online: 2 December 2010

## Notes

In this updated edition of our review article (December 10, 2023),

- a few notations, used throughout the published version, have been modified in this edition such that,
  - individual states are no longer enclosed in angle brackets, i.e.,  $m_i$  instead of  $\langle m_i \rangle$ ,
  - a transition from state  $i$  to  $j$  is represented by  $|j\rangle \langle i|$ , instead of  $(\langle i \rangle, \langle j \rangle)$ ,
  - single transition Zeeman order associated with states  $i$  and  $j$  is represented by  $[i, j]$ , instead of  $[\langle i \rangle, \langle j \rangle]$ .
  - the  $l$ th-rank spin transition symmetry function of the  $k$ th frequency component is represented as  $\xi_\ell^{(k)}(i, j)$ , instead of  $\xi_k(i, j)$
  - the  $L$ th-rank orientational spatial symmetry function of the  $k$ th frequency component is represented as  $\xi_\ell^{(k)}(\Theta)$ , instead of  $\Xi_k(\Theta)$ .
  - The transition symmetry function  $\mathbb{P}_{\text{IPS}}$  used in the weak coupling limit is replaced by  $\mathbb{d}_{\text{IS}}$ .
- the manuscript has been reformatted as a single column to improve readability and minimize line breaks in equations.
- figures were rearranged to match the single-column format better.
- a small error in the caption of Fig. 2 has been corrected
- An error in the Fig. 3 caption should have been...(A) for  $[-1, 0]$ , in (B) for  $[0, +1]$ , and in (C) for  $[-1, +1]$ , where  $[m_i, m_j]$  ...
- a missing factor of 2 has been added in Eqs. (55) and (58).

---

URL: <http://www.grandinetti.org> (Philip J. Grandinetti)

- an unnecessary scaling factor in Eqs. (105) and (106) have been eliminated.
- in Eq. (3), an incorrect  $\sum$  is replaced with  $\prod$  in the expression for the number of energy levels, and a similar adjustment is later in the paragraph.
- the sign of effective  $\langle D_n \mathbf{p}_I \rangle$  evolution during  $\epsilon$  in Fig. 38 has been reversed to be consistent with positive going echo associated with refocusing of rotor modulated anisotropic evolution.
- an incorrect factor of  $1/\sqrt{2}$  instead of  $\sqrt{\frac{3}{2}}$  was corrected in Eq. (A.185).
- an incorrect factor appeared in the first-order nuclear shielding proportionality constant. It shows the correct value, which was already given in Eq. (A.191).
- an incorrect factor of  $1/\sqrt{2}$  instead of  $\sqrt{\frac{3}{2}}$  was corrected in Eq. (A.222).
- the zero-rank first-order proportionality constant for the strong  $J$  coupling was eliminated since the spin transition part of the zero-rank term is zero.
- an incorrect factor of  $\sqrt{3}$  in the first-order strong  $J$  coupling proportionality constant given in Eq. (A.227) was eliminated.
- an incorrect factor appeared in the first-order strong  $J$  coupling proportionality constant. It shows the correct value, which was already given in Eq. (A.229).
- an incorrect factor appeared in the first-order weak  $J$  coupling proportionality constant. It shows the correct value, which was already given in Eq. (A.238).
- an incorrect factor of  $\sqrt{\frac{2}{3}}$  instead of  $\sqrt{\frac{3}{2}}$  was corrected in Eq. (A.149).
- the symbols for the spherical tensor components of the dipolar coupling were mislabeled in Eqs. (A.264)-(A.266).
- the right hand side of Eq. (A.269) should have been  $-\frac{\mu_0}{2\pi}\zeta_d\gamma_1\gamma_2\hbar$ .
- an incorrect factor of  $1/4$  in Eqs. (A.270), (A.271), (A.273), (A.274), (A.276), (A.280), (A.281), (A.283), (A.284), (A.285) was eliminated, with corresponding changes for  $d_{II}$  and  $d_{IS}$  in Table I.
- a missing negative sign was added to Eq.(A.202) for the  $\pi_{2,4}^{\{1,2\}}$  coefficient.
- a missing factor of  $1/2$  was added to Eqs. (A.288)-(A.290) and Eqs. (A.292)-(A.294) with corresponding changes for  $d_{II}$  and  $d_{IS}$  in Table I.
- Changed convention for the definition of  $\eta$  to

$$\eta = \frac{\lambda_{yy} - \lambda_{xx}}{\zeta},$$

and propagated this change to other equations.

- corrected typos in Table A.12 for  $\hat{T}_{3,m}$  elements
- corrected error in Eqs. (56), (57), (59) and (60) for the  $(\mathbb{p}\mathbb{d})_{IS}$  and  $(\mathbb{d}\mathbb{p})_{IS}$  spin transition functions.
- updated Figs. 12 and 13 for the  $(\mathbb{p}\mathbb{d})_{IS}$  and  $(\mathbb{d}\mathbb{p})_{IS}$  spin transition functions

## Contents

<b>1</b>	<b>Introduction</b>	<b>9</b>
<b>2</b>	<b>Frequency component symmetries</b>	<b>10</b>
<b>3</b>	<b>Echo classification</b>	<b>35</b>
3.1	p Echoes . . . . .	35
3.1.1	The Hahn echo . . . . .	35
3.1.2	SEDOR . . . . .	37
3.1.3	The double quantum echo . . . . .	39
3.2	$d_I$ Echoes . . . . .	39
3.2.1	The solid echo . . . . .	39
3.2.2	The Jeener-Broekaert echo . . . . .	41
3.2.3	The Solomon echoes . . . . .	41
3.3	$(pp)_{IS}$ Echoes . . . . .	43
3.3.1	HETCOR . . . . .	43
3.3.2	HSQC . . . . .	45
3.4	$\mathbb{D}_1, \mathbb{D}_2$ , and $\mathbb{G}_1, \mathbb{G}_2, \mathbb{G}_3, \mathbb{G}_4$ Echoes . . . . .	45
3.4.1	D-MAS . . . . .	45
3.4.2	TOP . . . . .	47
3.4.3	2D PASS . . . . .	50
3.4.4	DOR . . . . .	52
3.5	$c_4$ Echoes . . . . .	55
3.5.1	MQ-MAS . . . . .	55
3.5.2	ST-MAS . . . . .	57
3.6	$c_2$ Echoes . . . . .	61
3.6.1	COASTER . . . . .	62
3.7	$c_0$ Echoes . . . . .	66
3.7.1	MQ-DOR . . . . .	67
3.8	$\mathbb{D}_0$ and $\mathbb{G}_0$ Echoes . . . . .	69
3.8.1	MAF . . . . .	70
3.8.2	VACSY . . . . .	70
3.8.3	DAS . . . . .	70
<b>4</b>	<b>Pure absorption mode lineshapes</b>	<b>74</b>
4.1	One dimension . . . . .	74
4.2	Two dimensions . . . . .	76
4.2.1	Hypercomplex approach . . . . .	77
4.2.2	Shifted-echo approach . . . . .	79
<b>5</b>	<b>Affine transformations</b>	<b>83</b>
5.1	Translation . . . . .	83
5.2	Scaling . . . . .	84
5.3	Shearing . . . . .	85
5.4	Single shear and scale . . . . .	86
5.5	Double shear and scale . . . . .	90
5.6	Spinning sidebands . . . . .	92

<b>6</b>	<b>Spatial averaging symmetries</b>	<b>92</b>
<b>7</b>	<b>Summary</b>	<b>96</b>
<b>A</b>	<b>Frequency component derivations</b>	<b>98</b>
A.1	Rotating tilted frame . . . . .	98
A.2	Irreducible spherical tensors . . . . .	99
A.3	Perturbation theory . . . . .	102
A.4	Spherical tensor products and commutators . . . . .	102
A.5	Sample motion . . . . .	104
A.5.1	Single axis rotation . . . . .	105
A.5.2	Double axis rotation . . . . .	106
A.5.3	Spinning sidebands . . . . .	107
A.6	Hamiltonians . . . . .	108
A.6.1	Zeeman . . . . .	108
A.6.2	Electric quadrupole coupling . . . . .	108
A.6.3	Nuclear shielding . . . . .	113
A.6.4	$J$ coupling . . . . .	115
A.6.5	Magnetic dipole coupling . . . . .	120



## Symbols

$\Omega(\Theta, i, j)$	resonance frequency of $i \rightarrow j$ transition in a sample with orientation $\Theta$
$\Omega_k(\Theta, i, j)$	$k$ th frequency component in $\Omega(\Theta, i, j)$
$\omega_k$	strength of the $k$ th frequency component
$\xi_\ell^{(k)}(\Theta)$	the $L^{\text{th}}$ -rank orientational spatial symmetry function of the $k$ th frequency component
$\xi_\ell^{(k)}(i, j)$	the $l^{\text{th}}$ -rank spin transition symmetry function of the $k$ th frequency component
$i$	quantum number(s) associated with a quantized energy level $E_i$
$m_i$	quantum number(s) associated with a quantized energy level $E_{m_i}$
$M_i$	quantum number(s) associated with a quantized energy level $E_{M_i}$
$m_{I_i} m_{S_i}$	quantum number(s) associated with a quantized energy level $E_{m_{I_i}, m_{S_i}}$
$\{I_1, I_2, \dots, I_N\}$	coupled nuclear spin system
$ j\rangle \langle i $	transition from quantized state $i$ to $j$
$[i, j]$	single transition Zeeman order associated with quantized states $i$ and $j$
$[z_I]$	Zeeman order associated with spin $I$
$[z_I^2]$	quadrupolar order associated with spin $I$
$[z_{II}^2]$	dipolar order associated with two strongly coupled nuclei
$\Theta$	orientation of crystal axis frame in laboratory axis frame system
$\Upsilon_{\{I_1, I_2, \dots, I_N\}}$	number of quantized nuclear spin states in the spin system $\{I_1, I_2, \dots, I_N\}$
$\mathbb{S}$	spatial symmetry function from irreducible 0th-rank tensor
$\mathbb{P}(\Theta)$	spatial symmetry function from irreducible 1st-rank tensor
$\mathbb{D}(\Theta)$	spatial symmetry function from irreducible 2nd-rank tensor
$\mathbb{F}(\Theta)$	spatial symmetry function from irreducible 3rd-rank tensor
$\mathbb{G}(\Theta)$	spatial symmetry function from irreducible 4th-rank tensor
$S$	phase shifted spatial symmetry function under single axis rotation from irreducible 1st-rank tensor
$P_m(\Theta)$	phase shifted spatial symmetry function under single axis rotation from irreducible 1st-rank tensor
$D_m(\Theta)$	phase shifted spatial symmetry function under single axis rotation from irreducible 2nd-rank tensor
$F_m(\Theta)$	phase shifted spatial symmetry function under single axis rotation from irreducible 3rd-rank tensor
$G_m(\Theta)$	phase shifted spatial symmetry function under single axis rotation from irreducible 4th-rank tensor
$\zeta$	second-rank symmetric spatial tensor anisotropy
$\eta$	the second-rank symmetric spatial tensor asymmetry parameter
$\zeta_\sigma$	second-rank symmetric nuclear shielding spatial tensor anisotropy
$\eta_\sigma$	second-rank symmetric nuclear shielding spatial tensor asymmetry parameter
$\zeta_J$	second-rank symmetric $J$ coupling spatial tensor anisotropy
$\eta_J$	second-rank symmetric $J$ coupling spatial tensor asymmetry parameter
$\zeta_d$	second-rank symmetric dipolar coupling spatial tensor anisotropy
$\zeta_q$	second-rank symmetric quadrupolar coupling spatial tensor anisotropy
$\eta_q$	second-rank symmetric quadrupolar coupling spatial tensor asymmetry parameter
$\theta_R$	single-axis sample rotation rotor angle
$\phi_R$	single-axis sample rotation rotor initial phase
$\theta_o$	double-axis sample rotation outer rotor angle

$\phi_o$  double-axis sample rotation outer rotor phase  
 $\chi_o$  double-axis sample rotation outer rotor initial phase  
 $\theta_i$  double-axis sample rotation inner rotor angle  
 $\phi_i$  double-axis sample rotation inner rotor phase  
 $\mathbb{S}^{\{\sigma\}}$  spatial symmetry function from irreducible 0th-rank tensor of 1st-order nuclear shielding  
 $\mathbb{P}^{\{\sigma\}}(\Theta)$  spatial symmetry function from irreducible 1st-rank tensor of 1st-order nuclear shielding  
 $\mathbb{D}^{\{\sigma\}}(\Theta)$  spatial symmetry function from irreducible 2nd-rank tensor of 1st-order nuclear shielding  
 $\mathbb{P}^{\{J_{II}\}}(\Theta)$  spatial symmetry function from irreducible 1st-rank tensor of 1st-order  $J$  strong coupling  
 $\mathbb{D}^{\{J_{II}\}}(\Theta)$  spatial symmetry function from irreducible 2nd-rank tensor of 1st-order  $J$  strong coupling  
 $\mathbb{S}^{\{J_{IS}\}}$  spatial symmetry function from irreducible 0th-rank tensor of 1st-order  $J$  weak coupling  
 $\mathbb{D}^{\{J_{IS}\}}(\Theta)$  spatial symmetry function from irreducible 2nd-rank tensor of 1st-order  $J$  weak coupling  
 $\mathbb{D}^{\{d_{II}\}}(\Theta)$  spatial symmetry function from irreducible 2nd-rank tensor of 1st-order strong dipolar coupling  
 $\mathbb{D}^{\{d_{IS}\}}(\Theta)$  spatial symmetry function from irreducible 2nd-rank tensor of 1st-order weak dipolar coupling  
 $\mathbb{D}^{\{q\}}(\Theta)$  spatial symmetry function from irreducible 2nd-rank tensor of 1st-order quadrupolar coupling  
 $\mathbb{S}^{\{qq\}}$  spatial symmetry function from irreducible 0th-rank tensor of 2nd-order quadrupolar coupling  
 $\mathbb{D}^{\{qq\}}(\Theta)$  spatial symmetry function from irreducible 2nd-rank tensor of 2nd-order quadrupolar coupling  
 $\mathbb{G}^{\{qq\}}(\Theta)$  spatial symmetry function from irreducible 4th-rank tensor of 2nd-order quadrupolar coupling  
 $\mathbb{S}^{\{\sigma q\}}$  spatial symmetry function from irreducible 0th-rank tensor of 2nd-order shielding-quadrupolar coupling  
 $\mathbb{D}^{\{\sigma q\}}(\Theta)$  spatial symmetry function from irreducible 2nd-rank tensor of 2nd-order shielding-quadrupolar coupling  
 $\mathbb{G}^{\{\sigma q\}}(\Theta)$  spatial symmetry function from irreducible 4th-rank tensor of 2nd-order shielding-quadrupolar coupling  
 $\mathbb{S}^{\{J_{ISqI}\}}$  spatial symmetry function from irreducible 0th-rank tensor of 2nd-order  $J$ -quadrupolar coupling  
 $\mathbb{D}^{\{J_{ISqI}\}}(\Theta)$  spatial symmetry function from irreducible 2nd-rank tensor of 2nd-order  $J$ -quadrupolar coupling  
 $\mathbb{G}^{\{J_{ISqI}\}}(\Theta)$  spatial symmetry function from irreducible 4th-rank tensor of 2nd-order  $J$ -quadrupolar coupling  
 $\mathbb{S}^{\{d_{ISqI}\}}$  spatial symmetry function from irreducible 0th-rank tensor of 2nd-order weak dipolar-quadrupolar coupling  
 $\mathbb{D}^{\{d_{ISqI}\}}(\Theta)$  spatial symmetry function from irreducible 2nd-rank tensor of 2nd-order weak dipolar-quadrupolar coupling  
 $\mathbb{G}^{\{d_{ISqI}\}}(\Theta)$  spatial symmetry function from irreducible 4th-rank tensor of 2nd-order weak dipolar-quadrupolar coupling  
 $\mathfrak{s}(i, j)$  transition symmetry function from irreducible 0th-rank tensor  
 $\mathfrak{p}(i, j)$  transition symmetry function from irreducible 1st-rank tensor  
 $\mathfrak{d}(i, j)$  transition symmetry function from irreducible 2nd-rank tensor  
 $\mathfrak{f}(i, j)$  transition symmetry function from irreducible 3rd-rank tensor  
 $\mathbf{s}(i, j)$  transition symmetry function from irreducible 0th-rank tensor (scaled)  
 $\mathbf{p}(i, j)$  transition symmetry function from irreducible 1st-rank tensor (scaled)  
 $\mathbf{d}(i, j)$  transition symmetry function from irreducible 2nd-rank tensor (scaled)  
 $\mathbf{f}(i, j)$  transition symmetry function from irreducible 3rd-rank tensor (scaled)  
 $\mathfrak{s}_{\mathbb{I}}(m_i, m_j)$  single nucleus transition symmetry function from irreducible 0th-rank tensor  
 $\mathbf{p}_{\mathbb{I}}(m_i, m_j)$  single nucleus transition symmetry function from irreducible 1st-rank tensor  
 $\mathbf{d}_{\mathbb{I}}(m_i, m_j)$  single nucleus transition symmetry function from irreducible 2nd-rank tensor  
 $\mathfrak{f}_{\mathbb{I}}(m_i, m_j)$  single nucleus transition symmetry function from irreducible 3rd-rank tensor  
 $\mathfrak{s}_{\mathbb{II}}(M_i, M_j)$  two strongly coupled nuclei transition symmetry function from irreducible 1st-rank tensor  
 $\mathfrak{p}_{\mathbb{II}}(M_i, M_j)$  two strongly coupled nuclei transition symmetry function from irreducible 1st-rank tensor  
 $\mathfrak{d}_{\mathbb{II}}(M_i, M_j)$  two strongly coupled nuclei transition symmetry function from irreducible 2nd-rank tensor

$\mathbb{f}_{\mathbb{I}}(M_i, M_j)$  two strongly coupled nuclei transition symmetry function from irreducible 3rd-rank tensor  
 $(\mathbb{P}\mathbb{P})_{IS}(m_{I,i}, m_{S,i}, m_{I,j}, m_{S,j})$  two weakly coupled nuclei transition symmetry function from irreducible 1st-rank tensor  
 $(\mathbb{D}\mathbb{P})_{IS}(m_{I,i}, m_{S,i}, m_{I,j}, m_{S,j})$  two weakly coupled nuclei transition symmetry function from irreducible 2nd-rank tensor  
 $(\mathbb{P}\mathbb{D})_{IS}(m_{I,i}, m_{S,i}, m_{I,j}, m_{S,j})$  two weakly coupled nuclei transition symmetry function from irreducible 3rd-rank tensor  
 $(\mathbf{P}\mathbf{P})_{IS}(m_{I,i}, m_{S,i}, m_{I,j}, m_{S,j})$  two weakly coupled nuclei transition symmetry function from irreducible 1st-rank tensor (scaled)  
 $(\mathbf{D}\mathbf{P})_{IS}(m_{I,i}, m_{S,i}, m_{I,j}, m_{S,j})$  two weakly coupled nuclei transition symmetry function from irreducible 2nd-rank tensor (scaled)  
 $(\mathbf{P}\mathbf{D})_{IS}(m_{I,i}, m_{S,i}, m_{I,j}, m_{S,j})$  two weakly coupled nuclei transition symmetry function from irreducible 3rd-rank tensor (scaled)  
 $\mathbb{c}_0(m_i, m_j)$  single nucleus  $\mathbf{p}_{\mathbb{I}}$  and  $\mathbb{f}_{\mathbb{I}}$  hybrid transition symmetry function  
 $\mathbb{c}_2(m_i, m_j)$  single nucleus  $\mathbf{p}_{\mathbb{I}}$  and  $\mathbb{f}_{\mathbb{I}}$  hybrid transition symmetry function  
 $\mathbb{c}_4(m_i, m_j)$  single nucleus  $\mathbf{p}_{\mathbb{I}}$  and  $\mathbb{f}_{\mathbb{I}}$  hybrid transition symmetry function  
 $\mathbf{c}_0(m_i, m_j)$  single nucleus  $\mathbf{p}_{\mathbb{I}}$  and  $\mathbb{f}_{\mathbb{I}}$  hybrid transition symmetry function (scaled)  
 $\mathbf{c}_2(m_i, m_j)$  single nucleus  $\mathbf{p}_{\mathbb{I}}$  and  $\mathbb{f}_{\mathbb{I}}$  hybrid transition symmetry function (scaled)  
 $\mathbf{c}_4(m_i, m_j)$  single nucleus  $\mathbf{p}_{\mathbb{I}}$  and  $\mathbb{f}_{\mathbb{I}}$  hybrid transition symmetry function (scaled)  
 $\kappa^{(t)}$  the shear ratio for shearing multi-dimensional signal parallel to  $t$  axis.  
 $\kappa^{(\omega)}$  the shear ratio for shearing multi-dimensional signal parallel to  $\omega$  axis.  
 $\zeta^{(t)}$  scale factor for  $t$  axis.  
 $\zeta^{(\omega)}$  scale factor for  $\omega$  axis.  
 $\mathfrak{A}(\omega)$  absorption-mode lineshape  
 $\mathfrak{D}(\omega)$  dispersion-mode lineshape

## Acronyms

NMR Nuclear Magnetic Resonance  
 MAS Magic-Angle Spinning  
 MAF Magic-Angle Flipping  
 AHT Average Hamiltonian Theory  
 DAS Dynamic-Angle Spinning  
 DOR DObble Rotation  
 MQ-MAS Multiple-Quantum Magic-Angle Spinning  
 ST-MAS Satellite-Transition Magic-Angle Spinning  
 DQF-ST-MAS Double-Quantum Filtered Satellite-Transition Magic-Angle Spinning  
 MQ-DOR Multiple-Quantum DObble Rotation  
 SEDOR Spin Echo DObble Resonance  
 COASTER Correlation Of Anisotropies Separated Through Echo Refocusing  
 HETCOR HETeronuclear CORrelation

HSQC Heteronuclear Single-Quantum Correlation

PASS Phase Adjusted Spinning Sidebands

TOP Two-dimensional One Pulse

VACSY Variable-Angle Correlation SpectroscopY

## 1. Introduction

Nuclear Magnetic Resonance (NMR) spectroscopy has a wealth of nuclear spin interactions, each capable of providing exquisite detail about local structure and dynamics around a nucleus[1, 2]. Interpreting an NMR spectrum, however, can be challenging when many interactions manifest together in the spectrum. Fortunately, NMR spectroscopists can design experiments to remove the influence of specific interactions on an NMR spectrum. This suppression is achieved by manipulating the sample’s spatial and spin degrees of freedom, which in turn modulates each interaction’s contribution to the NMR frequency differently depending on its underlying spatial and spin symmetry[3, 4]. Clearly, a key to success when developing any new NMR method is understanding which frequency contributions change and which remain invariant under these spatial and spin manipulations.

NMR has an additional advantage in that spatial and spin degrees of freedom can be manipulated on a much faster time scale than the lifetime of the NMR excited state. In this context, the spin echo[5] has become a central theme in the design of many NMR experiments. For example, by applying a  $\pi$  pulse to a precessing nuclear magnetization, i.e., a manipulation of spin degrees of freedom, there will be a sign change for any frequency contributions arising from Hamiltonian contributions that are linearly dependent on the spin operator  $\hat{I}_z$ , such as nuclear shielding. This sign change leads to an effective time reversal of the system evolution and is responsible for forming a “Hahn” echo. Since frequency contributions arising from spin Hamiltonians that are bilinear in  $I_z$ , such as homonuclear  $J$  coupling, are unchanged by a  $\pi$  pulse, this symmetry difference can be used to separate linear and bilinear contributions to the NMR spectrum[6]. Similarly, Magic-Angle Spinning (MAS)[7, 8] manipulates spatial degrees of freedom: sample rotation causes anisotropic contributions to the NMR frequency to oscillate, leading to the formation of a train of rotary echoes. The NMR signal measured at these rotary echo tops has no contribution from the oscillating frequency components.

With the development of Average Hamiltonian Theory (AHT)[9], Waugh and coworkers provided the field with a powerful tool for understanding how NMR Hamiltonians transform under spatial and spin manipulations and for designing experiments that selectively eliminate the influence of specific nuclear spin interactions on the NMR spectrum. While this approach was initially applied in the context of solid samples with strong nuclear magnetic dipole couplings[10], it was soon adapted for designing all types of liquid- and solid-state NMR experiments[11]. This approach is particularly powerful when all contributions to the spin Hamiltonian are expressed in terms of irreducible spherical tensors[12, 13], whose symmetry properties under the orthogonal rotation subgroup are easily discerned. For electric quadrupole ( $I > 1/2$ ) nuclei, however, the manipulations of spin degrees of freedom are often poorly described by the orthogonal rotation subgroup since the rf field strength is typically orders of magnitude smaller than the electric quadrupole splitting. In this case, using AHT to design time reversal sequences can become challenging. This fact alone may explain why solid-state NMR of electric quadrupole nuclei has developed at a slower pace than that of coupled spin 1/2 nuclei.

Despite this difficulty, it is indeed possible to design time reversal experiments for electric quadrupole nuclei, and over the years, a systematic approach has developed in many laboratories around the world. In this review, we attempt to distill these approaches into their essential elements and present them in a single consistent framework. In Section 2, we define these elements, showing how the various frequency components transform under manipulations of spatial and spin degrees of freedom. Once these definitions are in place, we generalize Bodenhausen and coworkers’[14] concept of coherence transfer pathways to the “spatial pathway” which maps into a set of *spatial symmetry pathways* and the “transition pathway,” also referred to as “coherence transfer walkways” by Kwak and Gan[15], which maps into a set of *transition symmetry pathways*. In Section 3, we give several illustrative examples of how these symmetry pathways can be used to describe experiments that selectively eliminate specific contributions to an NMR spectrum. In Section 4, we examine how symmetry pathways provide a more complete context for designing experiments that yield pure absorption mode lineshapes using either the hypercomplex[16] or shifted-echo approach[17]. In Section 5, we review the mathematics of affine transforms for simplifying the analysis and interpretation of multi-dimensional

spectra and also discuss their implementation during signal processing. In Section 6, we give a short review of the work of Samoson, Sun, and Pines[3] on the use of group theory to understand the averaging of spatial symmetries. And finally, for the reader who would like to dig a little deeper into the theoretical background, we present the supporting theory behind this framework with the derivations of various first- and second-order corrections to the NMR frequency in the Appendix.

## 2. Frequency component symmetries

The degrees of freedom influencing an NMR resonance frequency in the semi-classical approximation can be separated into those associated with the quantized reorientations of nuclear spin angular momentum vectors and those associated with the macroscopic (classical) translations and reorientations of the lattice containing the NMR active nuclei. We assume that the sample is placed in a uniform external magnetic field, so the sample's macroscopic translational degrees of freedom will not influence the NMR transition frequency. Thus, we begin by noting that the NMR frequency,  $\Omega(\Theta, i, j)$ , of an  $i \rightarrow j$  transition between the eigenstates of the stationary-state semi-classical Hamiltonian in a sample with a lattice spatial orientation,  $\Theta$ , can be written as a sum of components,

$$\Omega(\Theta, i, j) = \sum_k \Omega_k(\Theta, i, j), \quad (1)$$

with each component,  $\Omega_k(\Theta, i, j)$ , separated into three parts:

$$\Omega_k(\Theta, i, j) = \omega_k \Xi_L^{(k)}(\Theta) \xi_\ell^{(k)}(i, j), \quad (2)$$

where  $\omega_k$  gives the size of the  $k$ th frequency component, and  $\Xi_L^{(k)}(\Theta)$  and  $\xi_\ell^{(k)}(i, j)$  are functions of the sample's spatial orientation and the quantized NMR transition, respectively. The experimentalist indirectly influences a frequency component  $\Omega_k$  by direct manipulation of the quantum transition,  $i \rightarrow j$ , and the spatial orientation,  $\Theta$  of the sample, as highlighted in Fig. 1. The orientation of the lattice,  $\Theta$ , typically described with Euler angles,  $\Theta = (\alpha, \beta, \gamma)$ , is that of the crystal axis frame,  $(X, Y, Z)$ , in the laboratory frame,  $(x, y, z)$ , fixed by the external magnetic field direction along  $z$ . The transition from quantized energy level  $i$  to  $j$  is one of  $\Upsilon!/(\Upsilon - 2)!$  possible transitions between  $\Upsilon$  levels. Here we count  $i \rightarrow j$  and  $j \rightarrow i$  as different transitions. The number of quantized energy levels for  $N$  coupled nuclei is

$$\Upsilon_{\{I_1, I_2, \dots, I_N\}} = \prod_{u=1}^N (2I_u + 1), \quad (3)$$

where  $I_u$  is the total spin angular momentum quantum number of the  $u$ th nucleus and the system of coupled nuclei under consideration is represented with the notation,  $\{I_1, I_2, \dots, I_N\}$ . Thus, a single spin with angular momentum quantum number  $I$ , indicated by  $\{I\}$ , will have  $\Upsilon_{\{I\}} = 2I + 1$  energy levels and  $2I(2I + 1)$  possible NMR transitions. Similarly,  $\{I, S\}$ , a two spin system will have  $\Upsilon_{\{I, S\}} = (2I + 1) \cdot (2S + 1)$  energy levels and  $[(2I + 1) \cdot (2S + 1)]!/((2I + 1) \cdot (2S + 1) - 2)!$  transitions.

We represent a transition (coherence) from state  $i$  to  $j$  using the outer product notation  $|j\rangle\langle i|$ ; a notation which one can associate with a raising or lowering operator,  $\hat{I}_\pm^{(i-j)}$ , in a fictitious spin-half or single-transition operator formalism[18, 19] expansion of the density matrix. We also represent longitudinal order involving states inside square brackets. For example, the single-transition longitudinal Zeeman order associated with states  $i$  and  $j$  is represented as  $[i, j]$ ; a notation which one could again associate with the  $\hat{I}_z^{(i-j)}$  operator in a fictitious spin-1/2 or single-transition operator formalism[18, 19]. Multi-state longitudinal orders, such as Zeeman order of a single spin  $I$ , are represented in square brackets as  $[z_I]$  and would be analogous to  $\hat{I}_z$  in a product operator[20] expansion of the density matrix. Similarly, we represent magnetic dipolar order in two coupled spins with the notation  $[z_{II}^2]$ , which, again, would be analogous to longitudinal two spin order  $\hat{I}_{1z}\hat{I}_{2z}$  in a product operator description. Likewise, the electric quadrupolar order of a single spin,  $I$ , will be represented with the notation  $[z_I^2]$ .

We will also find it convenient to represent the transition  $|j\rangle\langle i|$  as an open circle on a *transition diagram*, as shown in Fig. 2 for each of the six possible transitions in the  $\{I = 1\}$  case. Similarly, a single-transition Zeeman

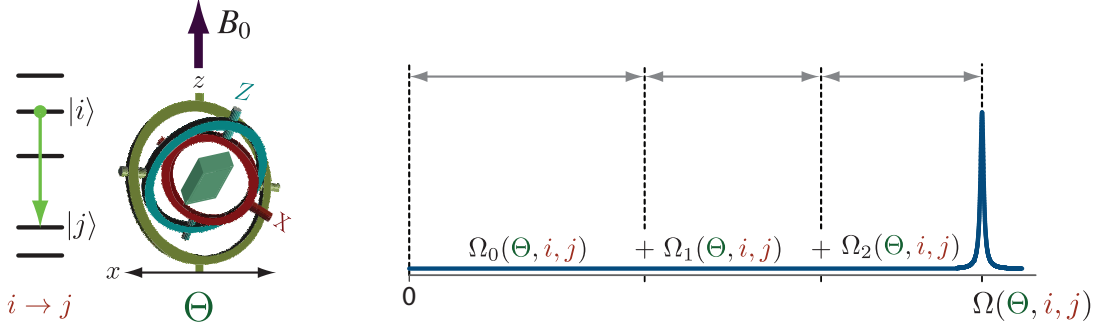


Figure 1: The degrees of freedom that influence a resonance frequency in an NMR spectrum in a uniform external magnetic field can be separated into those associated with transitions between eigenstates  $i \rightarrow j$  of the stationary state semi-classical Hamiltonian and the macroscopic orientational degrees of freedom associated with the lattice containing the NMR active nuclei. The orientation of the lattice,  $\Theta$ , is that of the crystal axis frame ( $X, Y, Z$ ) in the laboratory frame ( $x, y, z$ ) fixed by the external uniform magnetic field direction ( $z$ ), and described using Euler angles,  $\Theta = (\alpha, \beta, \gamma)$ . The NMR frequency,  $\Omega(\Theta, i, j)$ , is a sum of components, each a function of the  $i \rightarrow j$  transition and sample orientation  $\Theta$  with respect to a uniform external magnetic field direction.

order is represented on the horizontal dashed line of the transition diagram with two open squares around the two corresponding single transition Zeeman order states, as shown in Fig. 3A-C in the  $\{I = 1\}$  case. Multi-state longitudinal Zeeman order is represented as a solid line over the horizontal dashed line as shown in Fig. 3D. A transition diagram is labeled with states like a density matrix, except it is turned  $45^\circ$ , with longitudinal order among states appearing on the horizontal dashed line connecting solid gray circles and off-diagonal transitions (coherences) between states appearing above and below the horizontal dashed line. Note, however, that we use a transition diagram only to indicate when a particular transition (coherence) exists, and unlike a density matrix, do not represent the amplitude of a transition (or population) on a transition diagram. This is done in the same spirit as a coherence transfer pathway diagram, where the pathway efficiency is not represented in the diagram.

Manipulations of spatial and spin transition degrees of freedom can often be performed on a time scale faster than the lifetime of the NMR excited state. Knowing the time dependence of the spatial,  $\Theta(t)$ , and spin transition,  $(i \rightarrow j)(t)$ , functions, the average frequency of the  $k$ th component can be calculated using

$$\bar{\Omega}_k = \frac{\omega_k}{t} \int_0^t \left[ \Xi_L^{(k)}(\Theta(t')) \xi_\ell^{(k)}(i(t'), j(t')) \right] dt', \quad (4)$$

which one might call “Average Frequency Theory.”

Manipulations of a spatial orientation function,  $\xi_\ell(\Theta)$ , are well described using the orthogonal rotation subgroup. To emphasize spatial symmetries we classify the spatial functions,  $\xi_\ell(\Theta)$ , using the upper-case symbols  $\mathbb{S}$ ,  $\mathbb{P}(\Theta)$ ,  $\mathbb{D}(\Theta)$ ,  $\mathbb{F}(\Theta)$ , and  $\mathbb{G}(\Theta)$  according to:

$$\mathbb{S}^{\{\lambda\}} \propto R_{0,0}^{\{\lambda\}}, \quad \mathbb{P}^{\{\lambda\}}(\Theta) \propto R_{1,0}^{\{\lambda\}}(\Theta), \quad \mathbb{D}^{\{\lambda\}}(\Theta) \propto R_{2,0}^{\{\lambda\}}(\Theta), \quad \mathbb{F}^{\{\lambda\}}(\Theta) \propto R_{3,0}^{\{\lambda\}}(\Theta), \quad \mathbb{G}^{\{\lambda\}}(\Theta) \propto R_{4,0}^{\{\lambda\}}(\Theta), \quad (5)$$

where the  $R_{L,0}^{\{\lambda\}}(\Theta)$  are elements of irreducible tensors of rank  $L$  in the laboratory frame describing the spatial part of a frequency component arising from a given nuclear spin interaction, here generically labeled as  $\lambda$ . The proportionality constants are interaction specific, derived in A.6, and given in Table 1. Using the orthogonal rotation subgroup, the spatial reorientation trajectory,  $\Theta(t)$ , or *spatial pathway*, maps into a set of *spatial symmetry pathways* associated with each  $\Xi_k(\Theta)$ . One of the most common spatial pathways in NMR is reorienting the sample through an angle  $\phi_R = \omega_R t$  about a single axis at an angle  $\theta_R$  with respect to the external magnetic field, defined with  $\Theta_R = (\phi_R, \theta_R, 0)$ , as illustrated in Fig 4A. In this case, we further separate each spatial symmetry function into a sum of functions with

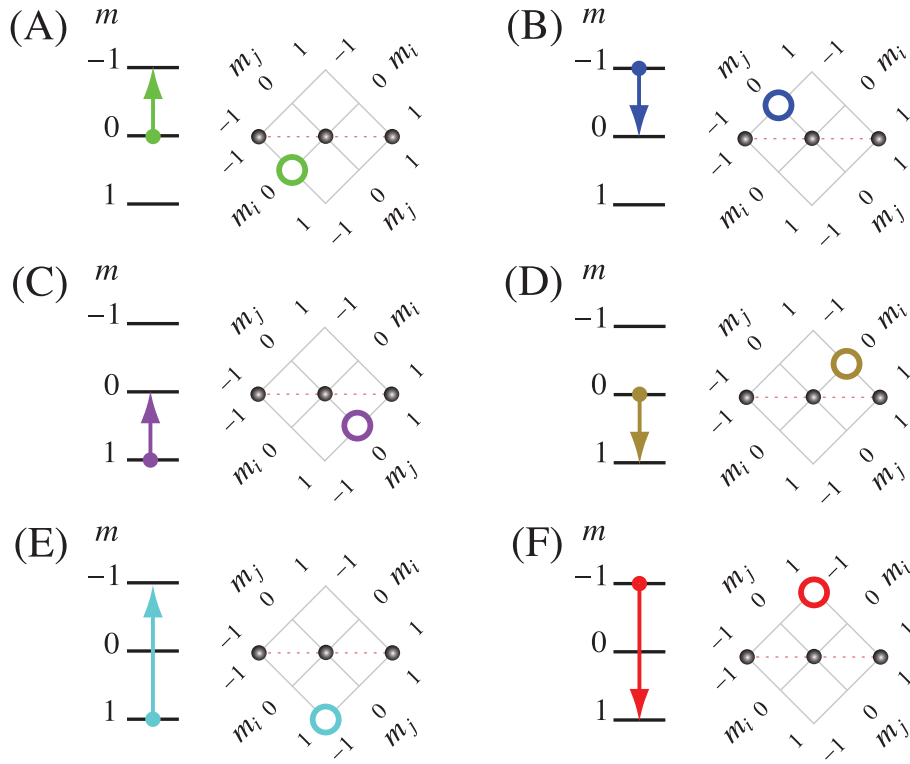


Figure 2: Transition diagrams illustrating the six possible transitions in a  $\{I = 1\}$  system: (A)  $|-1\rangle\langle 0|$ , (B)  $|0\rangle\langle -1|$ , (C)  $|0\rangle\langle 1|$ , (D)  $|1\rangle\langle 0|$ , (E)  $|-1\rangle\langle 1|$ , and (F)  $|1\rangle\langle -1|$ , where  $|m_j\rangle\langle m_i|$  indicates a transition from the initial state  $m_i$  to the final state  $m_j$ .

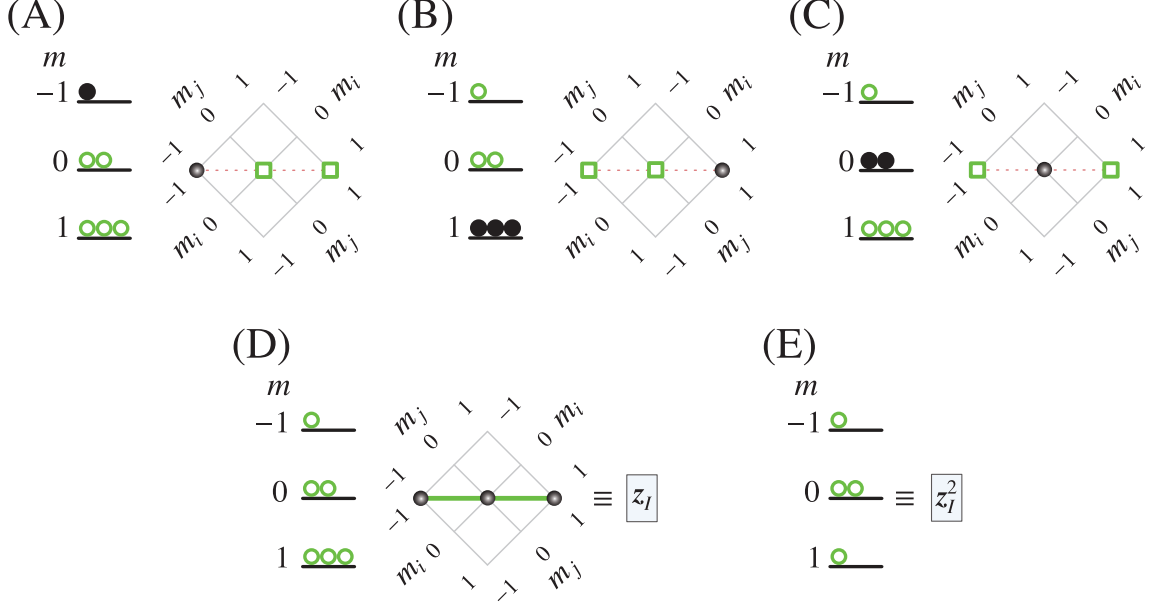


Figure 3: Energy level and transition diagrams illustrating various longitudinal orders in a  $\{I = 1\}$  system. Open circles on energy level diagrams represent populations associated with longitudinal order shown in the adjacent transition diagram, while closed circles on the energy level diagram represent populations not associated with the longitudinal order shown in the adjacent transition diagram. Single transition Zeeman order is indicated on the horizontal dashed line with two open squares around the two corresponding single transition Zeeman order states in (A) for  $[-1, 0]$ , in (B) for  $[0, +1]$ , and in (C) for  $[-1, +1]$ , where  $[m_i, m_j]$  indicates the single energy transition Zeeman order involving states  $m_i$  and  $m_j$ . In (D), multi-state longitudinal Zeeman order involving populations from all energy levels is represented by a solid horizontal line or the symbol  $z_I$  inside a square. In (E), multi-state longitudinal quadrupolar order involving populations from all energy levels is represented by the symbol  $z_I^2$  inside a square.



symbols  $\mathbb{P}_n^{\{\lambda\}}(\theta_R, \phi_R)$ ,  $\mathbb{D}_n^{\{\lambda\}}(\theta_R, \phi_R)$ ,  $\mathbb{F}_n^{\{\lambda\}}(\theta_R, \phi_R)$ , and  $\mathbb{G}_n^{\{\lambda\}}(\theta_R, \phi_R)$  and defined by:

$$\mathbb{P}^{\{\lambda\}}(\Theta_R) = \mathbb{P}_0^{\{\lambda\}}(\theta_R) + \mathbb{P}_1^{\{\lambda\}}(\theta_R, \phi_R), \quad (6)$$

$$\mathbb{D}^{\{\lambda\}}(\Theta_R) = \mathbb{D}_0^{\{\lambda\}}(\theta_R) + \mathbb{D}_1^{\{\lambda\}}(\theta_R, \phi_R) + \mathbb{D}_2^{\{\lambda\}}(\theta_R, \phi_R), \quad (7)$$

$$\mathbb{F}^{\{\lambda\}}(\Theta_R) = \mathbb{F}_0^{\{\lambda\}}(\theta_R) + \mathbb{F}_1^{\{\lambda\}}(\theta_R, \phi_R) + \mathbb{F}_2^{\{\lambda\}}(\theta_R, \phi_R) + \mathbb{F}_3^{\{\lambda\}}(\theta_R, \phi_R), \quad (8)$$

$$\mathbb{G}^{\{\lambda\}}(\Theta_R) = \mathbb{G}_0^{\{\lambda\}}(\theta_R) + \mathbb{G}_1^{\{\lambda\}}(\theta_R, \phi_R) + \mathbb{G}_2^{\{\lambda\}}(\theta_R, \phi_R) + \mathbb{G}_3^{\{\lambda\}}(\theta_R, \phi_R) + \mathbb{G}_4^{\{\lambda\}}(\theta_R, \phi_R), \quad (9)$$

as derived in A.5. Under continuous sample rotation, the  $n \neq 0$  components become modulated at a frequency of  $n\omega_R$  and average to zero at integer multiples of  $2\pi/n\omega_R$ . The  $n = 0$  components are not modulated by sample rotation and will be zero only when the sample rotation axis,  $\theta_R$ , is set to one of the corresponding roots of the  $L$ -rank Legendre polynomial, given in Table 2. Historically, ‘‘Magic’’-Angle Spinning (MAS) was developed to average away first-order anisotropies, which are second ( $L = 2$ ) rank in nature[7, 8]. Here we expand the usage of the term with the prefixes given in Table 2 to describe sample rotation about any single axis that removes anisotropies of rank  $L$ . To simplify usage in figures and discussions, we further define for the  $n \neq 0$  single-axis rotation spatial symmetry functions

$L$	$\theta_M^{(L)}$		Method
1	90.00°		P-MAS
2	54.74°		D-MAS
3	39.23°	90.00°	F-MAS
4	30.56°	70.12°	G-MAS

where

$$P_n^{\{\lambda\}}(\theta_R, \phi_R) = \mathbb{P}_n^{\{\lambda\}}\left(\theta_R, \phi_R - \gamma + \psi'_{1,n}^{\{\lambda\}} - \frac{\pi}{2n}\right), \quad (10)$$

$$D_n^{\{\lambda\}}(\theta_R, \phi_R) = \mathbb{D}_n^{\{\lambda\}}\left(\theta_R, \phi_R - \gamma + \psi'_{2,n}^{\{\lambda\}} - \frac{\pi}{2n}\right), \quad (11)$$

$$F_n^{\{\lambda\}}(\theta_R, \phi_R) = \mathbb{F}_n^{\{\lambda\}}\left(\theta_R, \phi_R - \gamma + \psi'_{3,n}^{\{\lambda\}} - \frac{\pi}{2n}\right), \quad (12)$$

$$G_n^{\{\lambda\}}(\theta_R, \phi_R) = \mathbb{G}_n^{\{\lambda\}}\left(\theta_R, \phi_R - \gamma + \psi'_{4,n}^{\{\lambda\}} - \frac{\pi}{2n}\right), \quad (13)$$

$$n\psi'_{L,n}^{\{\lambda\}} = \tan^{-1} \frac{\Im\{R'_{L,n}^{\{\lambda\}} e^{in\gamma}\}}{\Re\{R'_{L,n}^{\{\lambda\}} e^{in\gamma}\}}, \quad (14)$$

Table 2: Roots of Legendre polynomials of  $\cos \theta$  where  $P_L(\cos \theta_M^{(L)}) = 0$ , with the associated single axis rotation NMR spatial averaging method.

and  $\Re\{z\}$  and  $\Im\{z\}$  represent the real and imaginary parts, respectively, of a complex number  $z$ . Here,  $R'_{L,n}^{\{\lambda\}}$  are elements of irreducible spherical

$\lambda$	$q$	$\sigma$	$d_{II}$	$d_{IS}$	$J_{II}$	$J_{IS}$
$\mathbb{S}^{\{\lambda\}}/R_{0,0}^{\{\lambda\}}$	-	$-\frac{1}{\sigma_{\text{iso}}}\sqrt{\frac{1}{3}}$	-	-	-	$-\frac{1}{J_{\text{iso}}}\sqrt{\frac{1}{3}}$
$\mathbb{P}^{\{\lambda\}}/R_{1,0}^{\{\lambda\}}$	-	-	-	-	$-\frac{1}{\zeta_J^{(a)}}$	-
$\mathbb{D}^{\{\lambda\}}/R_{2,0}^{\{\lambda\}}$	$\frac{1}{3\zeta_q}$	$\frac{1}{\zeta_\sigma}\sqrt{\frac{2}{3}}$	$\frac{2}{\zeta_d}$	$\frac{2}{\zeta_d}\sqrt{\frac{2}{3}}$	$\frac{1}{\zeta_J}$	$\frac{1}{\zeta_J}\sqrt{\frac{2}{3}}$
$\mathbb{S}^{\{\lambda q_I\}}/R_{0,0}^{\{\lambda q_I\}}$	$\frac{1}{9\zeta_q^2}$	$\frac{1}{\zeta_\sigma}\frac{1}{3\zeta_q}\sqrt{\frac{6}{5}}$	-	$\frac{2}{\zeta_d}\frac{1}{3\zeta_q^{\{I\}}}\sqrt{\frac{6}{5}}$	-	$\frac{1}{\zeta_J}\frac{1}{3\zeta_q^{\{I\}}}\sqrt{\frac{6}{5}}$
$\mathbb{D}^{\{\lambda q_I\}}/R_{2,0}^{\{\lambda q_I\}}$	$\frac{1}{9\zeta_q^2}$	$-\frac{1}{\zeta_\sigma}\frac{1}{3\zeta_q}\sqrt{\frac{3}{7}}$	-	$-\frac{2}{\zeta_d}\frac{1}{3\zeta_q^{\{I\}}}\sqrt{\frac{3}{7}}$	-	$-\frac{1}{\zeta_J}\frac{1}{3\zeta_q^{\{I\}}}\sqrt{\frac{3}{7}}$
$\mathbb{G}^{\{\lambda q_I\}}/R_{4,0}^{\{\lambda q_I\}}$	$\frac{1}{9\zeta_q^2}$	$\frac{1}{\zeta_\sigma}\frac{1}{3\zeta_q}\sqrt{\frac{48}{35}}$	-	$-\frac{2}{\zeta_d}\frac{1}{3\zeta_q^{\{I\}}}\sqrt{\frac{48}{35}}$	-	$-\frac{1}{\zeta_J}\frac{1}{3\zeta_q^{\{I\}}}\sqrt{\frac{48}{35}}$

Table 1: Proportionality constants between  $\Xi^{\{\lambda\}}(\Theta)$  and the irreducible tensor element  $R_{L,0}^{\{\lambda\}}(\Theta)$  for various nuclear spin interactions. Here  $q \equiv$  electric quadrupole coupling,  $\sigma \equiv$  nuclear shielding,  $d_{II} \equiv$  strong dipolar coupling,  $d_{IS} \equiv$  weak dipolar coupling,  $J_{II} \equiv$  strong  $J$  coupling, and  $J_{IS} \equiv$  weak  $J$  coupling.

spatial tensors of rank  $L$  in the sample holder (rotor) frame for the  $\lambda$  interaction. The definitions for  $P_n(\theta_R, \phi_R)$ ,  $D_n(\theta_R, \phi_R)$ ,  $F_n(\theta_R, \phi_R)$ , and  $G_n(\theta_R, \phi_R)$  are constructed to have a  $\phi_R$  dependence that reflects the spatial symmetry independent of the interaction's principal axis system orientation. The symmetry pathways for  $S$  and  $D_n(\theta_R, \phi_R)$  under a spatial pathway of rotation about a single axis are shown in Fig 4B.

In DOR (DOR)[21, 22], where a sample is being reoriented through an angle  $\phi_i = \omega_{R_i} t$  about an axis at an angle  $\theta_i$  with respect to an axis that is also being reoriented through an angle  $\phi_o = \omega_{R_o} t$  at an angle  $\theta_o$  with respect to the external magnetic field, we divide the irreducible tensor element symbols of Eq. (5) into (see A.5)

$$\mathbb{P}^{\{\lambda\}}(\theta_o, \phi_o, \chi_o, \theta_i, \phi_i) = \mathbb{P}_{0,0}^{\{\lambda\}}(\theta_o, \theta_i) + \mathbb{P}_{0,1}^{\{\lambda\}}(\theta_o, \theta_i, \phi_i) + \mathbb{P}_{1,0}^{\{\lambda\}}(\theta_o, \phi_o, \chi_o, \theta_i) + \mathbb{P}_{1,1}^{\{\lambda\}}(\theta_o, \phi_o, \chi_o, \theta_i, \phi_i) \quad (15)$$

$$\begin{aligned} \mathbb{D}^{\{\lambda\}}(\theta_o, \phi_o, \chi_o, \theta_i, \phi_i) = & \mathbb{D}_{0,0}^{\{\lambda\}}(\theta_o, \theta_i) + \sum_{n_i=1}^2 \mathbb{D}_{0,n_i}^{\{\lambda\}}(\theta_o, \theta_i, \phi_i) + \sum_{n_o=1}^2 \mathbb{D}_{n_o,0}^{\{\lambda\}}(\theta_o, \phi_o, \chi_o, \theta_i) \\ & + \sum_{n_o=1}^2 \sum_{n_i=1}^2 \mathbb{D}_{n_o,n_i}^{\{\lambda\}}(\theta_o, \phi_o, \chi_o, \theta_i, \phi_i), \end{aligned} \quad (16)$$

$$\begin{aligned} \mathbb{F}^{\{\lambda\}}(\theta_o, \phi_o, \chi_o, \theta_i, \phi_i) = & \mathbb{F}_{0,0}^{\{\lambda\}}(\theta_o, \theta_i) + \sum_{n_i=1}^3 \mathbb{F}_{0,n_i}^{\{\lambda\}}(\theta_o, \theta_i, \phi_i) + \sum_{n_o=1}^3 \mathbb{F}_{n_o,0}^{\{\lambda\}}(\theta_o, \phi_o, \chi_o, \theta_i) \\ & + \sum_{n_o=1}^3 \sum_{n_i=1}^3 \mathbb{F}_{n_o,n_i}^{\{\lambda\}}(\theta_o, \phi_o, \chi_o, \theta_i, \phi_i), \end{aligned} \quad (17)$$

$$\begin{aligned} \mathbb{G}^{\{\lambda\}}(\theta_o, \phi_o, \chi_o, \theta_i, \phi_i) = & \mathbb{G}_{0,0}^{\{\lambda\}}(\theta_o, \theta_i) + \sum_{n_i=1}^4 \mathbb{G}_{0,n_i}^{\{\lambda\}}(\theta_o, \theta_i, \phi_i) + \sum_{n_o=1}^4 \mathbb{G}_{n_o,0}^{\{\lambda\}}(\theta_o, \phi_o, \chi_o, \theta_i) \\ & + \sum_{n_o=1}^4 \sum_{n_i=1}^4 \mathbb{G}_{n_o,n_i}^{\{\lambda\}}(\theta_o, \phi_o, \chi_o, \theta_i, \phi_i), \end{aligned} \quad (18)$$

where  $\chi_o$  is the initial phase of the outer rotor. Under continuous sample rotation the  $n_i \neq 0$  and  $n_o \neq 0$  components become modulated at frequencies of  $n_i \omega_{R_i} \pm n_o \omega_{R_o}$ , and average to zero at integer multiples of  $2\pi / (n_i \omega_{R_i} \pm n_o \omega_{R_o})$ . Typically,  $\theta_o$  and  $\theta_i$  are set to the zeroes of the second- and fourth-rank Legendre polynomials, so that  $\mathbb{D}_{0,0}(\theta_o, \theta_i) = \mathbb{G}_{0,0}(\theta_o, \theta_i) = 0$ . As before, to simplify usage in figures and discussions, we further define

$$P_{0,0}^{\{\lambda\}}(\theta_o, \theta_i) = \mathbb{P}_{0,0}^{\{\lambda\}}(\theta_o, \theta_i), \quad (19)$$

$$P_{0,n_i}^{\{\lambda\}}(\theta_o, \theta_i, \phi_i) = \mathbb{P}_{0,n_i}^{\{\lambda\}} \left( \theta_o, \theta_i, \phi_i - \gamma + \psi''_{1,n_i} - \frac{\pi}{2n_i} \right), \quad (20)$$

$$P_{n_o,0}^{\{\lambda\}}(\theta_o, \phi_o, \chi_o, \theta_i) = \mathbb{P}_{n_o,0}^{\{\lambda\}}(\theta_o, \phi_o, \chi_o, \theta_i), \quad (21)$$

$$P_{n_o,n_i}^{\{\lambda\}}(\theta_o, \phi_o, \chi_o, \theta_i, \phi_i) = \mathbb{P}_{n_o,n_i}^{\{\lambda\}} \left( \theta_o, \phi_o, \chi_o, \theta_i, \phi_i - \gamma + \psi''_{1,n_i} - \frac{\pi}{2n_i} \right), \quad (22)$$

$$D_{0,0}^{\{\lambda\}}(\theta_o, \theta_i) = \mathbb{D}_{0,0}^{\{\lambda\}}(\theta_o, \theta_i), \quad (23)$$

$$D_{0,n_i}^{\{\lambda\}}(\theta_o, \theta_i, \phi_i) = \mathbb{D}_{0,n_i}^{\{\lambda\}} \left( \theta_o, \theta_i, \phi_i - \gamma + \psi''_{1,n_i} - \frac{\pi}{2n_i} \right), \quad (24)$$

$$D_{n_o,0}^{\{\lambda\}}(\theta_o, \phi_o, \chi_o, \theta_i) = \mathbb{D}_{n_o,0}^{\{\lambda\}}(\theta_o, \phi_o, \chi_o, \theta_i), \quad (25)$$

$$D_{n_o,n_i}^{\{\lambda\}}(\theta_o, \phi_o, \chi_o, \theta_i, \phi_i) = \mathbb{D}_{n_o,n_i}^{\{\lambda\}} \left( \theta_o, \phi_o, \chi_o, \theta_i, \phi_i - \gamma + \psi''_{1,n_i} - \frac{\pi}{2n_i} \right), \quad (26)$$

$$F_{0,0}^{\{\lambda\}}(\theta_o, \theta_i) = \mathbb{F}_{0,0}^{\{\lambda\}}(\theta_o, \theta_i), \quad (27)$$

$$F_{0,n_i}^{\{\lambda\}}(\theta_o, \theta_i, \phi_i) = \mathbb{F}_{0,n_i}^{\{\lambda\}}\left(\theta_o, \theta_i, \phi_i - \gamma + \psi''_{1,n_i} - \frac{\pi}{2n_i}\right), \quad (28)$$

$$F_{n_o,0}^{\{\lambda\}}(\theta_o, \phi_o, \chi_o, \theta_i) = \mathbb{F}_{n_o,0}^{\{\lambda\}}(\theta_o, \phi_o, \chi_o, \theta_i), \quad (29)$$

$$F_{n_o,n_i}^{\{\lambda\}}(\theta_o, \phi_o, \chi_o, \theta_i, \phi_i) = \mathbb{F}_{n_o,n_i}^{\{\lambda\}}\left(\theta_o, \phi_o, \chi_o, \theta_i, \phi_i - \gamma + \psi''_{1,n_i} - \frac{\pi}{2n_i}\right), \quad (30)$$

$$G_{0,0}^{\{\lambda\}}(\theta_o, \theta_i) = \mathbb{G}_{0,0}^{\{\lambda\}}(\theta_o, \theta_i), \quad (31)$$

$$G_{0,n_i}^{\{\lambda\}}(\theta_o, \theta_i, \phi_i) = \mathbb{G}_{0,n_i}^{\{\lambda\}}\left(\theta_o, \theta_i, \phi_i - \gamma + \psi''_{1,n_i} - \frac{\pi}{2n_i}\right), \quad (32)$$

$$G_{n_o,0}^{\{\lambda\}}(\theta_o, \phi_o, \chi_o, \theta_i) = \mathbb{G}_{n_o,0}^{\{\lambda\}}(\theta_o, \phi_o, \chi_o, \theta_i), \quad (33)$$

$$G_{n_o,n_i}^{\{\lambda\}}(\theta_o, \phi_o, \chi_o, \theta_i, \phi_i) = \mathbb{G}_{n_o,n_i}^{\{\lambda\}}\left(\theta_o, \phi_o, \chi_o, \theta_i, \phi_i - \gamma + \psi''_{1,n_i} - \frac{\pi}{2n_i}\right), \quad (34)$$

where

$$n\psi''_{L,n}^{\{\lambda\}} = \tan^{-1} \frac{\Im \left\{ R''_{L,n}^{\{\lambda\}} e^{in\gamma} \right\}}{\Re \left\{ R''_{L,n}^{\{\lambda\}} e^{in\gamma} \right\}}. \quad (35)$$

Here,  $R''_{L,n}^{\{\lambda\}}$  are elements of irreducible spherical spatial tensors of rank  $L$  in the sample holder (inner rotor) frame for the  $\lambda$  interaction. The definitions for spatial symmetry functions  $P_{n_o,n_i}(\dots)$ ,  $D_{n_o,n_i}(\dots)$ ,  $F_{n_o,n_i}(\dots)$ , and  $G_{n_o,n_i}(\dots)$  are constructed to have a  $\phi_o$  and  $\phi_i$  dependence that reflects the spatial symmetry independent of the interaction's principal axis system orientation.

The spin transition function,  $\xi_\ell(i, j)$ , is typically manipulated via the coupling between nuclear magnetic dipole moments and the oscillating magnetic field of externally applied radio frequency pulses. Manipulations of a  $\xi_\ell(i, j)$  can also be described using the orthogonal rotation subgroup, provided the strength of the rf field coupling is orders of magnitude larger than internal spin couplings. To emphasize spin transition symmetries under the orthogonal rotation subgroup we classify the spin transition symmetry functions,  $\xi_\ell(i, j)$ , using the lower-case symbols  $\mathfrak{s}(i, j)$ ,  $\mathfrak{p}(i, j)$ ,  $\mathfrak{d}(i, j)$ , and  $\mathfrak{f}(i, j)$  according to:

$$\mathfrak{s}(i, j) = \langle j | \hat{T}_{0,0}^\circ | i \rangle - \langle i | \hat{T}_{0,0}^\circ | j \rangle, \quad (36)$$

$$\mathfrak{p}(i, j) = \langle j | \hat{T}_{1,0}^\circ | i \rangle - \langle i | \hat{T}_{1,0}^\circ | j \rangle, \quad (37)$$

$$\mathfrak{d}(i, j) = \langle j | \hat{T}_{2,0}^\circ | i \rangle - \langle i | \hat{T}_{2,0}^\circ | j \rangle, \quad (38)$$

$$\mathfrak{f}(i, j) = \langle j | \hat{T}_{3,0}^\circ | i \rangle - \langle i | \hat{T}_{3,0}^\circ | j \rangle, \quad (39)$$

where the  $\hat{T}_{l,0}^\circ$  are irreducible tensor operators[12, 13] in the rotating tilted frame[23]. To simplify usage in figures and discussions, we further define

$$\mathfrak{s}(i, j) = \mathfrak{s}(i, j), \quad \mathfrak{p}(i, j) = \mathfrak{p}(i, j), \quad \mathfrak{d}(i, j) = \sqrt{\frac{2}{3}} \mathfrak{d}(i, j), \quad \mathfrak{f}(i, j) = \sqrt{\frac{10}{9}} \mathfrak{f}(i, j). \quad (40)$$

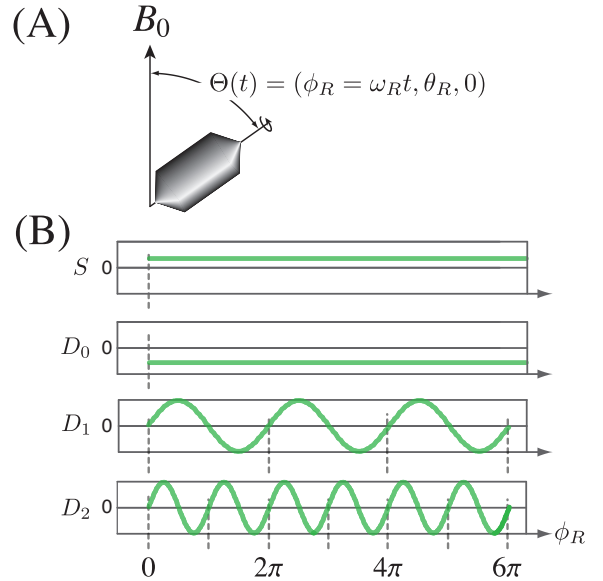


Figure 4: (A) Spatial pathway for sample reorientation through an angle  $\phi_R = \omega_R t$  about a single axis at an angle  $\theta_R$  with respect to the external magnetic field. (B)  $S$ ,  $D_1$ , and  $D_2$  symmetry pathways under a single axis rotation spatial pathway.

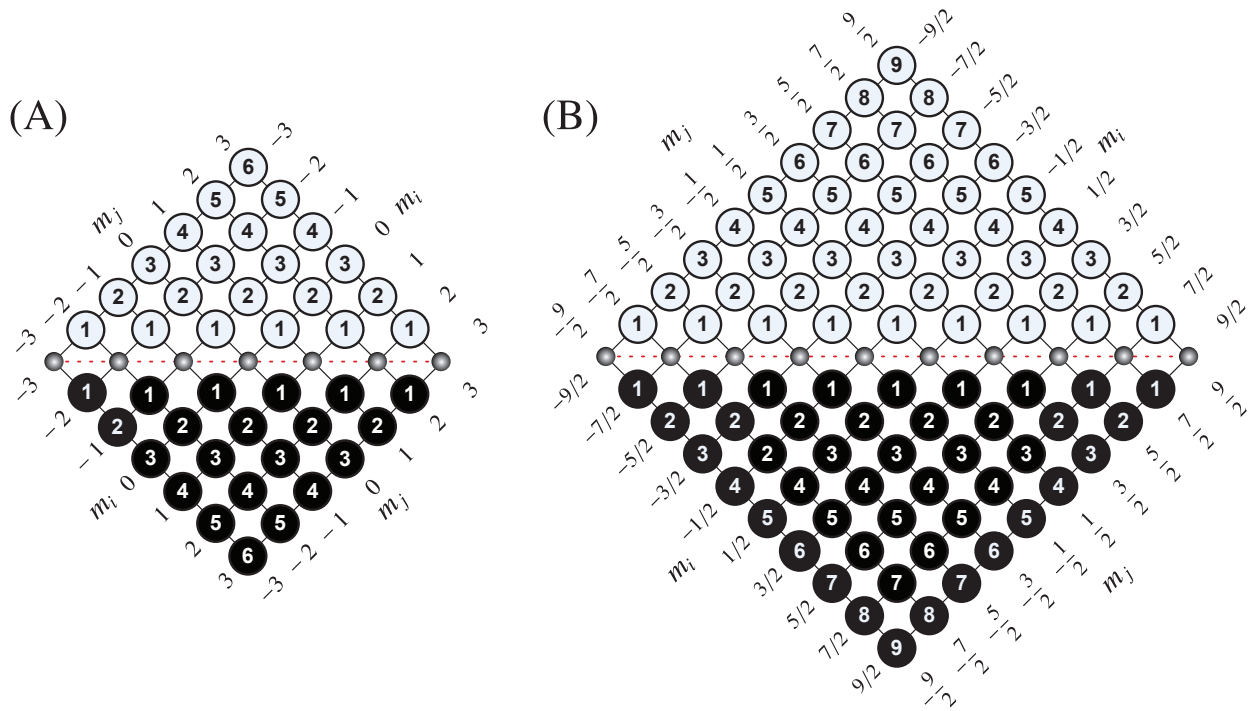


Figure 5: Values of spin transition symmetry function  $p_I(m_i, m_j)$  for a  $\{I\}$  system with (A) integer and (B) half-integer spin values. Values inside black circles are negative.

In the case of a single spin system,  $\{I\}$ , these evaluate to

$$\begin{aligned}
 s_I(m_i, m_j) &= 0, \\
 p_I(m_i, m_j) &= m_j - m_i, \\
 d_I(m_i, m_j) &= m_j^2 - m_i^2, \\
 f_I(m_i, m_j) &= \frac{1}{3} \left[ 5(m_j^3 - m_i^3) + (1 - 3I(I+1))(m_j - m_i) \right],
 \end{aligned} \tag{41}$$

and are given in the “transition symmetry” tables shown in Figs. 5-8 for  $p_I(m_i, m_j)$ ,  $d_I(m_i, m_j)$ , and  $f_I(m_i, m_j)$ . Values shown inside solid black circles are negative. Note that all  $d_I(m_i, m_j)$  are zero for spin  $I < 1$ , and all  $f_I(m_i, m_j)$  are zero for spin  $I < 3/2$ . Our definition of  $p_I(m_i, m_j)$  is identical to the “coherence order”,  $p$ , defined by Bodenhausen *et al.*[14], and our definition of  $d_I(m_i, m_j)$  is identical to the “satellite order”,  $q$ , recently defined by Antonijevic and Bodenhausen[24]. A well-known and important feature evident from Fig. 6 is that the  $d_I(m_i, m_j)$  values vanish for all symmetric  $m \rightarrow -m$  transitions. This has the greatest impact for the Zeeman-allowed  $m = \frac{1}{2} \rightarrow -\frac{1}{2}$  transition of half-integer electric quadrupole nuclei, i.e., the central transition, which as a result of this symmetry is unaffected by the electric quadrupole interaction to first order.

As noted, the spin transition functions  $s(i, j)$ ,  $p(i, j)$ ,  $d(i, j)$ , and  $f(i, j)$  reflect their symmetry under the orthogonal rotation subgroup, which is relevant during rf manipulations in the limit that the rf field strength is larger than all internal frequency contributions. In such a situation, familiar rules hold, such as  $d(i, j)$  values being invariant under a  $\pi$  pulse while  $p(i, j)$  and  $f(i, j)$  change sign. This symmetry is apparent in the transition symmetry tables taking an inversion of values through the  $i, j$  origin as isomorphic to the effect of a non-selective  $\pi$  pulse.

One could extend these definitions to include the transition frequencies of coupled nuclei. As is often the case, however, the problem quickly becomes intractable with an increasing number of coupled nuclei. Here, we will only consider two coupled nuclei in two special cases. In the first case of strong coupling between nuclei, we define the

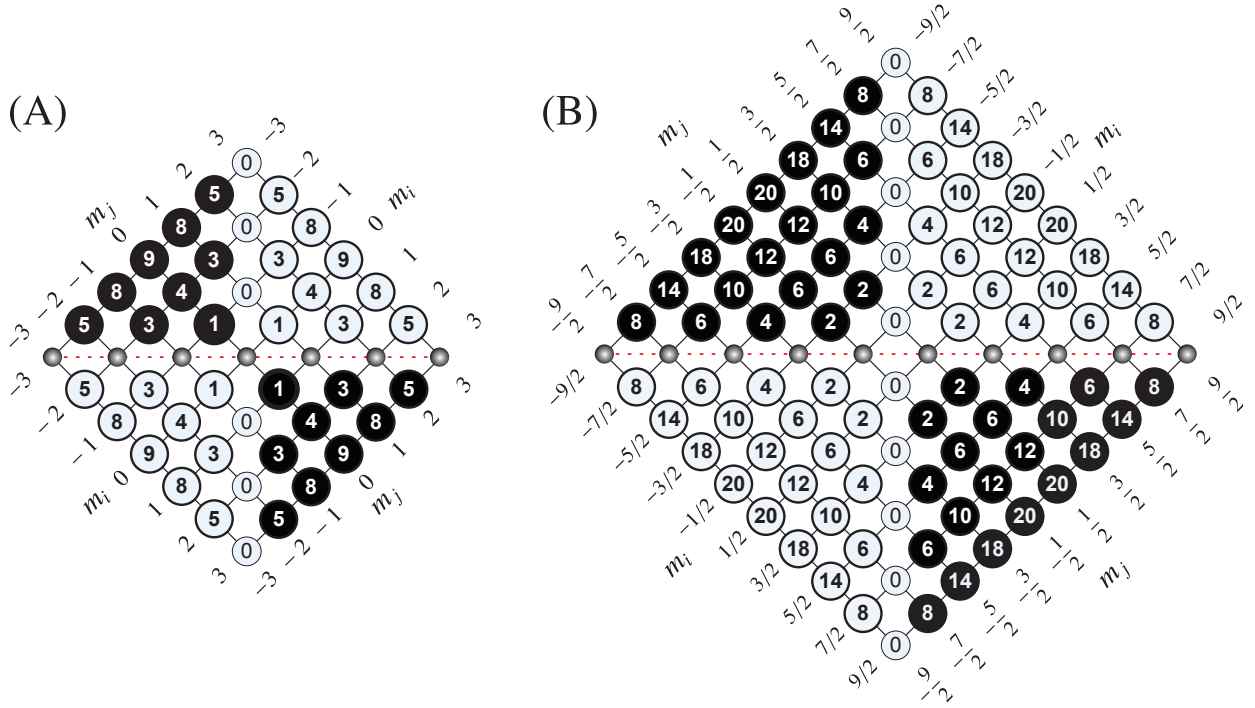


Figure 6: Values of spin transition symmetry function  $d_I(m_i, m_j)$  for a  $\{I\}$  system with (A) integer and (B) half-integer spin values. Values inside black circles are negative.

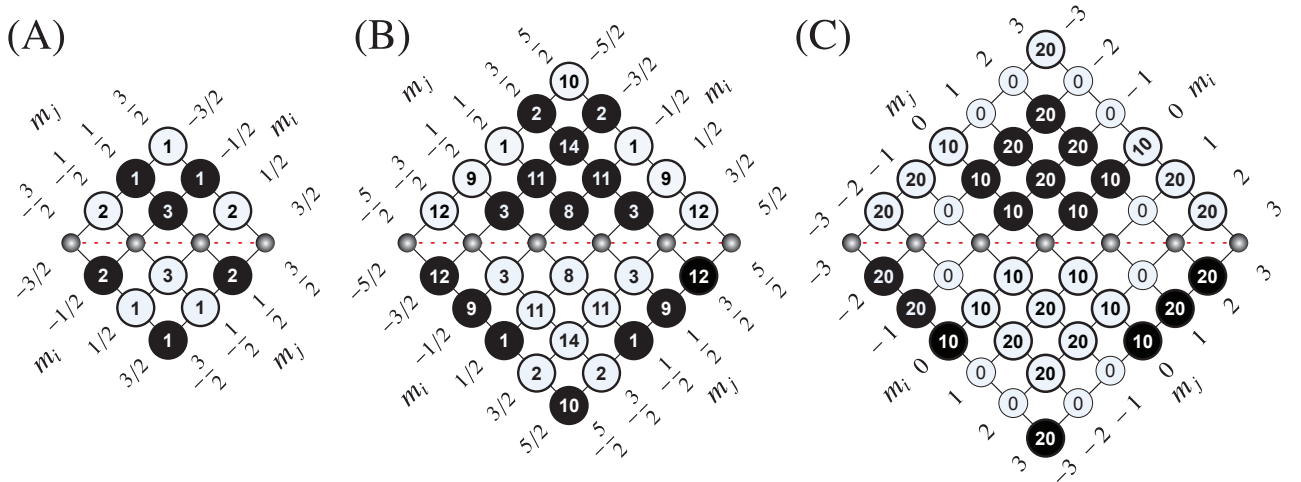


Figure 7: Values of spin transition symmetry functions  $f_I(m_i, m_j)$  for (A)  $\{I = 3/2\}$ , (B)  $\{I = 5/2\}$ , and (C)  $\{I = 3\}$ . Values inside black circles are negative.

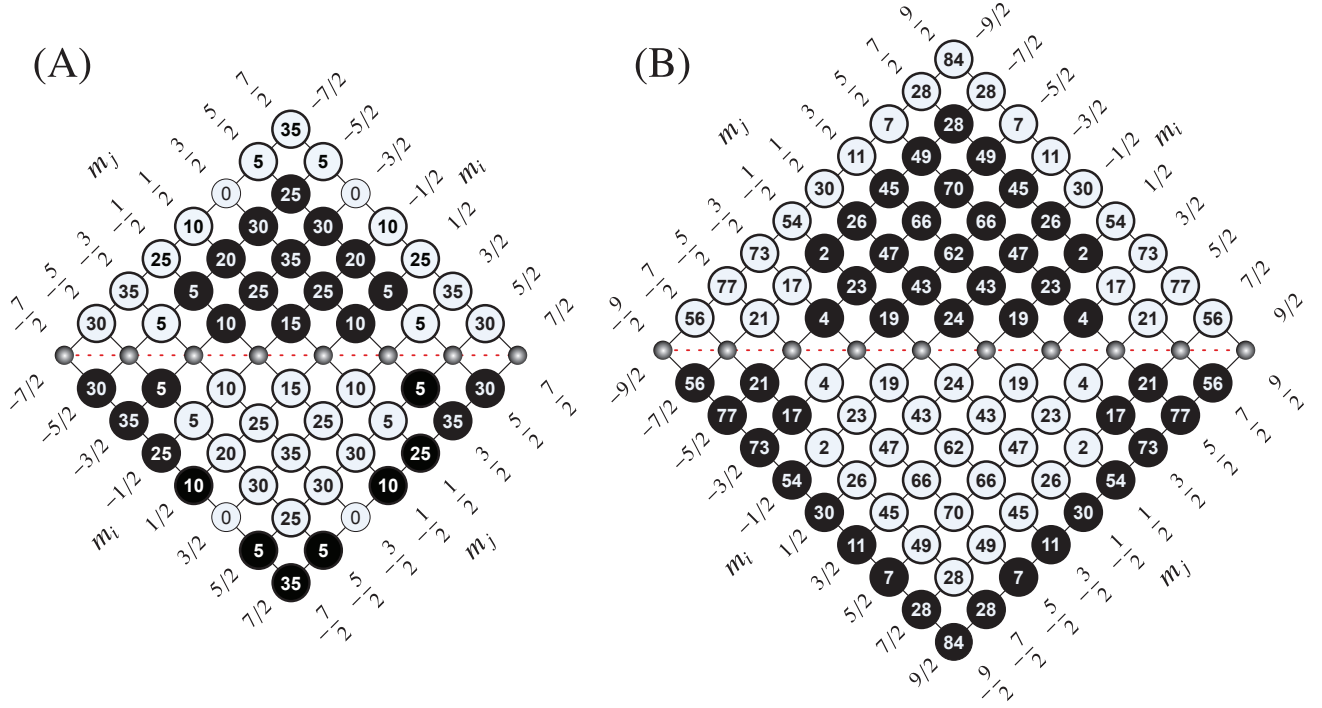


Figure 8: Values of spin transition symmetry functions  $f_I(m_i, m_j)$  for (A)  $\{I = 7/2\}$  and (B)  $\{I = 9/2\}$ . Values inside black circles are negative.

strongly coupled basis set in terms of the individual nuclear basis sets according to

$$|I, M\rangle = \sum_{m_1, m_2} \langle I_1 I_2 m_1 m_2 | I, M \rangle |m_1, m_2\rangle, \quad (42)$$

and write frequency in terms of this strongly coupled eigenstates,  $M_i$ , as

$$\Omega(\Theta, M_i, M_j) = \sum_k \Omega_k(\Theta, M_i, M_j), \quad (43)$$

with each component given by

$$\Omega_k(\Theta, M_i, M_j) = \omega_k \Xi_L^{(k)}(\Theta) \xi_\ell^{(k)}(M_i, M_j). \quad (44)$$

In this context, we define

$$\mathbb{P}_{II}(M_i, M_j) = \langle I, M_j | \hat{T}_{1,0}^\circ(\mathbf{I}_1, \mathbf{I}_2) | I, M_j \rangle - \langle I, M_i | \hat{T}_{1,0}^\circ(\mathbf{I}_1, \mathbf{I}_2) | I, M_i \rangle, \quad (45)$$

$$\mathbb{D}_{II}(M_i, M_j) = \langle I, M_j | \hat{T}_{2,0}^\circ(\mathbf{I}_1, \mathbf{I}_2) | I, M_j \rangle - \langle I, M_i | \hat{T}_{2,0}^\circ(\mathbf{I}_1, \mathbf{I}_2) | I, M_i \rangle. \quad (46)$$

In the second case of weakly coupled nuclei, we write

$$\Omega(\Theta, m_{I,i}, m_{S,i}, m_{I,j}, m_{S,j}) = \sum_k \Omega_k(\Theta, m_{I,i}, m_{S,i}, m_{I,j}, m_{S,j}), \quad (47)$$

with each component given by

$$\Omega_k(\Theta, m_{I,i}, m_{S,i}, m_{I,j}, m_{S,j}) = \omega_k \Xi_L^{(k)}(\Theta) \xi_{\ell_I, \ell_S}^{(k)}(m_{I,i}, m_{S,i}, m_{I,j}, m_{S,j}), \quad (48)$$

using the weakly coupled basis set,  $|m_I m_S\rangle$ , where  $m_{I,i}$  and  $m_{I,j}$  label the eigenstates of the nucleus,  $I$ , and  $m_{S,i}$  and  $m_{S,j}$  the eigenstates of the nucleus,  $S$ . In this context, we define

$$\mathbb{P}_I(m_{I,i}, m_{S,i}, m_{I,j}, m_{S,j}) = \langle m_{I,j}, m_{S,j} | \hat{T}_{1,0}^\circ(\mathbf{I}) | m_{I,j}, m_{S,j} \rangle - \langle m_{I,i}, m_{S,i} | \hat{T}_{1,0}^\circ(\mathbf{I}) | m_{I,i}, m_{S,i} \rangle, \quad (49)$$

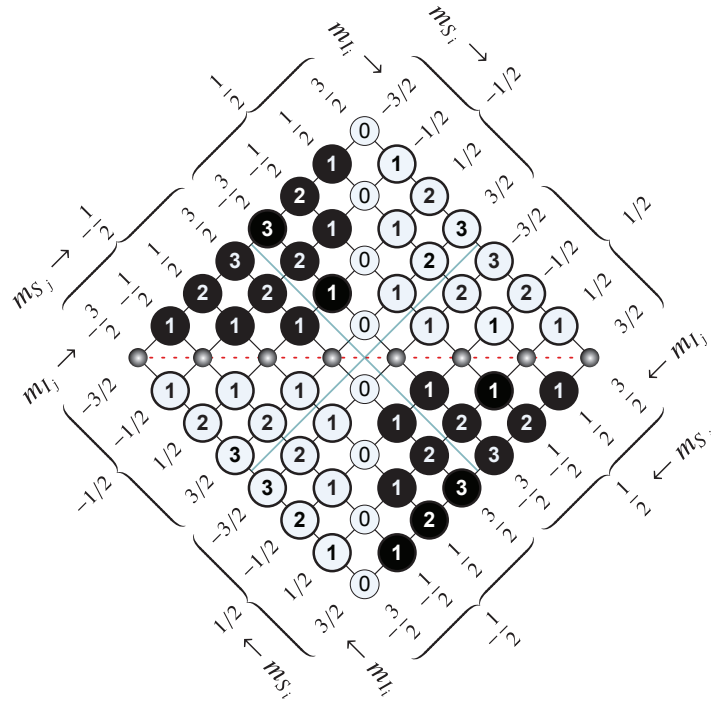


Figure 9: Values of spin transition symmetry functions  $2(\text{pp})_{IS}(m_{I,i}, m_{S,i}, m_{I,j}, m_{S,j})$  for a  $\{I = \frac{3}{2}, S = \frac{1}{2}\}$  system. Values inside black circles are negative.

$$\text{pS}(m_{I,i}, m_{S,i}, m_{I,j}, m_{S,j}) = \langle m_{I,j}, m_{S,j} | \hat{T}_{1,0}^\circ(\mathbf{S}) | m_{I,j}, m_{S,j} \rangle - \langle m_{I,i}, m_{S,i} | \hat{T}_{1,0}^\circ(\mathbf{S}) | m_{I,i}, m_{S,i} \rangle, \quad (50)$$

$$(\text{pp})_{IS}(m_{I,i}, m_{S,i}, m_{I,j}, m_{S,j}) = \langle m_{I,j}, m_{S,j} | \hat{T}_{1,0}^\circ(\mathbf{I}) \hat{T}_{1,0}^\circ(\mathbf{S}) | m_{I,j}, m_{S,j} \rangle - \langle m_{I,i}, m_{S,i} | \hat{T}_{1,0}^\circ(\mathbf{I}) \hat{T}_{1,0}^\circ(\mathbf{S}) | m_{I,i}, m_{S,i} \rangle, \quad (51)$$

$$(\text{dp})_{IS}(m_{I,i}, m_{S,i}, m_{I,j}, m_{S,j}) = \langle m_{I,j}, m_{S,j} | \hat{T}_{2,0}^\circ(\mathbf{I}) \hat{T}_{1,0}^\circ(\mathbf{S}) | m_{I,j}, m_{S,j} \rangle - \langle m_{I,i}, m_{S,i} | \hat{T}_{2,0}^\circ(\mathbf{I}) \hat{T}_{1,0}^\circ(\mathbf{S}) | m_{I,i}, m_{S,i} \rangle, \quad (52)$$

$$(\text{pd})_{IS}(m_{I,i}, m_{S,i}, m_{I,j}, m_{S,j}) = \langle m_{I,j}, m_{S,j} | \hat{T}_{1,0}^\circ(\mathbf{I}) \hat{T}_{2,0}^\circ(\mathbf{S}) | m_{I,j}, m_{S,j} \rangle - \langle m_{I,i}, m_{S,i} | \hat{T}_{1,0}^\circ(\mathbf{I}) \hat{T}_{2,0}^\circ(\mathbf{S}) | m_{I,i}, m_{S,i} \rangle. \quad (53)$$

For two weakly coupled homonuclear spins, it can also be convenient to define

$$\text{pIS}(m_{I,i}, m_{S,i}, m_{I,j}, m_{S,j}) = \text{pI}(m_{I,i}, m_{I,j}) + \text{pS}(m_{S,i}, m_{S,j}). \quad (54)$$

As before, to simplify usage, we further define

$$(\text{pp})_{IS}(m_{I,i}, m_{S,i}, m_{I,j}, m_{S,j}) = 2(\text{pp})_{IS}(m_{I,i}, m_{S,i}, m_{I,j}, m_{S,j}), \quad (55)$$

$$(\text{dp})_{IS}(m_{I,i}, m_{S,i}, m_{I,j}, m_{S,j}) = 2\sqrt{6} (\text{dp})_{IS}(m_{I,i}, m_{S,i}, m_{I,j}, m_{S,j}), \quad (56)$$

$$(\text{pd})_{IS}(m_{I,i}, m_{S,i}, m_{I,j}, m_{S,j}) = 2\sqrt{6} (\text{pd})_{IS}(m_{I,i}, m_{S,i}, m_{I,j}, m_{S,j}), \quad (57)$$

which evaluate to

$$(\text{pp})_{IS}(m_{I,i}, m_{S,i}, m_{I,j}, m_{S,j}) = 2m_{I,j}m_{S,j} - 2m_{I,i}m_{S,i} \quad \text{for } I \geq \frac{1}{2}, S \geq \frac{1}{2}, \quad (58)$$

$$(\text{dp})_{IS}(m_{I,i}, m_{S,i}, m_{I,j}, m_{S,j}) = 6(m_{I,j}^2 m_{S,j} - m_{I,i}^2 m_{S,i}) - 2I(I+1)(m_{S,j} - m_{S,i}), \quad \text{for } I \geq 1, S \geq \frac{1}{2}, \quad (59)$$

$$(\text{pd})_{IS}(m_{I,i}, m_{S,i}, m_{I,j}, m_{S,j}) = 6(m_{S,j}^2 m_{I,j} - m_{S,i}^2 m_{I,i}) - 2S(S+1)(m_{I,j} - m_{I,i}). \quad \text{for } I \geq \frac{1}{2}, S \geq 1. \quad (60)$$

Note that  $(\text{dp})_{IS}(m_{I,i}, m_{S,i}, m_{I,j}, m_{S,j}) = 0$  when  $I \leq \frac{1}{2}$ , and  $(\text{pd})_{IS}(m_{I,i}, m_{S,i}, m_{I,j}, m_{S,j}) = 0$  when  $S \leq \frac{1}{2}$ . Tables of transition symmetry function values for  $(\text{pp})_{IS}(m_{I,i}, m_{S,i}, m_{I,j}, m_{S,j})$ ,  $(\text{dp})_{IS}(m_{I,i}, m_{S,i}, m_{I,j}, m_{S,j})$ , and  $(\text{pd})_{IS}(m_{I,i}, m_{S,i}, m_{I,j}, m_{S,j})$  in selected  $\{I, S\}$  cases are given in Figs. 9 through 13.

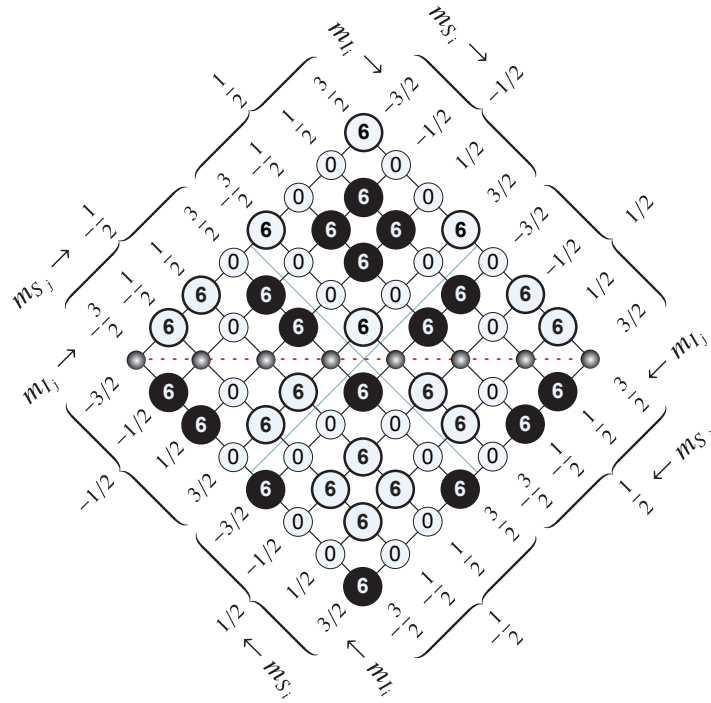


Figure 10: Values of spin transition symmetry functions  $2\sqrt{6}(\text{dip})_{IS}(m_{I,i}, m_{S,i}, m_{I,j}, m_{S,j})$  for an  $\{I = \frac{3}{2}, S = \frac{1}{2}\}$  system. Values inside black circles are negative.

Using the definitions in this section, the first-order contributions to the frequency of an NMR active nucleus can be written in the form of Eq. (1) for the nuclear shielding and electric quadrupole interactions as well as the magnetic dipole and  $J$  coupling interactions. These are given in Table 3 for a static sample and one averaged with D-MAS. As noted earlier, all spatial dependences with  $n \neq 0$  are averaged to zero in the high rotation speed limit under sample rotation. In Table 3, we see, as expected, that the isotropic nuclear shielding and  $J$  coupling contributions to the NMR frequency survive under D-MAS. We also see the lesser-known result that the contribution from the anisotropic antisymmetric  $J$  coupling in the strong coupling limit survives under D-MAS[25, 26].

When the electric quadrupole coupling of a nucleus is no longer negligible compared to the Zeeman coupling, there will be second-order and possibly higher-order contributions to the NMR frequency. For second-order corrections to the NMR frequency for the electric quadrupole interaction, we define the spin transition function  $\mathbb{C}_L(m_i, m_j)$  as a linear combination of  $\mathbb{P}_I(m_i, m_j)$  and  $\mathbb{F}_I(m_i, m_j)$ , according to

$$\mathbb{C}_L(m_i, m_j) = \pi_{L,1}^{\{2,2\}} \mathbb{P}_I(m_i, m_j) + \pi_{L,3}^{\{2,2\}} \mathbb{F}_I(m_i, m_j), \quad (61)$$

where  $\pi_{L,1}^{\{2,2\}}$  and  $\pi_{L,3}^{\{2,2\}}$  are constants defined in Table A.13 and Eq. (A.157) in A.6.2. With this definition, we obtain

$$\Omega_q^{(2)}(\Theta, m_i, m_j) = \frac{\omega_q^2}{\omega_0} \mathbb{S}^{\{qq\}} \mathbb{C}_0(m_i, m_j) + \frac{\omega_q^2}{\omega_0} \mathbb{D}^{\{qq\}}(\Theta) \mathbb{C}_2(m_i, m_j) + \frac{\omega_q^2}{\omega_0} \mathbb{G}^{\{qq\}}(\Theta) \mathbb{C}_4(m_i, m_j), \quad (62)$$

as the second-order correction to the NMR frequency arising from the electric quadrupole interaction. Notice that the three frequency components have different spatial symmetries,  $\mathbb{S}$ ,  $\mathbb{D}(\Theta)$ , and  $\mathbb{G}(\Theta)$ . The  $\mathbb{S}$ -containing component is the isotropic second-order quadrupole shift. Also note that the D-MAS spatial pathway does not have sufficient symmetry to average away all the anisotropies in this frequency contribution, leaving the  $\mathbb{G}_0(\theta_M^{(2)})$  containing component,

$$\langle \Omega_q^{(2)}(m_i, m_j) \rangle_{\text{D-MAS}} = \frac{\omega_q^2}{\omega_0} \mathbb{S}^{\{qq\}} \mathbb{C}_0(m_i, m_j) + \frac{\omega_q^2}{\omega_0} \mathbb{G}_0^{\{qq\}}(\theta_M^{(2)}) \mathbb{C}_4(m_i, m_j). \quad (63)$$

As with the  $\mathbb{F}_I(m_i, m_j)$  values, these values depend on the nuclear spin  $I$ . Once again, to simplify usage, we further



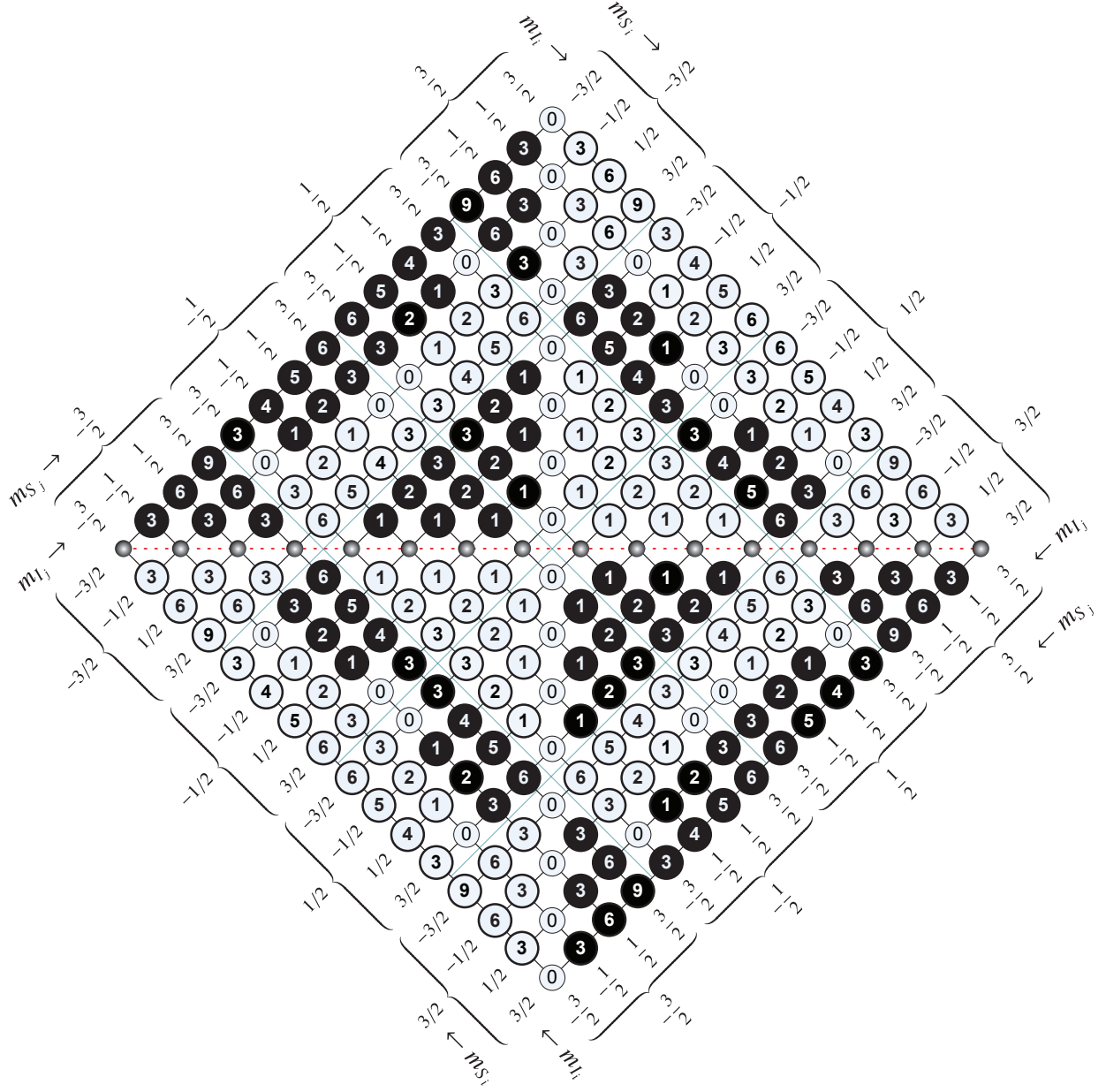


Figure 11: Values of spin transition symmetry functions  $2(\text{pp})_{IS}(m_{I,i}, m_{S,i}, m_{I,j}, m_{S,j})$  for an  $\{I = \frac{3}{2}, S = \frac{3}{2}\}$  system. Values inside black circles are negative.

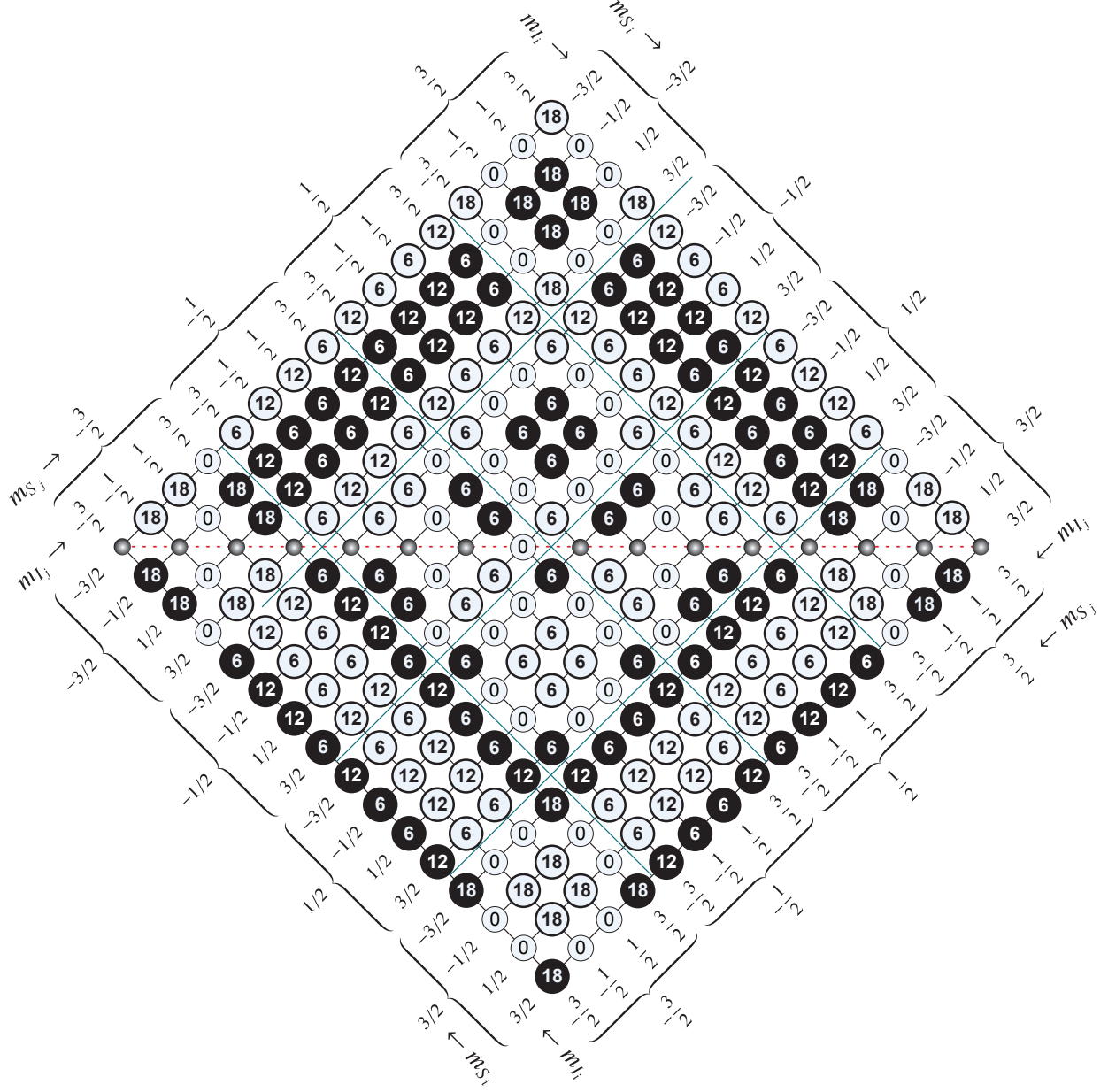


Figure 12: Values of spin transition symmetry functions  $2\sqrt{6}(\text{dp})_{IS}(m_{I,i}, m_{S,i}, m_{I,j}, m_{S,j})$  for an  $\{I = \frac{3}{2}, S = \frac{3}{2}\}$  system. Values inside black circles are negative.

Figure 13: Values of spin transition symmetry functions  $2\sqrt{6}(\text{pdc})_{IS}(m_{I,i}, m_{S,i}, m_{I,j}, m_{S,j})$  for a  $\{I = \frac{3}{2}, S = \frac{3}{2}\}$  system. Values inside black circles are negative.

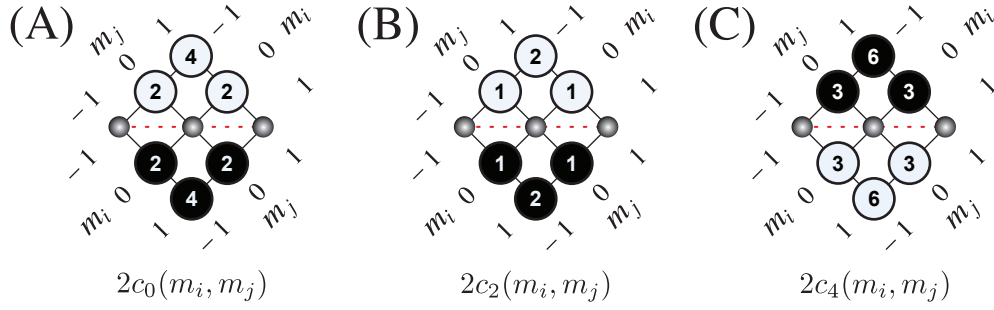


Figure 14: Values of spin transition symmetry functions (A)  $2c_0(m_i, m_j)$ , (B)  $2c_2(m_i, m_j)$ , and (C)  $2c_4(m_i, m_j)$  for a  $\{I = 1\}$  system. Values inside black circles are negative.

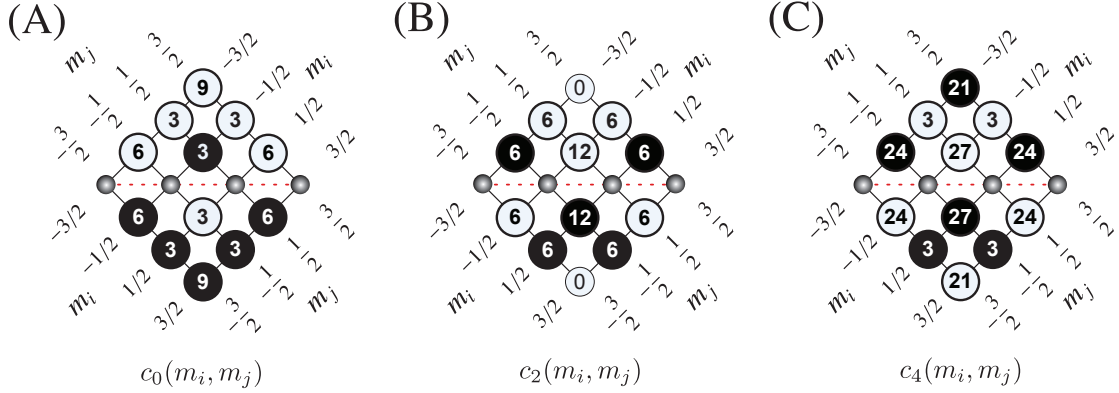


Figure 15: Values of spin transition symmetry functions (A)  $c_0(m_i, m_j)$ , (B)  $c_2(m_i, m_j)$ , and (C)  $c_4(m_i, m_j)$  for a  $\{I = \frac{3}{2}\}$  system. Values inside black circles are negative.

define

$$\begin{aligned}
 c_0(m_i, m_j) &= \sqrt{5} \mathfrak{c}_0(m_i, m_j), \\
 c_2(m_i, m_j) &= \sqrt{14} \mathfrak{c}_2(m_i, m_j), \\
 c_4(m_i, m_j) &= \sqrt{70} \mathfrak{c}_4(m_i, m_j).
 \end{aligned} \tag{64}$$

The transition symmetry tables for  $c_0(m_i, m_j)$ ,  $c_2(m_i, m_j)$ , and  $c_4(m_i, m_j)$  are given in Figs. 14, 15, 16, 17, 18 for spins  $I = 1, 3/2, 5/2, 3$ , and  $7/2$ , respectively. The transition symmetry tables for  $c_0(m_i, m_j)$ ,  $c_2(m_i, m_j)$ , and  $c_4(m_i, m_j)$  for spin  $I = 9/2$  are given in Figs. 19, 20, and 21, respectively.

Second-order contributions involve not only the electric quadrupole interaction but also any interactions that depend on the same spin angular momentum as the nuclear electric quadrupole moment. Thus, we also consider “cross terms” between the electric quadrupole coupling and the nuclear shielding, weak magnetic dipole, and weak  $J$ -couplings. These contributions, in the form of Eq. (1), are given in Table 4 for all transitions in a static sample. Detailed derivations of all frequencies in Tables 3 and 4 are given in the Appendix.

Manipulations of a spin transition function,  $\xi_\ell(i, j)$ , can be described with permutations of transitions. In this context, we introduce the idea of a *spin transition pathway*,  $(i \rightarrow j)(t)$ , in an NMR experiment. An NMR experiment can be defined using a single transition pathway or a set of transition pathways with the total NMR signal arising from the sum of transition pathway signals. In the high field limit, only transition pathways passing through transitions with  $m_j - m_i = \pm 1$  can be directly observed, although the convention is  $m_j - m_i = -1$ . Generally, each observable transition pathway will be associated with a single resonance in the NMR spectrum. For example, a Bloch decay

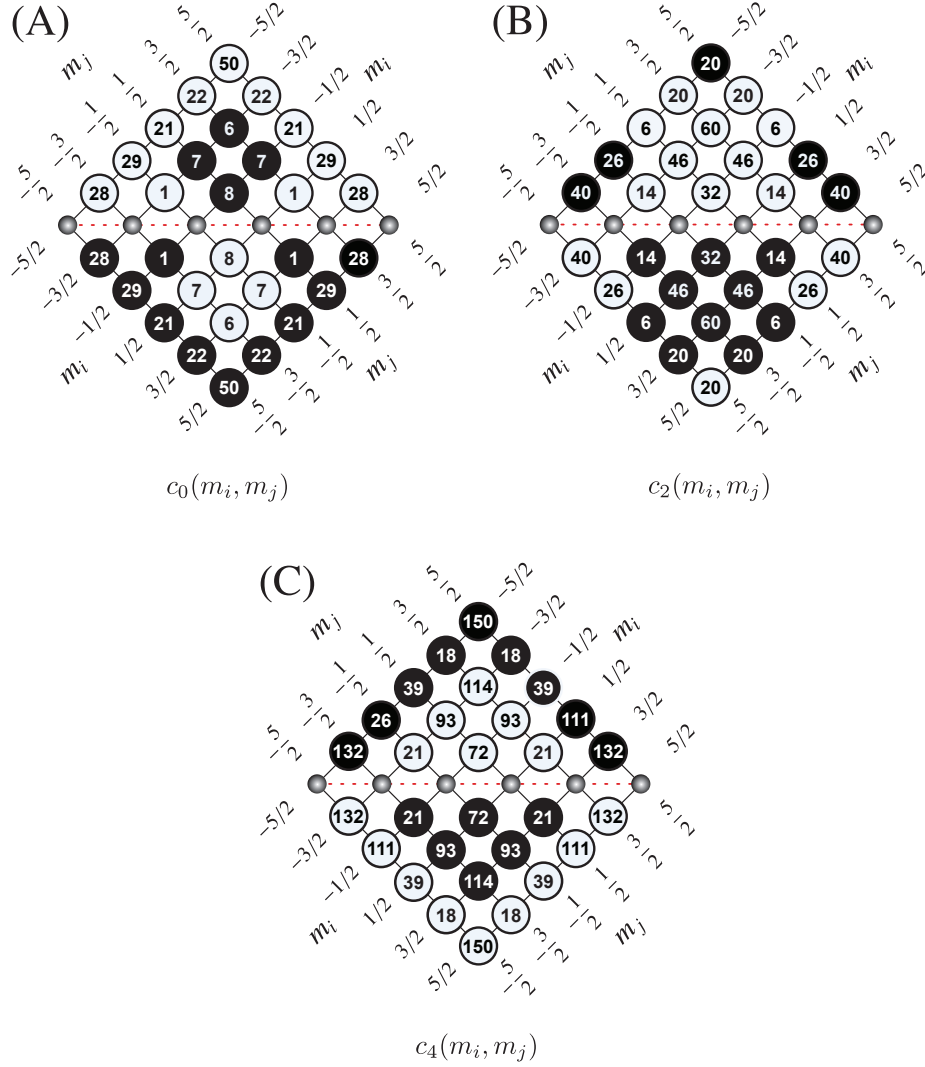


Figure 16: Values of spin transition symmetry functions (A)  $c_0(m_i, m_j)$ , (B)  $c_2(m_i, m_j)$ , and (C)  $c_4(m_i, m_j)$  for a  $\{I = \frac{5}{2}\}$  system. Values inside black circles are negative.

experiment on a spin  $I = 1$  nucleus will have two observable transition pathways:

$$\{I = 1\} : \begin{cases} [z_I] \rightarrow |-1\rangle \langle 0|, \\ [z_I] \rightarrow |0\rangle \langle +1|. \end{cases} \quad (65)$$

We can use transition diagrams to aid in visualizing these transition pathways, as shown in Fig. 22. In this example, a single rf pulse applied to a spin  $I = 1$  nucleus at equilibrium in an external magnetic field will create two observable transition pathways, here indicated as pathways 1 and 2. Each spin transition pathway can be mapped into a *transition symmetry pathway* for each spin transition symmetry function,  $\xi_\ell(m_i, m_j)$ , present in the frequency expression for the spin system. In the case of a spin  $I = 1$  nucleus in a polycrystalline sample, the frequency could, for example, include an isotropic nuclear shielding and an electric quadrupole splitting given by

$$\Omega(\Theta, m_i, m_j) = -\omega_0 \sigma_{\text{iso}} \mathbb{P}_I(m_i, m_j) + \omega_q \mathbb{D}^{\{q\}}(\Theta) \mathbb{D}_I(m_i, m_j). \quad (66)$$

For a Bloch decay experiment in this system, we overlay the two transition pathways on the  $\mathbb{P}_I(m_i, m_j)$  and  $\mathbb{D}_I(m_i, m_j)$  tables as shown in Fig. 23A, and write the  $\mathbb{P}_I(m_i, m_j)$  pathway as  $\mathbb{P}_I = 0 \rightarrow -1$  and  $\mathbb{D}_I(m_i, m_j)$  pathways as

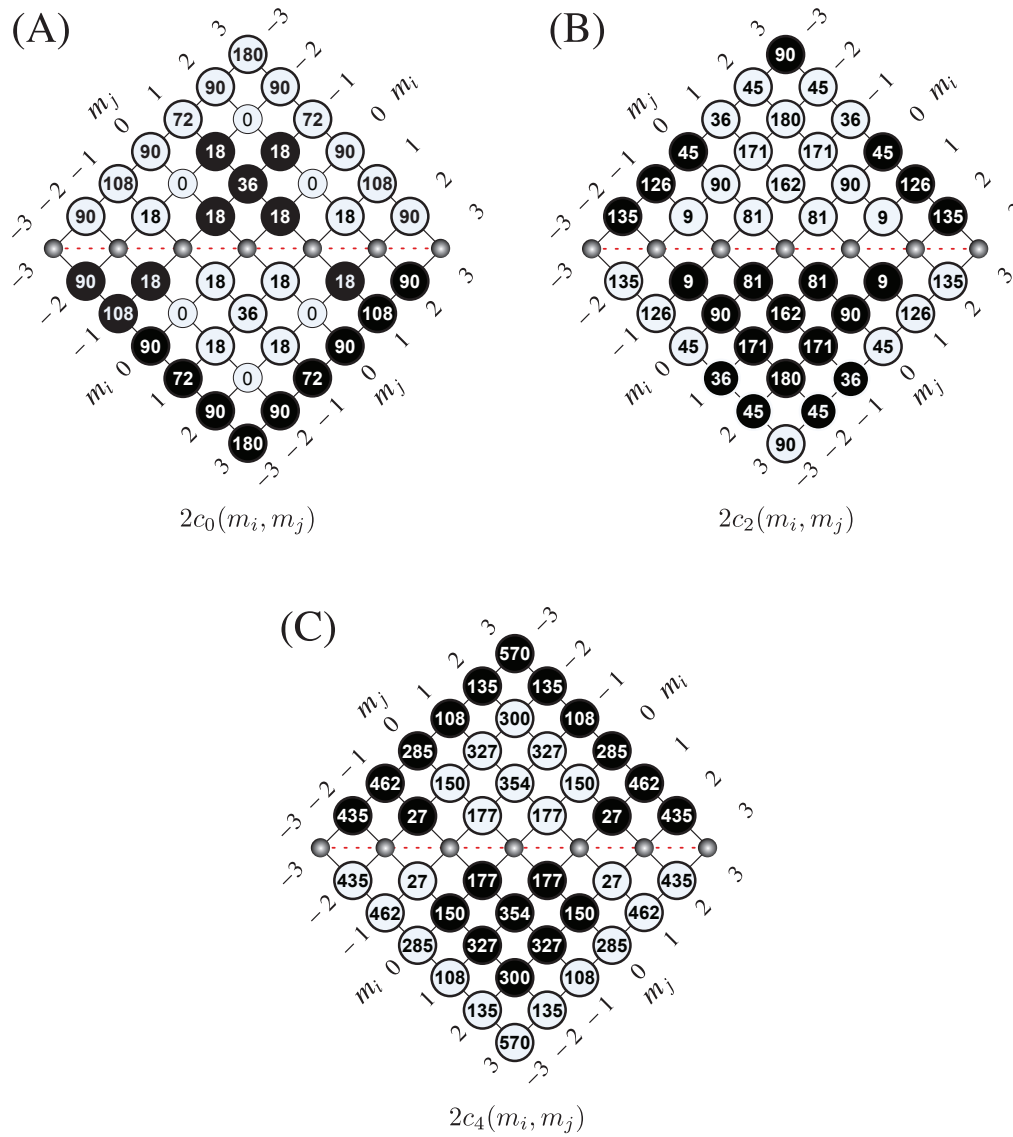


Figure 17: Values of spin transition symmetry functions (A)  $2c_0(m_i, m_j)$ , (B)  $2c_2(m_i, m_j)$ , and (C)  $2c_4(m_i, m_j)$  for a  $\{I = 3\}$  system. Values inside black circles are negative.

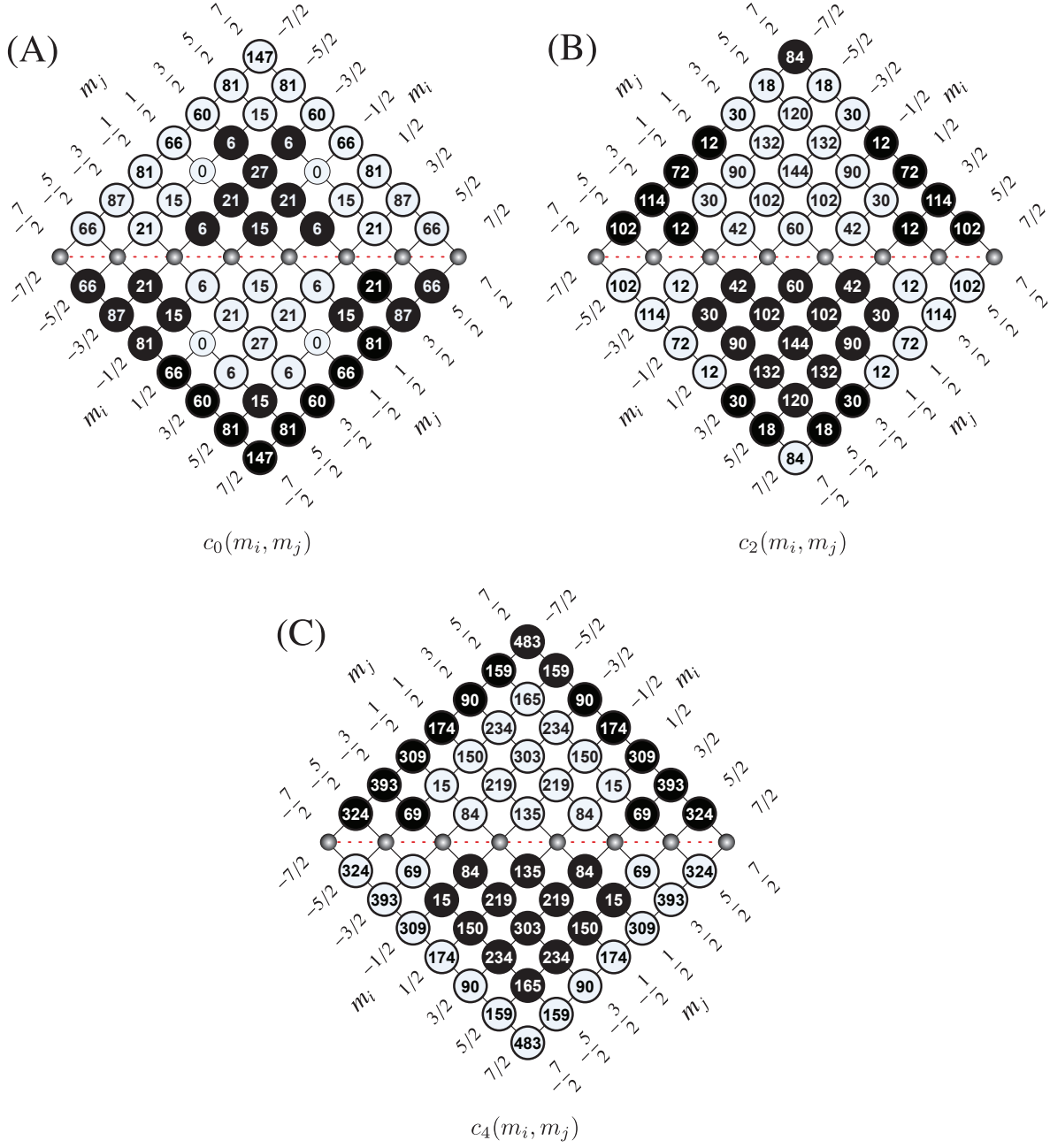


Figure 18: Values of spin transition symmetry functions (A)  $c_0(m_i, m_j)$ , (B)  $c_2(m_i, m_j)$ , (C)  $c_4(m_i, m_j)$  for a  $\{I = \frac{7}{2}\}$  system. Values inside black circles are negative.

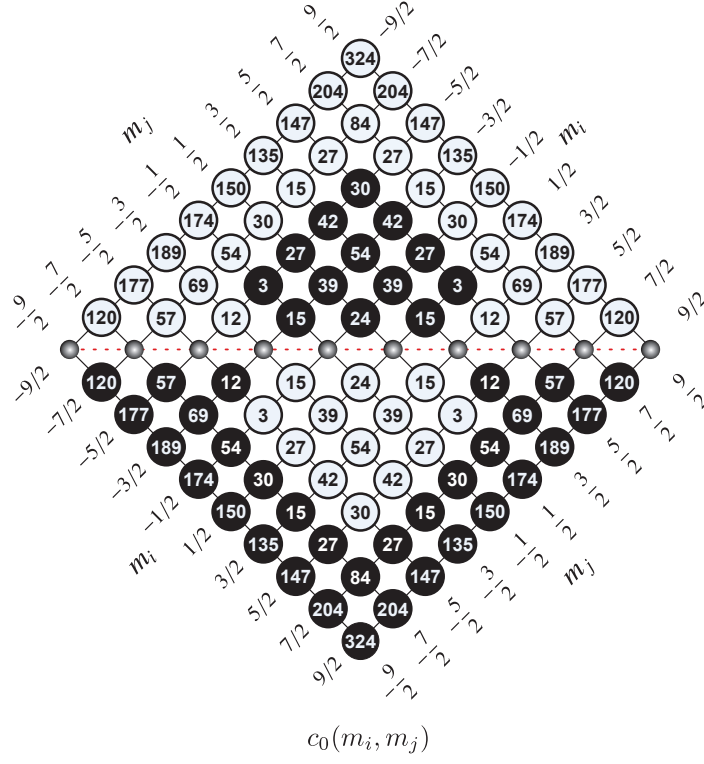


Figure 19: Values of spin transition symmetry functions  $c_0(m_i, m_j)$  for a  $\{I = \frac{9}{2}\}$  system. Values inside black circles are negative.

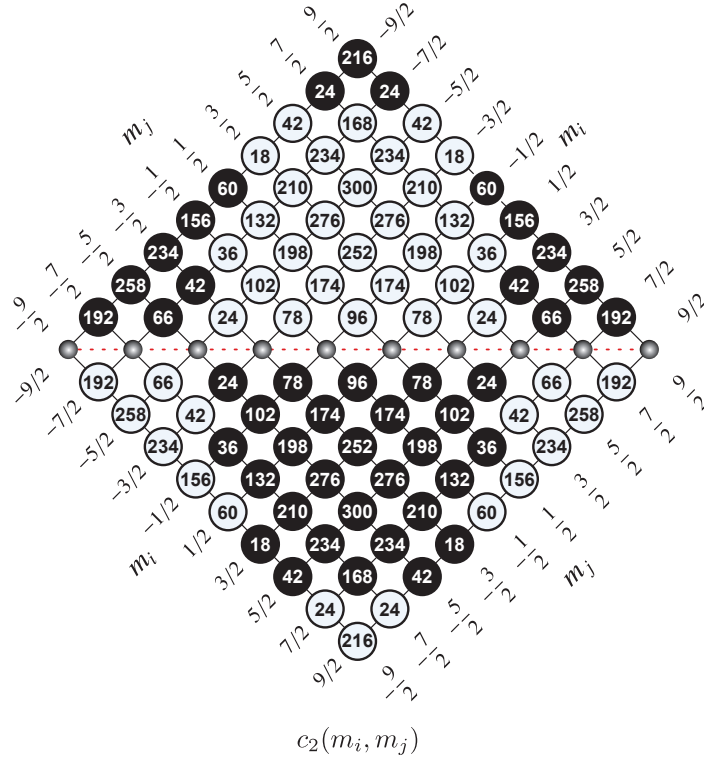


Figure 20: Values of spin transition symmetry functions  $c_2(m_i, m_j)$  for a  $\{I = \frac{9}{2}\}$  system. Values inside black circles are negative.



(A)

Diagram (A) illustrates two pathways for a quantum system. The legend shows a vertical axis  $m$  with levels 1, 0, and -1. Level 1 has a pink dot and a pink arrow labeled  $B$  pointing to level 0. Level 0 has a green dot and a green arrow labeled  $A$  pointing to level -1. Pathway 1 shows a diamond lattice with nodes labeled  $m_j$ ,  $m_i$ , and -1. A green line connects nodes at  $m_j = -1$  and  $m_i = 1$ , with a green circle at the  $m_i = 0$  node. A black pulse is applied. Pathway 2 is identical but with a pink line and circle.

(B)

Diagram (B) illustrates two pathways for a quantum system. Pathway 1 shows a diamond lattice with nodes labeled  $m_j$ ,  $m_i$ , and -1. A green line connects nodes at  $m_j = -1$  and  $m_i = 1$ , with a green circle at the  $m_i = 0$  node. A black pulse is applied. Pathway 2 is identical but with a pink line and circle.

Figure 22: (A) Three-dimensional representation of the two transition pathways in a one pulse experiment in a  $\{I = 1\}$  system. (B) Two-dimensional transition pathway diagrams for the two pathways in (A)

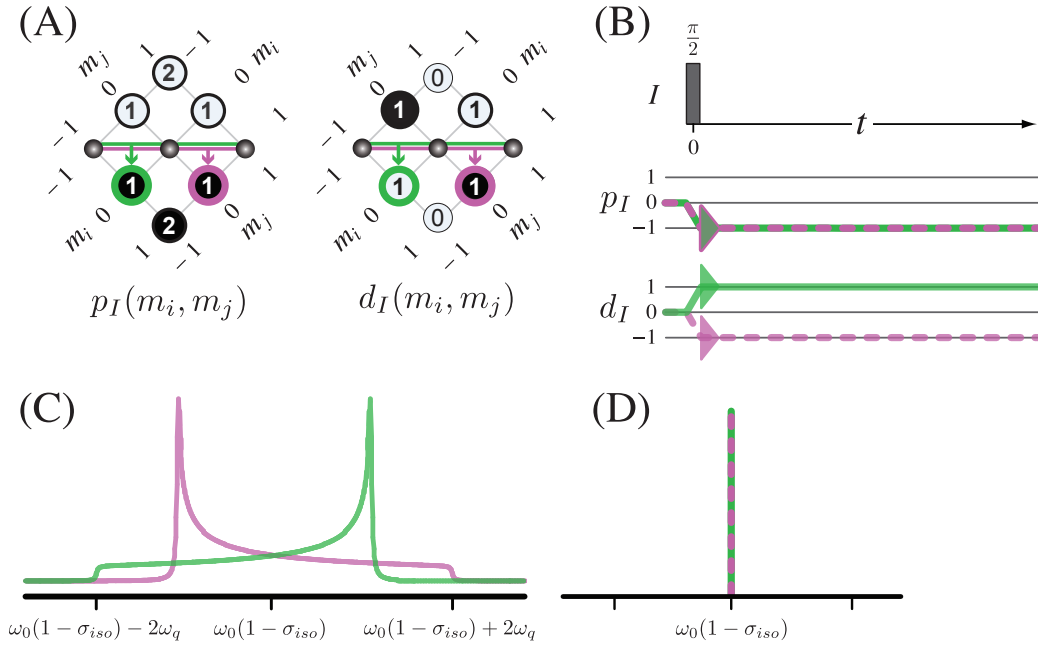


Figure 23: (A) Transition pathways on the  $p_I$  and  $d_I$  tables for a  $\{I = 1\}$  system with the transitions observed in a Bloch decay experiment enclosed in circles with thick lines. (B) The  $p_I$  and  $d_I$  symmetry pathway for the Bloch decay experiment. A solid triangle represents a contribution to the observable free induction decay. (C) Simulated spectrum showing the resonances from two transitions in a polycrystalline spin  $I = 1$  nucleus experiencing an isotropic nuclear shielding and an electric quadrupole coupling. (D) Simulated spectrum showing the resonances from two transitions in a spin  $I = 1$  nucleus experiencing only an isotropic nuclear shielding.

$d_I = 0 \rightarrow \pm 1$ , as shown in Fig. 23B. Thus, determining whether the spectrum will contain one or two distinct resonances will depend on the frequency component transition symmetries present. These two transition pathways give rise to a spectrum containing the two  $\mathbb{D}^{\{q\}}(\Theta)$  powder pattern resonances shown in Fig. 23C. In the liquid state, where molecules are undergoing rapid isotropic motion, all frequency components average to zero except those with a spatial part of  $\mathbb{S}$ . Thus, only the isotropic nuclear shielding frequency remains in the liquid state,

$$\Omega(\Theta, m_i, m_j) = -\omega_0 \sigma_{iso} \mathbb{P}_I(m_i, m_j), \quad (67)$$

leading to a spectrum with a single narrow resonance, as indicated in Fig. 23D.

As another example, consider a Bloch decay experiment on two weakly coupled spin  $I = 1/2$  nuclei in the liquid state. In a homonuclear AX system, we adjust our notation, replacing  $p_I$  with  $p_A$ ,  $p_S$  with  $p_X$ , and  $(pp)_{IS}$  with  $(pp)_{AX}$ . Here there will be four observable transition pathways:

$$\{I_A = \frac{1}{2}, I_X = \frac{1}{2}\} : \begin{cases} [z_A] \rightarrow |-\frac{1}{2}, +\frac{1}{2}\rangle \langle +\frac{1}{2}, +\frac{1}{2}|, \\ [z_A] \rightarrow |-\frac{1}{2}, -\frac{1}{2}\rangle \langle +\frac{1}{2}, -\frac{1}{2}|, \\ [z_X] \rightarrow |+\frac{1}{2}, -\frac{1}{2}\rangle \langle +\frac{1}{2}, +\frac{1}{2}|, \\ [z_X] \rightarrow |-\frac{1}{2}, -\frac{1}{2}\rangle \langle -\frac{1}{2}, +\frac{1}{2}|. \end{cases} \quad (68)$$

Again, determining the number of distinct resonances in the spectrum depends on the frequency component symmetries present. In the case of two weakly coupled spin  $I = 1/2$  nuclei experiencing both the isotropic nuclear shielding and  $J$  coupling, the frequency is

$$\begin{aligned} \Omega(\Theta, m_{A,i}, m_{X,i}, m_{A,j}, m_{X,j}) = & -\omega_0 \sigma_{iso,A} \mathbb{P}_A(m_{A,i}, m_{A,j}) - \omega_0 \sigma_{iso,X} \mathbb{P}_X(m_{X,i}, m_{X,j}) \\ & + 2\pi J_{iso} (\mathbb{P}\mathbb{P})_{AX}(m_{A,i}, m_{X,i}, m_{A,j}, m_{X,j}). \end{aligned} \quad (69)$$

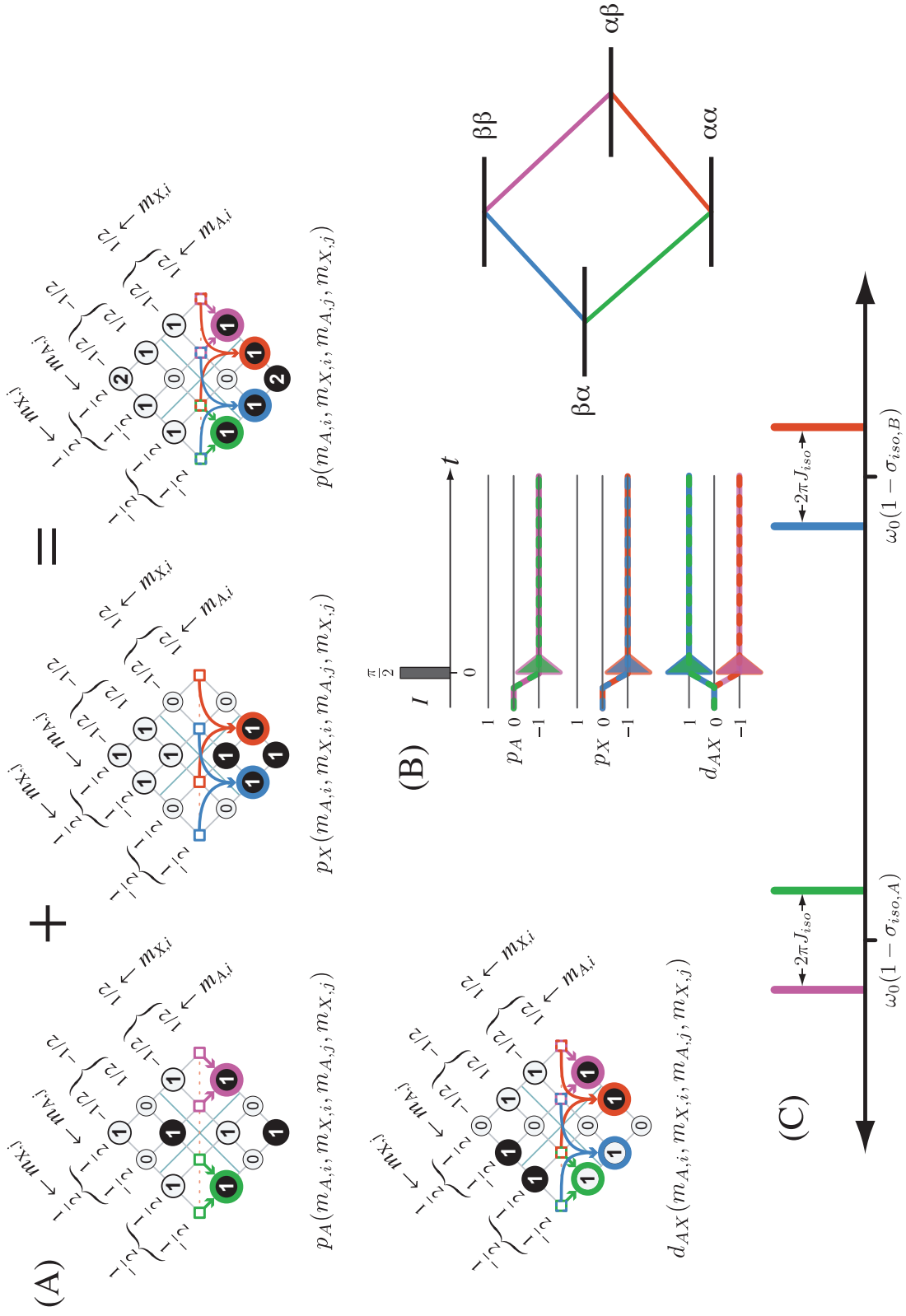


Figure 24: (A) The  $p_A$ ,  $p_X$ , and  $(pp)_{AX}$  tables for a  $\{A = \frac{1}{2}, X = \frac{1}{2}\}$  system with the transitions observed in a Bloch decay experiment enclosed in circles with thick lines. (B) The  $p_A$ ,  $p_X$ , and  $(pp)_{AX}$  symmetry pathway for the Bloch decay experiment. A solid triangle represents a contribution to the observable free induction decay. (C) Spectrum shows two resonances from two weakly coupled spin  $1/2$  nuclei experiencing an isotropic nuclear shielding and a  $J$  coupling.

For this Bloch decay experiment, we indicate the four transitions on the  $p_A$ ,  $p_X$ , and  $(pp)_{AX}$  tables, shown in Fig. 24A, and write the  $p_A$  pathway as  $p_A = 0 \rightarrow -1$ , the  $p_X$  pathway as  $p_X = 0 \rightarrow -1$ , and  $(pp)_{AX}$  pathways as  $(pp)_{AX} = 0 \rightarrow \pm 1$ , shown in Fig. 24B. These pathways give rise to a spectrum containing the four resonances shown in Fig. 24C.

Contribution		Static Sample	D-MAS
Isotropic Zeeman	$\Omega^{(0)}(m_i, m_j)$	$\omega_0 \mathbb{P}_I(m_i, m_j)$	$\omega_0 \mathbb{P}_I(m_i, m_j)$
Shielding	$\Omega_\sigma^{(1)}(\Theta, m_i, m_j)$	$-\omega_0 \sigma_{\text{iso}} \mathbb{P}_I(m_i, m_j) - \omega_0 \zeta_\sigma \mathbb{D}\{\sigma\}(\Theta) \mathbb{P}_I(m_i, m_j)$	$-\omega_0 \sigma_{\text{iso}} \mathbb{P}_I(m_i, m_j)$
Quadrupole	$\Omega_q^{(1)}(\Theta, m_i, m_j)$	$\omega_q \mathbb{D}\{q\}(\Theta) \mathbb{d}_I(m_i, m_j)$	0
Dipole (strong)	$\Omega_{d_{II}}^{(1)}(\Theta, M_i, M_j)$	$\omega_d \mathbb{D}\{d_{II}\}(\Theta) \mathbb{d}_{II}(M_i, M_j)$	0
Dipole (weak)	$\Omega_{d_{IS}}^{(1)}(\Theta, m_{I,i}, m_{S,i}, m_{I,j}, m_{S,j})$	$\omega_d \mathbb{D}\{d_{IS}\}(\Theta) \mathbb{d}_{IS}(m_{I,i}, m_{S,i}, m_{I,j}, m_{S,j})$	0
$J$ (strong)	$\Omega_{J_{II}}^{(1)}(\Theta, M_i, M_j)$	$2\pi \zeta_J^{(\alpha)} \mathbb{P}\{J_{II}\}(\Theta) \mathbb{P}_{II}(M_i, M_j) + 2\pi \zeta_J \mathbb{D}\{J_{II}\}(\Theta) \mathbb{d}_{II}(M_i, M_j)$	$2\pi \zeta_J^{(\alpha)} \mathbb{P}_0^{\{J_{II}\}} \left( \frac{\theta^{(2)}}{M} \right) \mathbb{P}_{II}(M_i, M_j)$
$J$ (weak)	$\Omega_{J_{IS}}^{(1)}(\Theta, m_{I,i}, m_{S,i}, m_{I,j}, m_{S,j})$	$2\pi J_{\text{iso}} \mathbb{d}_{IS}(m_{I,i}, m_{S,i}, m_{I,j}, m_{S,j}) + 2\pi \zeta_J \mathbb{D}\{J_{IS}\}(\Theta) \mathbb{d}_{IS}(m_{I,i}, m_{S,i}, m_{I,j}, m_{S,j})$	$2\pi J_{\text{iso}} \mathbb{d}_{IS}(m_{I,i}, m_{S,i}, m_{I,j}, m_{S,j})$

Table 3: Zeroth-order Zeeman and various first-order contributions from the nuclear shielding, electric quadrupole coupling, strong and weak magnetic dipole coupling, and strong and weak  $J$  coupling to the NMR frequency for all transitions in a static sample and all transitions in a sample undergoing D-MAS. For consistency, we have defined  $S^{(z)} = 1$ .

Contribution		Static Sample
Quadrupole-Quadrupole	$\Omega_{q,q}^{(2)}(\Theta, m_i, m_j)$	$\frac{\omega_q^2}{\omega_0} \mathbb{S}\{qq\} \mathbb{C}_0(m_i, m_j) + \frac{\omega_q^2}{\omega_0} \mathbb{D}\{qq\}(\Theta) \mathbb{C}_2(m_i, m_j) + \frac{\omega_q^2}{\omega_0} \mathbb{G}\{qq\}(\Theta) \mathbb{C}_4(m_i, m_j)$
Shielding-Quadrupole	$\Omega_{\sigma,q}^{(2)}(\Theta, m_i, m_j)$	$-\zeta_\sigma \omega_q \mathbb{S}\{\sigma q\} \mathbb{D}_I(m_i, m_j) - \zeta_\sigma \omega_q \mathbb{D}\{\sigma q\}(\Theta) \mathbb{D}_I(m_i, m_j) - \zeta_\sigma \omega_q \mathbb{G}\{\sigma q\}(\Theta) \mathbb{D}_I(m_i, m_j)$
Weak $J$ -Quadrupole	$\Omega_{JIS,qI}^{(2)}(\Theta, m_{I,i}, m_{S,i}, m_{I,j}, m_{S,j})$	$\frac{2\pi\zeta_J\omega_q}{\omega_0} \mathbb{S}\{JqI\} \mathbb{D}_{IS}(m_{I,i}, m_{S,i}, m_{I,j}, m_{S,j}) + \frac{2\pi\zeta_J\omega_q}{\omega_0} \mathbb{D}\{JqI\}(\Theta) \mathbb{D}_{IS}(m_{I,i}, m_{S,i}, m_{I,j}, m_{S,j})$ $+ \frac{2\pi\zeta_J\omega_q}{\omega_0} \mathbb{G}\{JqI\}(\Theta) \mathbb{D}_{IS}(m_{I,i}, m_{S,i}, m_{I,j}, m_{S,j})$
Weak Dipole-Quadrupole	$\Omega_{dIS,qI}^{(2)}(\Theta, m_{I,i}, m_{S,i}, m_{I,j}, m_{S,j})$	$\frac{\omega_d\omega_q}{\omega_0} \mathbb{S}\{dqI\} \mathbb{D}_{IS}(m_{I,i}, m_{S,i}, m_{I,j}, m_{S,j}) + \frac{\omega_d\omega_q}{\omega_0} \mathbb{D}\{dqI\}(\Theta) \mathbb{D}_{IS}(m_{I,i}, m_{S,i}, m_{I,j}, m_{S,j})$ $+ \frac{\omega_d\omega_q}{\omega_0} \mathbb{G}\{dqI\}(\Theta) \mathbb{D}_{IS}(m_{I,i}, m_{S,i}, m_{I,j}, m_{S,j})$

Table 4: Various second-order contributions from the electric quadrupole coupling and its cross-terms with the nuclear shielding, magnetic dipole coupling, and  $J$ -coupling to the NMR frequency for all transitions in a static sample.

### 3. Echo classification

With the definitions of the previous section in place, we generalize the concept of coherence transfer pathways[14, 27], which were originally developed as an approach for designing rf phase cycles but also provide a powerful approach to “see at a glance” why and when certain echoes form in a multiple pulse NMR experiment. For example, the well-known Hahn-echo occurs when frequency components containing  $p_1$  values change sign in an experiment. That is, a Hahn echo forms when

$$\overline{p_I} = \frac{1}{t} \int_0^t p_I(t') dt' = 0, \quad (70)$$

assuming a frequency component’s spatial multiplier,  $\Xi$ , remains constant during this period. A problem with showing only the pathway for  $p_I$  values is that it does not explain the formation of NMR echoes that result when other frequency components change sign during time evolution. As we have just seen, frequency components contain spin transition symmetry functions such as  $p_1$ ,  $d_1$ ,  $f_1$ ,  $c_0$ ,  $c_2$ ,  $c_4$ ,  $(pp)_{IS}$ ,  $(dp)_{IS}$ , or  $(pd)_{IS}$ , in products with spatial symmetry functions such as  $S$ ,  $P$ ,  $D$ , or  $G$ . In other words, the  $p_I$  pathway only shows a small part of how components of an NMR transition frequency can change between evolution periods. To fully understand when and which frequency components refocus into echoes, we must follow *all* relevant spatial, transition, or spatial-transition product symmetries through an NMR experiment. Thus, we generally classify echoes that refocus during a time interval as a *transition symmetry echo* when

$$\overline{\xi_\ell} = \frac{1}{t} \int_0^t \xi_\ell(t') dt' = 0, \quad \text{with constant } \Xi_L, \quad (71)$$

a *spatial symmetry echo* when

$$\overline{\Xi_L} = \frac{1}{t} \int_0^t \Xi_L(t') dt' = 0, \quad \text{with constant } \xi_\ell, \quad (72)$$

and a *spatial-transition symmetry product echo* when

$$\overline{\Xi_L \xi_\ell} = \frac{1}{t} \int_0^t \Xi_L(t') \xi_\ell(t') dt' = 0. \quad (73)$$

Within the class of transition echoes, we find subclasses such as  $p$  echoes, which include the Hahn echo[5] and the stimulated echo;  $d$  echoes, which include the solid echo[28] and Solomon echoes[29];  $c_0$  echoes, used in Multiple-Quantum DOuble Rotation (MQ-DOR)[30];  $c_2$  echoes, used in Correlation Of Anisotropies Separated Through Echo Refocusing (COASTER)[31]; and  $c_4$  echoes, used in Multiple-Quantum Magic-Angle Spinning (MQ-MAS)[32] and Satellite-Transition Magic-Angle Spinning (ST-MAS)[33]. Within the class of spatial echoes, we find subclasses such as  $D_1$  and  $D_2$  rotary echoes, which occur during sample rotation, and  $D_0$  and  $G_0$  echoes, which are designed to occur simultaneously during the Dynamic-Angle Spinning (DAS) experiment[21, 34].

Below we give illustrative examples of various types of echoes in several commonly used NMR experiments. Bear in mind that any particular NMR pulse sequence will generate many transition pathways, and generally, only signals from a particular pathway or subset of transition pathways will result in a desired signal. In each NMR experiment described below, we will restrict our discussion to its desired pathways. Signals from undesired transition pathways often result in spectrum artifacts which can be, but are not always, eliminated using techniques such as rf phase cycling, pulse length optimizations, selective pulses, multiple quantum filters, or field gradients.

#### 3.1. $p$ Echoes

##### 3.1.1. The Hahn echo

We begin with the familiar Hahn echo, an example of a  $p$ -echo. As a starting point, we examine the first-order nuclear shielding contribution to an NMR transition frequency given by

$$\Omega_\sigma^{(1)}(\Theta, m_i, m_j) = -\omega_0 \sigma_{\text{iso}} \mathbb{P}_I(m_i, m_j) - \omega_0 \zeta_\sigma \mathbb{D}^{\{\sigma\}}(\Theta) \mathbb{P}_I(m_i, m_j). \quad (74)$$

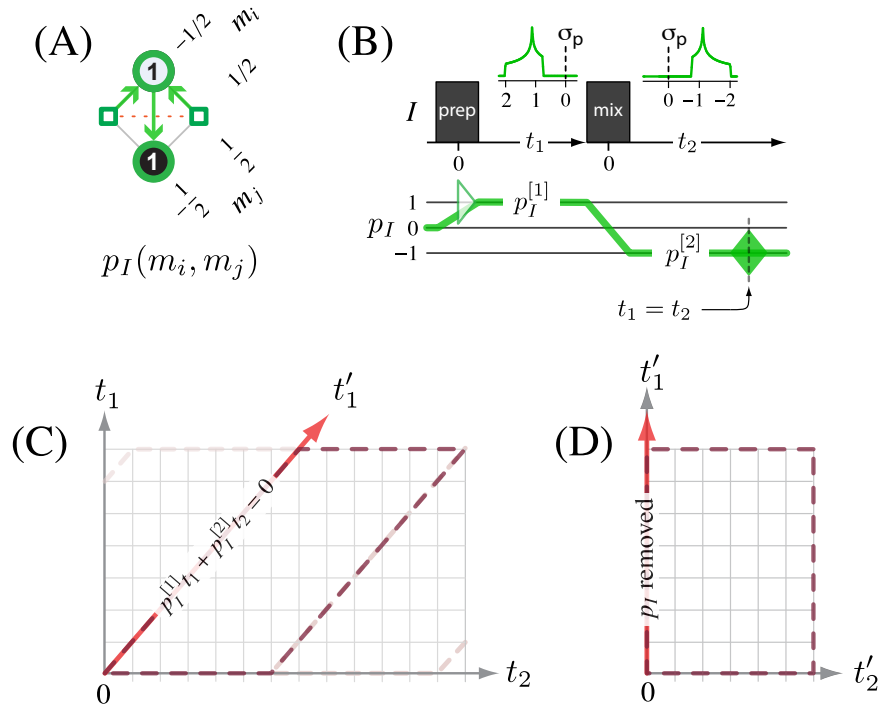


Figure 25: (A) Hahn echo transition pathway in Eq. (75) on the  $p_I$  table for a spin  $I = 1/2$  nucleus. (B) Pulse sequence and  $p_I$  pathway for spin echo experiment. A filled diamond represents a contribution to a directly observable echo. An open triangle represents a contribution to an indirectly observable free induction decay. (C) In the 2D signal acquired as a function of  $t_1$  and  $t_2$ , as defined in the pulse sequence in (B), both the isotropic and anisotropic nuclear shielding contributions are refocused into a  $p_I$ -echo along the line  $p_I^{[1]}t_1 + p_I^{[2]}t_2 = 0$ . The dashed line represents a passive affine transformation of the 2D coordinate system to create a time coordinate,  $t'_1$ , along which the signal is unaffected by frequency components containing  $p_I$ . (D) After applying an active affine transformation with a shearing ratio of  $\kappa^{(\omega_1)} = -(p_I^{[1]}/p_I^{[2]}) = 1$  and scaling factor of  $\varsigma_{t'_1} = |\kappa^{(\omega_1)}| + 1 = 2$ , the 2D signal along the  $t'_1$  coordinate is unaffected by frequency components containing  $p_I$ . See Section 5 for a complete description of the application of affine transformations.

The two contributions in Eq. (74) have the same transition function symmetry,  $p_I$ , but different spatial symmetries,  $\mathbb{S}$  and  $\mathbb{D}$ . These two frequency components can be separated in experiments that manipulate spatial degrees of freedom but cannot be separated in experiments that only manipulate spin degrees of freedom.

Consider the two pulse sequence in Fig. 25 on a spin  $1/2$  system that generates the transition pathway

$$\{I = \frac{1}{2}\} : [z_I] \rightarrow |+\frac{1}{2}\rangle \langle -\frac{1}{2}| \rightarrow |-\frac{1}{2}\rangle \langle +\frac{1}{2}|, \quad (75)$$

where  $[z_I]$  represents Zeeman order. Using the table in Fig. 25A, this transition pathway maps into the  $p_I$  pathway  $p_I = 0 \rightarrow +1 \rightarrow -1$ , shown in Fig. 25B, which show that both components of the nuclear shielding interaction are refocused into an echo during  $t_2$  when  $t_2 = t_1$ . More generally, if a coherence  $p_I^{[1]}$  is excited during  $t_1$  and then transferred to  $p_I^{[2]}$  during  $t_2$ , the accumulated signal phase from nuclear shielding evolution,

$$\Phi_\sigma(t_1, t_2) = \Omega_\sigma^{[1]}t_1 + \Omega_\sigma^{[2]}t_2, \quad (76)$$

will be zero when

$$p_I^{[1]}t_1 + p_I^{[2]}t_2 = 0, \quad (77)$$

leading to a  $p_I$  echo formed during  $t_2$  at  $t_2 = -(p_I^{[1]}/p_I^{[2]})t_1$ . As illustrated in Fig. 25C, the application of an affine transformation to the 2D signal with a shear parallel to the  $t_2$  coordinate using a shearing ratio of  $\kappa^{(\omega_1)} = -(p_I^{[1]}/p_I^{[2]}) = 1$  and scaling of the  $t_1$  coordinate by a factor of  $\varsigma_{t'_1} = 1 + |\kappa^{(\omega_1)}| = 2$  leads to a modified 2D signal, as illustrated in Fig. 25D, that associates the  $t'_1$  dimension with system evolution without any  $p_I$ -containing frequency contributions. Definitions and additional details on using affine transformations in NMR can be found



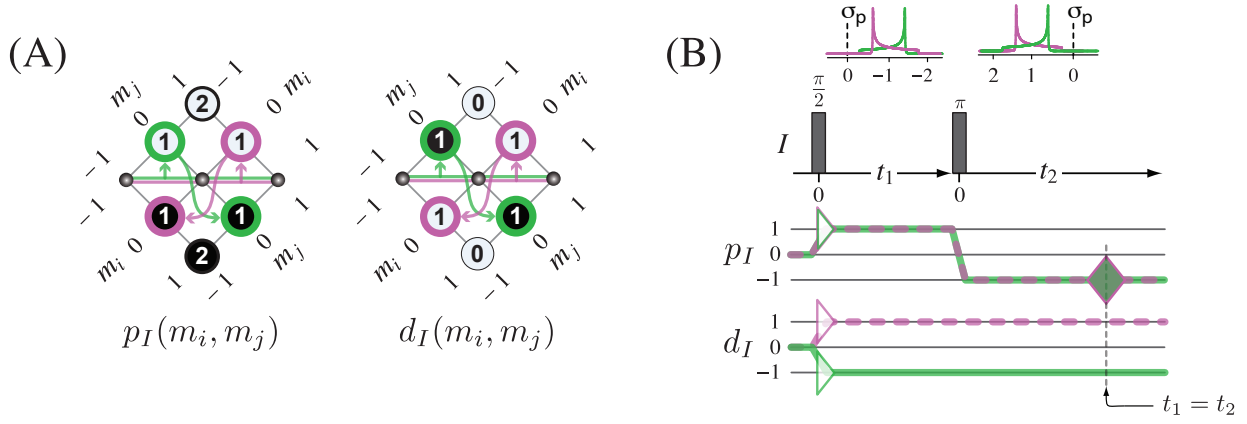


Figure 26: (A) Hahn echo transition pathways in Eq. (79) on the  $p_I$  and  $d_I$  tables for a spin  $I = 1$  nucleus. (B) Pulse sequence with  $p_I$  and  $d_I$  pathways for a two-pulse Hahn echo experiment. A filled diamond represents a contribution to a directly observable echo. An open triangle represents a contribution to an indirectly observable free induction decay.

in 5. In section (3.4), we will examine how D-MAS can be used to separate the S and D containing frequency components.

Next, consider a spin  $I = 1$  nucleus evolving not only under the first-order nuclear shielding frequency of Eq. (74) but also under the first-order contribution from the electric quadrupole coupling Hamiltonian given by

$$\Omega_q^{(1)}(\Theta, m_i, m_j) = \omega_q \mathbb{D}^{\{q\}}(\Theta) d_I(m_i, m_j). \quad (78)$$

In a Hahn echo,  $(\frac{\pi}{2} - t_1 - \pi - t_2)$ , experiment on a spin  $I = 1$  nucleus, there will be two transition pathways:

$$\{I = 1\} : \begin{cases} [z_I] \rightarrow |0\rangle \langle -1| \rightarrow |0\rangle \langle +1|, \\ [z_I] \rightarrow |+1\rangle \langle 0| \rightarrow |-1\rangle \langle 0|. \end{cases} \quad (79)$$

As shown in Fig. 26, these two transition pathways map into the single  $p_I$  pathway,  $p_I = 0 \rightarrow +1 \rightarrow -1$ , and two  $d_I$  pathways,  $d_I = 0 \rightarrow +1 \rightarrow +1$  and  $d_I = 0 \rightarrow -1 \rightarrow -1$ . Notice that a non-selective  $\pi$  pulse can generate a  $p_I$  echo but not a  $d_I$  echo since the  $d_I$  values are invariant under a non-selective  $\pi$  pulse. Thus, the signal acquired along the  $p_I$ -echo tops as a function of  $t_1 = t_2$  will be phase modulated by the  $d_I$  containing component of Eq. (78). By applying the affine transformation described in Fig. 25C and 25D, a 2D signal is obtained having both  $p_I$  and  $d_I$  containing frequency contributions along the  $t'_2$  axis, but only  $d_I$  containing frequency contributions along the  $t'_1$  axis. Generally, a transition frequency evolving along  $t'_1$  after a shearing parallel to the  $t_2$  coordinate and scaling of  $t_1$  is a weighted average of the transition frequencies during  $t_1$  and  $t_2$ , respectively, given by

$$\langle \Omega \rangle_{t'_1} = \frac{1}{1 + |\kappa \omega_1|} \langle \Omega \rangle_{t_1} + \frac{\kappa \omega_1}{1 + |\kappa \omega_1|} \langle \Omega \rangle_{t_2}, \quad (80)$$

while the transition frequencies along  $t'_2$  remains the same as along  $t_2$ . Additionally, to avoid truncation artifacts in a 2D separation of interactions, both echo tops need to occur simultaneously at some point inside the  $t_1, t_2$  acquisition window. Generally, 2D experiments are designed so this occurs when  $t_1 = t_2 = 0$  to avoid the need to apply large first-order phase corrections to the 2D spectrum.

### 3.1.2. SEDOR

The Spin Echo DOuble Resonance (SEDOR) experiment[35, 36] on two weakly coupled spin  $I = 1/2$  nuclei, shown in Fig. 27, is, in this sense, identical to the  $p_I$ -echo experiment on spin  $I = 1$ . Here we include the additional possible frequency contributions from the magnetic dipole and  $J$  couplings,

$$\Omega_{d_{IS}}^{(1)}(\Theta, m_{I,i}, m_{S,i}, m_{I,j}, m_{S,j}) = \omega_d \mathbb{D}^{\{d_{IS}\}}(\Theta) (\text{pp})_{IS}(m_{I,i}, m_{S,i}, m_{I,j}, m_{S,j}), \quad (81)$$

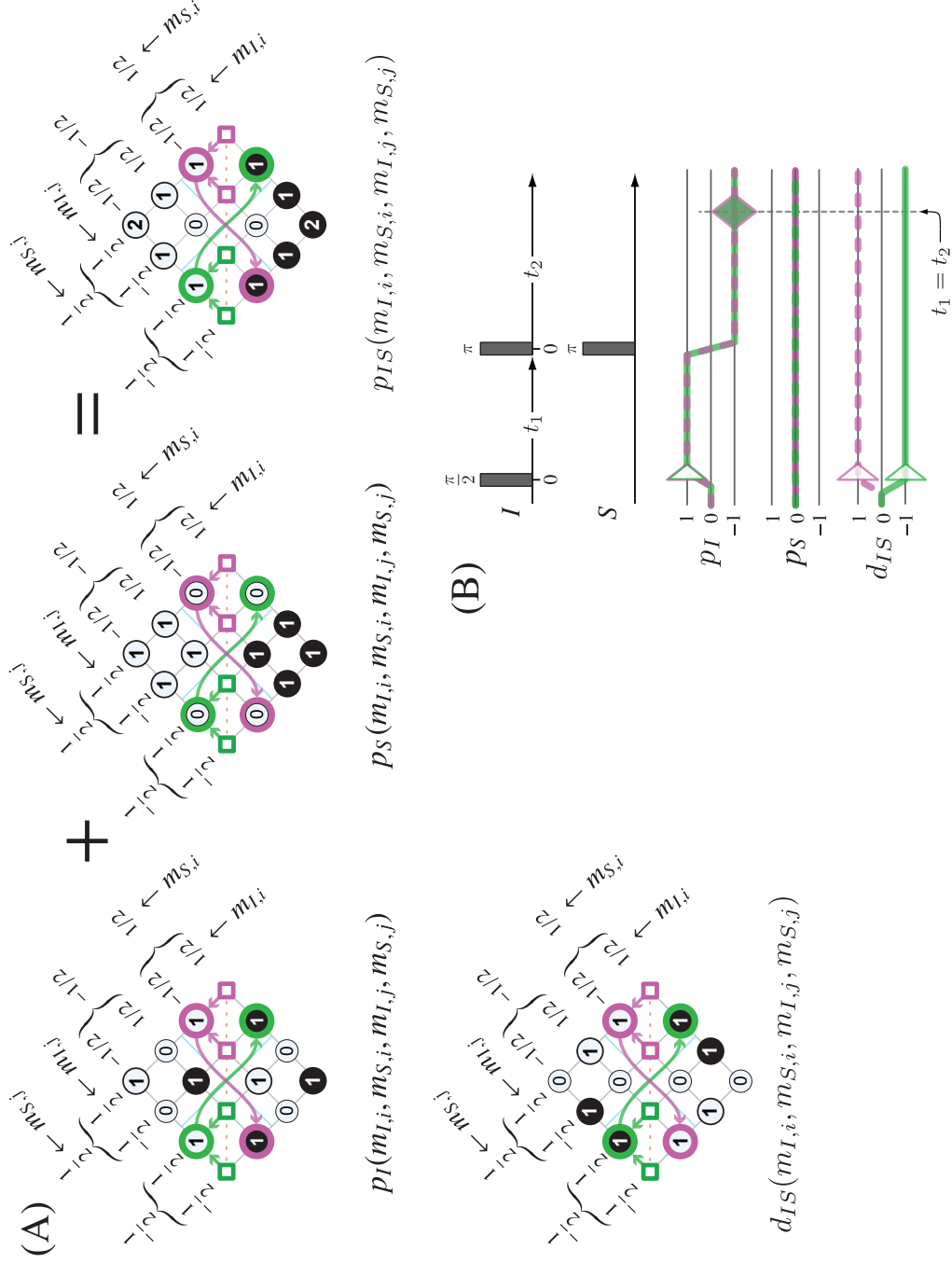


Figure 27: The SEDOR experiment transition pathways in Eq. (84) on the  $p_I$  and  $(pp)_{IS}$  tables for two weakly coupled spin  $\frac{1}{2}$  nuclei. (B) Pulse sequence with  $p_{IS}$  and  $(pp)_{IS}$  pathways for SEDOR experiment. A filled diamond represents a directly observable echo. An open triangle represents a contribution to an indirectly observable free induction decay.

$$\Omega_{JIS}^{(1)}(\Theta, m_{I,i}, m_{S,i}, m_{I,j}, m_{S,j}) = 2\pi J_{iso}(\text{pp})_{IS}(m_{I,i}, m_{S,i}, m_{I,j}, m_{S,j}) + 2\pi\zeta_J \mathbb{D}^{\{JIS\}}(\Theta)(\text{pp})_{IS}(m_{I,i}, m_{S,i}, m_{I,j}, m_{S,j}), \quad (82)$$

and write the two nuclear shielding contributions as

$$\Omega_{\sigma}^{(1)}(\Theta, m_{I,i}, m_{S,i}, m_{I,j}, m_{S,j}) = -\omega_0\sigma_{iso,I} \text{p}_I(m_{I,i}, m_{I,j}) - \omega_0\zeta_{\sigma,I} \mathbb{D}^{\{\sigma I\}}(\Theta) \text{p}_I(m_{I,i}, m_{I,j}) - \omega_0\sigma_{iso,S} \text{p}_S(m_{S,i}, m_{S,j}) - \omega_0\zeta_{\sigma,S} \mathbb{D}^{\{\sigma S\}}(\Theta) \text{p}_S(m_{S,i}, m_{S,j}). \quad (83)$$

In the SEDOR experiment, we consider two transition pathways:

$$\{I = \frac{1}{2}, S = \frac{1}{2}\} : \begin{cases} [z_I] \rightarrow |+\frac{1}{2}, -\frac{1}{2}\rangle \langle -\frac{1}{2}, -\frac{1}{2}| \\ \rightarrow |-\frac{1}{2}, +\frac{1}{2}\rangle \langle +\frac{1}{2}, +\frac{1}{2}|, \\ [z_I] \rightarrow |+\frac{1}{2}, +\frac{1}{2}\rangle \langle -\frac{1}{2}, +\frac{1}{2}| \\ \rightarrow |-\frac{1}{2}, -\frac{1}{2}\rangle \langle +\frac{1}{2}, -\frac{1}{2}|. \end{cases} \quad (84)$$

As shown in Fig. 27, these two transition pathways map into a single  $\text{p}_I$  pathway,  $\text{p}_I = 0 \rightarrow +1 \rightarrow -1$ , and two  $(\text{pp})_{IS}$  pathways,  $(\text{pp})_{IS} = 0 \rightarrow +1 \rightarrow +1$  and  $(\text{pp})_{IS} = 0 \rightarrow -1 \rightarrow -1$ . A  $(\text{pp})_{IS}$  echo can be generated with a selective  $\pi$  pulse on spin  $I$ ; however, as is evident in the  $(\text{pp})_{IS}$  table in Fig. 27A, the  $(\text{pp})_{IS}$  value will remain invariant through the transition pathway if a simultaneous selective  $\pi$  pulse is applied on spin  $S$ . Thus, the signal acquired along the  $\text{p}_I$ -echo tops as a function of  $t_1 = t_2$  will be modulated by the  $(\text{pp})_{IS}$  containing first-order spin coupling frequency component. Using the same affine transformation of Fig. 25C and 25D, a 2D SEDOR spectrum with pure  $(\text{pp})_{IS}$  interaction in the  $t_1'$  dimension is obtained.

### 3.1.3. The double quantum echo

Next, consider the double-quantum experiment[37] on spin  $I = 1$  shown in Fig. 28. In this experiment, a weak ( $\omega_1 \ll \omega_q$ ) rf pulse combined with proper phase cycling is used to excite the normally forbidden double-quantum transition, which is converted, after  $t_1$ , into single-quantum coherence using a strong ( $\omega_1 \gg \omega_q$ ) rf  $\pi/2$  pulse. The experiment has two transition pathways

$$\{I = 1\} : \begin{cases} [z_I] \rightarrow | +1 \rangle \langle -1 | \rightarrow | -1 \rangle \langle 0 |, \\ [z_I] \rightarrow | +1 \rangle \langle -1 | \rightarrow | 0 \rangle \langle +1 |, \end{cases} \quad (85)$$

which map into a single  $\text{p}_I$  pathway,  $\text{p}_I = 0 \rightarrow +2 \rightarrow -1$ , and two  $\text{d}_I$  pathways,  $\text{d}_I = 0 \rightarrow 0 \rightarrow +1$  and  $\text{d}_I = 0 \rightarrow 0 \rightarrow -1$ . As mentioned earlier, the  $\text{d}_I$  are zero for all  $m_I \rightarrow -m_I$  transitions, so the double-quantum transition in a spin  $I = 1$  nucleus is unaffected by the electric quadrupole interaction to first order. A double-quantum transition excited during  $t_1$  and transferred to a single-quantum transition during  $t_2$  leads to a  $\text{p}_I$ -echo at  $t_2 = 2t_1$  where all components from the nuclear shielding interaction refocus, whereas the first-order electric quadrupole splitting, dependent on  $\text{d}_I$ , is only active during  $t_2$ . This approach[38, 39] has been used in a 2D experiment to separate interactions with frequencies containing  $\text{p}_I$  and  $\text{d}_I$  into orthogonal axes by applying to the signal a shear along  $t_1$  with a shearing ratio of  $\kappa^{(\omega_2)} = 1/2$  and a scaling of  $t_2$  by  $\varsigma^{(t_2^*)} = 3/2$ , as shown in Fig. 28C and 28D. This approach is also similar to the idea behind the COASTER experiment[31] used to separate the anisotropic second-order electric quadrupole interaction from the first-order nuclear shielding in a 2D spectrum for half-integer electric quadrupole nuclei.

## 3.2. $\text{d}_I$ Echoes

### 3.2.1. The solid echo

The solid echo,  $(\frac{\pi}{2} - t_1 - \frac{\pi}{2} - t_2)$ , experiment[28, 29] is an example of a d-echo. This is illustrated in Fig. ?? for a spin  $I = 1$  nuclei experiencing the first-order electric quadrupole coupling. In this experiment, the formation of

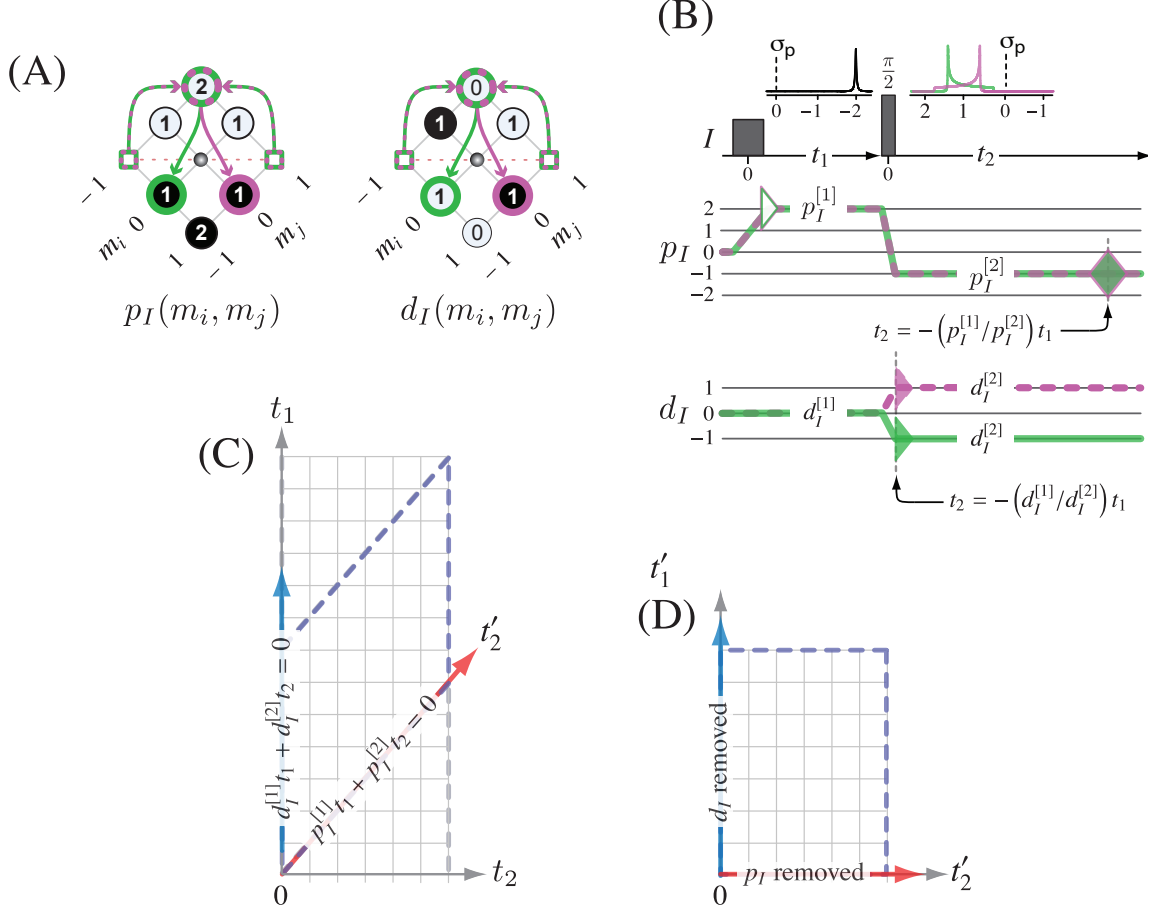


Figure 28: (A) Double-quantum spin echo transition pathways in Eq. (85) on the  $p_I$  and  $d_I$  tables for a spin  $I = 1$  nucleus. (B) Pulse sequence with  $p_I$  and  $d_I$  pathways for the two-pulse experiment. The filled diamond represents a directly observable echo. A filled or unfilled triangle represents a contribution to a free induction decay that is directly or indirectly observable, respectively. (C) In the 2D signal acquired as a function of  $t_1$  and  $t_2$ , there is no signal evolution due to the electric quadrupole coupling along the line  $d_I^{[1]}t_1 + d_I^{[2]}t_2 = 0$  (i.e., during  $t_1$ ), and both the isotropic and anisotropic nuclear shielding contributions are refocused into a  $p_I$ -echo along the line  $p_I^{[1]}t_1 + p_I^{[2]}t_2 = 0$ . The dashed line represents a passive affine transformation of the 2D coordinate system to create a time coordinate,  $t'_1$ , along which the 2D signal is unaffected by frequency components containing  $p_I$ . (D) After applying an active affine transformation with a shear parallel to the  $t_1$  coordinate using a shearing ratio of  $\kappa^{(\omega_2)} = 1/2$  and a scaling of  $t_2$  by  $\varsigma^{(t_2^*)} = 3/2$ , the 2D signal is unaffected by frequency components containing  $p_I$  along the  $t'_2$  coordinate and unaffected by frequency components containing  $d_I$  along the  $t'_1$  coordinate.

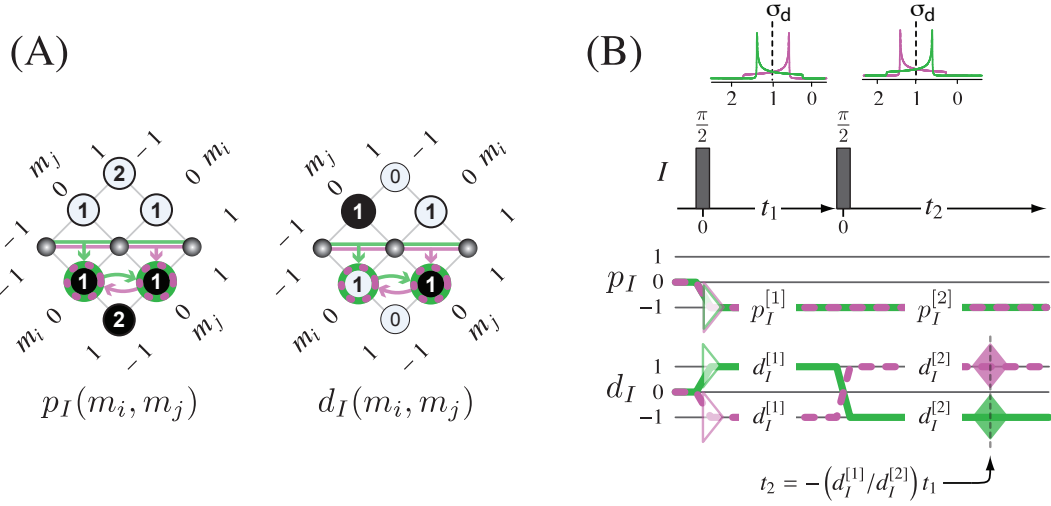


Figure 29: (A) Solid echo transition pathways in Eq. (86) on the  $p_I$  and  $d_I$  tables for a spin  $I = 1$  nucleus. (B) Pulse sequence with  $p_I$  and  $d_I$  pathways for two-pulse solid echo experiment. A filled diamond represents a contribution to a directly observable echo, while an open triangle represents a contribution to an indirectly observable free induction decay.

the d-echo is optimized by using a non-selective  $\pi/2$  pulse as the second (mixing) pulse instead of a non-selective  $\pi$  pulse. The experiment consists of the two transition pathways

$$\{I = 1\} : \begin{cases} [z_I] \rightarrow |-1\rangle \langle 0| \rightarrow |0\rangle \langle +1|, \\ [z_I] \rightarrow |0\rangle \langle +1| \rightarrow |-1\rangle \langle 0|. \end{cases} \quad (86)$$

These transition pathways map into a single  $p_I$  pathway,  $p_I = 0 \rightarrow -1 \rightarrow -1$ , and two  $d_I$  pathways,  $d_I = 0 \rightarrow +1 \rightarrow -1$  and  $d_I = 0 \rightarrow -1 \rightarrow +1$ . A non-selective  $\pi/2$  mixing pulse can also generate transition pathways that lead to a change in sign of the  $p_I$ ; however, with the proper phase cycling, these possibilities can be eliminated. Thus, the first-order electric quadrupole splitting is refocused into a  $d_I$ -echo along  $t_1 - t_2 = 0$ , and the signal acquired along the  $d_I$ -echo tops as a function of  $t_1 = t_2$  will be modulated by the  $p_I$  containing component of Eq. (74).

### 3.2.2. The Jeener-Broekaert echo

Another noteworthy d-echo occurs in the Jeener-Broekaert echo[40],  $(\frac{\pi}{2} - t_1 - \frac{\pi}{4} - \tau - \frac{\pi}{4} - t_2)$ , experiment, which could also be called a stimulated solid echo experiment. It is shown in Fig. 30 for a spin  $I = 1$  nuclei experiencing the first-order electric quadrupole coupling. The use of non-selective  $\pi/4$  pulses during the mixing period optimizes the conversion between coherence and longitudinal nuclear electric quadrupole order. The experiment consists of the two transition pathways

$$\{I = 1\} : \begin{cases} [z_I] \rightarrow |-1\rangle \langle 0| \rightarrow [z_I^2] \rightarrow |0\rangle \langle +1|, \\ [z_I] \rightarrow |0\rangle \langle +1| \rightarrow [z_I^2] \rightarrow |-1\rangle \langle 0|, \end{cases} \quad (87)$$

where the  $[z_I^2]$  represents nuclear electric quadrupole order. These transition pathways map into a single  $p_I$  pathway,  $p_I = 0 \rightarrow -1 \rightarrow 0 \rightarrow -1$ , and two  $d_I$  pathways,  $d_I = 0 \rightarrow +1 \rightarrow 0 \rightarrow -1$  and  $d_I = 0 \rightarrow -1 \rightarrow 0 \rightarrow +1$ . Thus, the  $d_I$  pathway predicts the  $d_I$  echo at  $t_1 = t_2$ .

### 3.2.3. The Solomon echoes

Solomon echoes[29, 41], discovered in the late 1950s, are yet another example of  $d_I$  echoes. These can be easily understood by examining the  $d_I$  tables for spin  $I = 5/2$  half-integer spin nuclei. In a two-pulse sequence, identical to the solid echo experiment of Fig. ??, using non-selective  $\pi/2$  pulses phase cycled for a pathway  $p_I = 0 \rightarrow -1 \rightarrow 0 \rightarrow -1$ ,

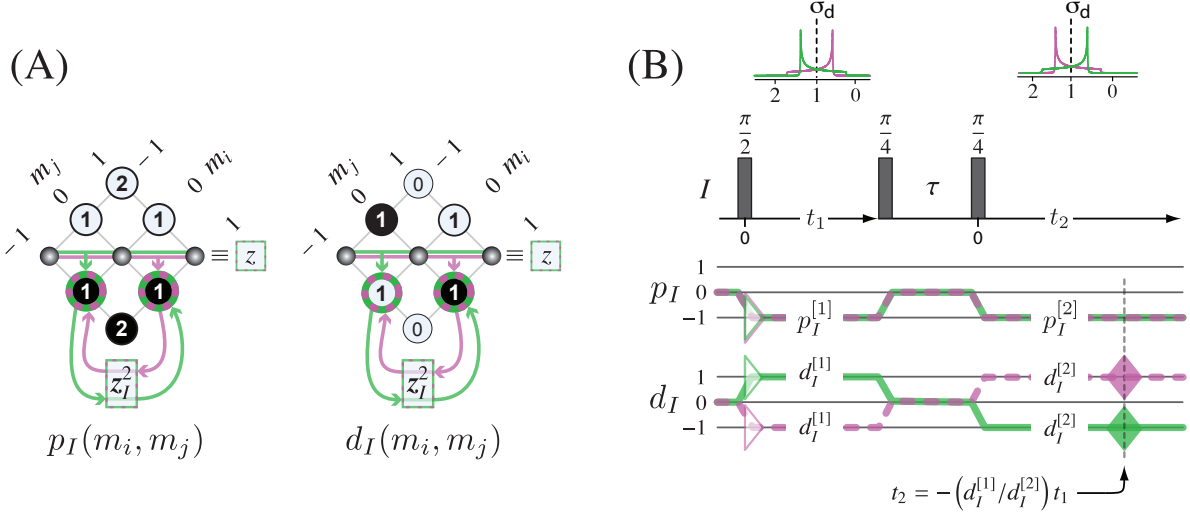


Figure 30: (A) Stimulated solid echo[40] transition pathways in Eq. (87) on the  $p_I$  and  $d_I$  tables for a spin  $I = 1$  nucleus. The arrows going through  $[z_I^2]$  represent the coherence transfer into longitudinal electric quadrupole order during the  $\tau$  period. (B) Pulse sequence with  $p_I$  and  $d_I$  pathways for two-pulse solid echo experiment. A filled diamond represents a contribution to an observable echo, while the open triangle represents an indirectly observable free induction decay.

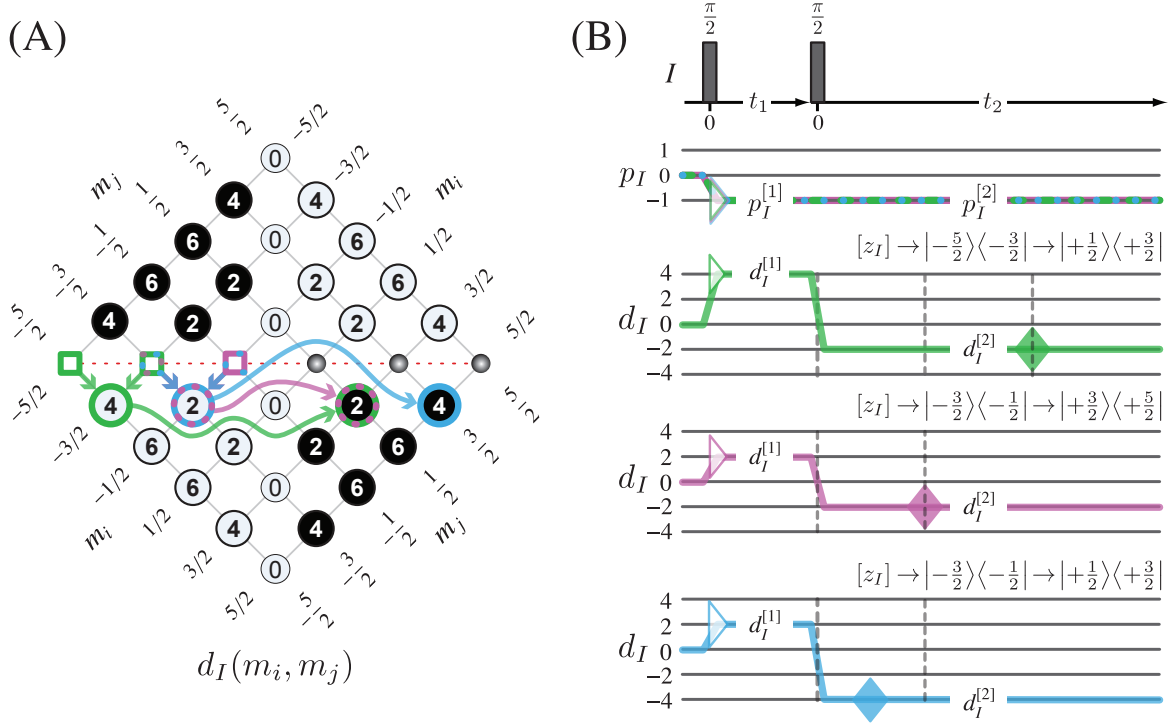


Figure 31: (A) Three Solomon echo transition pathways in Eq. (88) on the  $d_I$  tables for a spin  $I = 5/2$  nucleus. (B) Pulse sequence and three  $d_I$  pathways for a two-pulse Solomon echo experiment. A filled diamond represents a contribution to a directly observable echo, while an open triangle represents a contribution to an indirectly observable free induction decay.

a spin  $I = 5/2$  nuclei will have 20 transition pathways, with the six pathways given below leading to the formation of Solomon echoes,

$$\{I = \frac{5}{2}\} : \left\{ \begin{array}{l} [z_I] \rightarrow |-\frac{5}{2}\rangle \langle -\frac{3}{2}| \rightarrow |+\frac{1}{2}\rangle \langle +\frac{3}{2}|, \\ [z_I] \rightarrow |+\frac{3}{2}\rangle \langle +\frac{5}{2}| \rightarrow |-\frac{3}{2}\rangle \langle -\frac{1}{2}|, \\ \hline [z_I] \rightarrow |-\frac{3}{2}\rangle \langle -\frac{1}{2}| \rightarrow |+\frac{3}{2}\rangle \langle +\frac{5}{2}|, \\ [z_I] \rightarrow |+\frac{1}{2}\rangle \langle +\frac{3}{2}| \rightarrow |-\frac{5}{2}\rangle \langle -\frac{3}{2}|, \\ \hline [z_I] \rightarrow |-\frac{3}{2}\rangle \langle -\frac{1}{2}| \rightarrow |+\frac{1}{2}\rangle \langle +\frac{3}{2}|, \\ [z_I] \rightarrow |+\frac{1}{2}\rangle \langle +\frac{3}{2}| \rightarrow |-\frac{3}{2}\rangle \langle -\frac{1}{2}|. \end{array} \right. \quad (88)$$

These pathways are separated into three groups, each associated with forming a particular Solomon echo. The timings for the appearance of the three Solomon echoes become apparent when these transition pathways are mapped into  $d_I$  pathways,

$$d_I = \left\{ \begin{array}{l} 0 \rightarrow +4 \rightarrow -2, \\ 0 \rightarrow -4 \rightarrow +2, \\ \hline 0 \rightarrow +2 \rightarrow -2, \\ 0 \rightarrow -2 \rightarrow +2, \\ \hline 0 \rightarrow +2 \rightarrow -4, \\ 0 \rightarrow -4 \rightarrow +2. \end{array} \right. \quad (89)$$

A transition pathway from each Solomon echo group and its associated  $d_I$  pathway is illustrated in Fig. 31.

### 3.3. $(pp)_{IS}$ Echoes

#### 3.3.1. HETCOR

As an example of a  $(pp)_{IS}$  echo, we consider a heteronuclear coupled spin 1/2 system in the liquid state with the frequency components given below:

$$\Omega(\Theta, m_{I,i}, m_{S,i}, m_{I,j}, m_{S,j}) = -\omega_0^{\{I\}} \sigma_{iso,I} \mathbb{P}_I(m_{I,i}, m_{I,j}) - \omega_0^{\{S\}} \sigma_{iso,S} \mathbb{P}_S(m_{S,i}, m_{S,j}) + 2\pi J_{iso} (\mathbb{P}\mathbb{P})_{IS}(m_{I,i}, m_{S,i}, m_{I,j}, m_{S,j}). \quad (90)$$

The liquid-state HETeronuclear CORrelation (HETCOR) experiment[42] on this system consists of two transition pathways:

$$\{I = \frac{1}{2}, S = \frac{1}{2}\} : \left\{ \begin{array}{l} [z_I] \rightarrow |-\frac{1}{2}, -\frac{1}{2}\rangle \langle +\frac{1}{2}, -\frac{1}{2}| \\ \rightarrow |-\frac{1}{2}, +\frac{1}{2}\rangle \langle +\frac{1}{2}, +\frac{1}{2}| \\ \rightarrow |-\frac{1}{2}, -\frac{1}{2}\rangle \langle -\frac{1}{2}, +\frac{1}{2}| \\ \rightarrow |+\frac{1}{2}, -\frac{1}{2}\rangle \langle +\frac{1}{2}, +\frac{1}{2}| \\ \rightarrow |\times, -\frac{1}{2}\rangle \langle \times, +\frac{1}{2}|, \\ \hline [z_I] \rightarrow |-\frac{1}{2}, +\frac{1}{2}\rangle \langle +\frac{1}{2}, +\frac{1}{2}| \\ \rightarrow |-\frac{1}{2}, -\frac{1}{2}\rangle \langle +\frac{1}{2}, -\frac{1}{2}| \\ \rightarrow |+\frac{1}{2}, -\frac{1}{2}\rangle \langle +\frac{1}{2}, +\frac{1}{2}| \\ \rightarrow |-\frac{1}{2}, -\frac{1}{2}\rangle \langle -\frac{1}{2}, +\frac{1}{2}| \\ \rightarrow |\times, -\frac{1}{2}\rangle \langle \times, +\frac{1}{2}|, \end{array} \right. \quad (91)$$

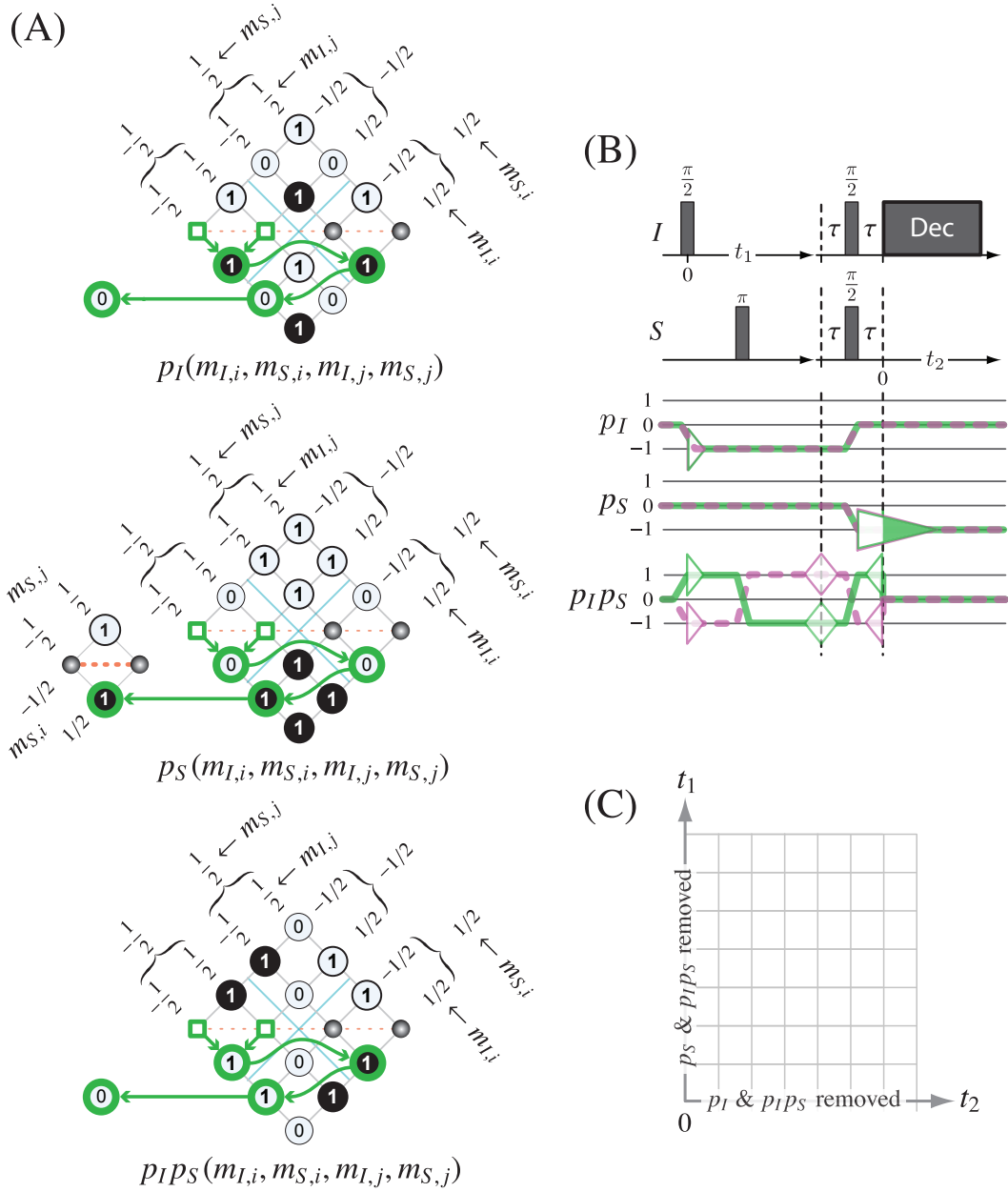


Figure 32: (A) A liquid-state HETCOR transition pathway in Eq. (91) on the  $p_I$ ,  $p_S$ , and  $(pp)_{IS}$  tables for two coupled spin  $I = 1/2$  nuclei. (B) HETCOR pulse sequence with  $p_I$ ,  $p_S$ , and  $(pp)_{IS}$  pathways. An open diamond represents a contribution to an indirectly observable echo, while an open triangle represents a contribution to an indirectly observable free induction decay. (C) The 2D signal along the  $t_1$  coordinate is unaffected by frequency components containing  $p_S$  and  $(pp)_{IS}$ , while the 2D signal along the  $t_2$  coordinate is unaffected by frequency components containing  $p_I$  and  $(pp)_{IS}$ .



where we use the symbol  $\times$  to indicate that the  $m_I$  states are removed from the system through  $I$  spin decoupling. These transition pathways map into a single  $p_I$  pathway,  $p_I = 0 \rightarrow -1 \rightarrow -1 \rightarrow 0$ , a single  $p_S$  pathway,  $p_S = 0 \rightarrow 0 \rightarrow 0 \rightarrow -1$ , and two  $(pp)_{IS}$  pathways,  $(pp)_{IS} \rightarrow +1 \rightarrow -1 \rightarrow +1 \rightarrow 0$  and  $(pp)_{IS} \rightarrow -1 \rightarrow +1 \rightarrow -1 \rightarrow 0$ . The first transition pathway is shown on the  $p_I$ ,  $p_S$ , and  $(pp)_{IS}$  tables in Fig. 32. The second transition pathway would appear as a mirror image of the first transition pathway about a vertical line bisecting the table.

With  $(pp)_{IS}$  refocusing into an echo at the end of  $t_1$ , and  $p_S = 0$  throughout  $t_1$ , the only frequency component active during  $t_1$  are those containing  $p_I$ . The most efficient coherence transfer between an  $I$  and  $S$  spin via the  $J$  coupling during the mixing period occurs when  $\tau = 1/(2J_{iso})$ . Finally, the application of  $I$  spin decoupling during  $t_2$  eliminates frequency components containing  $p_I$  and  $(pp)_{IS}$ , leaving only the frequency component containing  $p_S$  during  $t_2$ . The 2D signal, as illustrated in Fig. 32C, associates the  $t_1$  dimension with system evolution without frequency components containing  $p_S$  and  $(pp)_{IS}$  symmetries, while the  $t_2$  dimension is associated with evolution without frequency components containing  $p_I$  and  $(pp)_{IS}$  symmetries. Notice that the free induction decay arising from the frequency component containing  $p_S$  is only partially acquired in  $t_2$ . That is, acquisition of the  $p_S$  component free induction decay in  $t_2$  is delayed by  $\tau$ . The truncation of the initial part of the signal in  $t_2$  is why the liquid-state HETCOR experiment is often presented as a magnitude mode 2D spectrum[43].

### 3.3.2. HSQC

A related experiment that does not suffer from this drawback is the Heteronuclear Single-Quantum Correlation (HSQC) experiment[44], shown in Fig. 33. For clarity, only one HSQC transition pathway is shown in Fig. 33. The 2D HSQC signal, as illustrated in Fig. 33C, associates the  $t_1$  dimension with system evolution without frequency components containing  $p_I$  and  $(pp)_{IS}$  symmetries, while the  $t_2$  dimension is associated with evolution without frequency components containing  $p_S$  symmetries.

## 3.4. $\mathbb{D}_1$ , $\mathbb{D}_2$ , and $\mathbb{G}_1$ , $\mathbb{G}_2$ , $\mathbb{G}_3$ , $\mathbb{G}_4$ Echoes

### 3.4.1. D-MAS

As mentioned earlier, sample rotation about a single axis breaks the spatial functions into components. Under D-MAS, the first-order nuclear shielding contributions break up into three components,

$$\Omega_{\sigma}^{(1)}(m_i, m_j, \theta_M^{(2)}, \omega_R t) = -\omega_0 \sigma_{iso} \mathbb{P}_I(m_i, m_j) - \omega_0 \zeta_{\sigma} \mathbb{D}_1^{\{\sigma\}}(\theta_M^{(2)}, \omega_R t) \mathbb{P}_I(m_i, m_j) - \omega_0 \zeta_{\sigma} \mathbb{D}_2^{\{\sigma\}}(\theta_M^{(2)}, \omega_R t) \mathbb{P}_I(m_i, m_j). \quad (92)$$

In a one-pulse D-MAS experiment, shown in Fig. 34, the  $\mathbb{D}_1$  spatial pathway leads to an echo formed every rotor period and the  $\mathbb{D}_2$  pathway every half rotor period. It is also useful to rewrite Eq. (92) in a Fourier expansion as

$$\Omega_{\sigma}^{(1)}(m_i, m_j, \theta_M^{(2)}, \phi_R) = \varpi_0(\theta_M^{(2)}, \alpha, \beta) + \sum_{m \neq 0} \varpi_m(\theta_M^{(2)}, \alpha, \beta) e^{im(\phi_R + \gamma)}, \quad (93)$$

where

$$\varpi_{-m}(\theta_M^{(2)}, \alpha, \beta) = \varpi_m^*(\theta_M^{(2)}, \alpha, \beta). \quad (94)$$

Comparing Eq. (93) to Eq. (92) we find that  $\varpi_0$  is related to  $\mathbb{S}$  and  $\mathbb{D}_0$  by

$$\varpi_0(\theta_M^{(2)}, \alpha, \beta) = -\omega_0 \sigma_{iso} \mathbb{P}_I(m_i, m_j) - \omega_0 \zeta_{\sigma} \mathbb{D}_0^{\{\sigma\}}(\theta_M^{(2)}) \mathbb{P}_I(m_i, m_j), \quad (95)$$

and  $\varpi_{\pm 1}$  and  $\varpi_{\pm 2}$  are related to  $\mathbb{D}_m$  according to

$$\varpi_m(\theta_M^{(2)}, \alpha, \beta) e^{im[\phi_R + \gamma]} + \varpi_m^*(\theta_M^{(2)}, \alpha, \beta) e^{-im[\phi_R + \gamma]} = \omega_0 \zeta_{\sigma} \mathbb{D}_m^{\{\sigma\}}(\theta_M^{(2)}, \phi_R) \mathbb{P}_I(m_i, m_j), \quad (96)$$

In the simple Bloch decay experiment with a rotating sample, the signal phase as a function of  $t$ , where  $\phi_R(t) = \omega_R t + \chi_R$ , is

$$\Phi_{\sigma}(t, \chi_R) = \int_0^t \Omega_{\sigma}(s) ds = W_0 t + \sum_{m \neq 0} W_m e^{im(\chi_R + \gamma)} \left[ e^{im\omega_R t} - 1 \right], \quad (97)$$

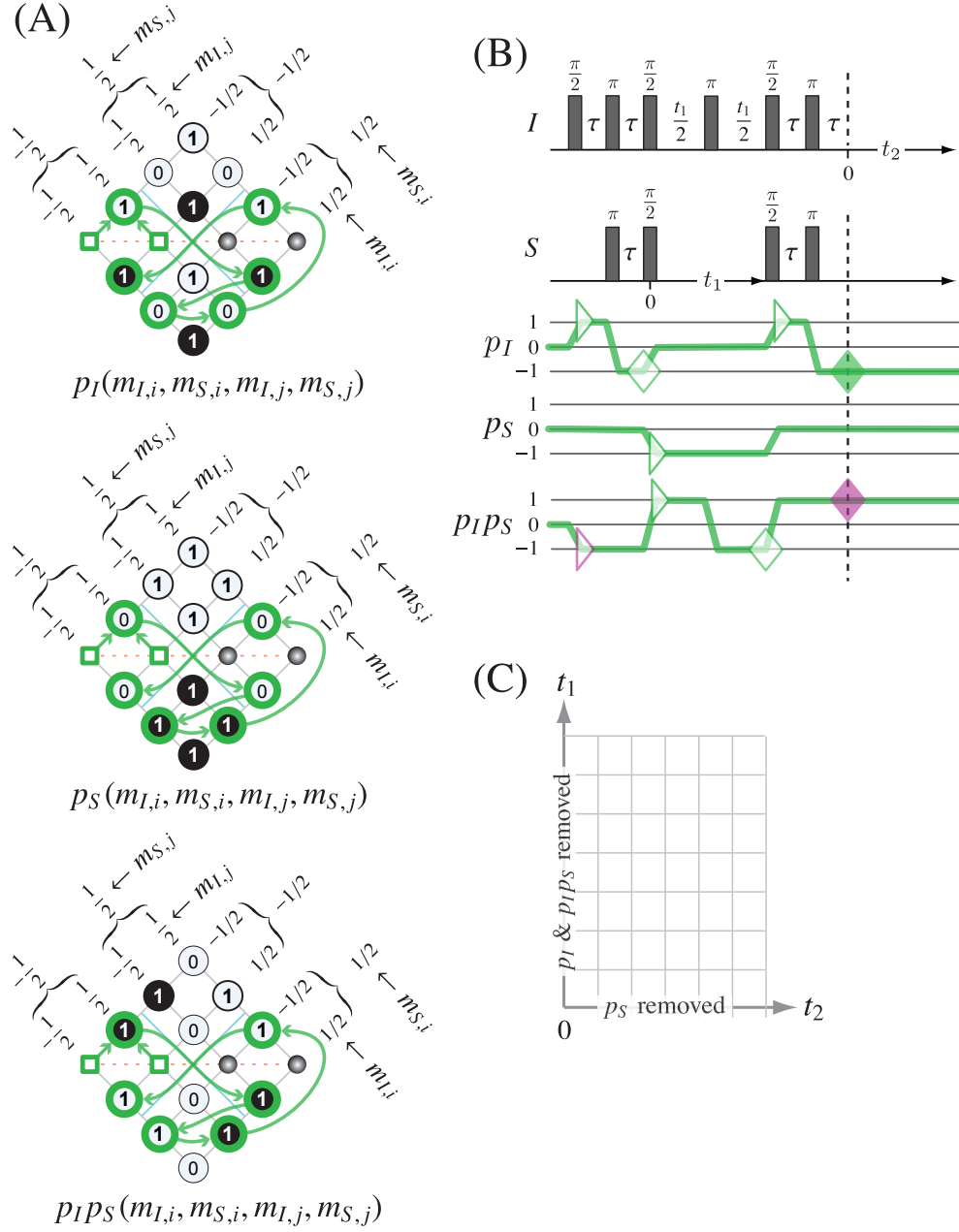


Figure 33: (A) A HSQC transition pathway on the  $p_I$ ,  $p_S$ , and  $(pp)_{IS}$  tables for two coupled spin  $I = 1/2$  nuclei. (B) HSQC pulse sequence with  $p_I$ ,  $p_S$ , and  $(pp)_{IS}$  pathways. A filled diamond represents a contribution to a directly observable echo, while a filled triangle represents a contribution to a directly observable free induction decay. (C) The 2D signal along the  $t_1$  coordinate is unaffected by frequency components containing  $p_I$  and  $(pp)_{IS}$ , while the 2D signal along the  $t_2$  coordinate is unaffected by frequency components containing  $p_S$ .

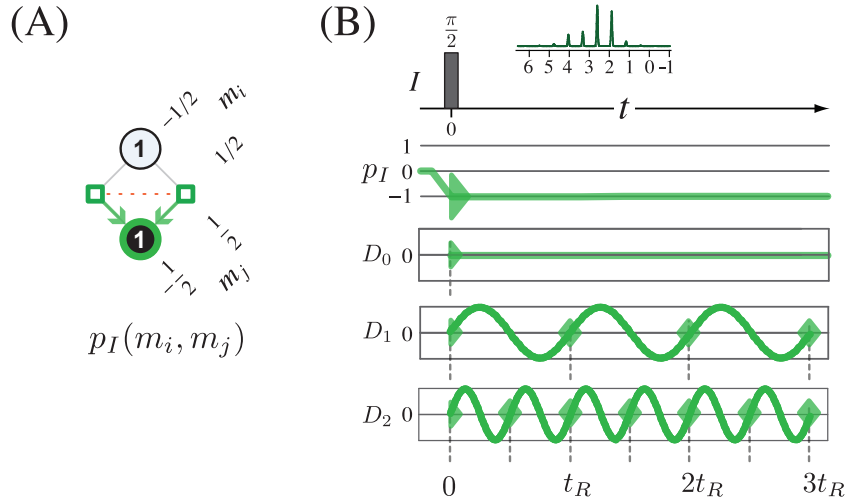


Figure 34: (A) Rotary echoes in a D-MAS Bloch decay experiment with transition pathway  $\{I\} : [z_I] \rightarrow |-\frac{1}{2}\rangle \langle \frac{1}{2}|$  on the  $p_I$  table for spin  $I = 1/2$ . (B) Pulse sequence with  $p_I$  and  $D_n$  pathways for one pulse D-MAS experiment. Only the anisotropic nuclear shielding contributions with  $D_1$  and  $D_2$  are refocused into rotary echoes, represented by diamonds. A filled triangle represents a contribution to an observable free induction decay, and a filled diamond represents a contribution to an observable echo.

where we define

$$W_0 = \varpi_0(\theta_R, \alpha, \beta), \quad \text{and} \quad W_m = \frac{\varpi_m(\theta_R, \alpha, \beta)}{im\omega_R}. \quad (98)$$

One can show (see Appendix) that the Bloch decay signal in a rotating sample is given by

$$\mathfrak{s}_B(t, \chi_R) = s^e(t) e^{i\Phi(t, \chi_R)} = s^e(t) e^{iW_0 t} \sum_{N_1, N_2} A(N_1) A^*(N_2) e^{-iN_1 \omega_R t} e^{i(N_2 - N_1)(\chi_R + \gamma)}, \quad (99)$$

where

$$A(N) = \frac{1}{2\pi} \int_0^{2\pi} \exp \left\{ i \sum_{m \neq 0} W_m e^{im\Theta} \right\} e^{iN\Theta} d\Theta, \quad (100)$$

and  $s^e(t)$  represents the envelope function due to the relaxation. A partial averaging of the Bloch decay signal over the angle  $\gamma$  yields

$$\langle \mathfrak{s}_B(t) \rangle_\gamma = s^e(t) e^{iW_0 t} \sum_N |A(N)|^2 e^{-iN \omega_R t}. \quad (101)$$

Notice that  $W_0$  is dependent only on frequency contributions with the spatial-transition symmetry product  $\mathbb{S} p_I$  during D-MAS, whereas the spinning sideband amplitudes,  $A(N)$ , are only dependent on contributions with the spatial-transition symmetry products  $\mathbb{D}_1 p_I$  and  $\mathbb{D}_2 p_I$ .

### 3.4.2. TOP

One can rewrite Eq. (101) in the form

$$\langle \mathfrak{s}(t_1, t_2) \rangle_\gamma = s^e(t_2) e^{iW_0 t_2} \sum_N |A(N)|^2 e^{-iN \omega_R t_1}, \quad (102)$$

and visualize the 1D Bloch decay signal from a rotating sample as a signal filling a 2D  $t_1$ - $t_2$  coordinate system, as illustrated in Fig. 35. Note that

$$\langle \mathfrak{s}(t_1 + kt_R, t_2) \rangle_\gamma = \langle \mathfrak{s}(t_1, t_2) \rangle_\gamma, \quad (103)$$

where  $t_R = 2\pi/\omega_R$  and  $k$  is an integer. The significance of this coordinate system is that the frequency contributions with the spatial-transition symmetry product  $\mathbb{S} p_I$  are removed along the  $t_1$  dimension, and the contributions with the spatial-transition symmetry products  $\mathbb{D}_1 p_I$  and  $\mathbb{D}_2 p_I$  are removed along the  $t_2$  dimension. This coordinate

system is particularly useful for understanding several important solid-state NMR experiments for manipulating  $\mathbb{D}_m$  (i.e.,  $m \neq 0$  rotary) echoes and their associated spectral spinning sidebands. Probably the simplest of these is the Two-dimensional One Pulse (TOP) processing approach [45, 46, 47], which samples the 2D signal of Eq. (102) using identical 1D Bloch decay signals running parallel to each other and separated by  $t_R$  in both  $t_1$  and  $t_2$ , as shown in Fig. 35.

In the TOP approach, one first generates a pseudo-2D signal,  $s_{\text{top}}(\epsilon, t)$ , in a  $\epsilon$ - $t$  coordinate system from the 1D Bloch decay signal,  $s_B(t)$ . This is illustrated in Fig. 36A, where a sampling of  $s_{\text{top}}(\epsilon, t)$  is generated using the relationship

$$s_{\text{top}}(k2\pi/\omega_R, t) = s_B(t), \quad (104)$$

for a range of positive and negative integer  $k$  values. The full sampling of the TOP signal in all four quadrants can be generated using the complex conjugate of the Bloch decay signal,  $s_B^*(t)$ , as illustrated in Fig. 36B and 36C.

After the 2D signal,  $s_{\text{top}}(\epsilon, t)$ , is created, an affine transformation, as illustrated in Fig. 37A, is applied to separate the frequency contributions with the spatial-transition symmetry product  $\mathbb{S}p_I$  into a dimension that is orthogonal to a dimension containing contributions with the spatial-transition symmetry products  $\mathbb{D}_1 p_I$  and  $\mathbb{D}_2 p_I$ . For the TOP signal, this is performed as a double shear, starting with a shear parallel to the  $t$  coordinate with a shear ratio of  $\kappa_t = -1$ , followed by a shear parallel to the  $t'_2$  coordinate with a shear ratio of  $\kappa_{t'_2} = 1$ , according to

$$\begin{bmatrix} t_2 \\ t_1 \end{bmatrix} = \underbrace{\begin{bmatrix} 1 & 1 \\ 0 & 1 \end{bmatrix}}_{\mathcal{K}_{t'_2}} \underbrace{\begin{bmatrix} 1 & 0 \\ -1 & 1 \end{bmatrix}}_{\mathcal{K}_t} \begin{bmatrix} \epsilon \\ t \end{bmatrix} = \begin{bmatrix} 0 & 1 \\ -1 & 1 \end{bmatrix} \begin{bmatrix} \epsilon \\ t \end{bmatrix}. \quad (105)$$

The application of this affine transformation to  $s(\epsilon, t)$  yields the TOP[47] signal in Eq. (102) whose Fourier transform yields a 2D spectrum correlating frequencies with  $\mathbb{S}p_I$  symmetry to those with  $\mathbb{D}_1 p_I$  and  $\mathbb{D}_2 p_I$  symmetries. Notice that the application of this affine transformation to the original digital sampling rates,  $\Delta\epsilon$  and  $\Delta t$ , yields transformed sampling rates of  $\Delta t_2 = \Delta\epsilon = t_R$  and  $\Delta t_1 = \Delta t$ , respectively, after the double shear transformation. A limitation of the TOP approach is that the spectral width in  $\omega_2$ , the isotropic frequency (i.e.,  $\mathbb{D}_1 p_I$  and  $\mathbb{D}_2 p_I$  removed) dimension, is limited to integer divisors of the rotor frequency, and this cannot be easily corrected by increasing the rotor frequency since it also reduces the information content in the sideband intensities. Nonetheless, TOP has several added advantages when applied to half-integer quadrupolar nuclei[47], and its main strength lies in its rapid interpretation of MAS signals. The experimental simplicity of TOP makes it a compelling method, and it is surprising that it has not been widely utilized. The spectral width limitation in the isotropic dimension of TOP can be overcome by employing well-known strategies for shifting the time origin for  $\mathbb{S}p_I$  frequency evolution away from the origin for  $\mathbb{D}_1 p_I$  and  $\mathbb{D}_2 p_I$  frequency evolution, such as the PASS[48, 49]. Alternatively, the separation of nuclear shielding frequency components with  $S$  symmetry from those with  $\mathbb{D}$  symmetry can be accomplished with a variety of other 2D experiments[50, 51, 52, 53, 49, 54, 55], some of which are discussed in Section 3.8.

Finally, it is worth noting that it may appear that the TOP transformation could be performed with only a single shear parallel to the  $\epsilon$  coordinate with a shear ratio of  $\kappa_\epsilon = -1$ , as outlined in Fig. 37B, and given by

$$\begin{bmatrix} t_1 \\ t_2 \end{bmatrix} = \underbrace{\begin{bmatrix} 1 & -1 \\ 0 & 1 \end{bmatrix}}_{\mathcal{K}_\epsilon} \begin{bmatrix} \epsilon \\ t \end{bmatrix} = \begin{bmatrix} -1 & 1 \\ 0 & 1 \end{bmatrix} \begin{bmatrix} \epsilon \\ t \end{bmatrix}. \quad (106)$$

With this transformation, however, the original digital sampling rates,  $\Delta\epsilon$  and  $\Delta t$ , after the single shear become  $\Delta t_1 = \Delta\epsilon = t_R$  and  $\Delta t_2 = \Delta t$ , respectively. Such a sampling rate in  $t_1$  will not resolve any spinning sidebands arising from the  $\mathbb{D}_1 p_I$  and  $\mathbb{D}_2 p_I$  frequency contributions in the  $\omega_1$  dimension.

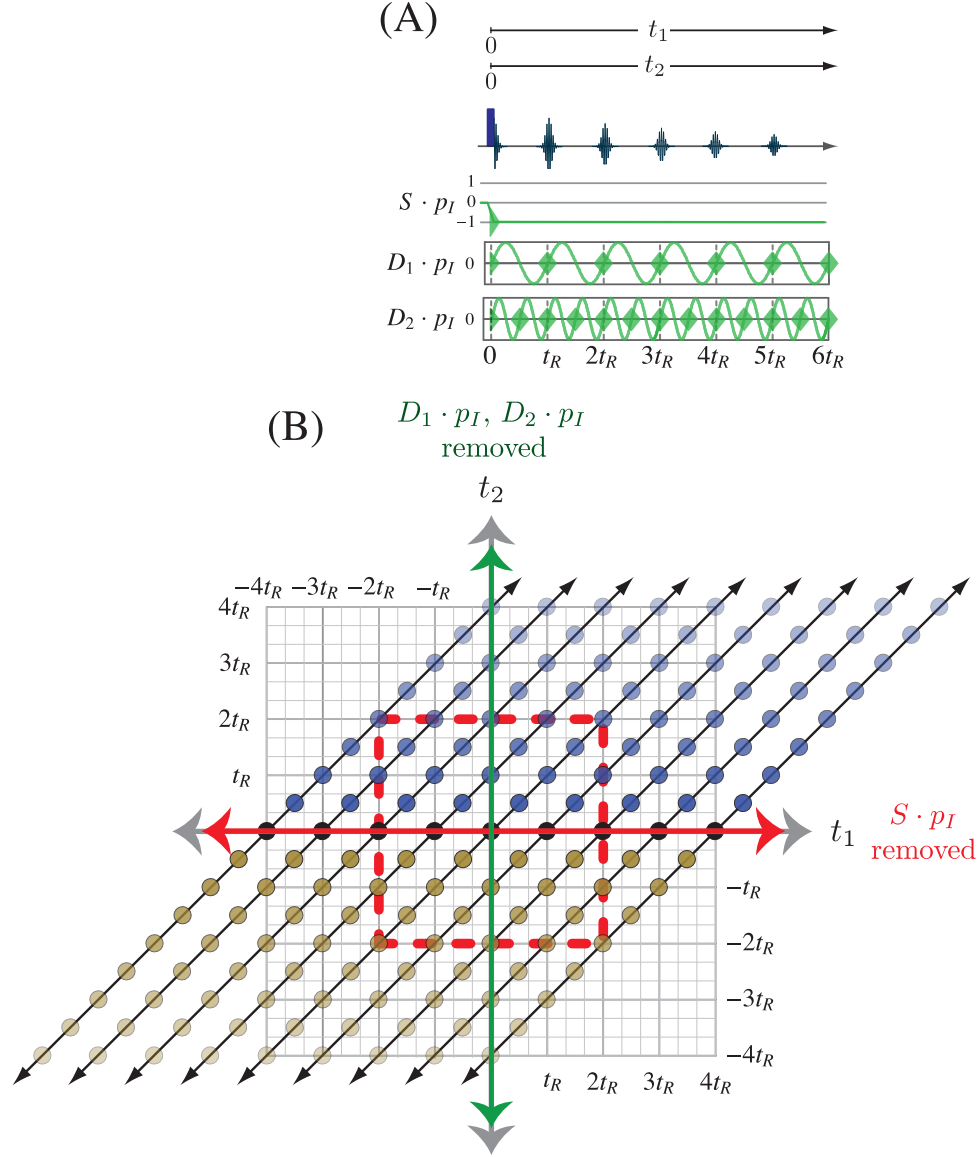


Figure 35: (A) One-dimensional Bloch decay experiment in a rotating sample with associated symmetry pathways. (B) TOP sampling in the  $t_1$ - $t_2$  coordinate system with solid circles and arrows represent the sampling trajectory of the (blue circles) 1D Bloch decay signal and (brown circles) its complex conjugate signal from a rotating sample. The slope of the sampling trajectory in the  $t_1$ - $t_2$  coordinate system is 1. Identical signals run parallel, separated by  $t_R$  in  $t_1$  and  $t_2$ , respectively. Frequency contributions with the spatial-transition symmetry product  $S p_I$  are absent along the  $t_1$  dimension, and contributions with spatial-transition symmetry products  $D_1 p_I$  and  $D_2 p_I$  are absent along the  $t_2$  dimension.

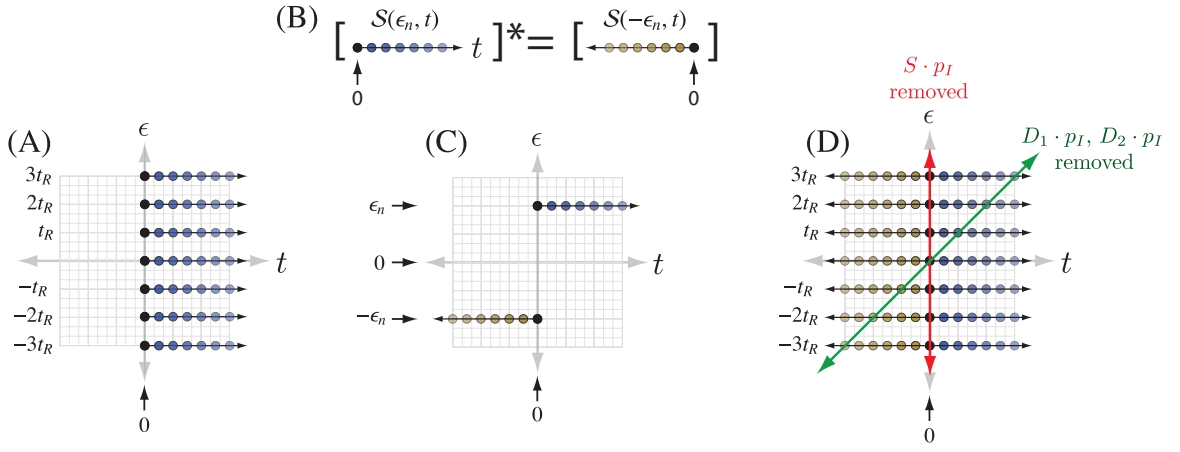


Figure 36: Scheme for generating the pseudo-2D signal for TOP processing from the 1D Bloch decay signal in a rotating sample. (A) Identical Bloch decay signals are laid down in a coordinate system at integer multiples of the rotor period along the  $\epsilon$  dimension. (B) The complex conjugate of the 1D Bloch decay signal is used to generate a Bloch decay signal going backward in time. (C) Identical complex conjugate Bloch decay signals are placed in the opposite quadrant in the  $t$ - $\epsilon$  coordinate system. (D) The TOP signal before the application of the affine transformation has the spatial-transition symmetry product  $S p_I$  removed along the  $\epsilon$  coordinate, and the contributions with the spatial-transition symmetry products  $D_1 p_I$  and  $D_2 p_I$  are removed along the line  $\epsilon + t_1 = 0$ .

### 3.4.3. 2D PASS

Closely related to the TOP experiment is the Phase Adjusted Spinning Sidebands (PASS) experiment. Generally, the NMR signal in a rotating sample can be manipulated into several desirable forms by applying a series of  $\pi$  pulses between the initial excitation pulse and the start of signal acquisition. In the PASS experiment, a time coordinate is defined where the initial excitation pulse is applied at  $t = -T$  and signal acquisition begins at  $t = 0$ . Between the initial excitation pulse and signal acquisition are  $Q$   $\pi$ -pulses, applied at times  $-T + \tau_1, -T + \tau_2, \dots, -T + \tau_Q$ . The signal phase at  $t = 0$ , a duration of  $\tau_{Q+1} = T$  after the initial excitation pulse, is given by

$$\begin{aligned} \Phi_Q(t=0, \chi_R) &= (-1)^Q \sum_{q=0}^Q (-1)^q \int_{-T+\tau_q}^{-T+\tau_{q+1}} \Omega(s) ds = W_0 \left[ T - 2(-1)^Q \sum_{q=1}^Q (-1)^q \tau_q \right] \\ &+ \sum_{m \neq 0} W_m e^{im(\chi_R + \gamma)} \left[ 1 - 2(-1)^Q \sum_{q=1}^Q (-1)^q e^{im\theta_q} e^{-im\theta_T} - (-1)^Q e^{-im\theta_T} \right], \quad (107) \end{aligned}$$

where  $\tau_0 = 0$ ,  $\theta_T = \omega_R T$ , and  $\theta_q = \omega_R \tau_q$ .

In the PASS experiment [56, 48] the timings of the  $Q$   $\pi$  pulses are manipulated so the signal phase at  $t = 0$  has the form

$$\Phi_{\text{pass}}(\epsilon, t=0, \chi_R) = W_0 [0] + \sum_{m \neq 0} W_m e^{im(\chi_R + \gamma)} \left[ 1 - e^{-im\omega_R \epsilon} \right], \quad (108)$$

where  $\epsilon$  can be varied independent of  $t$ . Evolving forward from  $t = 0$ , the PASS signal phase then becomes

$$\Phi_{\text{pass}}(\epsilon, t, \chi_R) = W_0 t + \sum_{m \neq 0} W_m e^{im(\chi_R + \gamma)} \left[ e^{im\omega_R t} - e^{-im\omega_R \epsilon} \right]. \quad (109)$$

Such a phase leads to a PASS signal when averaged over the crystallite angle  $\gamma$ , of the form (see Appendix)

$$\langle s_{\text{pass}}(\epsilon, t) \rangle_\gamma = e^{iW_0 t} \sum_N |A(N)|^2 e^{-iN\omega_R(t+\epsilon)}, \quad (110)$$

which, just like the Bloch decay signal in a rotating sample, can be used to fill the 2D signal in a  $\epsilon$ - $t$  coordinate system. In the case of PASS, the application of a single shear parallel to the  $\epsilon$  coordinate with a shear ratio of  $\kappa_\epsilon = -1$ , as

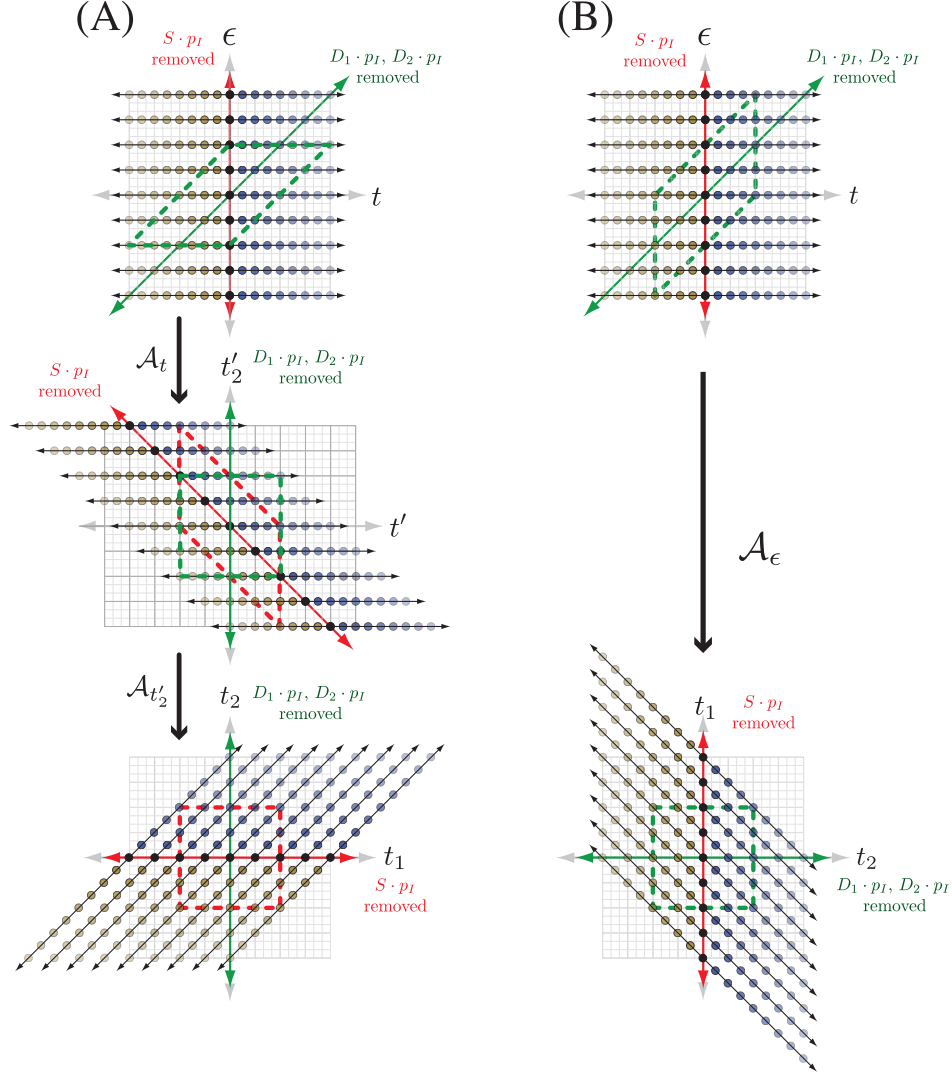


Figure 37: (A) The TOP signal acquired as a function of  $\epsilon$  and  $t_2$ , the  $\mathbb{D}_1 p_I$  and  $\mathbb{D}_2 p_I$  contributions are refocused into an echo along the line  $\epsilon + t_1 = 0$ , and the  $S p_I$  contribution is refocused along  $t = 0$ . After,  $\mathcal{A}_t$ , a shear parallel to  $t$ , a 2D signal with  $\mathbb{D}_1 p_I$  and  $\mathbb{D}_2 p_I$  refocused along the  $t'_2$  axis is obtained, the  $S p_I$  contribution is refocused along  $t + \epsilon = 0$ . After  $\mathcal{A}_{t'_2}$ , a shear parallel to  $t'_2$ , a 2D signal with  $\mathbb{D}_1 p_I$  and  $\mathbb{D}_2 p_I$  refocused along the  $t_2$  axis is obtained, the  $S p_I$  contribution is refocused along  $t_1$ . (B) Although  $\mathcal{A}_\epsilon$ , a shear parallel to  $\epsilon$ , will also give a 2D signal with  $\mathbb{D}_1 p_I$  and  $\mathbb{D}_2 p_I$  refocused along the  $t_2$  axis and the  $S p_I$  contribution is refocused along  $t_1$ , the discrete sampling of the TOP signal does not yield a sampling along the  $t_1$  faster than one rotor period, and thus all spinning sidebands are aliased into the centerband upon Fourier transform with respect to  $t_1$ .

illustrated in Fig. 37B, is sufficient for obtaining a 2D spectrum correlating frequencies with  $\mathbb{S} p_I$  symmetry to those with  $\mathbb{D}_1 p_I$  and  $\mathbb{D}_2 p_I$  symmetries.

The PASS approach for obtaining the signal phase of Eq. (108) comes from equating Eqs. (107) and (108) to obtain the PASS equations:

$$\theta_T - 2(-1)^Q \sum_{q=1}^Q (-1)^q \theta_q = 0, \quad (111)$$

and

$$2(-1)^Q \sum_{q=1}^Q (-1)^q e^{im\theta_q} e^{-im\theta_T} + (-1)^Q e^{-im\theta_T} = e^{-im\Theta}, \quad (112)$$

where  $\Theta = \omega_R \epsilon$ . Levitt and coworkers[49] suggested a five  $\pi$  pulse ( $Q = 5$ ) 2D PASS experiment, of constant duration  $T$ , with  $\theta_T = 2\pi$ , and obtained the equations

$$2 \sum_{q=1}^5 (-1)^q \theta_q + 2\pi = 0, \quad (113)$$

and

$$-2 \sum_{q=1}^5 (-1)^q e^{im\theta_q} - 1 = e^{-im\Theta}, \quad \text{for } m = 1, 2. \quad (114)$$

These equations can be solved numerically for the  $\pi$  pulse timings shown in Fig. 38 and are tabulated elsewhere[49].

#### 3.4.4. DOR

When the strength of a nuclear electric quadrupole coupling is a significant fraction of the nuclear Zeeman coupling, the NMR frequency needs to include second- and possibly higher-order corrections to properly describe the NMR spectrum. Thus, in addition to the first-order nuclear shielding and quadrupole coupling contributions

$$\Omega_{\sigma}^{(1)}(\Theta, m_i, m_j) = -\omega_0 \sigma_{\text{iso}} \mathbb{P}_I(m_i, m_j) - \omega_0 \zeta_{\sigma} \mathbb{D}^{\{\sigma\}}(\Theta) \mathbb{P}_I(m_i, m_j), \quad (115)$$

and

$$\Omega_q^{(1)}(\Theta, m_i, m_j) = \omega_q \mathbb{D}^{\{q\}}(\Theta) \mathbb{d}_I(m_i, m_j), \quad (116)$$

we must also include the second-order quadrupole coupling contributions

$$\Omega_q^{(2)}(\Theta, m_i, m_j) = \frac{\omega_q^2}{\omega_0} \mathbb{S}^{\{qq\}} c_0(m_i, m_j) + \frac{\omega_q^2}{\omega_0} \mathbb{D}^{\{qq\}}(\Theta) \mathbb{c}_2(m_i, m_j) + \frac{\omega_q^2}{\omega_0} \mathbb{G}^{\{qq\}}(\Theta) \mathbb{c}_4(m_i, m_j). \quad (117)$$

If our goal is to obtain a high-resolution isotropic spectrum, then the four components containing anisotropic spatial symmetry functions  $\mathbb{D}(\Theta)$  and  $\mathbb{G}(\Theta)$  need to be eliminated. There are different strategies for achieving this goal, all of which involve a combination of spatial and spin transition manipulations.

The first challenge is that the first-order quadrupole contribution can be on the order of megahertz in strength, creating an orientation-dependent frequency offset challenging to excite with rf pulses of conventional field strengths. In contrast, the other contributions are typically on the order of kilohertz in strength. Additionally, any attempt to eliminate the first-order quadrupole contribution with D-MAS will require accurate positioning of the rotor axis since any residual contribution from angle misset could easily be larger than the other contributions. Fortunately, there is an obvious solution, clearly seen in the  $\mathbb{d}_I$  tables of Fig. 6, that if one excites only symmetric  $m \rightarrow -m$  transitions, where all  $\mathbb{d}_I$  values are zero, then the first-order quadrupole contribution is eliminated. This is an important part of the strategy adopted by the MQ-MAS [32, 57, 58], DAS[21, 34, 17], and DOR[22, 21] experiments. Where these three techniques differ is in how the remaining anisotropic contributions are removed. In contrast, the ST-MAS experiment[59, 15] employs non-symmetric transitions, and thus requires a highly accurate setting for the  $\mathbb{D}_0$  magic angle. The second challenge is that there exists no single rotor axis angle with respect to the external magnetic field about which spinning the sample will eliminate both  $\mathbb{D}$  and  $\mathbb{G}$  simultaneously. This is apparent from Table 2.



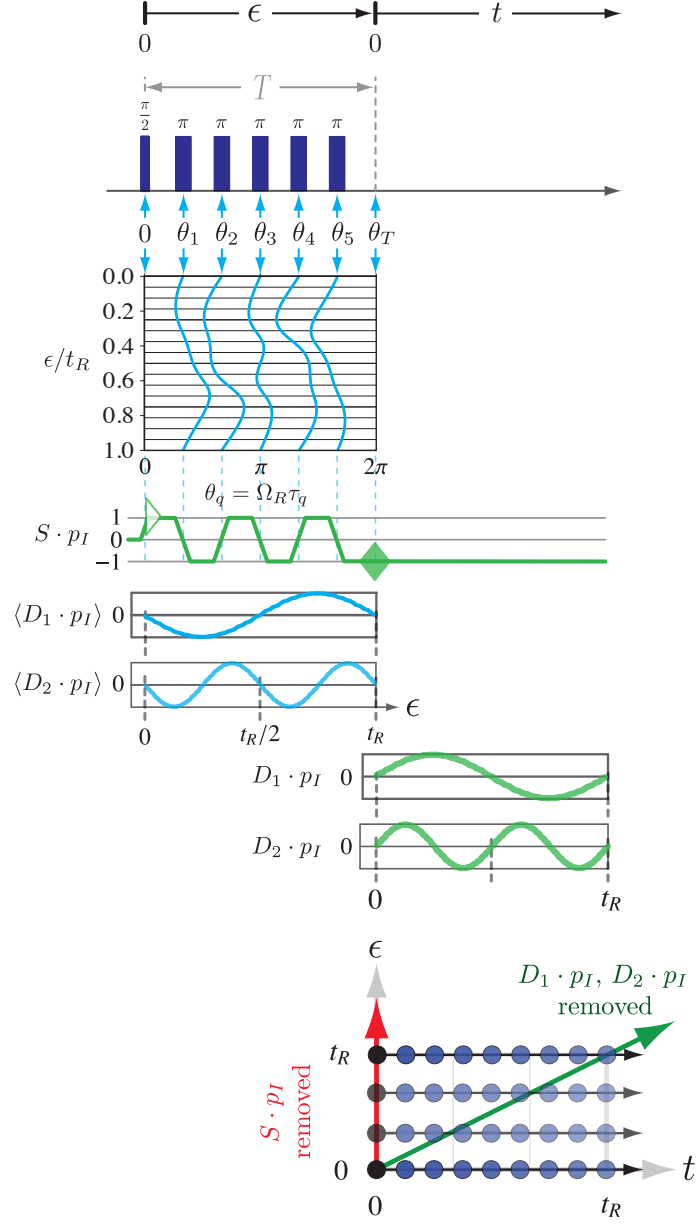


Figure 38: Pulse sequence and timings for the five  $\pi$  pulse constant time 2D PASS experiment of Antzutkin et al.[49] showing the  $S p_I$ ,  $D_1 p_I$  and  $D_2 p_I$  symmetry pathways. Here,  $\omega_R$  is the rotor spinning frequency.

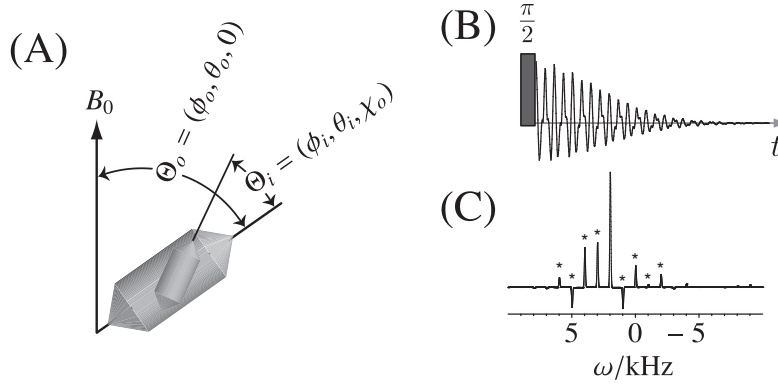


Figure 39: (A) In Double Rotation, a sample is reoriented through an angle  $\phi_i = \omega_{R_i} t$  about an axis at an angle  $\theta_i$  with respect to an axis that is also being reoriented through an angle  $\phi_o = \omega_{R_o} t + \chi_o$  at an angle  $\theta_o$  with respect to the external magnetic field. Typically,  $\theta_o$  and  $\theta_i$  are set to the zeroes of the second- and fourth-rank Legendre polynomials, so that  $\mathbb{D}_{0,0}(\theta_o, \theta_i) = \mathbb{G}_{0,0}(\theta_o, \theta_i) = 0$ . (B) Simulated DOR Bloch decay signal showing  $\mathbb{D}_{n_o, n_i}$  or  $\mathbb{G}_{n_o, n_i}$  echoes. (C) Spinning sidebands, indicated with asterisks, often appear at integer multiples of  $n_i \omega_{R_i} \pm n_o \omega_{R_o}$  in the spectrum and can appear with mixed absorption and dispersion mode lineshapes [60, 61].

The most straightforward theoretical solution, but by far the most challenging experimental solution for half-integer quadrupole nuclei, is DOR. The DOR solution is to selectively excite the central  $m = \frac{1}{2} \rightarrow -\frac{1}{2}$  transition, so the first-order quadrupole contribution is eliminated while employing the spatial pathway shown in Fig. 39A; that is, spinning the sample about an axis that is at a fixed angle from an axis that is also spinning about a fixed angle away from the external magnetic field direction. Under continuous sample rotation, the spatial functions are time-dependent, and the first-order shielding and second-order quadrupole contributions become

$$\Omega_\sigma^{(1)}(m_i, m_j, t) = -\omega_0 \sigma_{\text{iso}} \mathbb{P}_I(m_i, m_j) - \sum_{n_i=0}^2 \sum_{n_o=0}^2 \omega_0 \zeta_\sigma \mathbb{D}_{n_i, n_o}^{\{\sigma\}}(t) \mathbb{P}_I(m_i, m_j), \quad (118)$$

and

$$\begin{aligned} \Omega_q^{(2)}(m_i, m_j, t) = & \frac{\omega_q^2}{\omega_0} \mathbb{S}^{\{qq\}} \mathbb{C}_0(m_i, m_j) + \sum_{n_i=0}^2 \sum_{n_o=0}^2 \frac{\omega_q^2}{\omega_0} \mathbb{D}_{n_i, n_o}^{\{qq\}}(t) \mathbb{C}_2(m_i, m_j) \\ & + \sum_{n_i=0}^4 \sum_{n_o=0}^4 \frac{\omega_q^2}{\omega_0} \mathbb{G}_{n_i, n_o}^{\{qq\}}(t) \mathbb{C}_4(m_i, m_j). \end{aligned} \quad (119)$$

In both equations, as shown in A.5, the  $n_i \neq 0$  and  $n_o \neq 0$  components become modulated at frequencies of  $n_i \omega_{R_i} \pm n_o \omega_{R_o}$ , and average to zero at integer multiples of  $2\pi/(n_i \omega_{R_i} \pm n_o \omega_{R_o})$ . Typically,  $\beta_o$  and  $\beta_i$  are set to the zeroes of the second- and fourth-rank Legendre polynomials, that is,  $54.74^\circ$  and  $30.56^\circ$ , respectively, so that  $\mathbb{D}_{0,0} = \mathbb{G}_{0,0} = 0$ . It is best to have  $\omega_{R_i} > 5\omega_{R_o}$  in the DOR experiment to avoid any possible inadvertent recoupling of  $\mathbb{D}_{n_o, n_i}$  or  $\mathbb{G}_{n_o, n_i}$  terms. In the infinite rotation speed limit, the average frequency becomes

$$\langle \Omega(m_i, m_j) \rangle_{\text{DOR}} = -\omega_0 \sigma_{\text{iso}} \mathbb{P}_I(m_i, m_j) + \frac{\omega_q^2}{\omega_0} \mathbb{S}^{\{qq\}} \mathbb{C}_0(m_i, m_j), \quad (120)$$

yielding a spectrum with no anisotropic frequency components present. In practice, however, DOR speeds are insufficiently fast, particularly the outer rotor speed,  $\omega_{R_o}$ , and spinning sidebands often appear at integer multiples of  $n_i \omega_{R_i} \pm n_o \omega_{R_o}$  in the spectrum. Additionally, spinning sidebands can appear with mixed absorption and dispersion mode lineshapes[60, 61]. Through signal averaging with rf excitation occurring at random outer rotor positions, however, the dispersion mode components cancel, and mostly absorption mode spinning sidebands are observed. This dependence of the spinning sideband phase on the outer rotor position has been exploited by Samoson and Lippmaa[62] to design a DOR experiment with rotor synchronized signal averaging to eliminate half the spinning sidebands in a DOR spectrum.

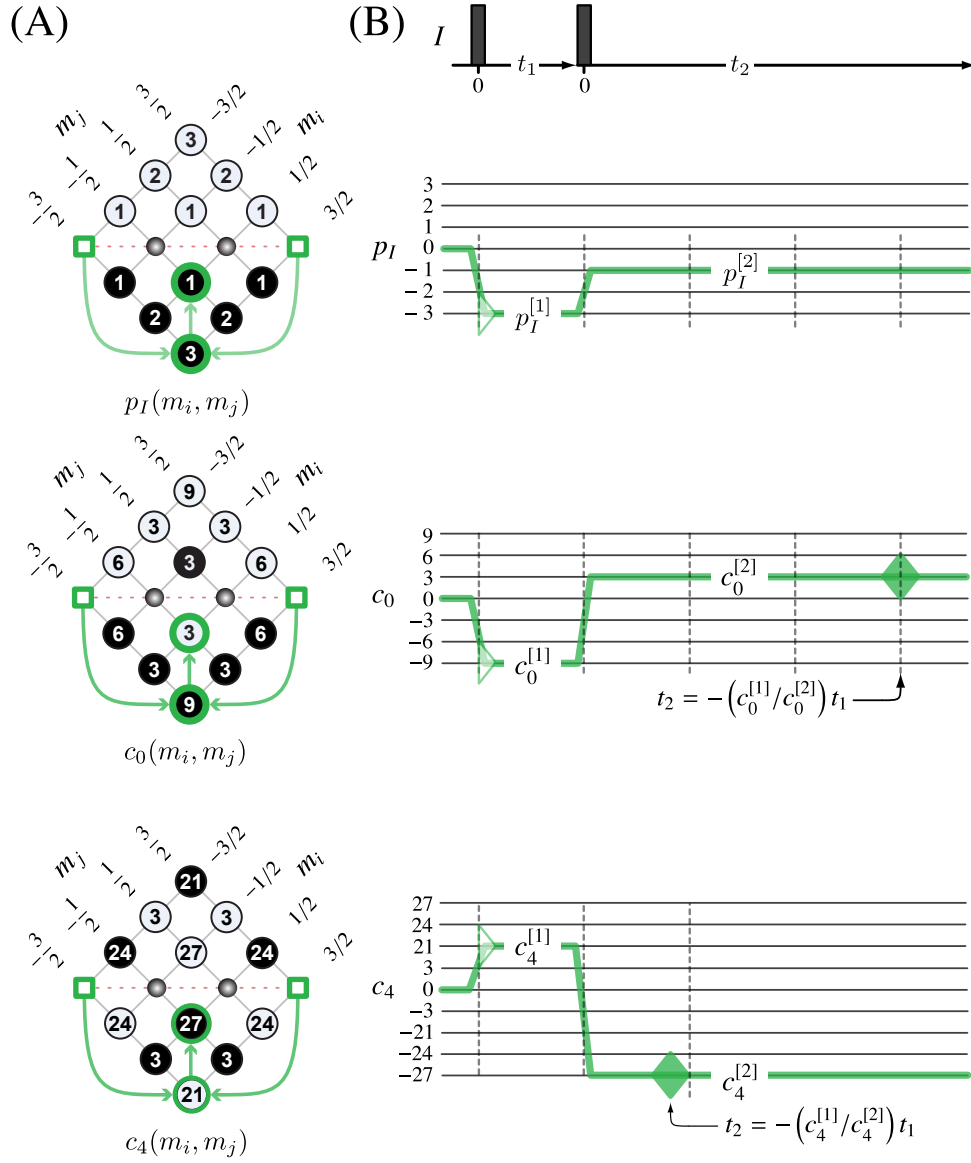


Figure 40: (A) 3Q-MAS experiment transition pathways in Eq. (122) on the  $p_I$ ,  $c_0$ , and  $c_4$  tables for a spin  $I = 3/2$  nucleus. (B) Pulse sequence with  $p_I$ ,  $c_0$ , and  $c_4$  pathways for 3Q-MAS experiment. A filled diamond represents a contribution to a directly observable echo, while an open triangle represents a contribution to an indirectly observable free induction decay.

### 3.5. $c_4$ Echoes

The MQ-MAS[32, 57] and ST-MAS[33] solutions for half-integer quadrupole nuclei are similar, with both employing D-MAS and the remaining challenge in removing the component containing  $G_0$  in the expression

$$\langle \Omega(m_i, m_j) \rangle_{\text{D-MAS}} = -\omega_0 \sigma_{\text{iso}} \mathbb{P}_I(m_i, m_j) + \frac{\omega_q^2}{\omega_0} \mathbb{S}^{\{qq\}} c_0(m_i, m_j) + \frac{\omega_q^2}{\omega_0} \mathbb{G}_0^{\{qq\}}(\theta_M^{(2)}) c_4(m_i, m_j). \quad (121)$$

Both MQ-MAS and ST-MAS solve this problem by employing the  $c_4$  echo, discovered by Frydman and Harwood[32] in 1995 and described below.

#### 3.5.1. MQ-MAS

A  $c_4$  echo is generated in the MQ-MAS experiment[32, 57] using a transition pathway that goes through a normally forbidden symmetric multiple quantum ( $m \rightarrow -m$ ) transition[63, 18, 64] for  $t_1$  evolution and ends on the central

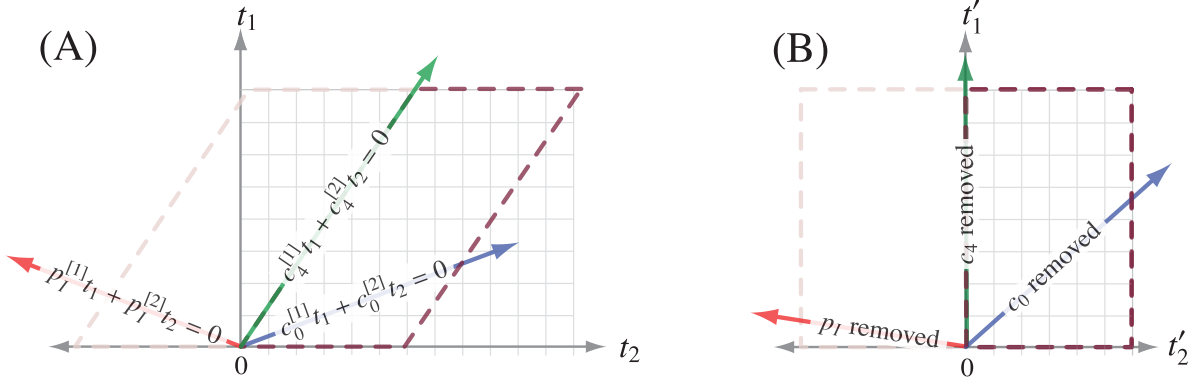


Figure 41: (A) The 2D MQ-MAS signal acquired as a function of  $t_1$  and  $t_2$ , the isotropic nuclear shielding contribution is refocused into a  $p_I$ -echo along the line  $p_I^{[1]}t_1 + p_I^{[2]}t_2 = 0$ , the isotropic quadrupolar contribution is refocused into a  $c_0$ -echo along the line  $c_0^{[1]}t_1 + c_0^{[2]}t_2 = 0$ , and the anisotropic quadrupolar contribution is refocused into a  $c_4$ -echo along the line  $c_4^{[1]}t_1 + c_4^{[2]}t_2 = 0$ . The dashed line represents a passive affine transformation of the 2D coordinate system to create a time coordinate,  $t'_1$ , along which the 2D signal is unaffected by frequency components containing  $c_4$ . (B) After applying an active affine transformation with a shear parallel to  $t_2$  and scaling along  $t'_1$ , the 2D signal is unaffected by frequency components containing  $c_4$  along the  $t'_1$  coordinate.

$(\frac{1}{2} \rightarrow -\frac{1}{2})$  transition during  $t_2$  evolution. Consider the case of a 3Q-MAS experiment on a spin  $I = 3/2$  nucleus. The relevant 3Q-MAS transition pathway is

$$\{I = \frac{3}{2}\} : [-\frac{3}{2}, +\frac{3}{2}] \rightarrow |-\frac{3}{2}\rangle \langle +\frac{3}{2}| \rightarrow |-\frac{1}{2}\rangle \langle +\frac{1}{2}|. \quad (122)$$

This transition pathway maps into the symmetry pathways  $p_I = 0 \rightarrow -3 \rightarrow -1$ ,  $c_0 = 0 \rightarrow -9 \rightarrow +3$  and  $c_4 = 0 \rightarrow +21 \rightarrow -27$ , as shown in Fig. 40. What is most important is that the  $p_I$  and  $c_0$  do not form simultaneous echoes with  $c_4$ . That is, the  $c_4$  echo tops are modulated by the  $p_I$  and  $c_0$  frequency components, and a Fourier transform of the  $c_4$  echo tops as a function of  $t_1$  yields a site-resolved and purely isotropic spectrum. Figure 41A indicates the paths of the  $p_I$ ,  $c_0$ , and  $c_4$  echoes during an MQ-MAS experiment with the  $c_4$  echo along the line

$$c_4^{[1]}t_1 + c_4^{[2]}t_2 = 0, \quad (123)$$

the  $c_0$  echo along the line

$$c_2^{[1]}t_1 + c_2^{[2]}t_2 = 0, \quad (124)$$

and the  $p$  echo along the line

$$p_I^{[1]}t_1 + p_I^{[2]}t_2 = 0. \quad (125)$$

For the 3Q-MAS experiment on an  $I = 3/2$  nucleus the  $c_4$  components refocus into an echo along the line  $21t_1 - 27t_2 = 0$ , the  $c_0$  components refocus into an echo along the line  $-9t_1 + 3t_2 = 0$ , and the  $p_I$  components refocus into an anti-echo along the line  $3t_1 - t_2 = 0$ . An affine transformation consisting of a shear parallel to the  $t_2$  coordinate with a shear ratio of

$$\kappa^{(\omega_1)} = -\frac{c_4^{[1]}}{c_4^{[2]}}, \quad (126)$$

and a scaling of the  $t_1$  coordinate with the scaling factor

$$\varsigma_{t_1^*} = 1 + |\kappa^{(\omega_1)}|, \quad (127)$$

can be applied to the 2D signal, as described in 5.4, so the isotropic spectrum can be obtained from a simple projection of the final 2D spectrum[58]. In the case of 3Q-MAS for a spin  $I = 3/2$  nucleus the affine parameters are  $\kappa^{(\omega_1)} = 21/27$  and  $\varsigma_{t_1^*} = 48/27$ . The  $\kappa^{(\omega_1)}$  and  $\varsigma_{t_1^*}$  values for the different symmetric multiple quantum transitions and nuclear spin values are given in Table 5. After the affine transformation, the position of the resonance in the

Spin	$t_1$ transition	$c_4^{[1]}$	$c_4^{[2]}$	$\kappa^{(\omega_1)} = -(c_4^{[1]}/c_4^{[2]})$	$\varsigma^{(t'_1)} = 1 +  \kappa^{(\omega_1)} $
3/2	$+\frac{3}{2} \rightarrow -\frac{3}{2}$	21	-27	21/27	48/27
5/2	$-\frac{3}{2} \rightarrow +\frac{3}{2}$	114	-72	114/72	186/72
	$+\frac{5}{2} \rightarrow -\frac{5}{2}$	150	-72	150/72	222/72
7/2	$-\frac{3}{2} \rightarrow +\frac{3}{2}$	303	-135	303/135	438/135
	$-\frac{5}{2} \rightarrow +\frac{5}{2}$	165	-135	165/135	300/135
	$+\frac{7}{2} \rightarrow -\frac{7}{2}$	483	-135	483/135	618/135
9/2	$-\frac{3}{2} \rightarrow +\frac{3}{2}$	546	-216	546/216	762/216
	$-\frac{5}{2} \rightarrow +\frac{5}{2}$	570	-216	570/216	786/216
	$-\frac{7}{2} \rightarrow +\frac{7}{2}$	84	-216	84/216	300/216
	$+\frac{9}{2} \rightarrow -\frac{9}{2}$	1116	-216	1116/216	1332/216

Table 5:  $\kappa^{(\omega_1)}$  shear ratios and  $\varsigma^{(t'_1)}$  scaling for MQ-MAS experiments for different nuclear spin values and symmetric multiple quantum transitions correlated to the central ( $\frac{1}{2} \rightarrow -\frac{1}{2}$ ) transition.

isotropic projection is a weighted average of the multiple quantum and central transition isotropic frequencies given by

$$\langle \Omega_{iso} \rangle_{\text{MQ-MAS}} = \frac{1}{1 + |\kappa^{(\omega_1)}|} \Omega_{iso}(m, -m) + \frac{\kappa^{(\omega_1)}}{1 + |\kappa^{(\omega_1)}|} \Omega_{iso}\left(\frac{1}{2}, -\frac{1}{2}\right). \quad (128)$$

If the spectrum is to be referenced to a frequency other than the rf carrier frequency (i.e., zero is not defined in the middle of the spectrum), then the reference offset used in the single-quantum dimension must be multiplied by a factor of  $\left(\frac{p_I^{[1]}}{p_I^{[2]}} + |\kappa^{(\omega_1)}|\right) / (1 + |\kappa^{(\omega_1)}|)$  when used in the isotropic dimension.

While MQ-MAS has the advantage that it can be performed with a conventional MAS probe, it has a disadvantage that the excitation and mixing of multiple-quantum coherences can be inefficient, leading to poor sensitivities and non-quantitative spectra.

### 3.5.2. ST-MAS

A  $c_4$  echo is generated in the ST-MAS experiment using a transition pathway that goes through a satellite single-quantum ( $m \rightarrow m - 1$ ) transition for  $t_1$  evolution and ends on the central transition during  $t_2$  evolution. In contrast to MQ-MAS, these satellite transitions are allowed, so sensitivity is improved compared to MQ-MAS. For an ST-MAS experiment on a spin  $I = 3/2$  nucleus, the relevant pathways are

$$\left\{ I = \frac{3}{2} \right\} : \begin{cases} [-\frac{3}{2}, -\frac{1}{2}] \rightarrow |-\frac{3}{2}\rangle \langle -\frac{1}{2}| \rightarrow |-\frac{1}{2}\rangle \langle +\frac{1}{2}|, \\ [+ \frac{1}{2}, +\frac{3}{2}] \rightarrow |+\frac{1}{2}\rangle \langle +\frac{3}{2}| \rightarrow |-\frac{1}{2}\rangle \langle +\frac{1}{2}|. \end{cases} \quad (129)$$

This transition pathway maps into the symmetry pathways  $p_I = 0 \rightarrow -1 \rightarrow -1$ ,  $c_0 = 0 \rightarrow -6 \rightarrow +3$  and  $c_4 = 0 \rightarrow +24 \rightarrow -27$ , as shown in Fig. 42. As with the MQ-MAS experiment,  $p_I$  and  $c_0$  components do not form simultaneous echoes with  $c_4$  components, and a Fourier transform of the  $c_4$  echo tops as a function of  $t_1$  yields a site-resolved and purely isotropic spectrum. Again, a shear parallel to the  $t_2$  coordinate with a shear ratio of

$$\kappa^{(\omega_1)} = -\frac{c_4^{[1]}}{c_4^{[2]}}, \quad (130)$$

Spin	$t_1$ transition	$c_4^{[1]}$	$c_4^{[2]}$	$\kappa^{(\omega_1)} = -(c_4^{[1]}/c_4^{[2]})$	$\varsigma^{(t'_1)} = 1 +  \kappa^{(\omega_1)} $
3/2	$+\frac{3}{2} \rightarrow +\frac{1}{2}, \quad -\frac{1}{2} \rightarrow -\frac{3}{2}$	24	-27	24/27	51/27
5/2	$-\frac{3}{2} \rightarrow -\frac{1}{2}, \quad +\frac{1}{2} \rightarrow +\frac{3}{2}$	21	-72	21/72	93/72
	$+\frac{5}{2} \rightarrow +\frac{3}{2}, \quad -\frac{3}{2} \rightarrow -\frac{5}{2}$	132	-72	132/72	204/72
7/2	$-\frac{3}{2} \rightarrow -\frac{1}{2}, \quad +\frac{1}{2} \rightarrow +\frac{3}{2}$	84	-135	84/135	219/135
	$-\frac{5}{2} \rightarrow -\frac{3}{2}, \quad +\frac{3}{2} \rightarrow +\frac{5}{2}$	69	-135	69/135	204/135
	$+\frac{7}{2} \rightarrow +\frac{5}{2}, \quad -\frac{5}{2} \rightarrow -\frac{7}{2}$	324	-135	324/135	459/135
9/2	$-\frac{3}{2} \rightarrow -\frac{1}{2}, \quad +\frac{1}{2} \rightarrow +\frac{3}{2}$	165	-216	165/216	381/216
	$-\frac{5}{2} \rightarrow -\frac{3}{2}, \quad +\frac{3}{2} \rightarrow +\frac{5}{2}$	12	-216	12/216	228/216
	$-\frac{7}{2} \rightarrow -\frac{5}{2}, \quad +\frac{5}{2} \rightarrow +\frac{7}{2}$	243	-216	243/216	459/216
	$+\frac{9}{2} \rightarrow +\frac{7}{2}, \quad -\frac{7}{2} \rightarrow -\frac{9}{2}$	600	-216	600/216	816/216

Table 6:  $\kappa^{(\omega_1)}$  shear ratios and  $\varsigma^{(t'_1)}$  scaling for the ST-MAS experiment for different nuclear spin values and satellite transitions correlated to the central ( $\frac{1}{2} \rightarrow -\frac{1}{2}$ ) transition.

and a scaling of the  $t_1$  coordinate with the scaling factor

$$\varsigma_{t_1^*} = 1 + |\kappa^{(\omega_1)}|, \quad (131)$$

can be applied, so the isotropic spectrum is obtained from a simple projection on the final 2D spectrum[58]. The  $\kappa^{(\omega_1)}$  and  $\varsigma_{t_1^*}$  values for the different satellite single-quantum transitions and nuclear spin values are given in Table 6. The isotropic frequency in an ST-MAS spectrum is a weighted average of the satellite transition and central transition frequencies according to

$$\langle \Omega_{iso} \rangle_{\text{ST-MAS}} = \frac{1}{1 + |\kappa^{(\omega_1)}|} \Omega_{iso}(m, m-1) + \frac{\kappa^{(\omega_1)}}{1 + |\kappa^{(\omega_1)}|} \Omega_{iso}\left(\frac{1}{2}, -\frac{1}{2}\right). \quad (132)$$

ST-MAS, like MQ-MAS, shares the advantage that it can be performed with a conventional MAS probe. A disadvantage of ST-MAS is that the resolution in ST-MAS spectra can be easily degraded by extremely small missets in the magic-angle rotor axis[65] and occasionally third-order effects[66, 23]. While ST-MAS does have an advantage over MQ-MAS in that the excitation of the single-quantum satellite transitions is allowed, the broadband excitation of the satellite transitions is neither an efficient nor selective process. In fact, the ST-MAS experiment, as presented in Fig. 42, will often be complicated by resonances from undesired transition pathways, the most troublesome of which is the transition pathway that excites the central transition during  $t_1$  evolution. This and other undesired pathways that go through single-quantum coherences during  $t_1$  cannot be separated from the desired transition pathway using traditional phase cycling techniques. Attempts to remove the central transition from  $t_1$  include pre-saturating the central transition or simply subtracting the central transition[67]. However, these methods are typically either incomplete or inefficient at removing the central transition. One efficient solution to this problem is the Double-Quantum Filtered Satellite-Transition Magic-Angle Spinning (DQF-ST-MAS) experiment proposed by Kwak and Gan[15]. By applying a selective  $\pi$  pulse on the central transition, the coherence of the innermost satellite transition is converted into double-quantum coherence, while the central transition is only inverted. With this modification, the two transition pathways pass through different  $p_I$  values and can now be separated by phase cycling. The shifted-echo version of DQF-ST-MAS, depicted in Fig. 43, eliminates the central transition during

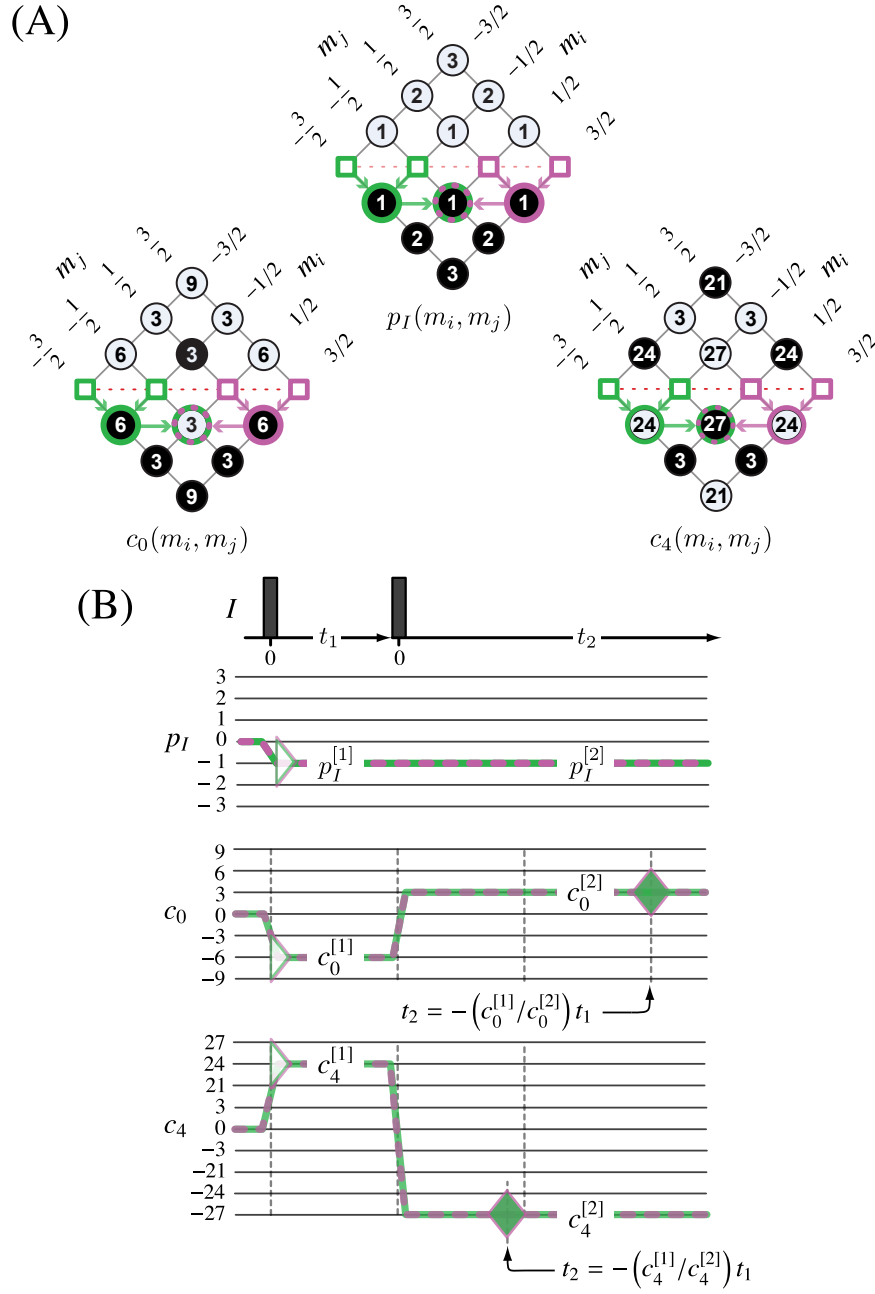


Figure 42: (A) ST-MAS experiment transition pathways in Eq. (129) on the  $p_I$ ,  $c_0$ , and  $c_4$  tables for a spin  $I = 3/2$  nucleus. (B) Pulse sequence with  $p_I$ ,  $c_0$ , and  $c_4$  pathways for ST-MAS experiment. A filled diamond represents a contribution to a directly observable echo, while an open triangle represents a contribution to an indirectly observable free induction decay.

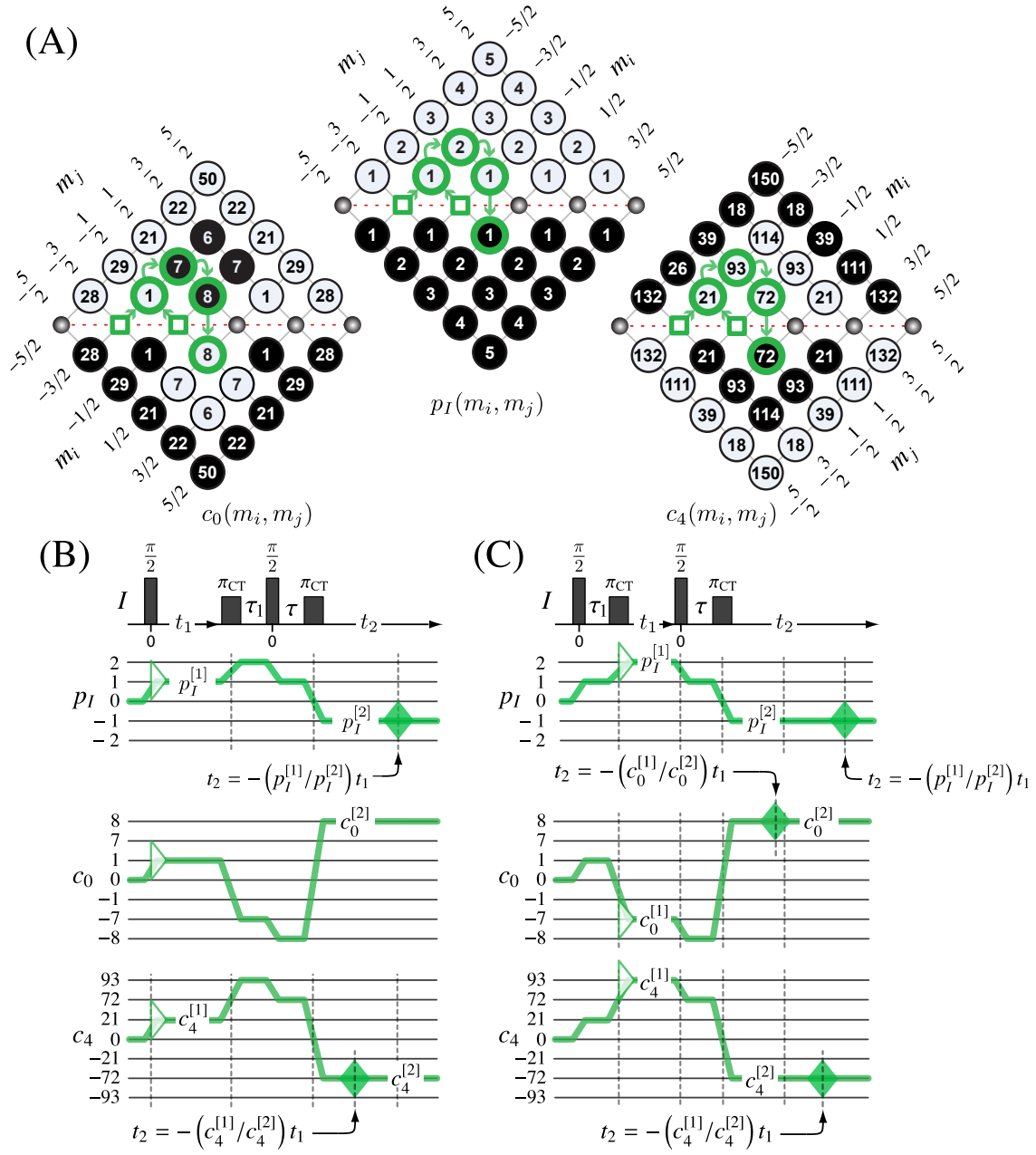


Figure 43: (A) Transition pathway in Eq. (133) on the  $p_I$ ,  $c_0$ , and  $c_4$  tables for spin  $I = 5/2$  nucleus for the Shifted-Echo double-quantum filtered-ST-MAS and Shifted-Echo double-quantum-ST-MAS experiment. (B) Pulse sequence and timings with  $p_I$ ,  $c_0$ , and  $c_4$  pathways for Shifted-Echo DQF-ST-MAS experiment. (C) Pulse sequence and timings with  $p_I$ ,  $c_0$ , and  $c_4$  pathways for Shifted Echo DQ-ST-MAS experiment. A filled diamond represents a contribution to a directly observable echo, while an open triangle represents a contribution to an indirectly observable free induction decay.



$t_1$  evolution and also correlates only the innermost satellite transitions with the central transition. The desired transition pathway for this experiment is

$$\{I\} : [-\frac{3}{2}, -\frac{1}{2}] \longrightarrow |-\frac{1}{2}\rangle \langle -\frac{3}{2}| \longrightarrow |+\frac{1}{2}\rangle \langle -\frac{3}{2}| \longrightarrow |+\frac{1}{2}\rangle \langle -\frac{1}{2}| \longrightarrow |-\frac{1}{2}\rangle \langle +\frac{1}{2}|. \quad (133)$$

Alternatively, one can use the same transition pathway and pulse sequence to generate a  $c_4$  echo by correlating the double-quantum transition during  $t_1$  to the central transition in  $t_2$ . The pulse sequence and timings for this experiment, known as Double Quantum ST-MAS (DQ-ST-MAS), are also shown in Fig. 43C.

It is apparent that MQ-MAS and ST-MAS represent only a fraction of possible experiments that can produce an isotropic spectrum of a quadrupole nucleus with second-order broadenings. Most existing experiments involve the central transition since it is the easiest to excite and detect. One experiment where the isotropic spectrum is not constructed from the central transition is the Mixed Multiple Quantum MAS experiment [68]. For  $I = 5/2, 7/2$ , or  $9/2$ , there exists more than one symmetric multiple quantum coherence. The evolution in  $t_1$  can be split between the two symmetric multiple-quantum transitions to refocus the  $c_4$  components. The coherence is then transferred to the central transition, as multiple quantum coherences are not directly detectable. Additionally, it has been shown that an isotropic spectrum can be obtained by correlating the satellite transition to the double-quantum transition [15, 69, 70]. A selective  $\pi$  pulse on the central transition can efficiently transfer coherence from the satellite transition to a double-quantum coherence and back:  $(\pm\frac{3}{2} \rightarrow \pm\frac{1}{2}) \xrightarrow{(\pi)_{CT}} (\pm\frac{3}{2} \rightarrow \mp\frac{1}{2})$ . Unlike the Mixed Multiple Quantum MAS experiment, the satellite transition can be directly detected without having to transfer to the central transition. Of course, to generate a  $c_4$  echo, these two transitions must exhibit a change in sign of  $c_4$ , and a close examination of the  $c_4$  tables indicates that only occurs for  $I = 3/2$  nuclei.

### 3.6. $c_2$ Echoes

The frequency of a symmetric transition of a half-integer quadrupole nucleus in a static sample experiencing both the nuclear shielding and quadrupolar interactions will depend on five components,

$$\begin{aligned} \Omega(\Theta, m_i, m_j) = & -\omega_0 \sigma_{\text{iso}} \mathbb{P}_I(m_i, m_j) - \omega_0 \zeta_\sigma \mathbb{D}^{\{\sigma\}}(\Theta) \mathbb{P}_I(m_i, m_j) + \frac{\omega_q^2}{\omega_0} \mathbb{S}^{\{qq\}} \mathbb{C}_0(m_i, m_j) \\ & + \frac{\omega_q^2}{\omega_0} \mathbb{D}^{\{qq\}}(\Theta) \mathbb{C}_2(m_i, m_j) + \frac{\omega_q^2}{\omega_0} \mathbb{G}^{\{qq\}}(\Theta) \mathbb{C}_4(m_i, m_j). \end{aligned} \quad (134)$$

The lineshape of a site in a polycrystalline sample with this frequency dependence would depend on eight parameters:  $C_q$ ,  $\eta_q$ ,  $\sigma_{\text{iso}}$ ,  $\zeta_\sigma$ ,  $\eta_\sigma$ , and the three Euler angles,  $\alpha$ ,  $\beta$ , and  $\gamma$ , for the relative orientation of the quadrupolar and nuclear shielding tensors. While D-MAS does not remove all anisotropy for quadrupolar nuclei with second-order broadenings, it does eliminate the second-rank anisotropies, and then the frequency depends only on three components:

$$\begin{aligned} \left\langle \Omega \left( \theta_M^{(2)}, m_i, m_j \right) \right\rangle_{\text{D-MAS}} = & -\omega_0 \sigma_{\text{iso}} \mathbb{P}_I(m_i, m_j) + \frac{\omega_q^2}{\omega_0} \mathbb{S}^{\{qq\}} \mathbb{C}_0(m_i, m_j) \\ & + \frac{\omega_q^2}{\omega_0} \mathbb{G}_0^{\{qq\}} \left( \theta_M^{(2)} \right) \mathbb{C}_4(m_i, m_j). \end{aligned} \quad (135)$$

Thus, the D-MAS lineshape of a site depends only on three parameters:  $C_q$ ,  $\eta_q$ , and  $\sigma_{\text{iso}}$ . In other words, the dependence on the nuclear shielding anisotropy,  $\zeta_\sigma$ ,  $\eta_\sigma$ , and the relative tensor orientation,  $\alpha$ ,  $\beta$ , and  $\gamma$ , are removed from the spectrum. This simplification, or elimination of five out of eight parameters, allows a more accurate and precise determination of  $C_q$ ,  $\eta_q$ , and  $\sigma_{\text{iso}}$  from an analysis of the D-MAS spectrum.

It is also desirable to have an analogous experiment for obtaining a spectrum with the dependences on the quadrupolar anisotropy, and the relative tensor orientation suppressed, leaving only isotropic shifts and the nuclear shielding anisotropy. We can approach this goal with G-MAS, where the second-order quadrupolar component with  $G$  spatial anisotropy is eliminated while the  $D$  spatial anisotropy of the nuclear shielding and second-order quadrupolar

components remain,

$$\begin{aligned} \left\langle \Omega \left( \theta_M^{(4)}, m_i, m_j \right) \right\rangle_{\text{G-MAS}} &= -\omega_0 \sigma_{\text{iso}} \mathbb{P}_I(m_i, m_j) - \omega_0 \zeta_\sigma \mathbb{D}_0^{\{\sigma\}} \left( \theta_M^{(4)} \right) \mathbb{P}_I(m_i, m_j) \\ &\quad + \frac{\omega_q^2}{\omega_0} \mathbb{S}^{\{qq\}} \mathbb{C}_0(m_i, m_j) + \frac{\omega_q^2}{\omega_0} \mathbb{D}_0^{\{qq\}} \left( \theta_M^{(4)} \right) \mathbb{C}_2(m_i, m_j). \end{aligned} \quad (136)$$

This expression suggests eliminating the quadrupolar anisotropy by combining G-MAS with a  $c_2$  echo, assuming this echo is not coincident with a  $p_I$  echo, so only the anisotropy from the nuclear shielding component will remain.

### 3.6.1. COASTER

The Correlation of Anisotropies Separated Through Echo Refocusing (COASTER)[31] experiment for half-integer spin nuclei uses a  $c_2$  echo for obtaining a spectrum with the dependences on the quadrupolar anisotropy and the relative tensor orientation suppressed, leaving only isotropic shifts and the nuclear shielding anisotropy. The COASTER experiment not only provides this spectrum but also provides a spectrum that depends only on  $C_q$ ,  $\eta_q$ , and  $\sigma_{\text{iso}}$ , even though COASTER does not employ D-MAS conditions. These two 1D spectra come from the 1D projections of the 2D COASTER spectrum. Additionally, information about the relative tensor orientation, that is,  $\alpha$ ,  $\beta$ , and  $\gamma$  is available within the full 2D COASTER spectrum.

The COASTER experiment [31] achieves this separation of the anisotropic nuclear shielding and the quadrupolar anisotropies into orthogonal dimensions through the use of  $p_I$  and  $c_2$  echoes. Like MQ-MAS, the COASTER experiment uses a transition pathway that goes through a forbidden symmetric multiple quantum ( $m \rightarrow -m$ ) transition for  $t_1$  evolution and ends on the central ( $\frac{1}{2} \rightarrow -\frac{1}{2}$ ) transition during  $t_2$ . Consider the 3Q COASTER experiment on a spin  $I = 5/2$  nucleus. The relevant transition pathway is

$$\{I = \frac{5}{2}\} : \left[-\frac{3}{2}, +\frac{3}{2}\right] \rightarrow \left|+\frac{3}{2}\right\rangle \left\langle -\frac{3}{2}\right| \rightarrow \left|-\frac{1}{2}\right\rangle \left\langle +\frac{1}{2}\right|. \quad (137)$$

This transition pathway maps into the symmetry pathways  $p_I = 0 \rightarrow +3 \rightarrow -1$ ,  $c_0 = 0 \rightarrow -6 \rightarrow +8$  and  $c_2 = 0 \rightarrow +60 \rightarrow -32$ , as shown in Fig. 44A and 44B. With this pathway, the anisotropic nuclear shielding and the quadrupole frequency components can be separated by generating  $p_I$  echoes along

$$p_I^{[1]} t_1 + p_I^{[2]} t_2 = 0, \quad (138)$$

and  $c_2$  echoes along

$$c_2^{[1]} t_1 + c_2^{[2]} t_2 = 0. \quad (139)$$

These lines are illustrated in Fig. 45A. If one first applies a shear parallel to the  $t_2$  coordinate with the shear ratio

$$\kappa^{(\omega_1)} = -\frac{c_2^{[1]}}{c_2^{[2]}}, \quad (140)$$

and a scaling of the  $t_1$  coordinate with the scaling factor

$$\zeta^{(t'_1)} = 1 + |\kappa^{(\omega_1)}|, \quad (141)$$

then the  $p_I$  echo path in the new coordinate will be given by

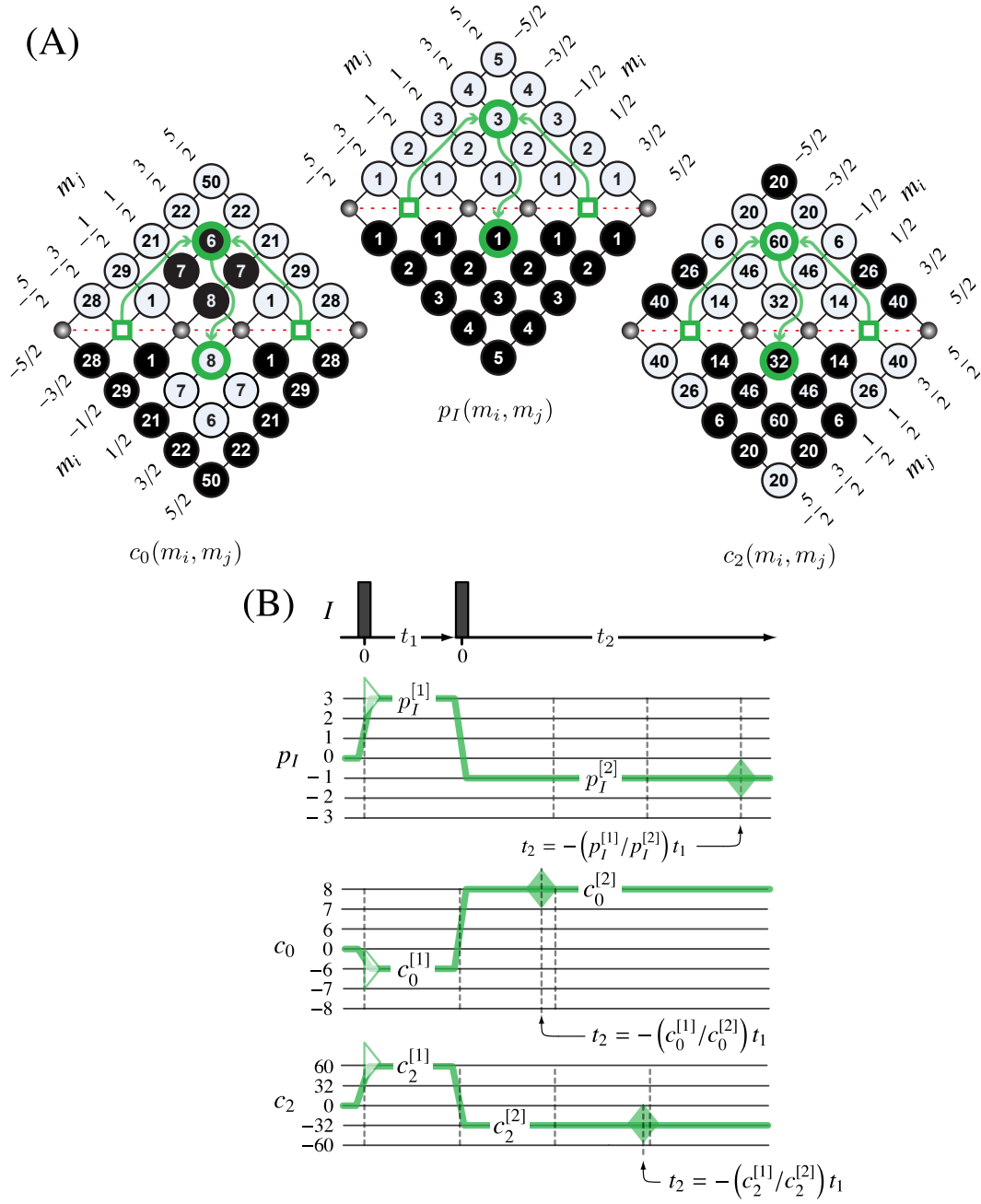
$$p_I'^{[1]} t_1 + p_I'^{[2]} t_2 = 0, \quad (142)$$

where

$$p_I'^{[1]} = \frac{1}{\zeta^{(t'_1)}} p_I^{[1]} + \frac{\kappa^{(\omega_1)}}{\zeta^{(t'_1)}} p_I^{[2]}, \quad (143)$$

and

$$p_I'^{[2]} = p_I^{[2]}, \quad (144)$$



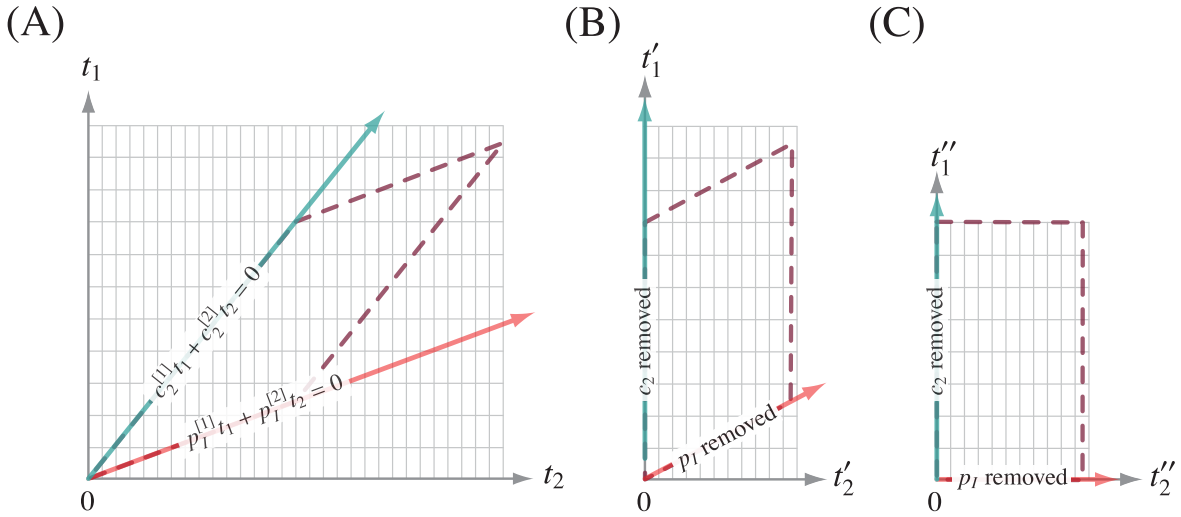


Figure 45: (A) The 2D COASTER signal acquired as a function of  $t_1$  and  $t_2$ , the nuclear shielding contribution is refocused into a  $p_I$ -echo at  $t_2 = -(p_I^{[1]}/p_I^{[2]})t_1$  and the anisotropic quadrupolar contribution is refocused into a  $c_2$ -echo at  $t_2 = -(c_2^{[1]}/c_2^{[2]})t_1$ . The dashed line represents a passive affine transformation of the 2D coordinate system to create a coordinate,  $t'_1$ , along which the 2D signal is unaffected by frequency components containing  $c_2$  and a coordinate,  $t'_2$ , along which the 2D signal is unaffected by frequency components containing  $p_I$ . (B) After applying an active affine transformation with a shear parallel to  $t_2$  and a scaling along  $t'_1$ , a 2D signal with  $c_2$  refocused along the  $t'_1$  axis is obtained. Here the dashed line represents a passive affine transformation of the 2D coordinate system to create a coordinate,  $t''_2$ , along which the 2D signal is unaffected by frequency components containing  $p_I$ . (C) After applying an active affine transformation with a shear parallel to  $t'_1$  and a scaling along  $t''_2$ , a 2D signal with  $p_I$  refocused along the  $t''_2$  axis is obtained.

as illustrated in Fig. 45B. Then one applies a shear parallel to the  $t'_1$  coordinate with the shear ratio

$$\kappa^{(\omega'_2)} = -\frac{p_I^{[2]}}{p_I^{[1]}}, \quad (145)$$

and a scaling of the  $t'_2$  coordinate with the scaling factor

$$\zeta^{(t'_2)} = 1 + |\kappa^{(\omega'_2)}|, \quad (146)$$

as illustrated in Fig. 45C. The  $\kappa^{(\omega_1)}$  shear ratios and  $\zeta^{(t'_1)}$  scaling and  $\kappa^{(\omega'_2)}$  shear ratios and  $\zeta^{(t'_2)}$  scaling for the COASTER experiment are given in Table 7. Note that in the case of a spin  $I = 3/2$  nucleus, the  $c_2$  components lies along the  $t_1$  axis prior to the shear, so an affine transformation with only a single shear and scale is required. Also, notice that certain COASTER experiments require a negative  $\kappa^{(\omega_1)}$  shear ratio. These are cases where the  $c_2$  echo path lies in a different signal quadrant than the  $p_I$  echo path, as illustrated in Fig. 46. Using the hypercomplex 2D acquisition approach, the 2D signal in an adjacent quadrant can be obtained and processed as described in detail in section 4.2.1.

In Fig. 47 are simulated 2D COASTER spectra showing the effect of the changing quadrupolar coupling and nuclear shielding asymmetry parameters in the case where the quadrupolar coupling and nuclear shielding tensors have the same principal axis systems. Generally, whenever the two tensors are diagonal in the same coordinate system, the 2D spectrum will form a triangular pattern, except in the case with  $\eta_q = \eta_\sigma = 0$ , where the resulting pattern is a line in the 2D spectrum. The triangle's vertices correspond to the principal components of the two tensors and unambiguously establish which components are aligned. The sensitivity of the COASTER spectrum to the relative orientation of the two tensors is shown in the simulations of Fig. 48. Notice that the projections onto the individual axes are unchanged as the nuclear shielding and quadrupolar coupling tensors are fixed. The principal components of the nuclear shielding and quadrupolar coupling tensors can be determined solely by analysis of the corresponding 1D projections, which are independent of the relative orientation of the two tensors. In contrast, the relative orientation of the two tensors can be obtained by analysis of the pattern contained in the 2D COASTER

Spin	$t_1$ transition	$c_2^{[1]}$	$c_2^{[2]}$	$\kappa^{(\omega_1)}$	$\zeta^{(t_1^*)}$	$p_I^{[2]}, p_I'^{[2]}$	$p_I^{[1]}$	$p_I'^{[1]}$	$\kappa^{(\omega_2')}$	$\zeta^{(t_2'^*)}$
3/2	$-\frac{3}{2} \rightarrow +\frac{3}{2}$	0	-12	0	1	-1	3	3	1/3	4/3
5/2	$-\frac{3}{2} \rightarrow +\frac{3}{2}$	60	-32	60/32	92/32	-1	3	36/92	92/36	128/36
	$-\frac{5}{2} \rightarrow +\frac{5}{2}$	-20	-32	-20/32	52/32	-1	5	180/52	52/180	232/180
7/2	$-\frac{3}{2} \rightarrow +\frac{3}{2}$	144	-60	144/60	204/60	-1	3	36/204	204/36	240/36
	$-\frac{5}{2} \rightarrow +\frac{5}{2}$	120	-60	120/60	180/60	-1	5	180/180	180/180	360/180
	$-\frac{7}{2} \rightarrow +\frac{7}{2}$	-84	-60	-84/60	144/60	-1	7	504/144	144/504	648/504
9/2	$-\frac{3}{2} \rightarrow +\frac{3}{2}$	252	-96	252/96	348/96	-1	3	36/348	348/36	384/36
	$-\frac{5}{2} \rightarrow +\frac{5}{2}$	300	-96	300/96	396/96	-1	5	180/396	396/180	576/180
	$-\frac{7}{2} \rightarrow +\frac{7}{2}$	168	-96	168/96	264/96	-1	7	504/264	264/504	768/504
	$-\frac{9}{2} \rightarrow +\frac{9}{2}$	-216	-96	-216/96	312/96	-1	9	1080/312	312/1080	1392/1080

Table 7:  $\kappa^{(\omega_1)}$  shear ratios and  $\zeta^{(t_1^*)}$  scaling and  $\kappa^{(\omega_2')}$  shear ratios and  $\zeta^{(t_2'^*)}$  scaling for the COASTER experiment that correlates a symmetric ( $m \rightarrow -m$ ) multiple quantum transition to the central ( $\frac{1}{2} \rightarrow -\frac{1}{2}$ ) transition.

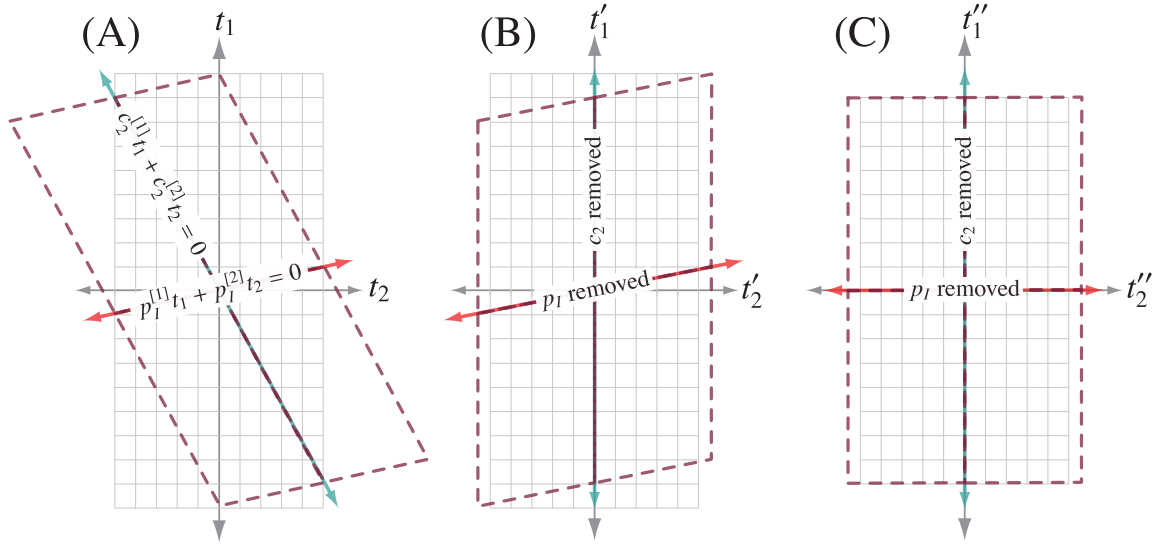


Figure 46: (A) The 2D COASTER signal acquired as a function of  $t_1$  and  $t_2$ , the nuclear shielding contribution is refocused into a  $p_I$ -echo at  $t_2 = -\left(p_I^{[1]}/p_I^{[2]}\right)t_1$  and the anisotropic quadrupolar contribution is refocused into a  $c_2$ -echo at  $t_2 = -\left(c_2^{[1]}/c_2^{[2]}\right)t_1$  in the adjacent signal quadrant. The dashed line represents a passive affine transformation of the 2D coordinate system to create a coordinate,  $t'_1$ , along which the 2D signal is unaffected by frequency components containing  $c_2$  and a coordinate,  $t'_2$ , along which the 2D signal is unaffected by frequency components containing  $p_I$ . (B) After applying an active affine transformation with a shear parallel to  $t_2$  and a scaling along  $t'_1$ , a 2D signal with  $c_2$  refocused along the  $t'_1$  axis is obtained. Here the dashed line represents a passive affine transformation of the 2D coordinate system to create a coordinate,  $t''_2$ , along which the 2D signal is unaffected by frequency components containing  $p_I$ . (C) After applying an active affine transformation with a shear parallel to  $t'_1$  and a scaling along  $t''_2$ , a 2D signal with  $p_I$  refocused along the  $t''_2$  axis is obtained.

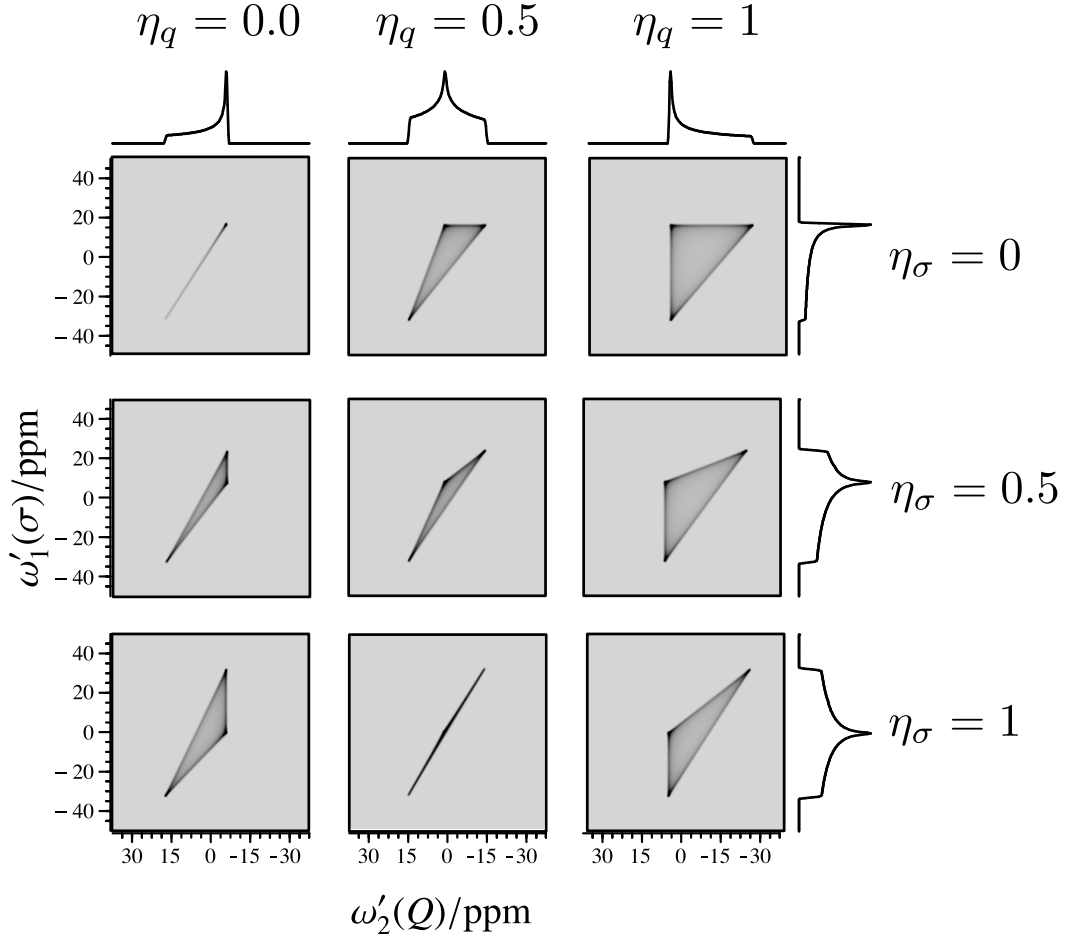


Figure 47: Comparison of simulated 2D COASTER spectra showing the effect of the changing quadrupolar coupling and chemical shift asymmetry parameters in the case where the quadrupolar coupling and chemical shift tensors have the same principal axis systems. Other simulation parameters included  $I = 3/2$ ,  $\omega_0 = 100$  MHz,  $C_q = 3$  MHz,  $\sigma_{\text{iso}} = 0$  ppm and  $\zeta_\sigma = 33$  ppm. The 1D projections onto the quadrupolar anisotropy axis,  $\omega'_2(Q)$ , are the same for each  $\eta_q$  value. Similarly, the 1D projections onto the shielding anisotropy axis,  $\omega'_1(\sigma)$ , are the same for each  $\eta_\sigma$  value.

spectrum. In these examples, one Euler angle varies from  $90^\circ$  to  $0^\circ$ , while the other two angles are fixed at  $90^\circ$ . Note that when the Euler angles are all multiples of  $90^\circ$ , the spectrum forms a triangular pattern, as the two tensors are diagonal in a common coordinate system. When an Euler angle is not a multiple of  $90^\circ$ , however, the pattern becomes elliptical.

### 3.7. $c_0$ Echoes

Under fast DOR, the first-order nuclear shielding and second-order quadrupole coupling contributions to the central ( $\frac{1}{2} \rightarrow -\frac{1}{2}$ ) transition frequency are

$$\langle \Omega(m_i, m_j) \rangle_{\text{DOR}} = -\omega_0 \sigma_{\text{iso}} P_{\parallel}(m_i, m_j) + \frac{\omega_q^2}{\omega_0} S^{\{qq\}} \mathbb{C}_0(m_i, m_j). \quad (147)$$

The two contributions in Eq. (147) have the same spatial dependence,  $S$ , but different spin transition symmetries,  $p_I$  and  $c_0$ . Shortly after the  $c_4$  echo was discovered by Frydman and Harwood[32], Samoson [30] realized that a  $c_0$  echo could be exploited to separate the isotropic chemical shift from the isotropic second-order quadrupolar shift in the Multiple-Quantum DOuble Rotation (MQ-DOR) experiment.

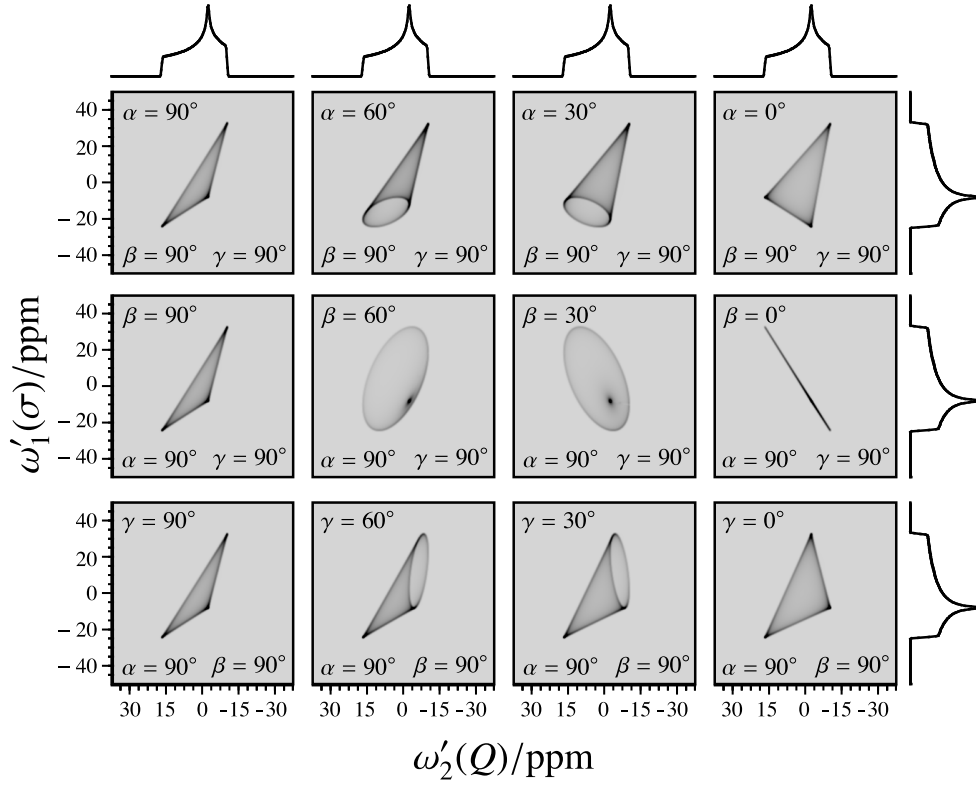


Figure 48: Comparison of simulated COASTER spectra showing the effect of the relative orientation on the 2D spectrum. Other simulation parameters included  $I = 3/2$ ,  $\omega_0 = 100$  MHz,  $C_q = 3$  MHz,  $\eta_q = 0.25$ ,  $\sigma_{\text{iso}} = 0$  ppm,  $\zeta_\sigma = 33$  ppm, and  $\eta_\sigma = 0.5$ . Again, note that the projection onto each axis remains unchanged as the relative orientation of the quadrupolar coupling and chemical shift tensors change.

### 3.7.1. MQ-DOR

In the MQ-DOR experiment, the first-order quadrupole contributions are eliminated by using symmetric ( $m \rightarrow -m$ ) transitions and the anisotropic  $D$  and  $G$  components eliminated with DOR. The remaining isotropic nuclear shielding and isotropic quadrupolar interactions are then separated into orthogonal dimensions by employing  $p_I$  and  $c_2$  echoes. Like the MQ-MAS and COASTER experiments, this is done by using a transition pathway that goes through a forbidden symmetric multiple quantum ( $m \rightarrow -m$ ) transition for  $t_1$  evolution and ends on the central ( $\frac{1}{2} \rightarrow -\frac{1}{2}$ ) transition during  $t_2$ . Consider the 3Q-DOR experiment on a spin  $I = 5/2$  nucleus. The relevant transition pathway is

$$\{I = \frac{3}{2}\} : [-\frac{3}{2}, +\frac{3}{2}] \rightarrow |+\frac{3}{2}\rangle \langle -\frac{3}{2}| \rightarrow |-\frac{1}{2}\rangle \langle +\frac{1}{2}|. \quad (148)$$

This transition pathway maps into the symmetry pathways  $p_I = 0 \rightarrow +3 \rightarrow -1$  and  $c_0 = 0 \rightarrow -6 \rightarrow +8$ , as shown in Fig. 49A and 49B. With this pathway, the isotropic nuclear shielding and isotropic second-order quadrupole components can be separated by using  $p_I$  echoes along

$$p_I^{[1]}t_1 + p_I^{[2]}t_2 = 0, \quad (149)$$

and  $c_0$  echoes along

$$c_0^{[1]}t_1 + c_0^{[2]}t_2 = 0. \quad (150)$$

The MQ-DOR signal can be processed identically as COASTER[31, 71] except that the shear parallel to the  $t_2$  coordinate is performed with the shear ratio

$$\kappa^{(\omega_1)} = -\frac{c_0^{[1]}}{c_0^{[2]}}. \quad (151)$$

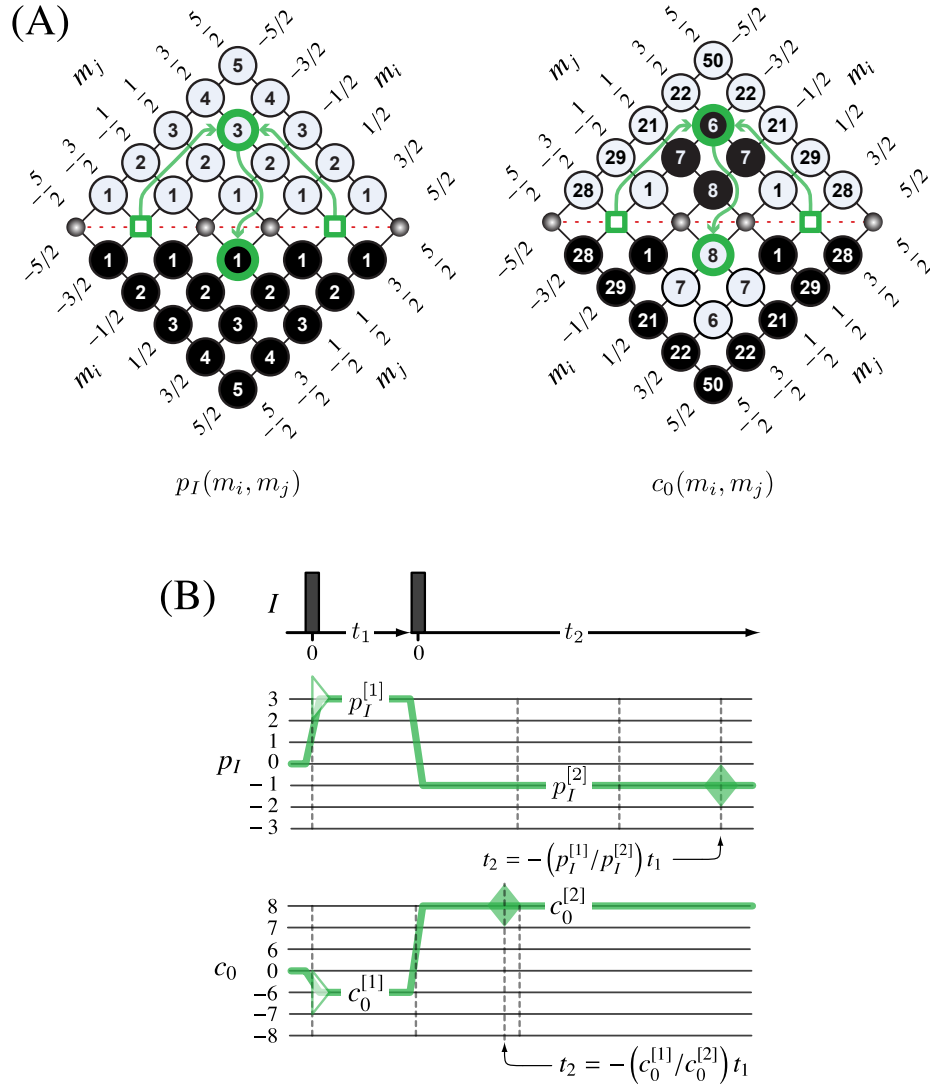


Figure 49: (A) MQ-DOR experiment transition pathways in Eq. (148) on the  $p_I$ , and  $c_0$  tables for  $\{I = 3/2\}$ . (B) Pulse sequence with  $p_I$  and  $c_0$  pathways for MQ-DOR experiment. A filled diamond represents a contribution to a directly observable echo, while an open triangle represents a contribution to an indirectly observable free induction decay.



Spin	$t_1$ transition	$c_0^{[1]}$	$c_0^{[2]}$	$\kappa^{(\omega_1)}$	$\zeta^{(t_1^*)}$	$p_I^{[2]}, p_I^{[2]}$	$p_I^{[1]}$	$p_I^{[1]}$	$\kappa^{(\omega_2')}$	$\zeta^{(t_2'^*)}$
3/2	$-\frac{3}{2} \rightarrow +\frac{3}{2}$	9	3	-9/3	12/3	-1	3	18/12	12/18	30/18
5/2	$-\frac{3}{2} \rightarrow +\frac{3}{2}$	-6	8	6/8	14/8	-1	3	18/14	14/18	32/18
	$-\frac{5}{2} \rightarrow +\frac{5}{2}$	50	8	-50/8	58/8	-1	5	90/58	58/90	115/90
7/2	$-\frac{3}{2} \rightarrow +\frac{3}{2}$	-27	15	27/15	42/15	-1	3	18/42	42/18	60/18
	$-\frac{5}{2} \rightarrow +\frac{5}{2}$	15	15	-15/15	30/15	-1	5	90/30	30/90	120/90
	$-\frac{7}{2} \rightarrow +\frac{7}{2}$	147	15	-147/15	162/15	-1	7	252/162	162/252	414/252
9/2	$-\frac{3}{2} \rightarrow +\frac{3}{2}$	-54	24	54/24	78/24	-1	3	18/78	78/18	96/18
	$-\frac{5}{2} \rightarrow +\frac{5}{2}$	-30	24	30/24	54/24	-1	5	90/54	54/90	144/90
	$-\frac{7}{2} \rightarrow +\frac{7}{2}$	84	24	-84/24	108/24	-1	7	252/108	108/252	360/252
	$-\frac{9}{2} \rightarrow +\frac{9}{2}$	324	24	-324/24	348/24	-1	9	540/348	348/540	888/540

Table 8:  $\kappa^{(\omega_1)}$  shear ratios and  $\zeta^{(t_1^*)}$  scaling and  $\kappa^{(\omega_2')}$  shear ratios and  $\zeta^{(t_2'^*)}$  scaling for the MQ-DOR experiment that correlates a symmetric ( $m \rightarrow -m$ ) multiple quantum transition to the central ( $\frac{1}{2} \rightarrow -\frac{1}{2}$ ) transition.

The  $\kappa^{(\omega_1)}$  shear ratios and  $\zeta^{(t_1^*)}$  scaling and  $\kappa^{(\omega_2')}$  shear ratios and  $\zeta^{(t_2'^*)}$  scaling for the MQ-DOR experiment are given in Table 8. As with COASTER, certain MQ-DOR experiments require a negative  $\kappa^{(\omega_1)}$  shear ratio. In MQ-DOR, these are cases where the  $c_0$  echo path lies in a different signal quadrant than the  $p_I$  echo path. Like COASTER, the hypercomplex 2D acquisition approach can be used to obtain the 2D signal in an adjacent quadrant and processed as described in detail in section 4.2.1.

### 3.8. $\mathbb{D}_0$ and $\mathbb{G}_0$ Echoes

Here we examine the use of spatial echoes to separate the anisotropic contributions to the NMR frequency under fast Variable single axis Angle sample Spinning (VAS), where the first-order nuclear shielding contribution to the NMR frequency can be written as

$$\left\langle \Omega^{\{\sigma\}}(\theta_R, m_i, m_j) \right\rangle_{\text{VAS}} = -\omega_0 \sigma_{\text{iso}} \mathbb{P}_I(m_i, m_j) - \omega_0 \zeta_\sigma \mathbb{D}_0^{\{\sigma\}}(\theta_R) \mathbb{P}_I(m_i, m_j), \quad (152)$$

and the second-order quadrupole coupling contribution as

$$\left\langle \Omega^{\{qq\}}(\theta_R, m_i, m_j) \right\rangle_{\text{VAS}} = \frac{\omega_q^2}{\omega_0} \mathbb{S}^{\{qq\}} c_0(m_i, m_j) + \frac{\omega_q^2}{\omega_0} \mathbb{D}_0^{\{qq\}}(\theta_R) c_2(m_i, m_j) + \frac{\omega_q^2}{\omega_0} \mathbb{G}_0^{\{qq\}}(\theta_R) c_4(m_i, m_j), \quad (153)$$

where  $\theta_R$  is the rotor angle. Since  $\mathbb{D}_0(\theta_R)$  and  $\mathbb{G}_0(\theta_R)$  are scaled by the second- and fourth-rank Legendre polynomials

$$\mathbb{D}_0(\theta_R) = P_2(\cos \theta_R) \mathbb{D}(\Theta'), \quad \mathbb{G}_0(\theta_R) = P_4(\cos \theta_R) \mathbb{G}(\Theta'), \quad (154)$$

respectively, we can rewrite the frequency expressions as

$$\left\langle \Omega^{\{\sigma\}}(\theta_R, m_i, m_j) \right\rangle_{\text{VAS}} = -\omega_0 \sigma_{\text{iso}} \mathbb{P}_I(m_i, m_j) - \omega_0 \zeta_\sigma \mathbb{D}^{\{\sigma\}}(\Theta') \mathbb{P}_I(m_i, m_j) P_2(\cos \theta_R), \quad (155)$$

and

$$\begin{aligned} \left\langle \Omega^{\{qq\}}(\theta_R, m_i, m_j) \right\rangle_{\text{VAS}} &= \frac{\omega_q^2}{\omega_0} \mathbb{S}^{\{qq\}} c_0(m_i, m_j) + \frac{\omega_q^2}{\omega_0} \mathbb{D}^{\{qq\}}(\Theta') c_2(m_i, m_j) P_2(\cos \theta_R) \\ &\quad + \frac{\omega_q^2}{\omega_0} \mathbb{G}^{\{qq\}}(\Theta') c_4(m_i, m_j) P_4(\cos \theta_R). \end{aligned} \quad (156)$$

### 3.8.1. MAF

One of the earliest 2D solid-state experiments for separating isotropic and anisotropic contributions to the NMR transition frequency of spin 1/2 nuclei is the Magic-Angle Flipping experiment [72, 50]. In MAF, fast sample rotation is employed to remove the  $D_1$  and  $D_2$  spatial symmetries leaving only the  $S$  and  $D_0$  spatial symmetries, as given in Eq. (155). The MAF experiment then uses the transition pathway,

$$\{I = 1/2\} : [-\frac{1}{2}, +\frac{1}{2}] \rightarrow |-\frac{1}{2}\rangle \langle +\frac{1}{2}| \rightarrow [-\frac{1}{2}, +\frac{1}{2}] \rightarrow |-\frac{1}{2}\rangle \langle +\frac{1}{2}|, \quad (157)$$

and the spatial pathway  $\theta_R^{[1]} \rightarrow \theta_R^{[2]}$ , where  $\theta_R^{[1]} \neq \theta_R^{[2]} = \theta_M^{(2)}$ . The transition pathway maps into the symmetry pathway  $p_I = 0 \rightarrow -1 \rightarrow 0 \rightarrow -1$ , and the spatial pathway maps into the  $D_0$  symmetry pathway,

$$\mathbb{D}_0 = \mathbb{D}(\Theta') P_2(\cos \theta_R^{[1]}) \rightarrow \mathbb{D}(\Theta') P_2(\cos \theta_M^{(2)}) = \mathbb{D}(\Theta') P_2(\cos \theta_R^{[1]}) \rightarrow 0, \quad (158)$$

as shown in Fig. 50. The first pulse excites the magnetization while spinning at the rotor angle  $\theta_R^{[1]}$ . The mixing period consists of two  $\pi/2$  pulses; the first stores the magnetization along the  $z$ -axis during the hop of the rotor angle, and the second re-excites the magnetization at  $\theta_M^{(2)}$ , the  $\mathbb{D}$  symmetry magic-angle. As acquired, the signal the  $D_0 p_I$  echo path is aligned along  $t_2$  while the  $S p_I$  echo path moves along the line  $t_1 + t_2 = 0$ . Typically, 2D MAF spectra are presented without the application of an affine transformation. An affine transformation can be applied to place the  $S p_I$  echo path is aligned along  $t'_1$  as shown in Fig. 50D, to obtain a 2D spectrum correlating  $S p_I$  with  $\mathbb{D}_0 p_I$  frequency contributions. Additionally, to reduce the effects of angle mis-set on the anisotropic lineshapes, the first rotor angle is often set to  $\theta_R^{[1]} = \pi/2$  [17, 73, 74, 75].

### 3.8.2. VACS

An alternative approach to MAF that does not require a switch of the rotor axis during the experiment is the Variable Angle Correlation Spectroscopy (VACS) [76, 77] experiment. As in MAF, fast sample rotation is employed to remove the  $\mathbb{D}_1$  and  $\mathbb{D}_2$  spatial symmetries leaving only the  $S$  and  $\mathbb{D}_0$  spatial symmetries. Through systematic variation of the rotor axis,  $\theta_R$ , in independent one-dimensional VAS experiments, the  $\mathbb{D}_0$  spatial symmetry function can be varied independently from the  $S$  function, and the two functions correlated in a 2D signal created from uncorrelated 1D VAS experiments. Each 1D VAS experiment, with a signal phase given by

$$\Phi_{\text{VAS}}(t) = -\omega_0 \sigma_{\text{iso}} p_I(m_i, m_j) t - \omega_0 \zeta_\sigma \mathbb{D}^{\{\sigma\}}(\Theta') p_I(m_i, m_j) P_2(\cos \theta_R) t, \quad (159)$$

is used to fill the same two-dimensional  $t'_1$ - $t'_2$  coordinate of MAF where  $S p_I$  is removed along the  $t'_1$  coordinate and  $\mathbb{D}_0 p_I$  is removed along the  $t'_2$  coordinate. In VACS this is done by defining  $t'_1 = P_2(\cos \theta_R) t$  and  $t'_2 = t$ , to create a two-dimensional signal phase with

$$\Phi_{\text{VACS}}(t'_1, t'_2) = -\omega_0 \sigma_{\text{iso}} p_I(m_i, m_j) t'_2 - \omega_0 \zeta_\sigma \mathbb{D}^{\{\sigma\}}(\Theta') p_I(m_i, m_j) t'_1. \quad (160)$$

The signal acquired as a function of  $P_2(\cos \theta_R)$  is illustrated in Fig. 51B. There is no affine transformation between the acquired 2D signal as a function of  $P_2(\cos \theta_R)$  and the 2D signal as a function of  $t'_1$  and  $t'_2$ , illustrated in Fig. 51C. Therefore, the acquired signal must be interpolated onto a uniformly sampled Cartesian grid in the  $t'_1$ - $t'_2$  coordinate system. The bigger challenge with VACS, however, is that it is not possible to sample an entire 2D signal quadrant, as shown in Fig. 51C, and this results in a 2D spectrum that may be distorted with phase-twisted two-dimensional lineshapes. If there is sufficient anisotropic broadening in the  $\omega'_1$  dimension, however, these distortions are minimal. Additionally, the use of linear prediction methods has also been proposed to remove these phase artifacts [78].

### 3.8.3. DAS

For half-integer quadrupolar nuclei broadened to second-order, the spatial anisotropies of both  $\mathbb{D}_0$  and  $\mathbb{G}_0$  are removed with the Dynamic-Angle Spinning (DAS) experiment [34, 17] by reorienting the spinning sample between two rotor angles,  $\theta_R^{[1]}$  and  $\theta_R^{[2]}$  to create  $\mathbb{D}_0$  and  $\mathbb{G}_0$  echoes along the path,

$$\begin{aligned} P_2(\cos \theta_R^{[1]}) t_1 + P_2(\cos \theta_R^{[2]}) t_2 &= 0, \\ P_4(\cos \theta_R^{[1]}) t_1 + P_4(\cos \theta_R^{[2]}) t_2 &= 0. \end{aligned} \quad (161)$$

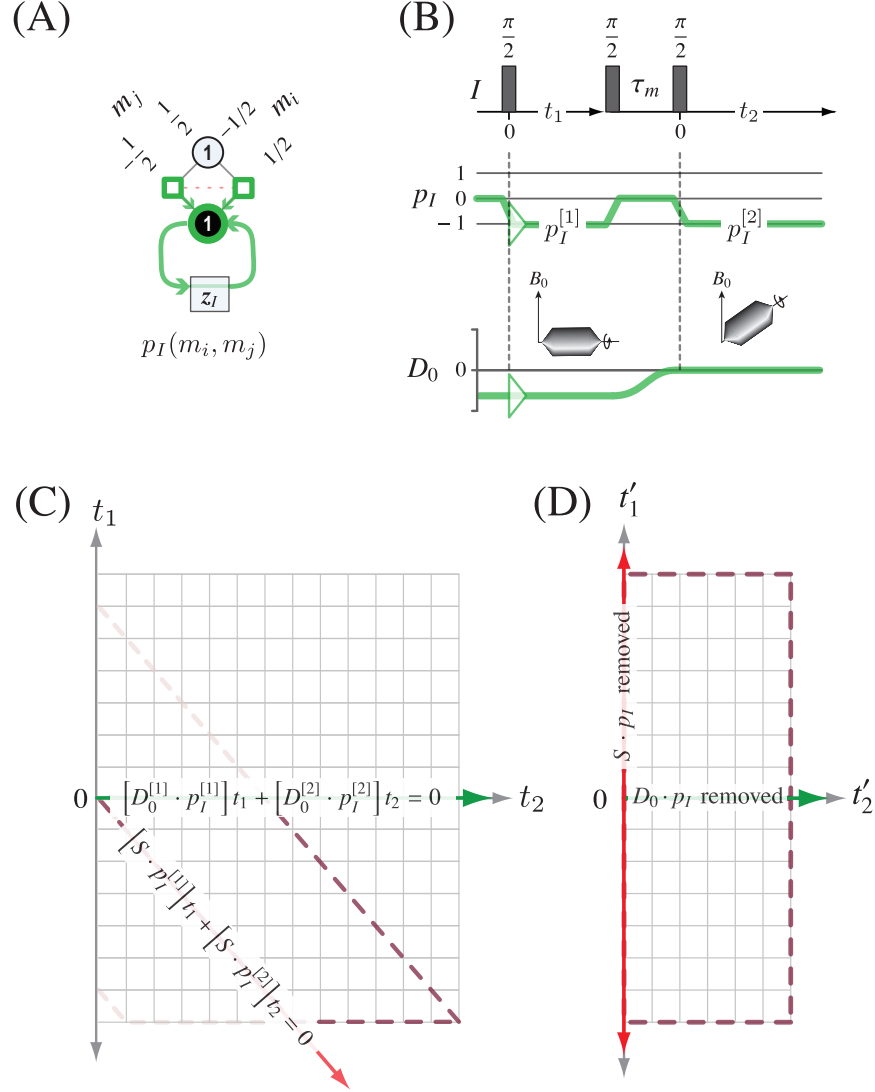


Figure 50: (A) MAF experiment transition pathways in Eq. (157) on the  $p_I$  table for  $\{I = 1/2\}$ . (B) Pulse sequence with  $p_I$  and  $D_0$  pathways for MAF experiment. An open triangle represents a contribution to an indirectly observable free induction decay. (C) The 2D MAF signal acquired as a function of  $t_1$  and  $t_2$ , the isotropic nuclear shielding contribution is refocused into a  $S p_I$  echo along the line  $[S p_I^{[1]}] t_1 + [S p_I^{[2]}] t_2 = 0$  and the anisotropic nuclear shielding contribution is refocused into a  $D_0 p_I$  echo along the line  $[D_0^{[1]} p_I^{[1]}] t_1 + [D_0^{[2]} p_I^{[2]}] t_2 = 0$ . The dashed line represents a passive affine transformation of the 2D coordinate system to create a coordinate,  $t_1'$ , along which the 2D signal is unaffected by frequency components containing  $S p_I$ . (D) After applying an active affine transformation with a shear parallel to  $t_2$  and a scaling along  $t_1^*$ , the 2D signal is unaffected by frequency components containing  $S p_I$  along the  $t_1'$  coordinate.

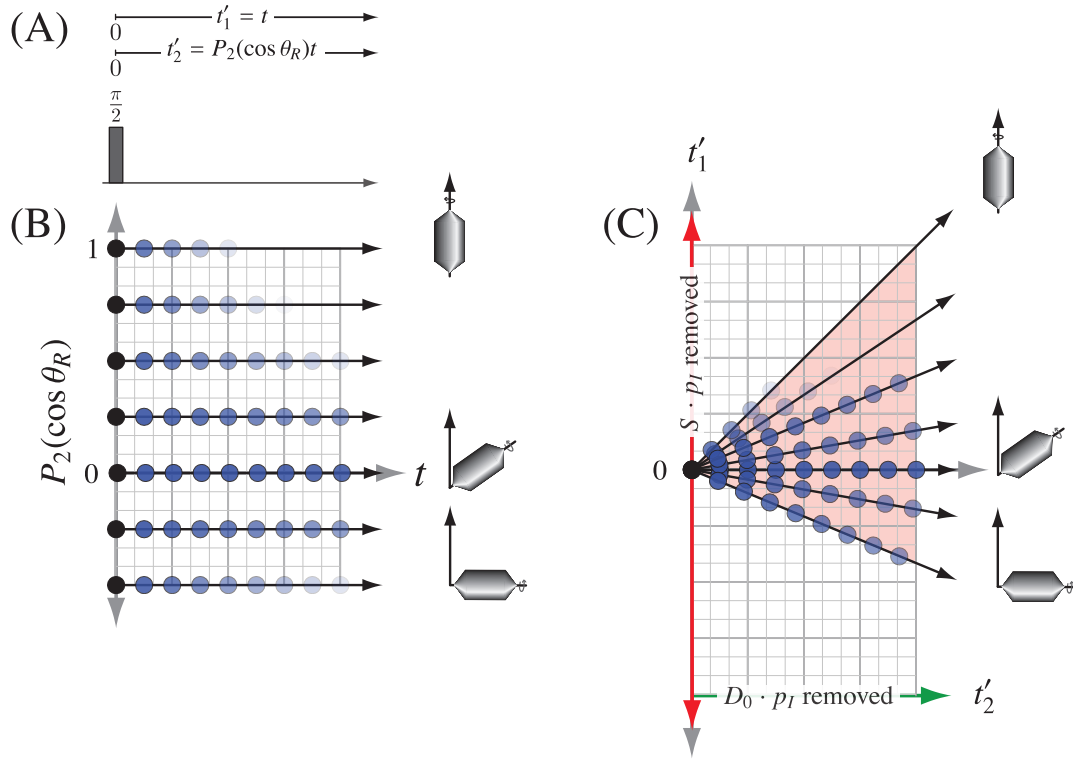


Figure 51: (A) VACSY experiment pulse sequence. (B) The signal is acquired in a series of independent 1D experiments as a function of the second-rank Legendre polynomial of the cosine of the rotor axis angle. This signal is interpolated onto a  $t'_1$ - $t'_2$  coordinate system in (C) where  $\mathbb{S}p_I$  is removed along the  $t'_1$  coordinate and  $\mathbb{D}_0 p_I$  is removed along the  $t'_2$  coordinate. Because sampling the signal in the  $t'_1$ - $t'_2$  coordinate system is only possible inside the shaded area, there may be phase artifacts in the 2D VACSY spectrum.

$\theta_R^{[1]}$	$\theta_R^{[2]}$	$\kappa^{(\omega_1)} = -P_L(\cos \theta_R^{[1]})/P_L(\cos \theta_R^{[2]})$	$\zeta(t'_1)$
0°	63.43°	5	6
30.56°	70.12°	1.87	2.87
37.38°	79.19°	1	2
39.23°	90°	0.87	1.87

Table 9: Selected DAS angle pairs with associated  $\kappa^{(\omega_1)}$  values for removing  $L = 2$  and 4 anisotropies.

The DAS angle pairs needed to create simultaneous  $\mathbb{D}_0$  and  $\mathbb{G}_0$  echoes are obtained by solving the simultaneous equations in Eq. (161) and are given by

$$\theta_R^{[1]} = \cos^{-1} \sqrt{\frac{1 + \sqrt{\frac{4\kappa^{(\omega_1)}}{5}}}{3}}, \quad \theta_R^{[2]} = \cos^{-1} \sqrt{\frac{1 - \sqrt{\frac{4}{5\kappa^{(\omega_1)}}}}{3}}, \quad (162)$$

where

$$\kappa^{(\omega_1)} = -\frac{P_2(\cos \theta_R^{[1]})}{P_2(\cos \theta_R^{[2]})} = -\frac{P_4(\cos \theta_R^{[1]})}{P_4(\cos \theta_R^{[2]})}. \quad (163)$$

Here  $0.8 \leq \kappa^{(\omega_1)} \leq 5$ , and a plot of the angle pair  $(\theta_R^{[1]}, \theta_R^{[2]})$  as a function of  $\kappa^{(\omega_1)}$  values are shown in Fig. 53. Selected DAS angle pairs and associated  $\kappa^{(\omega_1)}$  values are given in Table 9.

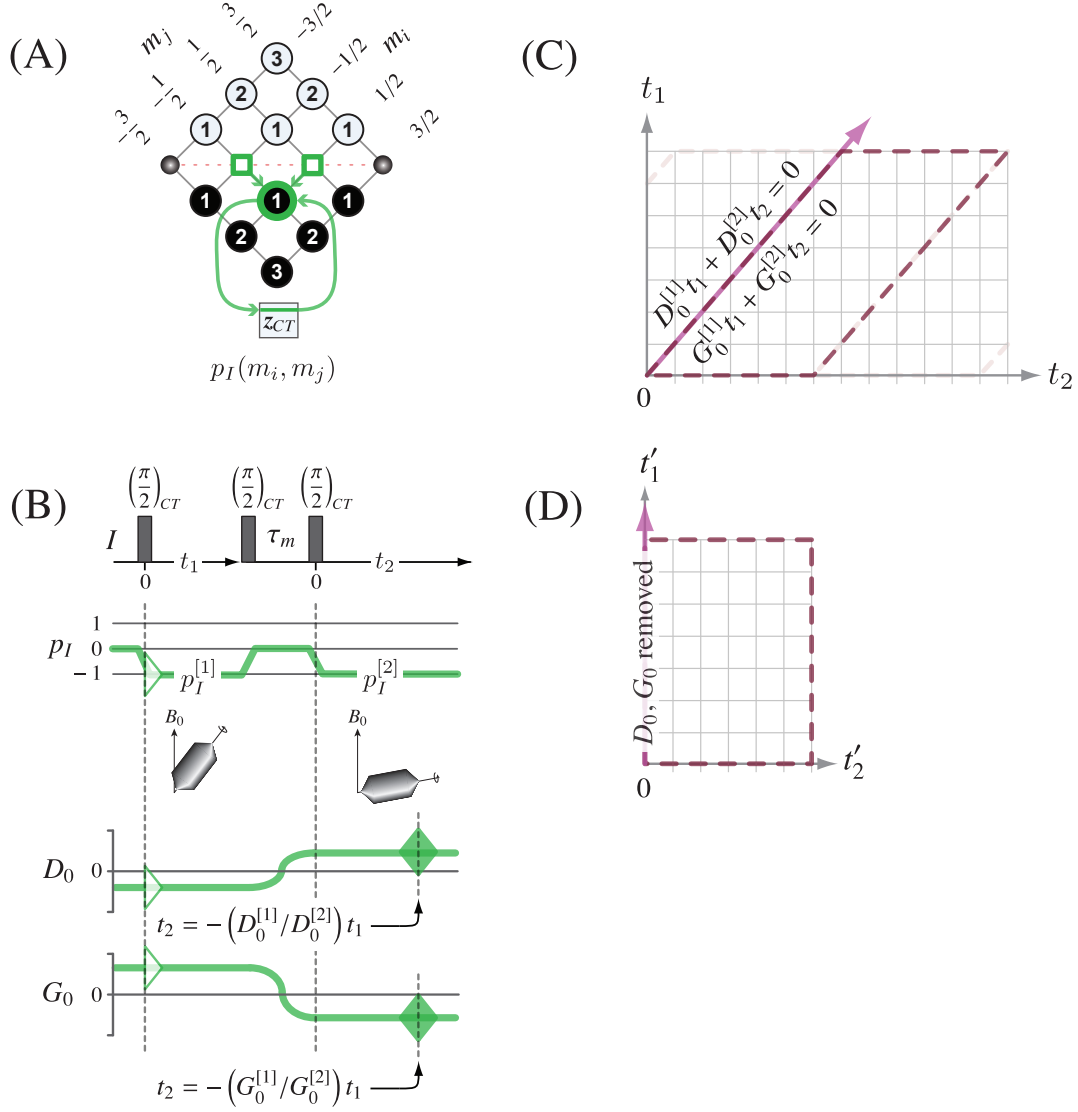


Figure 52: (A) DAS experiment transition pathways in Eq. (164) on the  $p_I$  tables for spin  $I = 3/2$ . (B) Pulse sequence with  $p_I$ ,  $D_0$  and  $G_0$  pathways for DAS experiment. A filled diamond represents a contribution to a directly observable echo, while an open triangle represents a contribution to an indirectly observable free induction decay. (C) For a 2D DAS signal acquired as a function of  $t_1$  and  $t_2$  the contributions to the frequency with  $D_0$  and  $G_0$  symmetry are refocused simultaneously into echoes at  $t_2 = \kappa^{(\omega_1)}t_1$ . The dashed line represents a passive affine transformation of the 2D coordinate system to create a coordinate,  $t'_1$ , along which the 2D signal is unaffected by frequency components containing  $D_0$  and  $G_0$ . (D) After applying an active affine transformation with a shear parallel to  $t_2$ , and a scaling along  $t'_1$ , a 2D signal with  $D_0$  and  $G_0$  removed along the  $t'_1$  coordinate is obtained.

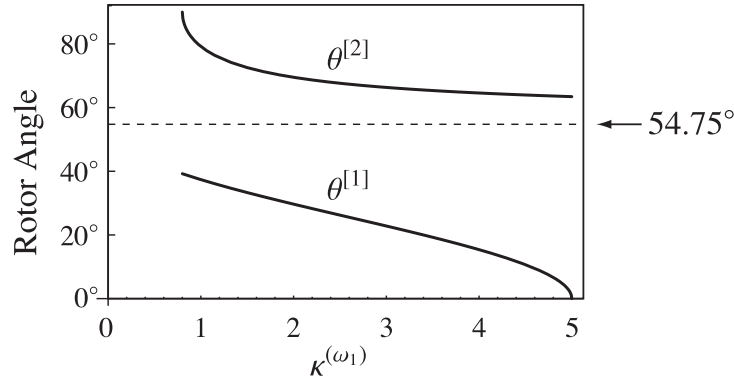


Figure 53: Solutions to the DAS simultaneous equations given in Eq. (162). The dashed line represents the  $P_2(\cos\theta_M^{(2)})$  magic-angle,  $54.74^\circ$ .

In the DAS experiment only the central symmetric  $m_I = \frac{1}{2} \rightarrow -\frac{1}{2}$  transition is excited, with the transition pathway,

$$\{I\} : [-\frac{1}{2}, +\frac{1}{2}] \rightarrow |-\frac{1}{2}\rangle \langle +\frac{1}{2}| \rightarrow [-\frac{1}{2}, +\frac{1}{2}] \rightarrow |-\frac{1}{2}\rangle \langle +\frac{1}{2}|, \quad (164)$$

and the spatial pathway  $\theta_R^{[1]} \rightarrow \theta_R^{[2]}$ . The transition pathway maps into the symmetry pathway  $p_I = 0 \rightarrow -1 \rightarrow 0 \rightarrow -1$ , and the spatial pathway maps into the  $\mathbb{D}_0$  and  $\mathbb{G}_0$  symmetry pathways, as shown in Fig. 52B. The first pulse selectively excites the central transition while spinning at the rotor angle  $\theta_R^{[1]}$ . The mixing period typically consists of two central-transition selective  $\pi/2$  pulses, the first stores the magnetization along the  $z$ -axis during the hop of the rotor angle [79, 80], and the second re-excites the central transition at angle  $\theta_R^{[2]}$ . After an affine transformation, the  $\mathbb{D}_0$  and  $\mathbb{G}_0$  echo paths are aligned along the  $t'_1$  axis, removing the anisotropic components, as shown in Fig. 52D.

#### 4. Pure absorption mode lineshapes

In the previous section, we saw situations in both COASTER and MQ-DOR where the complete acquisition of two different echo symmetry paths requires the acquisition of the 2D signal in adjacent quadrants in the  $(t_1, t_2)$  time domain. One would think that the signal acquisition during negative  $t_1$  or  $t_2$  violates causality. There are, however, approaches developed in the context of obtaining pure absorption-mode multidimensional lineshapes that achieve the effective acquisition of an NMR signal going backward in time. In this section we explore how symmetry pathways can serve as a helpful guide in implementing these approaches.

##### 4.1. One dimension

To better understand how pure absorption mode lineshapes are obtained in a multi-dimensional NMR spectrum, it is instructive to review some fundamental aspects of absorption and dispersion mode lineshapes in 1D NMR spectra. As shown in Fig. 54, the Fourier transform of the free induction decay from a single transition pathway contains a single resonance, and assuming the free induction decay was acquired with the proper receiver phase, the real part of the spectrum contains an absorption mode resonance lineshape, centered at  $\omega = \Omega$ , and the imaginary part of the spectrum contains a dispersion mode resonance lineshape, also at  $\omega = \Omega$ . This can be easily shown, for example, in the simple case of the Fourier transform of an exponentially decaying signal,

$$\mathfrak{s}(\omega) = \int_0^\infty e^{-i\Omega t} e^{-|t|/T_2^*} e^{-i\omega t} dt = \mathfrak{A}(\omega - \Omega) + i\mathfrak{D}(\omega - \Omega), \quad (165)$$

where  $\mathfrak{A}(\omega)$  and  $\mathfrak{D}(\omega)$  are the absorption- and dispersion-mode Lorentzian lineshape functions. The presence of the dispersion-mode lineshape in the spectrum is not a serious problem in 1D NMR since the different signals are

segregated into the real and imaginary parts in the receiver. Although, it is more likely that zeroth and first-order phase corrections are needed to make this segregation complete.

It is often possible to design a transition pathway where all frequency components refocus into a simultaneous echo during signal acquisition. Additionally, when there is a strong inhomogeneous broadening of the resonance arising from field inhomogeneities or other spatial frequency anisotropies, it may also be possible to acquire the full echo signal envelope, as shown in Fig. 55. By shifting the time origin to the echo top and applying a Fourier transform of this signal, only an absorption mode lineshape in the real part of the spectrum is obtained. That is, there will be no dispersion mode lineshape in the imaginary part, as shown in Fig. 55. Again, for the simple example of an exponentially decaying signal, one can readily show that

$$\mathfrak{s}(\omega) = \int_{-\infty}^{\infty} e^{-i\Omega t} e^{-|t|/T_2^*} e^{-i\omega t} dt = 2\mathfrak{A}(\omega - \Omega). \quad (166)$$

The dispersion mode lineshape appears in the imaginary part of the free induction decay spectrum when the lower limit of the Fourier integral is changed from  $-\infty$  to zero. Whole echo acquisition for obtaining pure absorption mode lineshapes is not that useful in liquid-state NMR since one rarely acquires resonances with such strong inhomogeneous broadenings. It has, however, become particularly useful in solid-state NMR[17] for obtaining not only pure absorption mode lineshapes but also for eliminating lineshape distortions due to receiver dead time.

Essential for employing whole echo acquisition is the ability to create simultaneous echoes of all frequency components contributing to a resonance. For example, in Fig. 25, where only frequency components with  $p_I$  symmetry are present in the system, all the frequency components are refocused into an echo simultaneously at  $t_2 = t_1$  using a Hahn echo,  $(\frac{\pi}{2} - t_1 - \pi - t_2)$ , sequence. In contrast, for a spin  $I = 1$  system, as shown in Fig. 26, the frequency components with  $d_I$  symmetry do not refocus into an echo with the  $p_I$  components. Thus, using this sequence on a spin  $I = 1$  system would not be appropriate for whole echo acquisition. For such a system one can obtain simultaneous  $p_I$  and  $d_I$  echoes using the transition pathways

$$\{I = 1\} : \begin{cases} [z_I] \rightarrow |0\rangle \langle -1| \rightarrow |-1\rangle \langle 0|, \\ [z_I] \rightarrow |+1\rangle \langle 0| \rightarrow |0\rangle \langle +1|, \end{cases} \quad (167)$$

with the symmetry pathways and sequence shown in Fig. 56. Selection of these transition pathways can be achieved through phase cycling and accurate calibration of the rf pulse lengths.

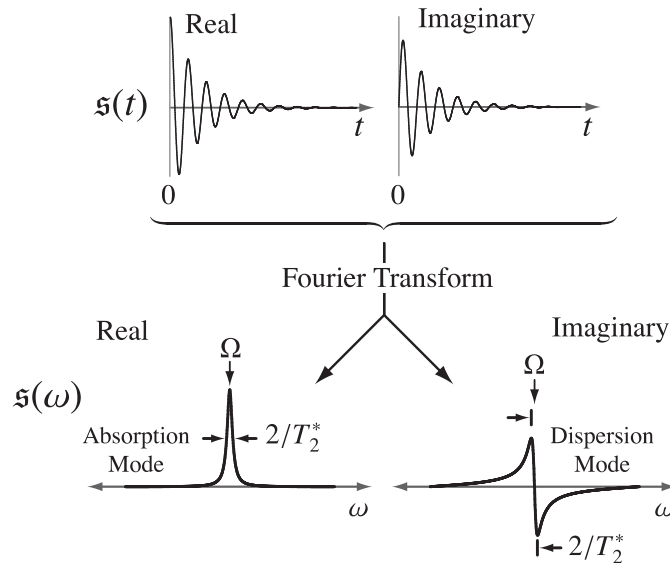


Figure 54: One dimensional Fourier transform of a free induction decay.

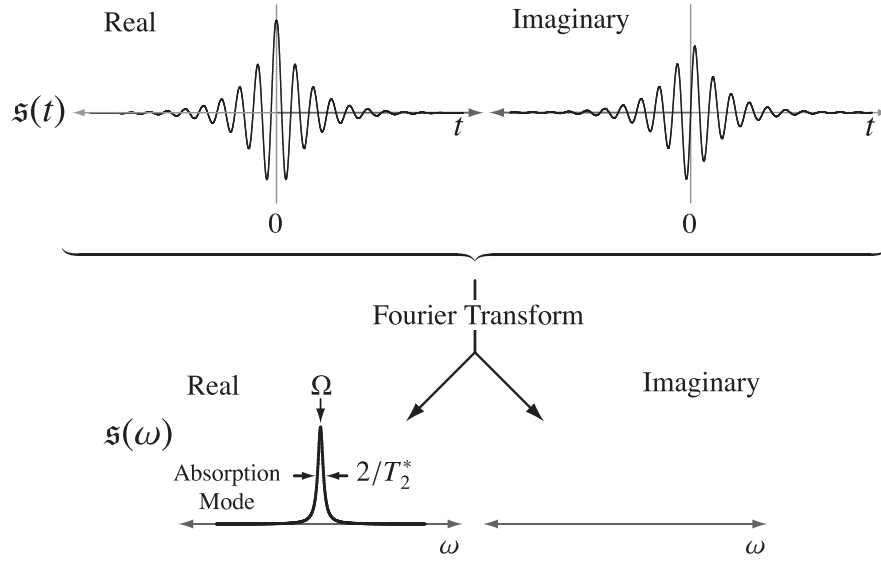


Figure 55: One dimensional Fourier transform of a whole echo with the time origin set at the echo top.

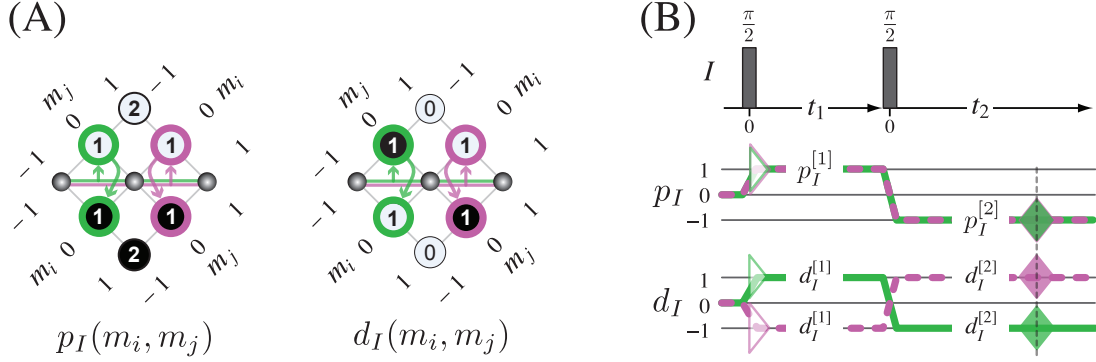


Figure 56: (A) Transition pathways in Eq. (167) on the  $p_I$  and  $d_I$  tables for spin  $I = 1$ . (B) Pulse sequence with  $p_I$  and  $d_I$  pathways for two pulse experiment to generate simultaneous  $p_I$ ,  $d_I$  echoes for a spin  $I = 1$  nucleus.

#### 4.2. Two dimensions

In two and higher dimensions, separating absorption and dispersion mode lineshapes becomes more complicated. Consider a 2D exponentially decaying time domain signal

$$s(t_1, t_2) = e^{-i\Omega t_1} e^{-i\Omega t_2} e^{-|t_1|/T_2} e^{-|t_2|/T_2}, \quad (168)$$

acquired only in the  $(t_1 > 0, t_2 > 0)$  quadrant. A 2D Fourier transform yields

$$\begin{aligned} s(\omega_1, \omega_2) &= \left[ \int_0^\infty e^{-i\Omega t_1} e^{-|t_1|/T_2} e^{-i\omega_1 t_1} dt_1 \right] \times \left[ \int_0^\infty e^{-i\Omega t_2} e^{-|t_2|/T_2} e^{-i\omega_2 t_2} dt_2 \right] \\ &= \mathfrak{A}(\omega_1 - \Omega) \mathfrak{A}(\omega_2 - \Omega) - \mathfrak{D}(\omega_1 - \Omega) \mathfrak{D}(\omega_2 - \Omega) + i [\mathfrak{A}(\omega_1 - \Omega) \mathfrak{D}(\omega_2 - \Omega) + \mathfrak{A}(\omega_2 - \Omega) \mathfrak{D}(\omega_1 - \Omega)]. \end{aligned} \quad (169)$$

The real part of the 2D spectrum contains a 2D lineshape that contains a mixed absorption- and dispersion-mode lineshape, as shown in Fig. 57C. Obtaining a pure absorption-mode lineshape is no longer a matter of finding the right phase correction. Generally, dispersion-mode lineshapes are less desirable because of their tails which fall off slower than absorption-mode lineshapes, a feature that can lead to greater overlap of resonances in a multisite spectrum.

If the lower limits of our 2D Fourier integrals were  $-\infty$ , the dispersion-mode 2D lineshapes would be eliminated,



that is,

$$\mathfrak{s}(\omega_1, \omega_2) = \left[ \int_{-\infty}^{\infty} e^{-i\Omega t_1} e^{-|t_1|/T_2} e^{-i\omega_1 t_1} dt_1 \right] \times \left[ \int_{-\infty}^{\infty} e^{-i\Omega t_2} e^{-|t_2|/T_2} e^{-i\omega_2 t_2} dt_2 \right] = 4\mathfrak{A}(\omega_1 - \Omega)\mathfrak{A}(\omega_2 - \Omega), \quad (170)$$

and a pure absorption-mode 2D lineshape, as shown in Fig. 57A, is obtained. Again, note that we have an absorption-mode lineshape only in the real part and zero in the imaginary part. Thus, to obtain a pure absorption-mode 2D lineshape in the real part, one only needs to extend one of the two integral limits to  $-\infty$ , such as,

$$\begin{aligned} \mathfrak{s}(\omega_1, \omega_2) &= \left[ \int_{-\infty}^{\infty} e^{-i\Omega t_1} e^{-|t_1|/T_2} e^{-i\omega_1 t_1} dt_1 \right] \times \left[ \int_0^{\infty} e^{-i\Omega t_2} e^{-|t_2|/T_2} e^{-i\omega_2 t_2} dt_2 \right] \\ &= 2\mathfrak{A}(\omega_1 - \Omega)\mathfrak{A}(\omega_2 - \Omega) + i2\mathfrak{A}(\omega_1 - \Omega)\mathfrak{D}(\omega_1 - \Omega). \end{aligned} \quad (171)$$

Here, the real part contains the pure absorption-mode 2D lineshape, and the imaginary part contains a mixed absorption/dispersion-mode 2D lineshape. Extending only the lower integral limit in  $t_2$  to  $-\infty$  would have also produced a similar result. Clearly, a solution for obtaining a pure absorption-mode 2D lineshape is somehow to acquire signal in a quadrant adjacent to the  $(t_1 > 0, t_2 > 0)$  quadrant, as illustrated in Fig. 58. There are two approaches for finding this solution, depending on which adjacent quadrant is acquired. Generally, the  $(t_1 < 0, t_2 > 0)$  quadrant is acquired with the hypercomplex approach [16] and the  $(t_1 > 0, t_2 < 0)$  quadrant with the shifted-echo approach [17], although either approach can be used for obtaining either adjacent quadrant.

#### 4.2.1. Hypercomplex approach

The hypercomplex approach [16] employs a transition pathway and its complementary *anti-transition pathway*. This is also the basis behind the TPPI approach [81]. The symmetry and *anti-symmetry* pathways derived from the transition and anti-transition pathways, respectively, are identical except during  $t_1$ , where the symmetry and anti-symmetry pathways take on values that are equal in magnitude but opposite in sign. This is illustrated in Fig. 59 for a generic symmetry and anti-symmetry pathway. Only transition pathways that map into an anti-symmetry pathway for every spatial-transition product symmetry present in the system can serve as an anti-transition pathway, generating a signal that acts like the transition pathway signal evolving backward in time during the  $t_1$  period. In this manner, one obtains a signal in the  $(t_1 < 0, t_2 > 0)$  quadrant.

For example, if only  $p_I$  symmetry is relevant in the system, then the signals for the transition and anti-transition pathway are identical except for the sign of the  $p_I$  symmetry part during  $t_1$  evolution, that is,

$$\mathfrak{s}(t_1, t_2) = \exp \left\{ i \frac{p_I^{[1]}}{|p_I^{[1]}|} \Omega(p_I^{[1]}) t_1 \right\} \exp \left\{ i \Omega(p_I^{[2]}) t_2 \right\} e^{-|t_1|/T_2} e^{-|t_2|/T_2}. \quad (172)$$

Both the transition and anti-transition pathway signals can be experimentally measured at positive  $t_1$  and  $t_2$  values. If the positive  $t_1$  values in the measured transition pathway signal are multiplied by  $-1$  (i.e., reverse the order of data

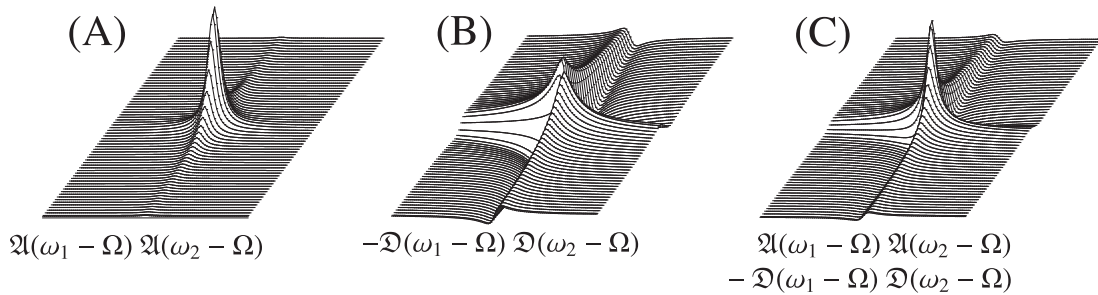


Figure 57: Shown from left to right are examples of (A) 2D pure absorption-mode lineshape, (B) 2D pure dispersion-mode lineshape, and (C) 2D mixed-mode lineshape.

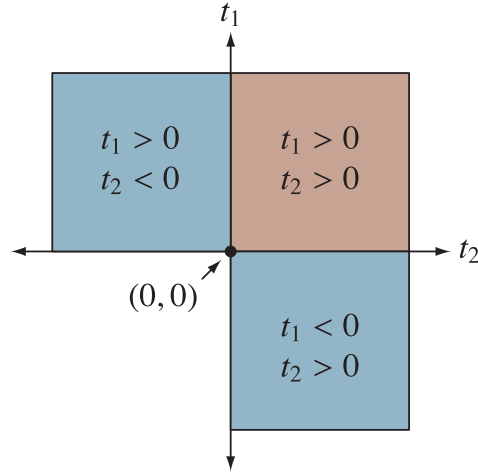


Figure 58: Obtaining a pure absorption mode 2D lineshape requires signal from at least one quadrant adjacent to the  $(t_1 > 0, t_2 > 0)$  quadrant. Generally, the hypercomplex approach[16] focuses on obtaining the negative  $t_1$  quadrant through an anti-transition pathway, and the shifted-echo approach[17] focuses on obtaining the negative  $t_2$  quadrant by generating an echo of all pathway symmetries. However, either approach can be used for obtaining either adjacent quadrant.

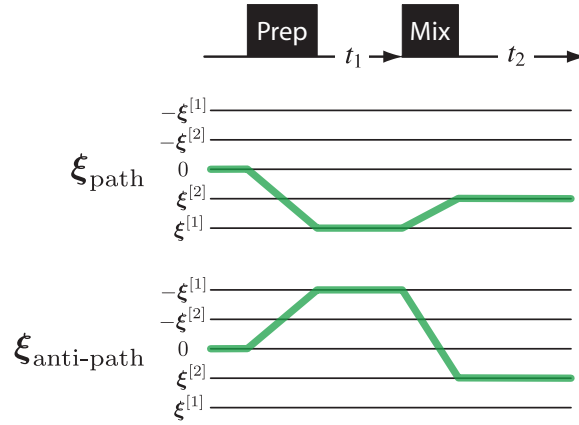


Figure 59: Symmetry and anti-symmetry pathways for obtaining pure absorption mode 2D lineshapes using the hypercomplex approach. For the hypercomplex approach, an anti-symmetry pathway must exist for every spatial-transition product symmetry pathway present in the system.

in  $t_1$  and take the complex conjugate), then the transition pathway signal would appear to be the anti-transition pathway signal measured at negative  $t_1$  values. Thus, we could use the transition and anti-transition pathway signals to create one signal that runs from  $-\infty$  to  $+\infty$  in  $t_1$  according to

$$\mathfrak{s}_{\text{total}}(t_1, t_2) = \begin{cases} \mathfrak{s}_{\text{anti}}^*(-t_1, t_2) & \text{for } t_1 < 0, \\ \mathfrak{s}_{\text{path}}(t_1, t_2) & \text{for } t_1 \geq 0, \end{cases} \quad (173)$$

where the asterisk represents the complex conjugate. The Fourier transform of this signal is

$$\mathfrak{s}_{\text{total}}(\omega_1, \omega_2) = \mathfrak{s}_{\text{anti}}(-\omega_1, \omega_2) + \mathfrak{s}_{\text{path}}(\omega_1, \omega_2). \quad (174)$$

Since  $\mathfrak{A}(\omega)$  is an even function of  $\omega$  and  $\mathfrak{D}(\omega)$  is an odd function, we obtain

$$\mathfrak{s}_{\text{total}}(\omega_1, \omega_2) = 2\mathfrak{A}(\omega_1 - \Omega_1)\mathfrak{A}(\omega_2 - \Omega_2) + i2\mathfrak{A}(\omega_1 - \Omega_1)\mathfrak{D}(\omega_2 - \Omega_2). \quad (175)$$

To separate the transition and anti-transition pathway signals from the undesired transition pathway signals, we could perform two experiments: one that selectively detects the transition pathway signal and another that selectively detects the anti-transition pathway signal. This approach, however, would be wasteful since it cancels out perfectly good anti-transition pathway signals when doing a transition pathway experiment and vice versa. A more efficient approach is to design an experiment using proper phase cycling[11] that separates the experimental signal sum into two parts,  $\mathfrak{s}_x(t_1, t_2)$  and  $\mathfrak{s}_y(t_1, t_2)$ , with both parts selectively detecting the transition and anti-transition pathway signals (i.e., the transition and anti-transition pathways are aliased together). These two signals can then be combined to obtain either the transition or anti-transition pathway signals according to

$$\begin{aligned} \mathfrak{s}_{\text{path}}(t_1, t_2) &= \mathfrak{s}_x(t_1, t_2) + i\mathfrak{s}_y(t_1, t_2), \\ \mathfrak{s}_{\text{anti}}(t_1, t_2) &= \mathfrak{s}_x(t_1, t_2) - i\mathfrak{s}_y(t_1, t_2). \end{aligned} \quad (176)$$

If needed, a shear parallel to  $t_2$  can be applied to  $\mathfrak{s}_{\text{path}}(t_1, \omega_2)$  and  $\mathfrak{s}_{\text{anti}}(t_1, \omega_2)$  using shear ratios of  $\kappa^{(\omega_1)}$  and  $-\kappa^{(\omega_1)}$ , respectively, while the same scale factor,  $\varsigma^{(t_1)}$  is used for both signals. After finishing the double Fourier transform on the transition and anti-transition pathway signals, one can combine them according to Eq. (174) to obtain a spectrum with pure absorption mode 2D lineshapes. A flowchart for processing hypercomplex data is given in Fig. 60.

A potential complication with the hypercomplex approach arises when the efficiency of coherence transfer through the transition and anti-transition pathways are not identical. This imbalance will introduce dispersion mode components into the pure absorption mode 2D lineshape. One solution is to modify the pulse sequences to find transition and anti-transition pathways that have more equal efficiencies[82, 83], while another is to use the shifted-echo approach [17, 83, 84], described in the next section, instead of the hypercomplex method.

#### 4.2.2. Shifted-echo approach

In the shifted-echo approach[17], a simultaneous echo of all spatial-transition product pathway symmetries is generated during  $t_2$ . By shifting this simultaneous echo far enough into  $t_2$  acquisition, a whole echo is acquired for all values of  $t_1$  including  $t_1 = 0$ . The origin in  $t_2$  can then be shifted to the simultaneous echo top, and the lower limit of the Fourier integral in  $t_2$  is extended to  $-\infty$ . In this manner, one obtains a signal in the  $(t_1 > 0, t_2 < 0)$  quadrant. This approach is illustrated in Fig. 61 with a single pathway symmetry.

In experiments with strong inhomogeneous broadenings, this approach leads to a factor of  $\sqrt{2}$  improvement in sensitivity compared to the hypercomplex method. The reason for this sensitivity enhancement is apparent when examining the flowchart for processing hypercomplex data in Fig. 60. In the presence of strong inhomogeneous broadenings, there will be little signal volume in the anti-transition pathway, and most of the signal volume will be in the transition pathway. While adding the anti-transition spectrum eliminates the small dispersion mode components in the combined spectrum, it can come at the cost of introducing more noise than signal, particularly in the case

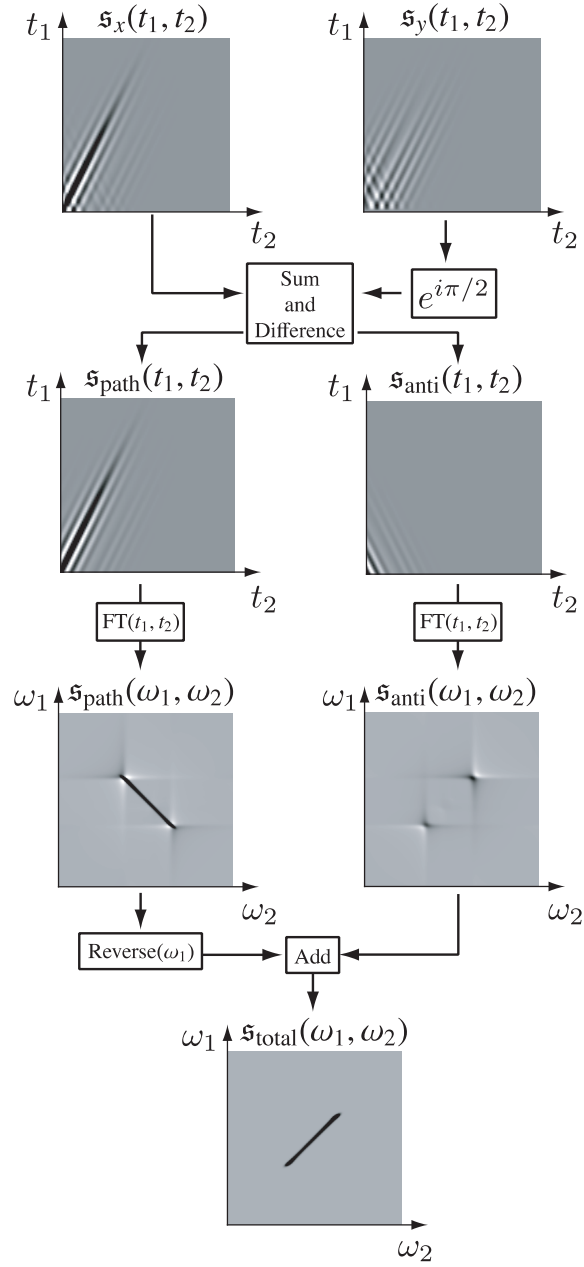


Figure 60: Possible flow chart for processing hypercomplex data to obtain a pure absorption mode 2D spectrum. The transition and anti-transition pathway signals are constructed using Eq. (176) from the experimentally measured  $\mathfrak{s}_x(t_1, t_2)$  and  $\mathfrak{s}_y(t_1, t_2)$ . If needed, a shear parallel to  $t_2$  can be applied to  $\mathfrak{s}_{\text{path}}(t_1, \omega_2)$  and  $\mathfrak{s}_{\text{anti}}(t_1, \omega_2)$  using shear ratios of  $\kappa^{(\omega_1)}$  and  $-\kappa^{(\omega_1)}$ , respectively, while the same scale factor,  $\varsigma^{(t_1^*)}$  is used for both signals. The transition pathway spectrum is reversed about the  $\omega_1$  direction after the Fourier transform and added to the anti-transition pathway spectrum to yield the pure absorption mode spectrum.

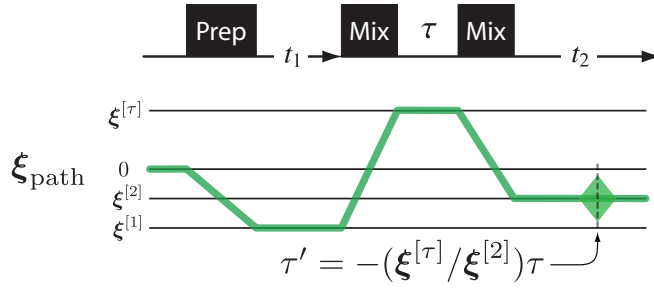


Figure 61: Generic 2D pulse sequence and symmetry pathway for obtaining pure absorption mode 2D lineshapes using the shifted-echo approach. For shifted-echo acquisition to work, a simultaneous echo in  $t_2$  must be generated for every spatial-transition product symmetry present in the system.

of inhomogeneous second-order broadening of signals from quadrupolar nuclei. Thus the s/n ratio of the transition pathway spectrum by itself will be greater than the final combined spectrum by a factor up to  $\sqrt{2}$ . By shifting the simultaneous echo forward in  $t_2$  so that a whole simultaneous echo can be acquired for  $t_1 = 0$ , we remove the small dispersion mode component in the echo spectrum and thus eliminate the need to add in the “noisy” anti-transition pathway spectrum. Another advantage of the shifted echo approach over the hypercomplex approach is that it avoids the potential problem of combining pathways with unequal efficiencies. A flowchart for processing shifted-echo signal is given in Fig. 62.

The hypercomplex and shifted echo approach can be combined at no extra cost in time, although the anti-transition pathway signal obtained in this manner is often not useful. There are cases, however, when the dispersion in isotropic shifts is greater than the anisotropic linewidth (e.g., glasses), and then the anti-transition pathway signal should be used instead of the transition pathway signal since it will contain the majority of the signal volume. In such a case, the transition and anti-transition pathway signals will appear to have switched behaviors, with the anti-transition pathway simultaneous echo tops moving forward with increasing  $t_1$  and the simultaneous echo tops moving backward. In specific cases, when the dispersion in isotropic shifts is approximately equal to the anisotropic linewidth, then either the transition pathway and anti-transition pathway signal can be used to obtain a pure absorption mode 2D spectrum, and subsequently, these spectra can be combined for an additional  $\sqrt{2}$  sensitivity enhancement with respect to the single pathway shifted echo signal, or with respect to the traditional hypercomplex approach. See Ref. [17] for a detailed comparison of these approaches.

Another advantage of the shifted-echo approach is that the phase correction needed to place the pure absorption mode 2D spectrum into the real part of the spectrum can be determined without any user interaction. The algorithm consists of (1) finding the complex point in 2D time domain data sets with maximum magnitude, (2) applying the zeroth-order phase correction to the entire data set that makes this point have its maximum intensity in the real part of data, (3) shift the time origin in  $t_2$  to this point, (4) Fourier transform with respect to  $t_2$ , and (5) apply the first-order phase correction  $\exp(-i\omega_2\tau')$  to correct for the shifted time origin. The error in calculating the necessary first-order phase correction using this approach is on the order of the dwell time used in  $t_2$ .

A potential difficulty with the shifted-echo approach is that  $\tau'$  must be adjusted to be large enough to obtain the whole echo signal. If the homogeneous broadenings, e.g.  $\lambda$ , are so large that

$$e^{-2\lambda\tau'} \leq 1/2^{1/2}, \quad (177)$$

then the hypercomplex approach is preferred. Using a shorter  $\tau'$  value can alleviate this problem; however, any truncation of the simultaneous echo tail will add dispersion-mode components into the 2D spectrum. In practice, however, some truncation of the simultaneous echo tail can be tolerated since this distortion is often no worse than the distortions obtained from acquisition dead times in the simple hypercomplex sequences.

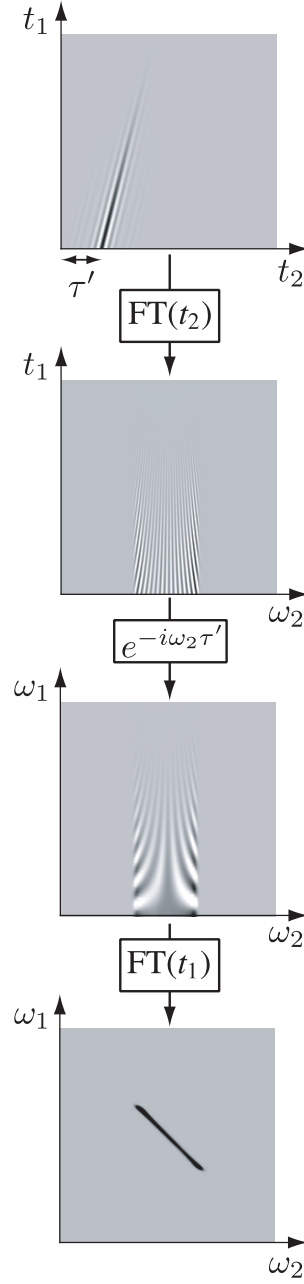


Figure 62: Possible flow chart for processing Shifted Echo data to obtain a pure absorption mode 2D spectrum. Apodizations and phase corrections (also shearing transformations) are usually applied before and/or in between the Fourier transforms with respect to  $t_1$  and  $t_2$ . If necessary, the echo spectrum can be reversed about the  $\omega_1$  direction after the Fourier transform.

## 5. Affine transformations

The ability to refocus different spatial and transition symmetries into echoes with different paths in time-resolved NMR experiments creates opportunities for generating multi-dimensional spectra that correlate different interactions. These spectra can be made easier to interpret through similarity transformations. Here we examine the mathematics behind these similarity transformations relating to magnetic resonance experiments. Most similarity transformations in NMR are affine transformations, as they preserve the colinearity of points and ratios of distances. Important in any similarity transformation is whether to implement the transformation actively or passively. Active transformations change the appearance of the signal while leaving the coordinate system unchanged, whereas passive transformations leave the appearance of the signal unchanged while changing the coordinate system. Both active and passive transformations are used extensively in NMR. A helpful theorem in employing these coordinate transformations is the  $n$ -dimensional Fourier Affine theorem[85], summarized by the expressions

$$\mathfrak{s}(\mathcal{A}_t \mathbf{t} + \Delta \mathbf{t}) \leftrightarrow \exp\{i \mathbf{t} \cdot \mathcal{A}_t^{-T} \boldsymbol{\omega}\} \frac{\mathfrak{s}(\mathcal{A}_t^{-T} \boldsymbol{\omega})}{|\det \mathcal{A}_t|}, \quad (178)$$

and

$$\mathfrak{s}(\mathcal{A}_\omega \boldsymbol{\omega} + \Delta \boldsymbol{\omega}) \leftrightarrow \exp\{i \boldsymbol{\omega} \cdot \mathcal{A}_\omega^{-T} \mathbf{t}\} \frac{\mathfrak{s}(\mathcal{A}_\omega^{-T} \mathbf{t})}{|\det \mathcal{A}_\omega|}, \quad (179)$$

where  $\mathcal{A}$  is an  $n \times n$  affine transformation matrix,  $\mathcal{A}^{-T}$  is the inverse transpose of  $\mathcal{A}$ ,  $\mathbf{t}$  and  $\boldsymbol{\omega}$  are  $n$ -dimensional vectors for time and frequency coordinates, respectively, and  $\Delta \mathbf{t}$  and  $\Delta \boldsymbol{\omega}$  are  $n$ -dimensional vectors for translating time and frequency coordinates, respectively. In this section, we examine three specific types of affine transformations: translation, scaling, and shearing transformations, and their relevance to various multidimensional NMR experiments.

### 5.1. Translation

Translations can be utilized in NMR experiments of any dimensionality. For 1D NMR experiments, a translation involving the time domain is implemented with

$$t' = t + \Delta t, \quad (180)$$

and a translation involving the frequency domain with

$$\omega' = \omega + \Delta \omega, \quad (181)$$

where  $\Delta t$  and  $\Delta \omega$  are the respective translations. The adjustment of the reference frequency in an NMR spectrum is probably the most common example of a passive frequency translation. For discretely sampled signals, it might appear that active translations would be limited to integer multiples of the digital resolution; however, the Fourier shift theorem,

$$\mathfrak{s}(t + \Delta t) \leftrightarrow e^{i\omega \Delta t} \mathfrak{s}(\omega) \quad \text{and} \quad \mathfrak{s}(\omega + \Delta \omega) \leftrightarrow e^{i\Delta \omega t} \mathfrak{s}(t), \quad (182)$$

removes this restriction. Consider, for example, the need for time translation when processing the NMR signal obtained with whole echo acquisition[17] as shown in Fig. 63 and further described in Section 4. A Fourier transform of the whole echo signal with the original (as acquired) time coordinate axis yields a strongly phase modulated lineshape because the echo top did not coincide with the time coordinate origin. One could actively shift the signal directly in the time domain, but this would be restricted to integer multiples of the receiver dwell time. Using the Fourier shift theorem, as illustrated in Fig. 63, the signal can be shifted by an arbitrary time,  $\Delta t = -t_0$ , by Fourier transforming the signal with the original time domain coordinate into the frequency domain where a first-order phase correction of  $e^{-i\omega t_0}$  is applied to the signal. Then, an inverse Fourier transformation back into the time domain yields a signal that has been actively translated by  $-t_0$ . A well-written Fourier transform method that is aware of the shift theorem will take the position of the signal's coordinate origin into account when calculating the Fourier integral. Thus, in principle, one could also apply a passive transformation, that is, define a new time coordinate, using Eq. (180) with  $t_0 = -\Delta t$ , before Fourier transformation to obtain a properly phased spectrum from a signal with whole echo acquisition.

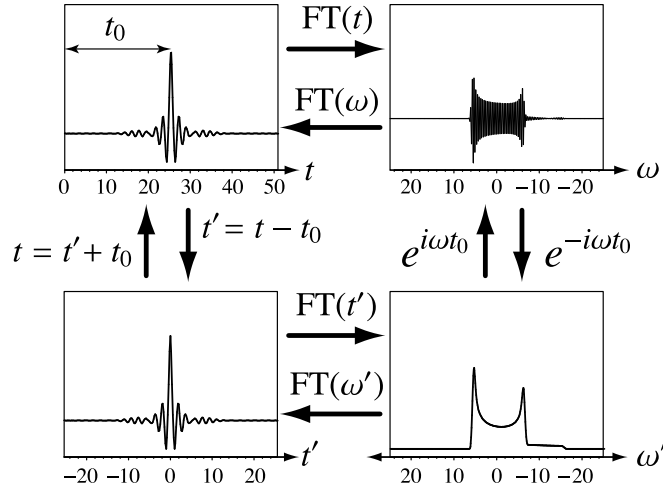


Figure 63: Application of the Fourier shift theorem when processing a signal with whole echo acquisition[17]. Clockwise from the top left, a Fourier transformation of the original time coordinate  $t$  results in a strongly phase-modulated frequency spectrum. This phase modulation can be removed by applying a first-order phase correction determined by  $t_0$ . Inverse Fourier transformation of the phase-corrected spectrum to the time domain confirms this to be a time translation. Counterclockwise from the top left, a passive translation of the coordinate system defines a new time variable  $t'$  whose origin is at the echo top. As described in Section 4, a Fourier transformation with respect to  $t'$  results in a pure absorption mode spectrum.

For 2D NMR signals, a translation is given by

$$\begin{bmatrix} t'_1 \\ t'_2 \end{bmatrix} = \begin{bmatrix} t_1 \\ t_2 \end{bmatrix} + \begin{bmatrix} \Delta t_1 \\ \Delta t_2 \end{bmatrix} = \begin{bmatrix} t_1 + \Delta t_1 \\ t_2 + \Delta t_2 \end{bmatrix}, \quad (183)$$

where  $\Delta t_1$  and  $\Delta t_2$  are the translations. With an appropriate change in variables, the same approach can be taken for translation in a frequency or mixed domain 2D NMR signal. Active translations of the signal are easily performed using the  $n$ -dimensional Fourier shift theorem

$$\mathbf{s}(\mathbf{t} + \Delta \mathbf{t}) \leftrightarrow e^{i\boldsymbol{\omega} \cdot \Delta \mathbf{t}} \mathbf{s}(\boldsymbol{\omega}) \quad \text{or} \quad \mathbf{s}(\boldsymbol{\omega} + \Delta \boldsymbol{\omega}) \leftrightarrow e^{i\Delta \boldsymbol{\omega} \cdot \mathbf{t}} \mathbf{s}(\mathbf{t}), \quad (184)$$

where  $\mathbf{t}$ ,  $\Delta \mathbf{t}$ ,  $\boldsymbol{\omega}$ , and  $\Delta \boldsymbol{\omega}$  are  $n$ -dimensional vectors.

## 5.2. Scaling

For a 1D NMR signal, a scaling involving the time or frequency domain is given by

$$t' = \varsigma^{(t)} t, \quad \text{or} \quad \omega' = \varsigma^{(\omega)} \omega. \quad (185)$$

A scaling transformation preserves the coordinate origin. The scaling is a dilation when  $\varsigma > 1$ , a contraction when  $0 < \varsigma < 1$ , and when  $\varsigma < 0$ , it is considered a reflection followed by either a contraction or dilation, depending upon  $|\varsigma|$ .

For a 2D NMR signal, the scaling is given by

$$\begin{bmatrix} t'_1 \\ t'_2 \end{bmatrix} = \underbrace{\begin{bmatrix} \varsigma^{(t_1)} & 0 \\ 0 & \varsigma^{(t_2)} \end{bmatrix}}_{\mathbf{s}_t} \begin{bmatrix} t_1 \\ t_2 \end{bmatrix} = \begin{bmatrix} \varsigma^{(t_1)} t_1 \\ \varsigma^{(t_2)} t_2 \end{bmatrix}, \quad (186)$$



and with an appropriate change in variables used for scaling in a frequency or mixed domain 2D NMR signal. Using the Fourier Affine theorem in Eqs. (178) and (179) one can show that

$$\mathcal{S}_t^{-T} = [\mathcal{S}_t^{-1}]^T = \begin{bmatrix} \varsigma^{(t_1)} & 0 \\ 0 & \varsigma^{(t_2)} \end{bmatrix}^{-T} = \begin{bmatrix} 1/\varsigma^{(t_1)} & 0 \\ 0 & 1/\varsigma^{(t_2)} \end{bmatrix}^T = \begin{bmatrix} 1/\varsigma^{(t_1)} & 0 \\ 0 & 1/\varsigma^{(t_2)} \end{bmatrix}, \quad (187)$$

revealing the reciprocal relationship between frequency and time domain scalings, that is,  $\varsigma^{(\omega_1)} = 1/\varsigma^{(t_1)}$  and  $\varsigma^{(\omega_2)} = 1/\varsigma^{(t_2)}$ .

Generally, active scaling of discretely sampled signals in NMR can be problematic as it may require signal interpolation. Thus, it is more common to perform passive scaling in NMR.

### 5.3. Shearing

Another important affine transformation is the shearing transformation, which is only defined for two or higher-dimensional NMR signals. A shear parallel to the  $t_2$  coordinate is given by

$$\begin{bmatrix} t'_1 \\ t'_2 \end{bmatrix} = \underbrace{\begin{bmatrix} 1 & 0 \\ \kappa^{(t_2)} & 1 \end{bmatrix}}_{\mathcal{K}_{t_2}} \begin{bmatrix} t_1 \\ t_2 \end{bmatrix} = \begin{bmatrix} t_1 \\ t_2 + \kappa^{(t_2)} t_1 \end{bmatrix}, \quad (188)$$

and the shear parallel to the  $t_1$  coordinate by

$$\begin{bmatrix} t'_1 \\ t'_2 \end{bmatrix} = \underbrace{\begin{bmatrix} 1 & \kappa^{(t_1)} \\ 0 & 1 \end{bmatrix}}_{\mathcal{K}_{t_1}} \begin{bmatrix} t_1 \\ t_2 \end{bmatrix} = \begin{bmatrix} t_1 + \kappa^{(t_1)} t_2 \\ t_2 \end{bmatrix}, \quad (189)$$

where  $\kappa$  is a shearing ratio. Similarly, a shear parallel to the  $\omega_2$  coordinate is given by

$$\begin{bmatrix} \omega'_1 \\ \omega'_2 \end{bmatrix} = \underbrace{\begin{bmatrix} 1 & 0 \\ \kappa^{(\omega_2)} & 1 \end{bmatrix}}_{\mathcal{K}_{\omega_2}} \begin{bmatrix} \omega_1 \\ \omega_2 \end{bmatrix} = \begin{bmatrix} \omega_1 \\ \omega_2 + \kappa^{(\omega_2)} \omega_1 \end{bmatrix}, \quad (190)$$

and the shear parallel to the  $\omega_1$  coordinate by

$$\begin{bmatrix} \omega'_1 \\ \omega'_2 \end{bmatrix} = \underbrace{\begin{bmatrix} 1 & \kappa^{(\omega_1)} \\ 0 & 1 \end{bmatrix}}_{\mathcal{K}_{\omega_1}} \begin{bmatrix} \omega_1 \\ \omega_2 \end{bmatrix} = \begin{bmatrix} \omega_1 + \kappa^{(\omega_1)} \omega_2 \\ \omega_2 \end{bmatrix}. \quad (191)$$

Again, using the Fourier Affine theorem in Eqs. (178) and (179) one can show that

$$\mathcal{K}_{t_2}^{-T} = [\mathcal{K}_{t_2}^{-1}]^T = \begin{bmatrix} 1 & 0 \\ \kappa^{(t_2)} & 1 \end{bmatrix}^{-T} = \begin{bmatrix} 1 & 0 \\ -\kappa^{(t_2)} & 1 \end{bmatrix}^T = \begin{bmatrix} 1 & -\kappa^{(t_2)} \\ 0 & 1 \end{bmatrix}, \quad (192)$$

revealing that a shearing of the 2D time domain signal parallel to  $t_2$  with shearing ratio  $\kappa^{(t_2)}$  corresponds to a shearing of the corresponding 2D frequency domain signal parallel to  $\omega_1$  with shearing ratio  $\kappa^{(\omega_1)} = -\kappa^{(t_2)}$ . Similarly, one finds that a shearing of the 2D time domain signal parallel to  $t_1$  with shearing ratio  $\kappa^{(t_1)}$  corresponds to a shearing of the corresponding 2D frequency domain signal parallel to  $\omega_2$  with shearing ratio  $\kappa^{(\omega_2)} = -\kappa^{(t_1)}$ .

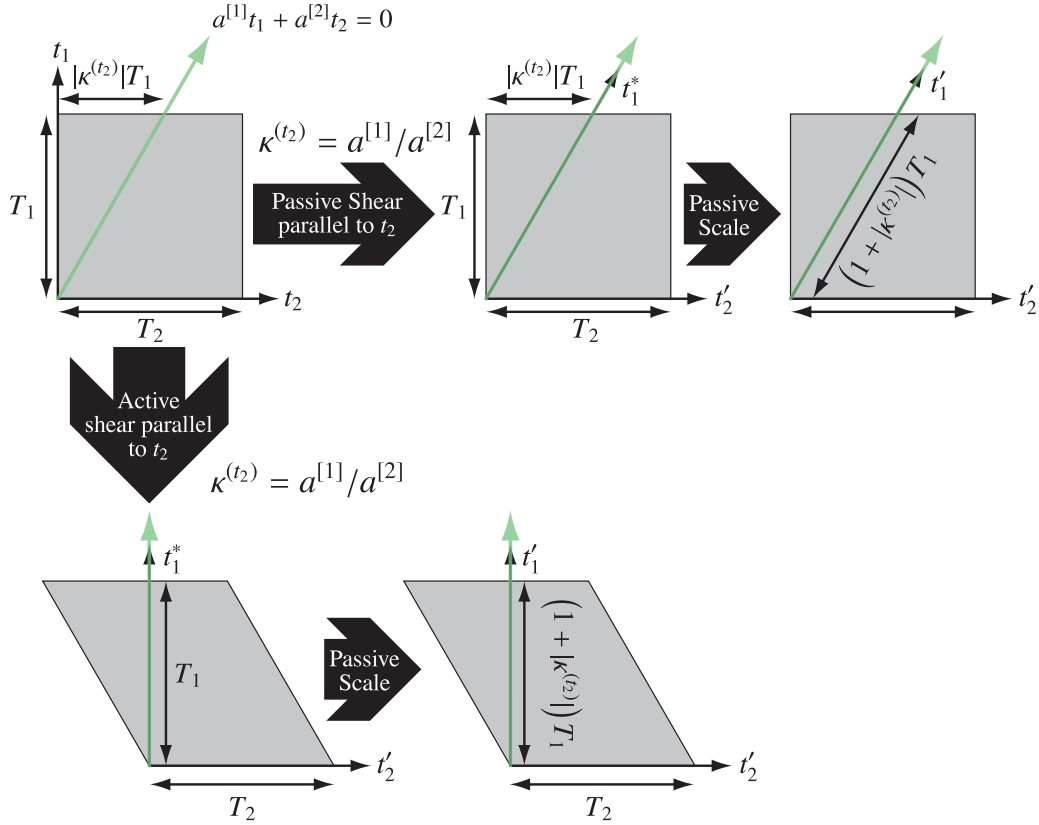


Figure 64: Illustration of a passive and active shear parallel to the  $t_2$  coordinate followed by a passive scaling of the  $t_1^*$  coordinate. The shaded area represents a region of the sampled signal.

It is generally preferable to perform active shearing in NMR to avoid the need for skew projections. As with translations, the active shear of discretely sampled signals is best performed by exploiting the Fourier shift theorem. For a shear parallel to  $t_2$ , this is done by applying a  $t_1$ -dependent first-order phase correction in the mixed  $(t_1, \omega_2)$  domain with

$$\mathfrak{s}(t'_1, t'_2) \leftrightarrow e^{i\omega_2 \kappa^{(t_2)} t_1} \mathfrak{s}(t_1, \omega_2), \quad (193)$$

and for a shear parallel to  $t_1$ , it is done by applying a  $t_2$ -dependent first-order phase correction in the mixed  $(\omega_1, t_2)$  domain with

$$\mathfrak{s}(t'_1, t'_2) \leftrightarrow e^{i\omega_1 \kappa^{(t_1)} t_2} \mathfrak{s}(\omega_1, t_2). \quad (194)$$

#### 5.4. Single shear and scale

Several 2D NMR experiments center on the refocusing of a single spatial or transition symmetry or the coincident refocusing of multiple symmetries. Though the implementation is experiment dependent, they are similar from a signal-processing standpoint. To connect with our discussion of symmetry pathways, we define the direction of the echo path with symmetry  $a$  in the original coordinate system with the line

$$a^{[1]}t_1 + a^{[2]}t_2 = 0, \quad (195)$$

and shear the echo signal parallel to the  $t_2$  coordinate using the shearing ratio

$$\kappa^{(t_2)} = \frac{a^{[1]}}{a^{[2]}}, \quad (196)$$

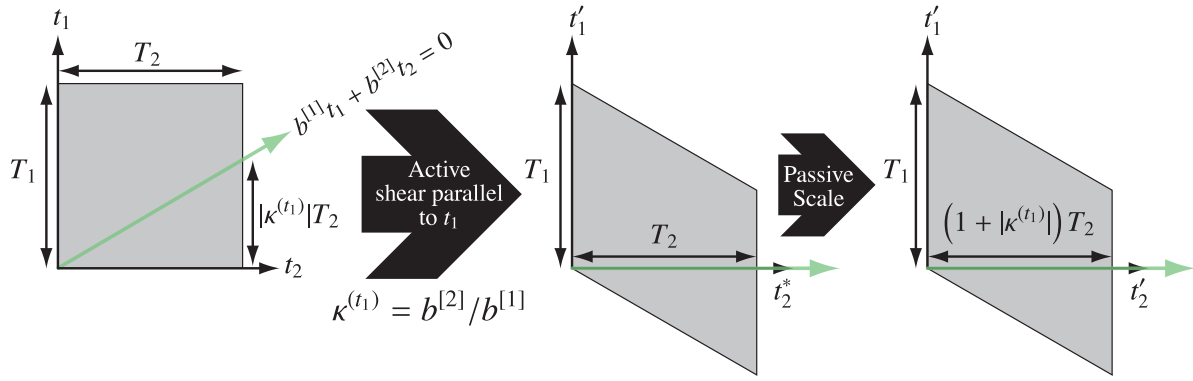


Figure 65: Illustration of a passive and active shear parallel to the  $t_1$  coordinate followed by a passive scaling of the  $t_2^*$  coordinate. The shaded area represents a region of the sampled signal.

to place the echo path entirely along the new coordinate  $t_1^*$ , as shown in Fig. 64. After the shear, the  $t_1^*$  coordinate is scaled to give a  $t_1'$  coordinate that reflects the dephasing and refocusing time of the echo path using the scaling factor

$$\zeta^{(t_1^*)} = 1 + |\kappa^{(t_2)}|. \quad (197)$$

The product of the shear and scale transformations gives

$$\mathcal{A}_{t_2} = \underbrace{\begin{bmatrix} \zeta^{(t_1^*)} & 0 \\ 0 & 1 \end{bmatrix}}_{S_{t_1^*}} \underbrace{\begin{bmatrix} 1 & 0 \\ \kappa^{(t_2)} & 1 \end{bmatrix}}_{\mathcal{K}_{t_2}} = \begin{bmatrix} \zeta^{(t_1^*)} & 0 \\ \kappa^{(t_2)} & 1 \end{bmatrix}. \quad (198)$$

Thus, the shearing and scaling transformations are completely determined by the value of  $\kappa^{(t_2)}$ , and we obtain

$$\begin{bmatrix} t_1' \\ t_2' \end{bmatrix} = \begin{bmatrix} 1 + |\kappa^{(t_2)}| & 0 \\ \kappa^{(t_2)} & 1 \end{bmatrix} \begin{bmatrix} t_1 \\ t_2 \end{bmatrix} = \begin{bmatrix} t_1 + |\kappa^{(t_2)}|t_1 \\ t_2 + \kappa^{(t_2)}t_1 \end{bmatrix}. \quad (199)$$

Note that the transformation becomes the identity matrix as  $\kappa^{(t_2)}$  goes to zero.

Although the transformation is more conveniently implemented in the time domain, the shear ratio for NMR experiments is often given for the 2D frequency domain signal. That is, for a shear parallel to  $t_2$ , the reported shear ratio is

$$\kappa^{(\omega_1)} = -\kappa^{(t_2)}. \quad (200)$$

Frequency components that do not refocus into an echo along the a symmetry line will phase modulate the signal along the  $t_1'$  dimension. In the transformed coordinate system, the signal phase modulation will be given by

$$\Phi(t_1', t_2') = [\Omega^{[1]}, \Omega^{[2]}] \begin{bmatrix} t_1' \\ t_2' \end{bmatrix} = [\Omega^{[1]}, \Omega^{[2]}] \mathcal{A}_{t_2}^{-1} \begin{bmatrix} t_1 \\ t_2 \end{bmatrix}. \quad (201)$$

Using

$$\mathcal{A}_{t_2}^{-1} = \begin{bmatrix} \frac{1}{1 + |\kappa^{(\omega_2)}|} & 0 \\ \frac{\kappa^{(\omega_2)}}{1 + |\kappa^{(\omega_2)}|} & 1 \end{bmatrix}, \quad (202)$$

one calculates

$$\begin{bmatrix} \Omega'^{[1]} \\ \Omega'^{[2]} \end{bmatrix} = [\Omega^{[1]}, \Omega^{[2]}] \mathcal{A}_{t_2}^{-1} = \begin{bmatrix} \Omega^{[1]} + \kappa^{(\omega_2)}\Omega^{[2]} \\ \Omega^{[2]} \end{bmatrix}, \quad (203)$$

showing that the effective frequency during  $t'_1$  is a weighted average of the frequencies during  $t_1$  and  $t_2$ , weighted by  $\varsigma^{(t_1^*)}$  and  $\varsigma^{(t_1^*)}\kappa^{(\omega_2)}$ , respectively.

Conversely, one can define the direction of an echo path with symmetry  $b$  in the original coordinate system with the line

$$b^{[1]}t_1 + b^{[2]}t_2 = 0, \quad (204)$$

and shear the echo signal parallel to the  $t_1$  coordinate with

$$\kappa^{(t_1)} = \frac{b^{[2]}}{b^{[1]}}, \quad (205)$$

to place the echo path entirely along the new coordinate  $t_2^*$ , as shown in Fig. 65. After the shear, the  $t_2^*$  coordinate is scaled to give a  $t'_2$  coordinate that reflects the dephasing and refocusing time of the echo path using the scaling factor

$$\varsigma^{(t_2^*)} = 1 + |\kappa^{(t_1)}|. \quad (206)$$

The product of the shear and scale transformations gives

$$\mathcal{A}_{t_1} = \underbrace{\begin{bmatrix} 1 & 0 \\ 0 & \varsigma^{(t_2^*)} \end{bmatrix}}_{S_{t_2^*}} \underbrace{\begin{bmatrix} 1 & \kappa^{(t_1)} \\ 0 & 1 \end{bmatrix}}_{\mathcal{K}_{t_1}} = \begin{bmatrix} 1 & \kappa^{(t_1)} \\ 0 & \varsigma^{(t_2^*)} \end{bmatrix}. \quad (207)$$

Thus, the shearing and scaling transformations are completely determined by the value of  $\kappa^{(t_1)}$ , and we obtain

$$\begin{bmatrix} t'_1 \\ t'_2 \end{bmatrix} = \begin{bmatrix} 1 & \kappa^{(t_1)} \\ 0 & 1 + |\kappa^{(t_1)}| \end{bmatrix} \begin{bmatrix} t_1 \\ t_2 \end{bmatrix} = \begin{bmatrix} t_1 + \kappa^{(t_1)}t_2 \\ t_2 + |\kappa^{(t_1)}|t_2 \end{bmatrix}. \quad (208)$$

Again, note that the transformation becomes the identity matrix as  $\kappa^{(t_1)}$  goes to zero. As before, for a shear parallel to  $t_1$ , the shear ratio is often reported as

$$\kappa^{(\omega_2)} = -\kappa^{(t_1)}. \quad (209)$$

Additionally, using

$$\mathcal{A}_{t_1}^{-1} = \begin{bmatrix} 1 & \frac{\kappa^{(\omega_2)}}{1 + |\kappa^{(\omega_2)}|} \\ 0 & \frac{1}{1 + |\kappa^{(\omega_2)}|} \end{bmatrix}, \quad (210)$$

one calculates the frequencies in the transformed coordinate system as

$$\begin{bmatrix} \Omega'^{[1]} \\ \Omega'^{[2]} \end{bmatrix} = [\Omega^{[1]}, \Omega^{[2]}] \mathcal{A}_{t_1}^{-1} = \begin{bmatrix} \Omega^{[1]} \\ \frac{\kappa^{(\omega_2)}\Omega^{[1]} + \Omega^{[2]}}{1 + |\kappa^{(\omega_2)}|} \end{bmatrix}, \quad (211)$$

showing that the effective frequency during  $t'_2$  is a weighted average of the frequencies during  $t_1$  and  $t_2$ , weighted by  $\varsigma^{(t_2^*)}\kappa^{(\omega_1)}$  and  $\varsigma^{(t_2^*)}$ , respectively.

When actively shearing a discretely sampled 2D signal, it is best to exploit the Fourier shift theorem to avoid the need for interpolating data points onto an equally spaced Cartesian grid. A consequence of this approach is that there will be a wrapping of signal, as illustrated in Fig. 66.

A signal processing flow chart for applying a shear and scaling to a 2D NMR signal is given in Fig. 67. After Fourier transform with respect to  $t_2$ , the  $t_1$  dimension is sheared via a  $t_1$  dependent first-order phase correction, after which the  $t_1$  dimension is scaled. A second Fourier transform with respect to  $t'_1$  yields the 2D spectrum.

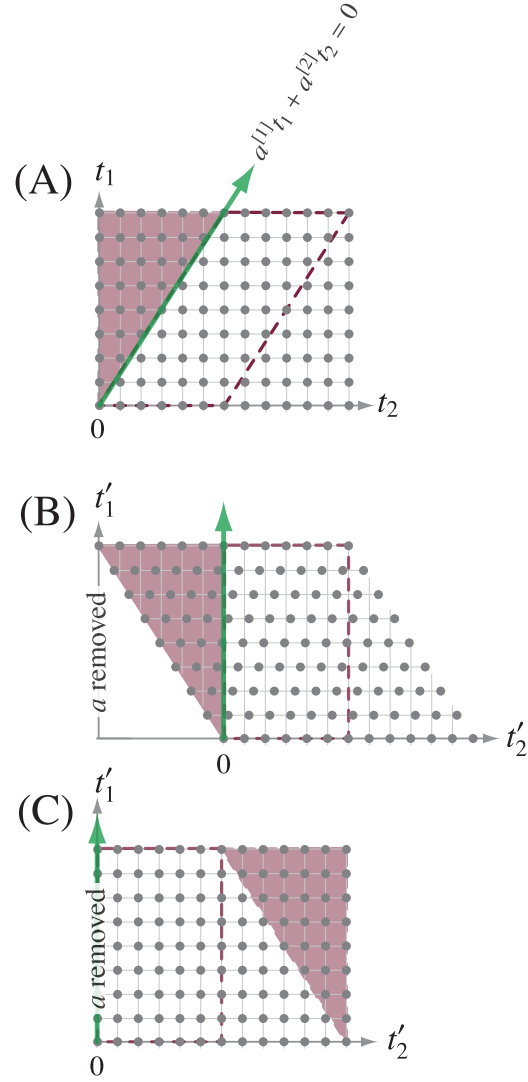


Figure 66: Illustration of shearing a discretely sampled 2D time domain signal. (A) Signal before the shear transformation. (B) Signal after active and direct shear transformation. Notice that sampling on a Cartesian grid will require an interpolation of points. (C) Signal after active shear transformation using the Fourier shift theorem. While sampled data remain on a Cartesian grid, some signal data (inside the shaded region) will get folded from low  $t_2$  values into higher  $t'_2$  values.

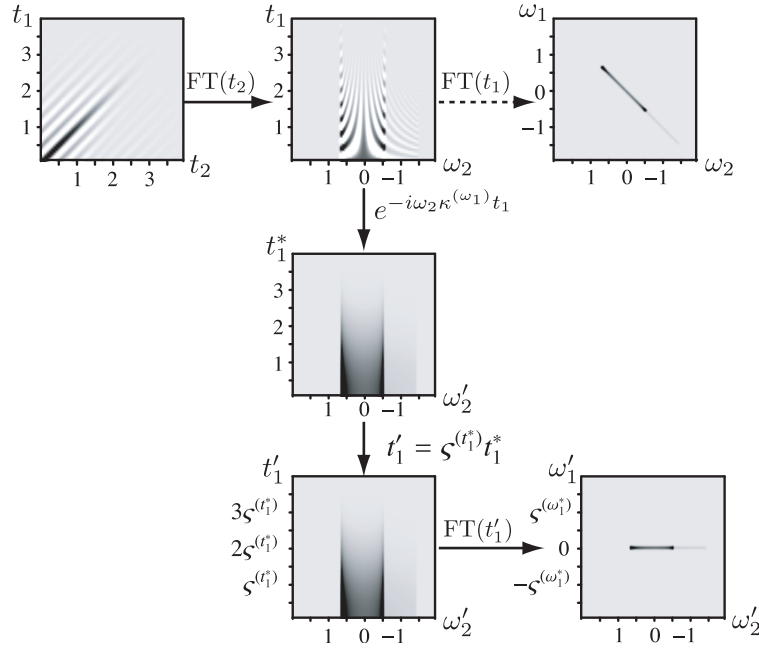


Figure 67: Flow chart for processing 2D NMR signal that refocuses a single or multiple symmetries along a single echo path. After Fourier transform with respect to  $t_2$ , the signal is sheared parallel to the  $t_2$  coordinate with dependent first-order phase correction using the shear ratio  $\kappa^{(\omega_1)}$ , after which the  $t_1$  dimension is scaled by  $\varsigma^{(t_1)*}$ . A second Fourier transform with respect to  $t'_1$  yields the affine transformed 2D spectrum.

### 5.5. Double shear and scale

When multiple symmetries are present, it is possible to refocus components with different symmetries along different echo paths. Using appropriate affine transformations, these multiple echo paths can be transformed to lie on orthogonal axes. In an experiment with two different echo paths, we define the direction of each echo path in the original coordinate system with the lines

$$a^{[1]}t_1 + a^{[2]}t_2 = 0, \quad (212)$$

and

$$b^{[1]}t_1 + b^{[2]}t_2 = 0, \quad (213)$$

and shear the a symmetry echo signal parallel to the  $t_2$  coordinate with the  $\mathcal{A}_{t_2}$  transformation of Eq. (198) using the shearing ratio in Eq. (196) and the  $t_1^*$  scaling factor in Eq. (197), to place the a symmetry echo path entirely along the new coordinate  $t'_1$ . After the  $\mathcal{A}_{t_2}$  transformation the b symmetry echo will lie along the path

$$b'^{[1]}t'_1 + b'^{[2]}t'_2 = 0, \quad (214)$$

in the  $(t'_1, t'_2)$  coordinate system. Using  $\mathcal{A}_{t_2}^{-1}$  one can calculate the new coefficients for the b symmetry echo path obtaining

$$\begin{bmatrix} b'^{[1]} \\ b'^{[2]} \end{bmatrix} = [b^{[1]}, b^{[2]}] \mathcal{A}_{t_2}^{-1} = \begin{bmatrix} \frac{b^{[1]} + \kappa^{(\omega_1)} b^{[2]}}{1 + |\kappa^{(\omega_1)}|} \\ b^{[2]} \end{bmatrix}. \quad (215)$$

Using the new coefficients, one can shear the echo signal parallel to the  $t'_1$  coordinate with the  $\mathcal{A}_{t'_1}$  transformation of Eq. (207) using the shearing ratio

$$\kappa^{(t'_1)} = \frac{b'^{[2]}}{b'^{[1]}} = \frac{b^{[2]}}{\left( \frac{b^{[1]} + \kappa^{(\omega_1)} b^{[2]}}{1 + |\kappa^{(\omega_1)}|} \right)}, \quad (216)$$

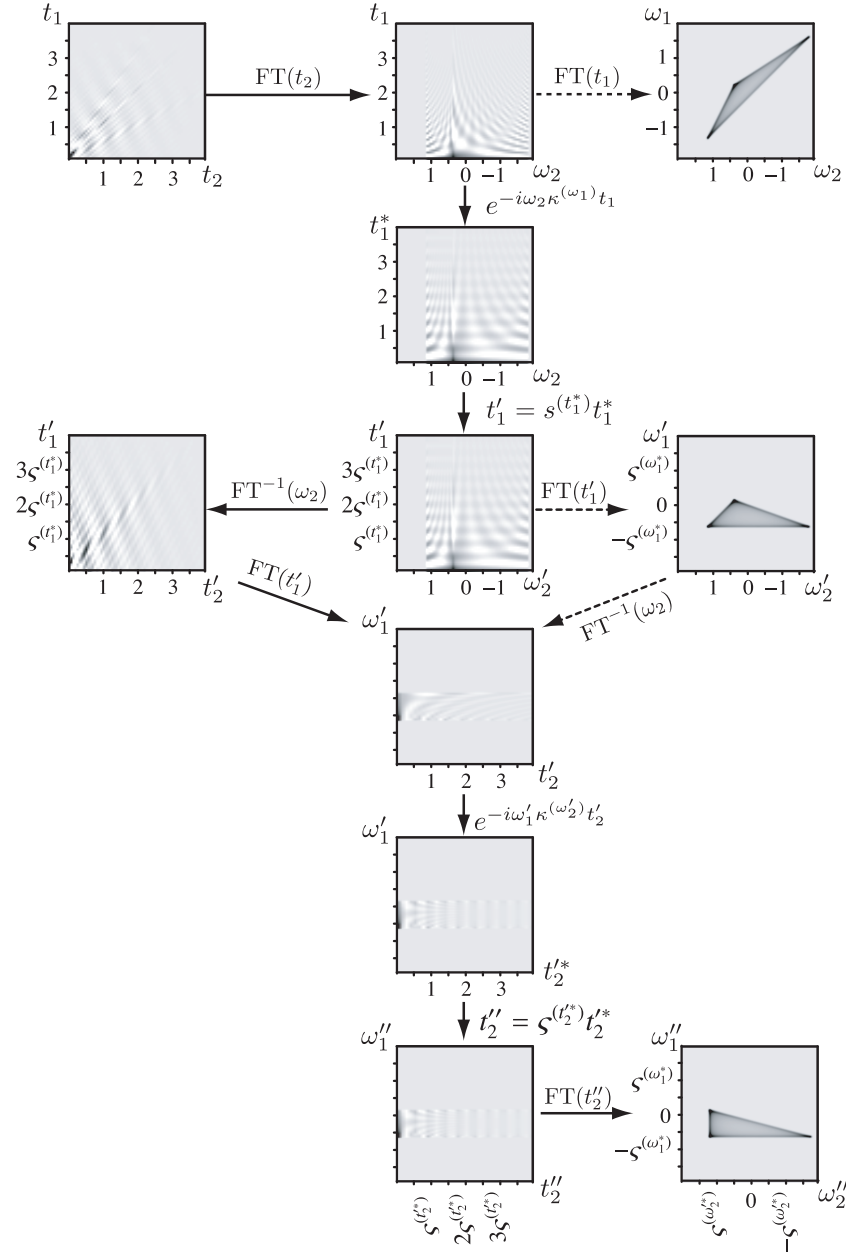


Figure 68: Flow chart for processing 2D NMR signal that refocuses multiple symmetries along two different echo paths. After Fourier transform with respect to  $t_2$ , the signal is sheared parallel to the  $t_2$  coordinate with dependent first-order phase correction using the shear ratio  $\kappa^{(\omega_1)}$ , after which the  $t_1$  dimension is scaled by  $s^{(t_1^*)}$ . Then an inverse Fourier transform with respect to  $\omega_2$  is performed, followed by a Fourier transform with respect to  $t_1'$ . The signal is then sheared parallel to the  $t_1'$  coordinate with dependent first-order phase correction using the shear ratio  $\kappa^{(\omega_2')}$ , after which the  $t_2'$  dimension is scaled by  $s^{(t_2^*)}$ . Finally, a Fourier transform with respect to  $t_2''$  yields the affine transformed 2D spectrum.

and the  $t_1'^*$  scaling factor in Eq. (206) to place the b symmetry echo path entirely along the new coordinate  $t_2''$ .

As suggested by the flowchart of the data processing protocols in Fig. 68, the data processing begins analogous to the single shear and scale approach, where the  $t_1$  dimension is sheared and scaled in the mixed  $(t_1, \omega_2)$  domain. The data is then inverse Fourier transformed in the  $\omega_2$  domain, and then Fourier transformed in the  $t_1'$  domain. Subsequently, a similar set of shearing and scaling transformations are applied along the  $t_2$  dimension prior to the final Fourier transform.

### 5.6. Spinning sidebands

One consequence of the shearing and scaling transformations in NMR spectroscopy is that the spinning sidebands can appear at non-integer multiples of the spinning speed in the transformed coordinate system[52]. A schematic example of the behavior of spinning sidebands after a shearing transformation is shown in Fig. 69 for the two cases  $\kappa^{(\omega_1')} = 1$  and  $\kappa^{(\omega_1')} = 7/9$ . The frequency axes in Fig. 69A are in units of  $\omega_R$ , the actual spinning speed. The example in Fig. 69B is the common situation in 2D echo spectroscopy, where the dephasing and refocusing times are equal (e.g., DAS ( $\kappa^{(\omega_1')} = 1$ ), 2D  $J$  spectroscopy, etc.). In this example, even though the spectrum is sheared, the sidebands remain aligned such that a projection onto the  $\omega_1'$  axis contains only sidebands at integer multiples of  $\omega_R/2$ . In contrast, the example shown in Fig. 69C corresponds to a 2D echo experiment with unequal dephasing and refocusing times, in this case, the 3Q-MAS of a spin  $I = 3/2$  nucleus where  $\kappa^{(\omega_1')} = 7/9$  and  $\varsigma^{(t_1^*)} = 16/9$ . In this situation, the spinning sidebands are not aligned in  $\omega_1'$ , and consequently, a projection onto  $\omega_1'$  (i.e., the isotropic axis of 3Q-MAS) will contain spinning sidebands that are separated by multiples of and also sum and difference frequencies of  $\varsigma^{(\omega_1^*)}\omega_R = 0.56\omega_R$  and  $\varsigma^{(\omega_1^*)}\kappa^{(\omega_1')}\omega_R = 0.44\omega_R$ .

## 6. Spatial averaging symmetries

During the development of the first coherent averaging schemes for removing second- and fourth-rank spatial anisotropies, Pines and coworkers[3, 60] asked the general question: “What is the minimum number of orientations and perhaps the simplest trajectory needed to average away the anisotropy of given set of tensor ranks?” Here we review their answer to this question. We start with the generic  $A_{L,0}$  orientation dependence contained in our solid-state NMR Hamiltonians expanded in the form

$$A_{L,0} = \sum_k A'_{L,k} \mathcal{D}_{k,0}^{(L)}(\Theta_{SFC}), \quad (217)$$

where  $\Theta_{SFC}$  is the orientation of the magnetic field in a sample fixed coordinate (SFC) frame (e.g., a goniometer frame), and  $\mathcal{D}_{k,0}^{(L)}(\Theta)$  is a matrix element of the Wigner rotation matrix,  $\mathcal{D}(\Theta)$ . If  $\Theta_{SFC}$  is varied according to the  $g$  symmetry operations  $G_a$  of the group  $\mathcal{G}$ , then we obtain an average

$$\overline{A_{L,0}}^{\mathcal{G}} = \sum_k A'_{L,k} \overline{\mathcal{D}_{k,0}^{(L)}}^{\mathcal{G}}, \quad (218)$$

where

$$\overline{\mathcal{D}^{(L)}}^{\mathcal{G}} = \frac{1}{g} \sum_{a=1}^g \mathcal{D}^{(L)}(G_a). \quad (219)$$

For our purposes, we consider the proper point subgroups of  $SO(3)$ , which contain only the proper rotation operations  $C_n^m$ . The matrix representation of the operation  $G_a$  for a given rank  $L$  can be reduced under the point group  $\mathcal{G}$  according to

$$\mathcal{D}^{(L)}(G_a) = \sum_{\alpha}^{\bullet} m_{\alpha,L} \mathbf{\Gamma}^{(\alpha)}(G_a), \quad (220)$$

where  $\alpha$  runs only over the inequivalent irreducible representations and the integer  $m_{\alpha,L}$  gives the number of times that the irreducible representation  $\mathbf{\Gamma}^{(\alpha)}(G_a)$  occurs in the reduction of the matrix  $\mathcal{D}^{(L)}(G_a)$ . The dot over the



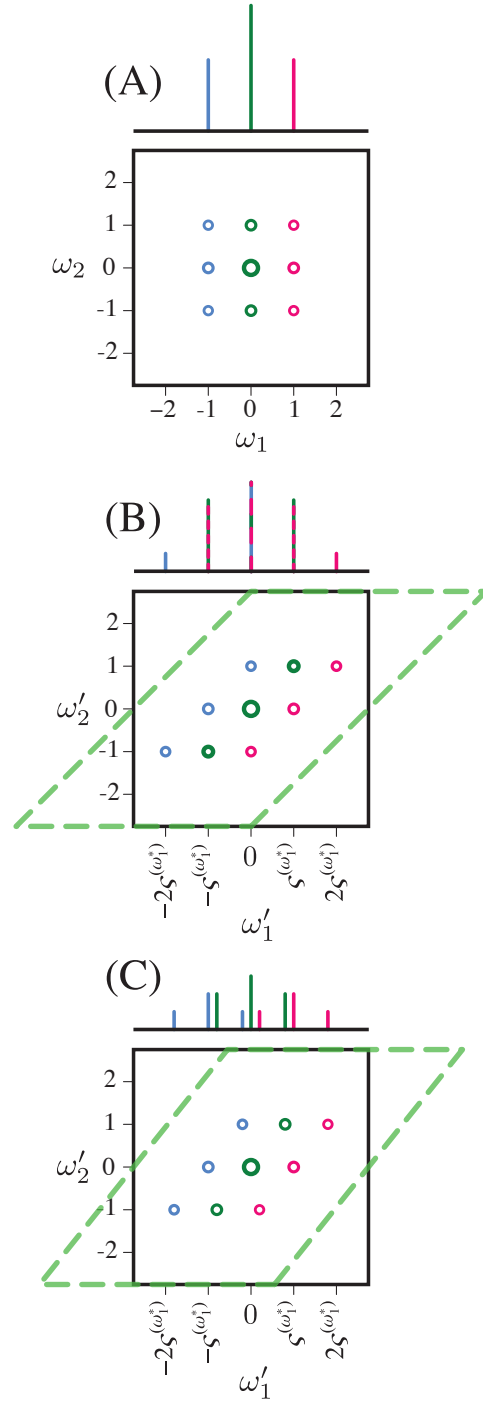


Figure 69: Schematic examples illustrating the effects of the affine transformation on a single resonance flanked by spinning sidebands in a 2D spectrum. (A) Before any affine transformation is applied, the spinning sidebands appear at integer multiples of the spinning frequency away from the center band in the 2D spectrum. (B) After the affine transformation is applied to the 2D spectrum in (A) by employing a shear parallel to  $t_2$  with a shear ratio  $\kappa^{(\omega_1')} = 1$  and a scaling of  $t_1$  by  $\zeta^{(t_1^*)} = 2$ . In this case, the spinning sidebands in the 2D spectrum are aligned with respect to  $\omega_1'$  so that a projection onto the  $\omega_1'$  axis contains only spinning sidebands separated by integer multiples of  $\omega_R/2$ . Here, the dashed lines represent a passive affine transformation back to the original coordinate system in (A). (C) After affine transformation applied to 2D spectrum in (A) by employing a shear parallel to  $t_2$  with a shear ratio  $\kappa^{(\omega_1')} = 7/9$  and a scaling of  $t_1$  by  $\zeta^{(t_1^*)} = 16/9$ . In this case, the spinning sidebands in the 2D spectrum are not aligned with respect to  $\omega_1'$  so that a projection onto the  $\omega_1'$  axis contains spinning sidebands that are separated by multiples of and also sum and difference frequencies of  $\zeta^{(\omega_1^*)}\omega_R = 0.56\omega_R$  and  $\zeta^{(\omega_1^*)}\kappa^{(\omega_1')}\omega_R = 0.44\omega_R$ . (Adapted from P. J. Grandinetti, Y. K. Lee, J. H. Baltisberger, B. Q. Sun, and A. Pines, *J. Magn. Reson. A*, 1993, **102**, 71). Here again, the dashed lines represent a passive affine transformation back to the original coordinate system in (A).

summation sign reminds us that this is not the usual matrix addition but signifies that  $\mathcal{D}^{(L)}(G_a)$  is composed of the square matrices  $\Gamma^{(\alpha)}(G_a)$  arranged down the diagonal[86]. Substituting Eq. (220) into Eq. (219) we obtain

$$\overline{\mathcal{D}^{(L)}}^{\mathcal{G}} = \frac{1}{g} \sum_{\alpha}^{\bullet} m_{\alpha,L} \sum_{a=1}^g \Gamma^{(\alpha)}(G_a). \quad (221)$$

From the general orthogonality properties of irreducible representations[87] we know that if  $\alpha = A_1$ , i.e., the totally symmetric representation, then we have

$$\sum_{a=1}^g \Gamma^{(A_1)}(G_a) \Gamma^{(\beta)}(G_a) = \sum_{a=1}^g \Gamma^{(\beta)}(G_a) = 0, \quad (222)$$

unless  $\beta = A_1$ . Thus we conclude that the average  $\overline{\mathcal{D}^{(L)}}^{\mathcal{G}}$  will be different from zero only if the expansion in Eq. (220) contains the  $A_1$  representation (i.e.,  $m_{A_1,L} \neq 0$ ).

The multiplicity  $m_{\alpha}$  of any irreducible representation  $\alpha$  can be evaluated from the general expression for traces

$$m_{\alpha} = \frac{1}{g} \sum_{a=1}^g \chi^{(\alpha)}(G_a) \chi^{(\alpha)}(G_a), \quad (223)$$

and the character of a rotation  $C_n^m$  is calculated from

$$\chi_L(C_n^m) = \frac{\sin(L + \frac{1}{2})\zeta_G}{\sin \frac{1}{2}\zeta_G}, \quad (224)$$

where  $\zeta_G$  is an angle of rotation about the symmetry axis whose orientation is entirely arbitrary. Using Eq. (224), the character tables for the point groups, and Eq. (223), one can determine which tensor ranks of  $A_{L,0}$  will average to zero under each point group. These calculations are summarized in Fig. 70 for  $L = 1-10$  under the groups  $\mathcal{G} = D_4, T, O, I$ , and  $SO(3)$ . From Fig. 70, we find that those reorientation trajectories passing through orientations related by octahedral symmetry will average away tensors of rank  $L = 1, 2, 3, 5$ , and  $7$ . While neither octahedral nor tetrahedral symmetry is capable of removing both the second- and fourth-rank anisotropies of our second-order electric quadrupole Hamiltonian, we see in Fig. 70 for tensors up to rank  $L = 10$  that icosahedral symmetry succeeds in removing not only tensors of rank  $L = 2$  and  $4$ , but also ranks  $L = 1, 3, 5, 7, 8$ , and  $9$ .

In Fig. 71a, we see that MAS, which was engineered to average away second-rank anisotropies, contains three octahedral symmetry-related orientations in its trajectory. Maciel and coworkers[88, 72] have demonstrated that the averaging of the continuous MAS trajectory can also be accomplished using a completely discontinuous trajectory called Magic-Angle Hopping (MAH), which hops between the octahedron vertices as shown in Fig. 71a. This technique also forms the basis of the Magic-Angle Turning (MAT) experiments of Gan[51] and Grant and coworkers[53]. Shown in Fig. 71b and 71c are two DAS solutions,  $(0^\circ, 63.43^\circ, k = 5)$  and  $(37.38^\circ, 79.19^\circ, k = 1)$ , that describe partially continuous trajectories that pass through the vertices related by icosahedral symmetry. In analogy with MAH, a purely discrete trajectory hopping amongst the icosahedron vertices is called Dynamic-Angle Hopping (DAH) and forms the basis of the DAH-180 experiment described by Gann et al.[89].

Although a point subgroup of  $SO(3)$  defining the minimum number of orientations capable of averaging away the anisotropy of a given set of tensor ranks may provide a convenient starting point for designing a trajectory, it is certainly not necessary for a trajectory to contain all the symmetry-related orientations of that point subgroup in order to accomplish the same averaging. For example, there exists a continuous set of DAS trajectories that do not contain orientations related by icosahedral symmetry, yet these trajectories average away second- and fourth-rank anisotropies. Likewise, the DOR trajectory does not contain orientations related by icosahedral symmetry.

In the case of DOR, its trajectory can be constructed from symmetry operations obtained using an iterative approach[3]. In this approach, one starts by noting that the anisotropy described by a tensor of rank  $L$  can be averaged away by reorienting the sample so that the field is directed at  $N = L + 1$  or more equally spaced directions to form a cone, that is,

$$\Theta_{SFC}^{(a)} = (\alpha_0 + \frac{2\pi}{N}a, \beta, \gamma), \quad (225)$$

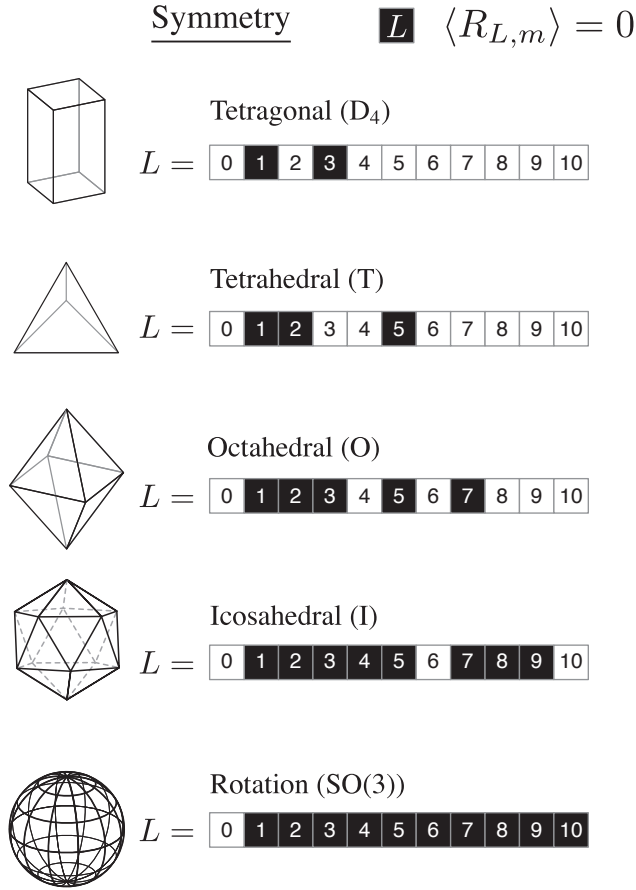


Figure 70: Averaging of spherical harmonics up to rank  $L = 10$  under selected proper point groups and  $SO(3)$ . (Adapted from A. Samoson, B. Q. Sun, and A. Pines, in *Pulsed Magnetic Resonance: NMR, ESR, and Optics - A recognition of E. L. Hahn*, Clarendon Press, Oxford, 1992.)

so that

$$\overline{\mathcal{D}_{k,0}^{(L)}} = \frac{1}{N} \sum_{a=1}^N \mathcal{D}_{k,0}^{(L)}(\Theta_{SFC}^{(a)}) = P_L(\cos \beta), \quad (226)$$

with  $\overline{\mathcal{D}_{k,0}^{(L)}}$  made zero by simply choosing one of the corresponding roots of  $P_L(\cos \beta)$ , given in Table ??, to obtain the cone's apex angle  $2\beta$ . For example, a second-rank tensor is averaged to zero by reorienting the sample so that the field is directed along three equally spaced directions forming a cone with an apex angle of  $2\beta^{(2)} = 2 \times 54.74^\circ$ , as shown in Fig. 72a. An iterative approach to selectively average away interactions of two different ranks,  $L_1$  and  $L_2$ , where  $L_1 < L_2$ , is developed by employing an additional splitting of  $N_2 = L_2 + 1$  directions given by

$$\Theta_{SFC}^{(a_2)} = (\alpha_{0,2} + \frac{2\pi}{N_2} a_2, \beta^{(L_2)}, \gamma_2), \quad (227)$$

about each of the  $N_1 = L_1 + 1$  orientations given by

$$\Theta^{(a_1)} = (\alpha_{0,1} + \frac{2\pi}{N_1} a_1, \beta^{(L_1)}, \gamma_1). \quad (228)$$

In the case of second-order electric quadrupole broadenings where  $L_1 = 2$  and  $L_2 = 4$ , we obtain the splitting shown in Fig. 72B with apex angles  $2\beta^{(2)} = 2 \times 54.74^\circ$  and  $2\beta^{(4)} = 2 \times 30.56^\circ$ . Thus one can visualize DOR as simply a continuous trajectory that includes these symmetry-related orientations.

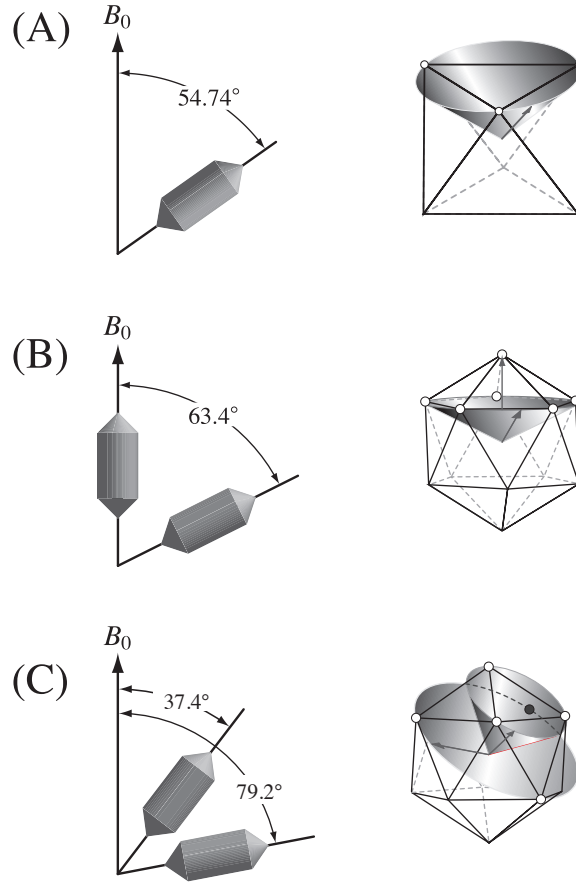


Figure 71: (A) Magic-Angle Spinning passes through three vertices of an octahedron with continuous rotation on a cone with an apex angle of  $54.74^\circ$ . Icosahedral symmetry can be implemented with just two continuous trajectories in cases where tensors of rank 2 and 4 are to be eliminated. Time spent along one particular trajectory is proportional to the number of vertices. DAS solutions that pass through the vertices of the icosahedron are the continuous rotation on two cones with apex angles of (B)  $\theta_1 = 0^\circ$  and  $\theta_2 = 63.43^\circ$ , where the ratio of times spinning at the two angles is 1:5, and (C)  $\theta_1 = 37.38^\circ$  and  $\theta_2 = 79.19^\circ$ , where the ratio of times spinning at the two angles is 1:1. (Adapted from B. Q. Sun, J. H. Baltisberger, Y. Wu, A. Samoson, and A. Pines, *Solid State NMR*, 1992, **1**, 267, and from A. Samoson, B. Q. Sun, and A. Pines, in *Pulsed Magnetic Resonance: NMR, ESR, and Optics - A recognition of E. L. Hahn*, Clarendon Press, Oxford, 1992.)

## 7. Summary

In this review, we have outlined a simple and consistent framework for designing NMR experiments, particularly for solid-state NMR. This framework extends the concept of coherence transfer pathways, starting with two main pathways called the spatial pathway and the spin transition pathway, which completely describe an NMR experiment. Given a pulse sequence and spin system's spatial and spin transition pathways, a series of related symmetry pathways can be derived, which show, at a glance, when and which frequency components for the system will refocus into echoes. Although these frequency components are classified according to familiar symmetries under the orthogonal rotation subgroup (i.e.,  $s$ ,  $p$ ,  $d$ ,  $f$ , ...), the power of this framework is in providing insight behind many experiments even when internal couplings are much larger than the rf coupling, and one can no longer rely on the symmetries under the orthogonal rotation subgroup as a guide to designing new experiments. Additionally, this framework provides a more physical picture behind the use of affine transformations when processing the multidimensional signals obtained in many solid-state NMR experiments and also serves as a helpful guide when designing multi-dimensional NMR experiments with pure absorption mode lineshapes.

We believe this framework not only provides a powerful tool for designing new NMR experiments but can be a useful pedagogical tool for NMR, allowing students to quickly grasp several modern solid-state NMR experiments

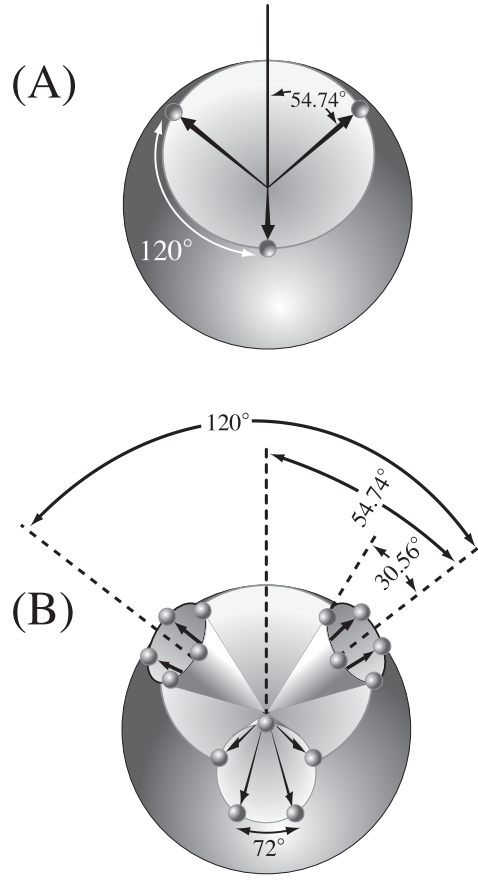


Figure 72: (A) The anisotropy described by a tensor of rank  $L$  can be averaged away by reorienting the sample so that the field vector is directed at  $N = L + 1$  directions with a spacing of  $\frac{2\pi}{L+1}$  to form a cone with apex angle  $2\beta^{(L)}$ . For  $L = 2$ , this is accomplished with three directions spaced  $120^\circ$  apart, forming a cone with an apex angle of  $2 \times 54.74^\circ$ . (B) Anisotropies of rank  $L_1$  and  $L_2$ , where  $L_1 < L_2$ , can be eliminated with an additional or secondary splitting of field directions. The symmetry axes of the new cones retain the original symmetry of the primary splitting shown in (A). For  $L_1 = 2$  and  $L_2 = 4$ , the averaging is accomplished with a secondary splitting of five directions spaced  $72^\circ$  apart, forming a cone with an apex angle of  $2 \times 30.56^\circ$ . (Adapted from A. Samoson, B. Q. Sun, and A. Pines, in *Pulsed Magnetic Resonance: NMR, ESR, and Optics - A recognition of E. L. Hahn*, Clarendon Press, Oxford, 1992.)

without the need to enter into a full density operator description of each experiment.

## Acknowledgments

This material is based upon work supported by the National Science Foundation under Grant No. NSF CHE-1012175.

## A. Frequency component derivations

### A.1. Rotating tilted frame

To begin our treatment, we define the laboratory frame by orienting the direction of the  $z$  axis along the static external magnetic field. We also define the  $x$ - $z$  plane to contain the long axis of the transmitter (and receiver) coil. In the absence of excitation, the spin system evolves under the stationary state Hamiltonian operator,  $\hat{\mathcal{H}}_s$ , whose representation,  $\hat{D}_s$ , in its diagonal frame, is related to the laboratory frame representation by

$$\hat{D}_s = \hat{V}^\dagger \hat{\mathcal{H}}_s \hat{V}, \quad (\text{A.1})$$

where  $\hat{V}$  is a unitary transformation operator between the diagonal and laboratory frames. The overall Hamiltonian,  $\hat{\mathcal{H}}_s$ , for the system can be separated into various contributions arising from magnetic dipolar couplings among nuclear spins as well as couplings of the system with the surroundings. Assuming that the dominant contribution is the Zeeman coupling to the external magnetic field,  $B_0$ , we write

$$\hat{\mathcal{H}}_s = \hat{\mathcal{H}}^{(0)} + \hat{\mathcal{H}}_s^{(1)}, \quad (\text{A.2})$$

where  $\hat{\mathcal{H}}^{(0)}$  is the Zeeman Hamiltonian and  $\hat{\mathcal{H}}_s^{(1)}$  contains all the contributions to the stationary state Hamiltonian arising from spin couplings internal to the sample,

$$\hat{\mathcal{H}}_s^{(1)} = \sum_{\lambda} \hat{\mathcal{H}}_{\lambda}. \quad (\text{A.3})$$

With the assumption of a dominant Zeeman interaction, our treatment can be further simplified by moving into the “rotating tilted” frame[90], *a frame rotating about the  $z$  axis of the diagonal frame*, and defined by the transformation

$$\hat{W}(t) = \hat{V} e^{-i(\omega_{rot}t + \phi_{rot})\hat{I}_z^{\circ}}, \quad (\text{A.4})$$

where  $\omega_{rot}$  is the rotating frame frequency and  $\phi_{rot}$  is the initial phase of the rotating frame[91, 23]. The orientation of the rotating tilted frame with respect to the laboratory frame will depend on crystallite orientation. Because this review considers nuclear spin interactions requiring higher-order corrections to the Zeeman eigenstates, all operators defined in the diagonal rotating tilted frame will be indicated with a circle superscript. We also assume that  $\omega_{rot}$  is chosen so that  $|\omega_0 - \omega_{rot}| \ll |\omega_0|$ . The propagator in this frame is given by

$$\hat{U}^{\circ}(t, 0) = \hat{T} \exp \left\{ - (i/\hbar) \int_0^t \hat{D}_s^{\circ}(s) ds \right\}, \quad (\text{A.5})$$

where  $\hat{T}$  is the time ordering operator, and  $\hat{D}_s^{\circ}(t)$  is the Hamiltonian in the rotating tilted frame, given by

$$\hat{D}_s^{\circ}(t) = \hat{W}^\dagger(t) \hat{\mathcal{H}}_s \hat{W}(t) + i\hbar \dot{\hat{W}}^\dagger(t) \hat{W}(t), \quad (\text{A.6})$$

where  $\hat{W}^\dagger(t) \hat{\mathcal{H}}_s \hat{W}(t)$  is the diagonalized laboratory frame stationary state Hamiltonian and  $i\hbar \dot{\hat{W}}^\dagger(t) \hat{W}(t)$  is the familiar quantum analogue of the inertial forces generated classically by transforming to a moving frame. This propagator can be related back to the lab frame according to

$$\hat{U}(t, 0) = \hat{W}(t) \hat{U}^{\circ}(t, 0) \hat{W}^\dagger(0). \quad (\text{A.7})$$

The density operator in the rotating tilted frame,  $\hat{\rho}^{\circ}(t)$ , is related to the laboratory frame density operator by

$$\hat{\rho}^{\circ}(t) = \hat{W}(t)^\dagger \hat{\rho}(t) \hat{W}(t). \quad (\text{A.8})$$

We follow the NMR experiment (i.e., define our coherences) in the rotating tilted frame[92]. Additionally, we take the equilibrium density operator in the high-temperature approximation to be proportional to the stationary state Hamiltonian, that is,

$$\hat{\rho}_{eq}^{\circ} \propto \hat{D}_s. \quad (\text{A.9})$$

We will calculate the total frequency of an  $|i\rangle \rightarrow |j\rangle$  transition in the rotating tilted frame as

$$\Omega(i, j) = \langle j | \hat{D}_s^{\circ} | j \rangle - \langle i | \hat{D}_s^{\circ} | i \rangle. \quad (\text{A.10})$$

### A.2. Irreducible spherical tensors

The nuclear spin interactions with significant contributions to  $\hat{\mathcal{H}}_s^{(1)}$  (i.e., quadrupolar, nuclear shielding,  $J$ , and dipolar couplings) have the general form

$$\hat{\mathcal{H}}_\lambda = \Lambda^{\{\lambda\}} \hat{\mathbf{U}} \cdot [\mathbf{R}^{\{\lambda\}}] \cdot \mathbf{V} = \Lambda^{\{\lambda\}} \begin{pmatrix} \hat{U}_x & \hat{U}_y & \hat{U}_z \end{pmatrix} \begin{pmatrix} R_{xx}^{\{\lambda\}} & R_{xy}^{\{\lambda\}} & R_{xz}^{\{\lambda\}} \\ R_{yx}^{\{\lambda\}} & R_{yy}^{\{\lambda\}} & R_{yz}^{\{\lambda\}} \\ R_{zx}^{\{\lambda\}} & R_{zy}^{\{\lambda\}} & R_{zz}^{\{\lambda\}} \end{pmatrix} \begin{pmatrix} V_x \\ V_y \\ V_z \end{pmatrix}. \quad (\text{A.11})$$

The vector  $\hat{\mathbf{U}}$  is a nuclear spin vector operator, whereas the vector  $\mathbf{V}$  can be the same nuclear spin vector operator (quadrupolar interaction), another nuclear spin vector operator (dipolar and  $J$  coupling), or the external magnetic field vector (Zeeman and nuclear shielding interactions). The  $R_{ik}^{\{\lambda\}}$  ( $i, k = x, y, z$ ) are generically given by

$$R_{ik}^{\{\lambda\}} = \frac{1}{\Lambda^{\{\lambda\}}} \frac{\partial^2 E^{\{\lambda\}}}{\partial U_i \partial V_k}, \quad (\text{A.12})$$

where  $E^{\{\lambda\}}$  is the energy of the nuclear spin's  $\lambda$  interaction.

This Hamiltonian can also be written

$$\hat{\mathcal{H}}_\lambda = \Lambda^{\{\lambda\}} \sum_{ik=xyz} R_{ik}^{\{\lambda\}} T_{ik}(\hat{\mathbf{U}}, \mathbf{V}), \quad (\text{A.13})$$

where  $T_{ik}^{\{\lambda\}}$  are Cartesian tensor elements constructed from the two vectors,  $\hat{\mathbf{U}}$  and  $\mathbf{V}$ :

$$\hat{T}_{ik}(\mathbf{U}, \mathbf{V}) = \hat{U}_i V_k. \quad (\text{A.14})$$

A real second-rank Cartesian tensor  $X_{ik}^{\{\lambda\}}$  can be decomposed into irreducible representations with respect to the full three-dimensional rotation group O3 according to

$$X_{ik} = E\delta_{ik} + A_{ik} + S_{ik}, \quad (\text{A.15})$$

where

$$E = \frac{1}{3} \text{Tr}\{\mathbf{X}\}, \quad (\text{A.16})$$

$$A_{ik} = \frac{1}{2} (X_{ik} - X_{ki}), \quad (\text{A.17})$$

$$S_{ik} = \frac{1}{2} (X_{ik} + X_{ki}) - \frac{1}{3} \text{Tr}\{\mathbf{X}\} \delta_{ik}. \quad (\text{A.18})$$

Here  $E$  is invariant under rotations of the system,  $A_{ik}$  is the traceless anti-symmetric part and is equivalent to an axial (or *pseudo*-) vector and  $S_{ik}$  is the traceless symmetric part of the tensor. Unlike a polar (or *true*) vector, the components of an axial vector do not change sign under an inversion of the coordinate system.

An irreducible pseudotensor of rank one,  $\zeta^{(a)}$ , can be formed from the antisymmetric components, and the principal axis system of this pseudotensor is defined as the coordinate system where

$$\lambda_x^{(a)} = \lambda_y^{(a)} = 0, \quad \lambda_z^{(a)} = \zeta^{(a)} = \sqrt{A_{yz}^2 + A_{zx}^2 + A_{xy}^2}, \quad (\text{A.19})$$

with  $\zeta^{(a)}$  as the antisymmetric first-rank tensor anisotropy.

The principal axis system of the second-rank symmetric tensor,  $\mathbf{S}$ , is defined as the coordinate system where  $\mathbf{S}$  is diagonal with principal components,  $\lambda_{zz}^{(s)}$ ,  $\lambda_{yy}^{(s)}$ , and  $\lambda_{xx}^{(s)}$  ordered, according to the Haeberlen convention[93], such that

$$|\lambda_{zz}^{(s)}| > |\lambda_{xx}^{(s)}| > |\lambda_{yy}^{(s)}|, \quad (\text{A.20})$$

and since  $\mathbf{S}$  is traceless we have

$$\lambda_{zz}^{(s)} + \lambda_{yy}^{(s)} + \lambda_{xx}^{(s)} = 0. \quad (\text{A.21})$$

Additionally, we define the second-rank symmetric tensor anisotropy,  $\zeta$ , and asymmetry parameter,  $\eta$ , according to

$$\zeta = \lambda_{zz}^{(s)}, \quad \text{and} \quad \eta = \frac{\lambda_{yy}^{(s)} - \lambda_{xx}^{(s)}}{\zeta}. \quad (\text{A.22})$$

The second-rank Cartesian tensor,  $X_{ik}^{\{\lambda\}}$ , can be decomposed into irreducible spherical tensor components given by [94]

$$X_{0,0} = -\frac{1}{\sqrt{3}}[X_{xx} + X_{yy} + X_{zz}], \quad (\text{A.23})$$

$$X_{1,0} = -\frac{i}{\sqrt{2}}[X_{xy} - X_{yx}], \quad (\text{A.24})$$

$$X_{1,\pm 1} = -\frac{1}{2}[X_{zx} - X_{xz} \pm i(X_{zy} - X_{yz})], \quad (\text{A.25})$$

$$X_{2,0} = \frac{1}{\sqrt{6}}[3X_{zz} - (X_{xx} + X_{yy} + X_{zz})], \quad (\text{A.26})$$

$$X_{2,\pm 1} = \mp \frac{1}{2}[X_{xz} + X_{zx} \pm i(X_{yz} + X_{zy})], \quad (\text{A.27})$$

$$X_{2,\pm 2} = \frac{1}{2}[X_{xx} - X_{yy} \pm i(X_{xy} + X_{yx})]. \quad (\text{A.28})$$

Calculated in terms of  $E$ ,  $A_{ik}$ , and  $S_{ik}$  the irreducible spherical tensor components are given by

$$X_{0,0} = -\sqrt{3} E, \quad (\text{A.29})$$

$$X_{1,0} = -i\sqrt{2} A_{xy}, \quad (\text{A.30})$$

$$X_{1,\pm 1} = -(A_{zx} \mp iA_{yz}), \quad (\text{A.31})$$

$$X_{2,0} = \sqrt{\frac{3}{2}} S_{zz}, \quad (\text{A.32})$$

$$X_{2,\pm 1} = \mp (S_{zx} \pm iS_{zy}), \quad (\text{A.33})$$

$$X_{2,\pm 2} = \frac{1}{2}(S_{xx} - S_{yy} \pm i2S_{xy}). \quad (\text{A.34})$$

The inverse relation between second-rank spherical tensor and second-rank symmetric Cartesian tensor elements are

$$E = -\frac{1}{\sqrt{3}}X_{0,0} \quad (\text{A.35})$$

$$A_{xy} = \frac{i}{\sqrt{2}}X_{1,0}, \quad (\text{A.36})$$

$$A_{zx} = -\frac{1}{2}(X_{1,1} + X_{1,-1}), \quad (\text{A.37})$$

$$A_{yz} = -\frac{i}{2}(X_{1,1} - X_{1,-1}), \quad (\text{A.38})$$

$$S_{xx} = \frac{1}{2}(X_{2,2} + X_{2,-2}) - \frac{1}{\sqrt{6}}X_{2,0}, \quad (\text{A.39})$$

$$S_{xy} = S_{yx} = \frac{i}{2}(X_{2,-2} - X_{2,2}), \quad (\text{A.40})$$

$$S_{yy} = -\frac{1}{2}(X_{2,2} + X_{2,-2}) - \frac{1}{\sqrt{6}}X_{2,0}, \quad (\text{A.41})$$

$$S_{xz} = S_{zx} = \frac{1}{2}(X_{2,-1} - X_{2,1}), \quad (\text{A.42})$$

$$S_{zz} = \sqrt{\frac{2}{3}}X_{2,0}, \quad (\text{A.43})$$

$$S_{yz} = S_{zy} = \frac{i}{2}(X_{2,-1} + X_{2,1}). \quad (\text{A.44})$$



	quadrupolar	nuclear shielding	dipolar	$J$
$\lambda$	$q$	$\sigma$	$d$	$J$
$\hat{\mathbf{U}}$	$\hat{\mathbf{I}}$	$\hat{\mathbf{I}}$	$\hat{\mathbf{I}}_1$	$\hat{\mathbf{I}}_1$
$\mathbf{V}$	$\hat{\mathbf{I}}$	$\mathbf{B}$	$\hat{\mathbf{I}}_2$	$\hat{\mathbf{I}}_2$
$\Lambda^{\{\lambda\}}$	$\frac{q_e Q_I}{2I(2I-1)}$	$\gamma_I$	$-(\mu_0/4\pi)\gamma_1\gamma_2\hbar$	$2\pi$
$\rho_{0,0}^{\{\lambda\}}$	0	$-\sqrt{3} \sigma_{\text{iso}}$	0	$-\sqrt{3} J_{\text{iso}}$
$\rho_{1,0}^{\{\lambda\}}$	0	$-i\sqrt{2} \zeta_{\sigma}^{(a)}$	0	$-i\sqrt{2} \zeta_J^{(a)}$
$\rho_{1,\pm 1}^{\{\lambda\}}$	0	0	0	0
$\rho_{2,0}^{\{\lambda\}}$	$\sqrt{\frac{3}{2}} \zeta_q$	$\sqrt{\frac{3}{2}} \zeta_{\sigma}$	$\sqrt{\frac{3}{2}} \zeta_d$	$\sqrt{\frac{3}{2}} \zeta_J$
$\rho_{2,\pm 1}^{\{\lambda\}}$	0	0	0	0
$\rho_{2,\pm 2}^{\{\lambda\}}$	$-\eta_q \zeta_q/2$	$-\eta_{\sigma} \zeta_{\sigma}/2$	0	$-\eta_J \zeta_J/2$

Table A.10: Definitions for the irreducible spherical tensor elements for the quadrupolar, nuclear shielding, and dipolar coupling tensors in the principal axis system (PAS) for a Hamiltonian in the form of Eq. (A.49). Here, we define the first rank nuclear shielding or  $J$  antisymmetric tensor in its PAS as  $\rho_{1,0}$ , which is related to its value,  $r_{1,m}$ , in the PAS of the second rank symmetric tensor by  $r_{1,m} = \sum_m \mathcal{D}_{0,m}^{(2)}(0, \beta, \gamma) \rho_{1,0}$ .

$k$	$T_{0,k}(\mathbf{U}, \mathbf{V})$	$T_{1,k}(\mathbf{U}, \mathbf{V})$	$T_{2,k}(\mathbf{U}, \mathbf{V})$
0	$-\frac{1}{\sqrt{3}} \mathbf{U} \cdot \mathbf{V}$	$-\frac{1}{2\sqrt{2}} [U_+ V_- - U_- V_+]$	$\frac{1}{\sqrt{6}} [3U_z V_z - \mathbf{U} \cdot \mathbf{V}]$
$\pm 1$	-	$\frac{1}{2} [U_z V_{\pm} - U_{\pm} V_z]$	$\mp \frac{1}{2} [U_z V_{\pm} + U_{\pm} V_z]$
$\pm 2$	-	-	$\frac{1}{2} U_{\pm} V_{\pm}$

Table A.11: Irreducible spherical tensors,  $T_{J,k}(\mathbf{U}, \mathbf{V})$ , formed from the tensor product of two vectors  $\mathbf{U}$  and  $\mathbf{V}$ , and expressed in terms of their Cartesian components for  $J \leq 2$ .

In the principal axis system of  $\mathbf{A}$ , we find

$$\rho_{1,0} = -i\sqrt{2} \zeta^{(a)}, \quad \rho_{1,\pm 1} = 0. \quad (\text{A.45})$$

In the principal axis system of  $\mathbf{S}$ , we find

$$\rho_{2,0} = \sqrt{\frac{3}{2}} \zeta, \quad \rho_{2,\pm 1} = 0, \quad \rho_{2,\pm 2} = -\frac{1}{2} \zeta \eta. \quad (\text{A.46})$$

We also find

$$\rho_{2,0} = \sqrt{\frac{3}{2}} \lambda_{zz}^{(s)}, \quad \rho_{2,\pm 1} = 0, \quad \rho_{2,\pm 2} = \frac{1}{2} (\lambda_{xx}^{(s)} - \lambda_{yy}^{(s)}), \quad (\text{A.47})$$

and conversely,

$$\lambda_{zz}^{(s)} = \sqrt{\frac{2}{3}} \rho_{2,0}, \quad \lambda_{xx}^{(s)} = \rho_{2,\pm 2} - \frac{1}{\sqrt{6}} \rho_{2,0}, \quad \lambda_{yy}^{(s)} = -\rho_{2,\pm 2} - \frac{1}{\sqrt{6}} \rho_{2,0}. \quad (\text{A.48})$$

Finally, using the definitions of this section, including Tables A.10 and A.11 or A.12, one can re-express Eq. (A.13) in terms of irreducible tensor elements of ranks  $L = 0, 1$ , and  $2$  as

$$\hat{\mathcal{H}}_{\lambda} = \Lambda^{\{\lambda\}} \sum_{L=0}^2 \sum_{m=-L}^L (-1)^m R_{L,-m}^{\{\lambda\}} \hat{T}_{L,m}^{\{\lambda\}}(\mathbf{U}, \mathbf{V}). \quad (\text{A.49})$$

### A.3. Perturbation theory

Using the static perturbation approach, as outlined by Goldman et al.[90], and limited here to non-degenerate systems,  $\hat{D}_s$  and  $\hat{V}$  can be obtained through the perturbation expansion,

$$\hat{D}_s = \hat{\mathcal{H}}^{(0)} + \hat{D}^{(1)} + \hat{D}^{(2)} + \dots, \quad (\text{A.50})$$

$$\hat{V} = \hat{1} + \hat{V}^{(1)} + \hat{V}^{(2)} + \dots, \quad (\text{A.51})$$

with each correction given by

$$\hat{D}^{(n)} = \sum_i E_i^{(n)} |i\rangle\langle i|, \quad (\text{A.52})$$

$$\hat{V}^{(n)} = \sum_i |v_i^{(n)}\rangle\langle i|, \quad (\text{A.53})$$

where the eigenvalues,  $E_i^{(n)}$ , and eigenvectors  $|v_i^{(n)}\rangle$ , can be obtained with conventional static perturbation theory[95]:

$$E_i^{(1)} = \sum_\lambda \langle i | \hat{\mathcal{H}}_\lambda^{(1)} | i \rangle, \quad (\text{A.54})$$

$$E_i^{(2)} = \sum_\lambda \left[ \sum_{j \neq i} \frac{\langle i | \hat{\mathcal{H}}_\lambda^{(1)} | j \rangle \langle j | \hat{\mathcal{H}}_\lambda^{(1)} | i \rangle}{E_i^{(0)} - E_j^{(0)}} \right] + \sum_\lambda \sum_{\mu \neq \lambda} \left[ \sum_{j \neq i} \frac{\langle i | \hat{\mathcal{H}}_\lambda^{(1)} | j \rangle \langle j | \hat{\mathcal{H}}_\mu^{(1)} | i \rangle}{E_i^{(0)} - E_j^{(0)}} \right], \quad (\text{A.55})$$

$$|v_i^{(1)}\rangle = \sum_\lambda \left[ \sum_{j \neq i} \frac{\langle j | \hat{\mathcal{H}}_\lambda^{(1)} | i \rangle}{E_i^{(0)} - E_j^{(0)}} |j\rangle \right], \quad (\text{A.56})$$

with

$$E_i^{(0)} = \langle i | \hat{\mathcal{H}}^{(0)} | i \rangle. \quad (\text{A.57})$$

Operators in terms of matrix elements and outer products are obtained when Eqs (A.52) and (A.53) are combined with Eqs. (A.54)-(A.57). As we show below, these matrix elements and outer products can be readily simplified in the case of NMR using the general selection rule for irreducible tensors,

$$\langle j | \hat{T}_{l,m} | i \rangle = \delta_{j,i+m} \langle i + m | \hat{T}_{l,m} | i \rangle, \quad (\text{A.58})$$

to obtain pure irreducible tensor expansions for the  $\hat{D}_s$  and  $\hat{V}$  operators[90]. In this review, we will consider only fundamental transitions, that is, Zeeman allowed ( $\Delta m = \pm 1$ ) transitions. For such situations, the transformation,  $\hat{V}$ , between the laboratory and diagonal frame[90, 23], will, to a good approximation, not need evaluation.

At conventional NMR magnetic field strengths, we will only consider the quadrupolar coupling as strong enough to require a correction higher than the first order. Note, however, that the second- and higher-order corrections involve the product of matrix elements and will mix together matrix elements coming from different contributions to  $\hat{\mathcal{H}}_s^{(1)}$ . While the second-order terms involving the product of quadrupolar Hamiltonian matrix elements will be the largest, there will be situations where cross-terms between the quadrupolar coupling and the nuclear shielding,  $J$ , or dipolar couplings will not be negligible[96, 97, 98, 99, 100, 101, 102, 103, 104, 105]. Additionally, there will be situations where third-order corrections are not negligible, particularly for non-symmetric transitions of quadrupolar nuclei[66, 106, 23].

### A.4. Spherical tensor products and commutators

The derivation of second-order energy corrections contains products of irreducible spherical tensors. These products can be reduced with the aid of the Clebsch-Gordon coefficients[107, 108, 109] according to

$$U_{l_1, m_1} V_{l_2, m_2} = \sum_{L=|l_1-l_2|}^{|l_1+l_2|} \langle L \ m_1+m_2 | l_1 \ l_2 \ m_1 \ m_2 \rangle \mathcal{X}_{L, m_1+m_2}, \quad (\text{A.59})$$

$k$	$\hat{T}_{0,k}(\mathbf{I})$	$\hat{T}_{1,k}(\mathbf{I})$	$\hat{T}_{2,k}(\mathbf{I})$	$\hat{T}_{3,k}(\mathbf{I})$
0	$\hat{1}$	$\hat{I}_z$	$(\frac{1}{6})^{1/2} [3\hat{I}_z^2 - I(I+1)]$	$(\frac{1}{10})^{1/2} [5\hat{I}_z^2 - (3I(I+1) - 1)]\hat{I}_z$
$\pm 1$	-	$\mp (\frac{1}{2})^{1/2} \hat{I}_{\pm}$	$\mp \frac{1}{2} \{\hat{I}_z, \hat{I}_{\pm}\}$	$\mp (\frac{3}{10})^{1/2} \frac{1}{4} \left\{ \left( 5\hat{I}_z^2 - I(I+1) - \frac{1}{2} \right), \hat{I}_{\pm} \right\}$
$\pm 2$	-	-	$\frac{1}{2} \hat{I}_{\pm}^2$	$(\frac{3}{4})^{1/2} \frac{1}{2} \{\hat{I}_z, \hat{I}_{\pm}^2\}$
$\pm 3$	-	-	-	$\mp \frac{1}{2} (\frac{1}{2})^{1/2} \hat{I}_{\pm}^3$

Table A.12: Irreducible spherical tensor operators,  $\hat{T}_{J,k}(\mathbf{I})$  formed from the tensor product with the same vector and expressed in terms of Cartesian operators for  $J \leq 3$  after Buckmaster et al.[13, 110]. Here  $\{\hat{A}, \hat{B}\}$  represents the anticommutator of operators  $\hat{A}$  and  $\hat{B}$ .

where

$$\mathcal{X}_{L,M} = \{\mathbf{U}^{(l_1)} \otimes \mathbf{V}^{(l_2)}\}_{L,M} = \sum_m \langle L M | l_1 l_2 m M-m \rangle U_{l_1,m} V_{l_2,M-m}. \quad (\text{A.60})$$

A few symmetry properties helpful in this appendix are

$$\langle L M | l_1 l_2 m_1 m_2 \rangle = (-1)^{l_1+l_2-L} \langle L M | l_2 l_1 m_2 m_1 \rangle, \quad (\text{A.61})$$

$$\langle L M | l_1 l_2 m_1 m_2 \rangle = (-1)^{l_1+l_2-L} \langle L-M | l_1 l_2 -m_1 -m_2 \rangle, \quad (\text{A.62})$$

$$\langle L M | l_1 l_2 m_1 m_2 \rangle = \langle L-M | l_2 l_1 -m_2 -m_1 \rangle. \quad (\text{A.63})$$

Since second-order energy corrections are needed only for interactions that depend on the same spin angular momentum as the nuclear electric quadrupole moment, we can narrow our focus to spatial tensor products of the form  $R_{l_1,-m}^{\{\lambda\}} R_{2,m}^{\{q\}}$ , which can be expanded as

$$R_{l_1,-m}^{\{\lambda\}} R_{2,m}^{\{q\}} = \frac{1}{2} \sum_{L=|l_1-2|}^{|l_1+2|} (1 + (-1)^{l_1-L}) \langle L 0 | l_1 2 -m m \rangle \mathcal{R}_{L,0}^{\{\lambda q\}}. \quad (\text{A.64})$$

This expansion shows that the product vanishes when  $l_1 - L$  is an odd value. Thus, for even values of  $l_1$  only terms in the sum with even values of  $L$  survive, and vice versa. The combined tensor,  $\mathcal{R}_{L,k}^{\{\lambda q\}}$ , can be expanded as

$$\mathcal{R}_{L,M}^{\{\lambda q\}} = \left\{ \mathbf{R}_{\{\lambda\}}^{(l_1)} \otimes \mathbf{R}_{\{q\}}^{(2)} \right\}_{L,M} = \sum_m \langle L M | l_1 2 m M-m \rangle R_{l_1,m}^{\{\lambda\}} R_{2,M-m}^{\{q\}}. \quad (\text{A.65})$$

The tensor elements  $\mathcal{R}_{L,k}^{\{\lambda q\}}$  are related to the tensor elements in the sample holder coordinate frame,  $\mathcal{R}'_{L,k}^{\{\lambda q\}}$ , using Eq. (A.77).

A commutator of irreducible spherical tensor operators can be generally expanded as

$$[\hat{T}_{l_1,m_1}(\mathbf{I}), \hat{T}_{l_2,m_2}(\mathbf{I})] = \sum_{J=|l_1-l_2|}^{|l_1+l_2|} \sum_{M=-J}^J \{1 - (-1)^{l_1+l_2+J}\} \langle J M | l_1 l_2 m_1 m_2 \rangle B(l_1, l_2, J) \hat{T}_{J,M}(\mathbf{I}), \quad (\text{A.66})$$

where the  $\hat{T}_{J,M}(\mathbf{I})$  are given in Table A.12 and

$$B(l_1, l_2, J) = \frac{\langle I | \hat{\mathbf{T}}^{(l_1)}(\mathbf{I}) | I \rangle \langle I | \hat{\mathbf{T}}^{(l_2)}(\mathbf{I}) | I \rangle}{\langle I | \hat{\mathbf{T}}^{(J)}(\mathbf{I}) | I \rangle} (-1)^{2I+2l_1+J} \sqrt{2J+1} \left\{ \begin{matrix} l_1 & l_2 & J \\ I & I & I \end{matrix} \right\}. \quad (\text{A.67})$$

Here, the term in curly brackets is a 6- $j$  symbol, and the reduced matrix elements are given by

$$\langle I | \hat{\mathbf{T}}^{(k)}(\mathbf{I}) | I \rangle = \left[ \frac{k!k!(2I+k+1)!}{2^k(2k)!(2I-k)!} \right]^{1/2}. \quad (\text{A.68})$$

We narrow our focus to the specific commutator

$$[\hat{T}_{l_1,m}(\mathbf{I}), \hat{T}_{2,-m}(\mathbf{I})] = \sum_{J=|l_1-2|}^{|l_1+2|} \{1 - (-1)^{l_1+J}\} \langle J \ 0 | l_1 \ 2 \ m \ -m \rangle B(l_1, 2, J) \hat{T}_{J,0}(\mathbf{I}), \quad (\text{A.69})$$

where

$$B(l_1, 2, J) = \frac{\langle I || \hat{\mathbf{T}}^{(l_1)}(\mathbf{I}) || I \rangle \langle I || \hat{\mathbf{T}}^{(2)}(\mathbf{I}) || I \rangle}{\langle I || \hat{\mathbf{T}}^{(J)}(\mathbf{I}) || I \rangle} (-1)^{2I+2l_1+J} \sqrt{2J+1} \begin{Bmatrix} l_1 & 2 & J \\ I & I & I \end{Bmatrix}. \quad (\text{A.70})$$

Equation (A.69) shows that the coefficient vanishes when  $l_1 + J$  is an even value. Thus, for even values of  $l_1$  only terms in the sum with odd values of  $J$  survive, and vice versa. For the commutator  $[\hat{T}_{1,m}(\mathbf{I}), \hat{T}_{2,-m}(\mathbf{I})]$ , we only need to evaluate  $B(1, 2, 2)$ , whereas for the commutator  $[\hat{T}_{2,m}(\mathbf{I}), \hat{T}_{2,-m}(\mathbf{I})]$  we need  $B(2, 2, 1)$  and  $B(2, 2, 3)$ .

Focusing on  $B(1, 2, 2)$  we have

$$B(1, 2, 2) = [I(I+1)(2I+1)]^{1/2} (-1)^{2I} \sqrt{5} \begin{Bmatrix} 1 & 2 & 2 \\ I & I & I \end{Bmatrix}. \quad (\text{A.71})$$

Using a symmetry property of the 6- $j$  symbols, we can write

$$\begin{Bmatrix} 1 & 2 & 2 \\ I & I & I \end{Bmatrix} = \begin{Bmatrix} I & I & 2 \\ 2 & 1 & I \end{Bmatrix}, \quad (\text{A.72})$$

and use the general relationship

$$\begin{Bmatrix} a & b & c \\ 2 & c-1 & b \end{Bmatrix} = (-1)^{s+1} 2(X-c-1) \left[ \frac{6(s+1)(s-2c+1)(s-2b)(s-2a)(2b-2)!(2c-3)!}{(2b+3)!(2c+2)!} \right]^{1/2}, \quad (\text{A.73})$$

where  $s = a + b + c$  and  $X = -a(a+1) + b(b+1) + c(c+1)$ , to obtain

$$\begin{Bmatrix} I & I & 2 \\ 2 & 1 & I \end{Bmatrix} = -\sqrt{\frac{3}{10}} (-1)^{2I} \left[ \frac{1}{I(I+1)(2I+1)} \right]^{1/2}, \quad (\text{A.74})$$

with  $s = 2(I+1)$  and  $X = 6$ . Thus, we obtain

$$B(1, 2, 2) = -\sqrt{\frac{3}{2}}. \quad (\text{A.75})$$

Similarly, one can show that

$$B(2, 2, 1) = \sqrt{\frac{2}{5}} [I(I+1) - 3/4], \quad \text{and} \quad B(2, 2, 3) = -2. \quad (\text{A.76})$$

#### A.5. Sample motion

With sample motion, the relative PAS orientation of the internal spin interactions with respect to the Zeeman interaction PAS (i.e., the laboratory frame) becomes time-dependent. This results in time-dependent eigenvalues (and frequencies) for the total Hamiltonian. If the strength of the internal spin interactions is sufficiently large compared to the Zeeman interaction, then sample motion can also result in time-dependent eigenstates. Fortunately, time-dependent eigenstates from sample motion can be easily handled in solid-state NMR since the time dependence is slow enough that the adiabatic approximation can be made[90, 23, 111].

### A.5.1. Single axis rotation

The spatial symmetry functions,  $\mathbb{S}^{(\lambda)}$ ,  $\mathbb{P}^{(\lambda)}(\Theta)$ ,  $\mathbb{D}^{(\lambda)}(\Theta)$ ,  $\mathbb{F}^{(\lambda)}(\Theta)$ , and  $\mathbb{G}^{(\lambda)}(\Theta)$ , given in Eqs. (5)-(9), are expanded by assuming that the sample can be reoriented through an angle  $\phi_R$  about a single axis at an angle  $\theta_R$  with respect to the external magnetic field. This motion will modulate the  $L$ th rank spatial tensor element according to:

$$R_{L,0} = \sum_{k=-L}^L \mathcal{D}_{k,0}^{(L)}(\phi_R, \theta_R, 0) R'_{L,k}, \quad (\text{A.77})$$

where  $R'_{L,k}$  are the tensor elements in the sample holder (e.g. the rotor) coordinate system,  $\mathcal{D}_{m,m'}^{(L)}(\alpha, \beta, \gamma)$  are Wigner rotation matrix elements, given by

$$\mathcal{D}_{m,m'}^{(L)}(\alpha, \beta, \gamma) = e^{-im\alpha} d_{m,m'}^{(L)}(\beta) e^{-im'\gamma}, \quad (\text{A.78})$$

where  $d_{m,m'}^{(L)}(\beta)$  are the reduced Wigner rotation matrix elements. A useful relationship between reduced Wigner rotation matrix elements is

$$d_{m,m'}^{(L)}(\beta) = (-1)^{m-m'} d_{-m,-m'}^{(L)}(\beta) = (-1)^{m-m'} d_{m',m}^{(L)}(\beta) = d_{-m',-m}^{(L)}(\beta). \quad (\text{A.79})$$

Although  $R_{L,0}$  is a real number, each term in the Eq. (A.77) sum may not be real. One can further expand the  $R'_{L,k}$  in terms of the irreducible spherical tensor elements in the crystal axis coordinate system with

$$R'_{L,k} = e^{-ik\gamma} \sum_{n=-L}^L e^{-in\alpha} d_{n,k}^{(L)}(\beta) R''_{L,n}, \quad (\text{A.80})$$

where  $\alpha$ ,  $\beta$ , and  $\gamma$  are the Euler angles specifying the orientation of the crystal axis coordinate system in the sample holder coordinate system. Noting that

$$R'^*_{L,k} = (-1)^k R'_{L,-k}, \quad (\text{A.81})$$

where  $R'^*_{L,k}$  is the complex conjugate of  $R'_{L,k}$ , and using the definition

$$R'_{L,k} = e^{-ik\gamma} r'_{L,k} e^{ik\psi'_{L,k}}, \quad (\text{A.82})$$

where

$$|r'_{L,k}|^2 = R'_{L,k} R'^*_{L,k}, \quad \text{and} \quad k\psi'_{L,k} = \tan^{-1} \frac{\Im\{R'_{L,k} e^{ik\gamma}\}}{\Re\{R'_{L,k} e^{ik\gamma}\}}, \quad (\text{A.83})$$

and  $\Re\{z\}$  and  $\Im\{z\}$  are the real and imaginary parts, respectively, of a complex number  $z$ , then one can rearrange Eq. (A.77) to obtain

$$R_{L,0} = d_{0,0}^{(L)}(\theta_R) R'_{L,0} + \sum_{k=1}^L 2 d_{k,0}^{(L)}(\theta_R) r'_{L,k} \cos(k(\phi_R + \gamma - \psi'_{L,k})). \quad (\text{A.84})$$

Thus, we identify

$$\mathbb{S} \propto \mathcal{P}_0(\cos \theta_R) R'_{0,0}, \quad (\text{A.85})$$

$$\mathbb{P}_0(\theta_R) \propto \mathcal{P}_1(\cos \theta_R) R'_{1,0}, \quad (\text{A.86})$$

$$\mathbb{D}_0(\theta_R) \propto \mathcal{P}_2(\cos \theta_R) R'_{2,0}, \quad (\text{A.87})$$

$$\mathbb{F}_0(\theta_R) \propto \mathcal{P}_3(\cos \theta_R) R'_{3,0}, \quad (\text{A.88})$$

$$\mathbb{G}_0(\theta_R) \propto \mathcal{P}_4(\cos \theta_R) R'_{4,0}, \quad (\text{A.89})$$

where  $\mathcal{P}_L(\cos \theta_R)$  are the Legendre polynomials, and for the  $k \neq 0$  variables we have

$$\mathbb{P}_k(\theta_R, \phi_R) \propto 2 d_{k,0}^{(1)}(\theta_R) r'_{1,k} \cos(k(\phi_R + \gamma - \psi'_{1,k})), \quad (\text{A.90})$$

$$\mathbb{D}_k(\theta_R, \phi_R) \propto 2 d_{k,0}^{(2)}(\theta_R) r'_{2,k} \cos(k(\phi_R + \gamma - \psi'_{2,k})), \quad (\text{A.91})$$

$$\mathbb{F}_k(\theta_R, \phi_R) \propto 2 d_{k,0}^{(3)}(\theta_R) r'_{3,k} \cos(k(\phi_R + \gamma - \psi'_{3,k})), \quad (\text{A.92})$$

$$\mathbb{G}_k(\theta_R, \phi_R) \propto 2 d_{k,0}^{(4)}(\theta_R) r'_{4,k} \cos(k(\phi_R + \gamma - \psi'_{4,k})). \quad (\text{A.93})$$

### A.5.2. Double axis rotation

In DOR (Double Rotation) [22, 21], a sample is being reoriented through an angle  $\phi_i$  about an axis at an angle  $\theta_i$  with respect to an axis that is also being reoriented through an angle  $\phi_o$  at an angle  $\theta_o$  with respect to the external magnetic field. In this situation, the  $L$ th rank spatial tensor is modulated according to.

$$R_{L,0} = \sum_{k_o=-L}^L \mathcal{D}_{k_o,0}^{(L)}(\phi_o, \theta_o, 0) R'_{L,k_o}, \quad (\text{A.94})$$

where  $R'_{L,k_o}$  are the tensor elements in the frame of the outer rotor, and

$$R'_{L,k_o} = \sum_{k_i=-L}^L \mathcal{D}_{k_i,k_o}^{(L)}(\phi_i, \theta_i, \chi_o) R''_{L,k_i}, \quad (\text{A.95})$$

where  $\chi_o$  is the initial phase of the outer rotor and  $R''_{L,k_i}$  are the tensor elements in the frame of the inner rotor.  $R_{L,0}$  can be expanded in terms of both rotors according to

$$R_{L,0} = \sum_{k_o=-L}^L \sum_{k_i=-L}^L \mathcal{D}_{k_o,0}^{(L)}(\phi_o, \theta_o, 0) \mathcal{D}_{k_i,k_o}^{(L)}(\phi_i, \theta_i, \chi_o) R''_{L,k_i}. \quad (\text{A.96})$$

Using the relationships in Eqs. (A.78)-(A.81), the sum can be rearranged as,

$$\begin{aligned} R_{L,0} = & d_{0,0}^{(L)}(\theta_o) d_{0,0}^{(L)}(\theta_i) R''_{L,0} + \sum_{k_i=1}^L 2 d_{0,0}^{(L)}(\theta_o) d_{k_i,0}^{(L)}(\theta_i) r''_{L,k_i} \cos(k_i(\phi_i + \gamma - \psi''_{L,k_i})) \\ & + \sum_{k_o=1}^L 2 d_{k_o,0}^{(L)}(\theta_o) d_{0,k_o}^{(L)}(\theta_i) r''_{L,0} \cos(k_o(\phi_o + \chi_o)) \\ & + \sum_{k_o=1}^L \sum_{k_i=1}^L 2 d_{k_o,0}^{(L)}(\theta_o) d_{k_i,k_o}^{(L)}(\theta_i) r''_{L,k_i} \cos(k_i(\phi_i + \gamma - \psi''_{L,k_i}) + k_o(\phi_o + \chi_o)) \\ & + \sum_{k_o=1}^L \sum_{k_i=1}^L 2 d_{-k_o,0}^{(L)}(\theta_o) d_{k_i,-k_o}^{(L)}(\theta_i) r''_{L,k_i} \cos(k_i(\phi_i + \gamma - \psi''_{L,k_i}) - k_o(\phi_o + \chi_o)). \quad (\text{A.97}) \end{aligned}$$

Now, we define for the case when  $k_o = 0$  and  $k_i = 0$ ,

$$\mathbb{S} \propto \mathcal{P}_0(\cos \theta_o) \mathcal{P}_0(\cos \theta_i) R''_{0,0}, \quad (\text{A.98})$$

$$\mathbb{P}_{0,0}(\theta_o, \theta_i) \propto \mathcal{P}_1(\cos \theta_o) \mathcal{P}_1(\cos \theta_i) R''_{1,0}, \quad (\text{A.99})$$

$$\mathbb{D}_{0,0}(\theta_o, \theta_i) \propto \mathcal{P}_2(\cos \theta_o) \mathcal{P}_2(\cos \theta_i) R''_{2,0}, \quad (\text{A.100})$$

$$\mathbb{F}_{0,0}(\theta_o, \theta_i) \propto \mathcal{P}_3(\cos \theta_o) \mathcal{P}_3(\cos \theta_i) R''_{3,0}, \quad (\text{A.101})$$

$$\mathbb{G}_{0,0}(\theta_o, \theta_i) \propto \mathcal{P}_4(\cos \theta_o) \mathcal{P}_4(\cos \theta_i) R''_{4,0}, \quad (\text{A.102})$$

for the case when  $k_o = 0$  and  $k_i \neq 0$ ,

$$\mathbb{P}_{0,k_i}(\theta_o, \theta_i, \phi_i) \propto \mathcal{P}_1(\cos \theta_o) 2 d_{k_i,0}^{(1)}(\theta_i) r''_{1,k_i} \cos(k_i(\phi_i + \gamma - \psi''_{1,k_i})), \quad (\text{A.103})$$

$$\mathbb{D}_{0,k_i}(\theta_o, \theta_i, \phi_i) \propto \mathcal{P}_2(\cos \theta_o) 2 d_{k_i,0}^{(2)}(\theta_i) r''_{2,k_i} \cos(k_i(\phi_i + \gamma - \psi''_{2,k_i})), \quad (\text{A.104})$$

$$\mathbb{F}_{0,k_i}(\theta_o, \theta_i, \phi_i) \propto \mathcal{P}_3(\cos \theta_o) 2 d_{k_i,0}^{(3)}(\theta_i) r''_{3,k_i} \cos(k_i(\phi_i + \gamma - \psi''_{3,k_i})), \quad (\text{A.105})$$

$$\mathbb{G}_{0,k_i}(\theta_o, \theta_i, \phi_i) \propto \mathcal{P}_4(\cos \theta_o) 2 d_{k_i,0}^{(4)}(\theta_i) r''_{4,k_i} \cos(k_i(\phi_i + \gamma - \psi''_{4,k_i})), \quad (\text{A.106})$$

for the case when  $k_o \neq 0$  and  $k_i = 0$ ,

$$\mathbb{P}_{k_o,0}(\theta_o, \phi_o, \chi_o, \theta_i) \propto 2 d_{k_o,0}^{(1)}(\theta_o) d_{0,k_o}^{(1)}(\theta_i) R''_{1,0} \cos(k_o(\phi_o + \chi_o)), \quad (\text{A.107})$$

$$\mathbb{D}_{k_o,0}(\theta_o, \phi_o, \chi_o, \theta_i) \propto 2 d_{k_o,0}^{(2)}(\theta_o) d_{0,k_o}^{(2)}(\theta_i) R''_{2,0} \cos(k_o(\phi_o + \chi_o)), \quad (\text{A.108})$$

$$\mathbb{F}_{k_o,0}(\theta_o, \phi_o, \chi_o, \theta_i) \propto 2 d_{k_o,0}^{(3)}(\theta_o) d_{0,k_o}^{(3)}(\theta_i) R''_{3,0} \cos(k_o(\phi_o + \chi_o)), \quad (\text{A.109})$$

$$\mathbb{G}_{k_o,0}(\theta_o, \phi_o, \chi_o, \theta_i) \propto 2 d_{k_o,0}^{(4)}(\theta_o) d_{0,k_o}^{(4)}(\theta_i) R''_{4,0} \cos(k_o(\phi_o + \chi_o)), \quad (\text{A.110})$$

and for the case when  $k_o \neq 0$  and  $k_i \neq 0$ ,

$$\begin{aligned} \mathbb{P}_{k_o, k_i}(\theta_o, \phi_o, \chi_o, \theta_i, \phi_i) &\propto 2 d_{k_o, 0}^{(1)}(\theta_o) d_{k_i, k_o}^{(1)}(\theta_i) r_{1, k_i}'' \cos(k_i(\phi_i + \gamma - \psi_{1, k_i}'') + k_o(\phi_o + \chi_o)) \\ &\quad + 2 d_{-k_o, 0}^{(1)}(\theta_o) d_{k_i, -k_o}^{(1)}(\theta_i) r_{1, k_i}'' \cos(k_i(\phi_i + \gamma - \psi_{1, k_i}'') - k_o(\phi_o + \chi_o)), \end{aligned} \quad (\text{A.111})$$

$$\begin{aligned} \mathbb{D}_{k_o, k_i}(\theta_o, \phi_o, \chi_o, \theta_i, \phi_i) &\propto 2 d_{k_o, 0}^{(2)}(\theta_o) d_{k_i, k_o}^{(2)}(\theta_i) r_{2, k_i}'' \cos(k_i(\phi_i + \gamma - \psi_{2, k_i}'') + k_o(\phi_o + \chi_o)), \\ &\quad + 2 d_{-k_o, 0}^{(2)}(\theta_o) d_{k_i, -k_o}^{(2)}(\theta_i) r_{2, k_i}'' \cos(k_i(\phi_i + \gamma - \psi_{2, k_i}'') - k_o(\phi_o + \chi_o)), \end{aligned} \quad (\text{A.112})$$

$$\begin{aligned} \mathbb{F}_{k_o, k_i}(\theta_o, \phi_o, \chi_o, \theta_i, \phi_i) &\propto 2 d_{k_o, 0}^{(3)}(\theta_o) d_{k_i, k_o}^{(3)}(\theta_i) r_{3, k_i}'' \cos(k_i(\phi_i + \gamma - \psi_{3, k_i}'') + k_o(\phi_o + \chi_o)), \\ &\quad + 2 d_{-k_o, 0}^{(3)}(\theta_o) d_{k_i, -k_o}^{(3)}(\theta_i) r_{3, k_i}'' \cos(k_i(\phi_i + \gamma - \psi_{3, k_i}'') - k_o(\phi_o + \chi_o)), \end{aligned} \quad (\text{A.113})$$

$$\begin{aligned} \mathbb{G}_{k_o, k_i}(\theta_o, \phi_o, \chi_o, \theta_i, \phi_i) &\propto 2 d_{k_o, 0}^{(4)}(\theta_o) d_{k_i, k_o}^{(4)}(\theta_i) r_{4, k_i}'' \cos(k_i(\phi_i + \gamma - \psi_{4, k_i}'') + k_o(\phi_o + \chi_o)), \\ &\quad + 2 d_{-k_o, 0}^{(4)}(\theta_o) d_{k_i, -k_o}^{(4)}(\theta_i) r_{4, k_i}'' \cos(k_i(\phi_i + \gamma - \psi_{4, k_i}'') - k_o(\phi_o + \chi_o)). \end{aligned} \quad (\text{A.114})$$

### A.5.3. Spinning sidebands

To calculate the signal during single axis rotation (SAR) of the sample in a Bloch decay or PASS experiment, we start with the signal phase as derived in Section 3.4

$$\Phi_{\text{SAR}}(\epsilon, t, \chi_R) = W_0 t + \sum_{m \neq 0} W_m e^{im(\chi_R + \gamma)} [e^{im\Omega_R t} - e^{-im\Omega_R \epsilon}], \quad (\text{A.115})$$

where  $\epsilon = 0$  in a Bloch decay experiment. From this phase, we obtain the signal

$$\mathfrak{s}_{\text{SAR}}(\epsilon, t, \chi_R) = e^{iW_0 t} \exp \left\{ i \sum_{m \neq 0} W_m e^{im(\Omega_R t + \chi_R + \gamma)} \right\} \exp \left\{ -i \sum_{m \neq 0} W_m e^{im(-\Omega_R \epsilon + \chi_R + \gamma)} \right\}. \quad (\text{A.116})$$

Following the derivation of Mehring[2], this can be rewritten using the property of delta functions to obtain

$$\begin{aligned} \mathfrak{s}_{\text{SAR}}(\epsilon, t, \chi_R) &= e^{iW_0 t} \\ &\quad \times \frac{1}{2\pi} \int_0^{2\pi} d\Theta_1 \delta(\Theta_1 - \Omega_R t - \chi_R - \gamma) \exp \left\{ i \sum_{m \neq 0} W_m e^{im\Theta_1} \right\} \\ &\quad \times \frac{1}{2\pi} \int_0^{2\pi} d\Theta_2 \delta(\Theta_2 + \Omega_R \epsilon - \chi_R - \gamma) \exp \left\{ -i \sum_{m \neq 0} W_m e^{im\Theta_2} \right\}. \end{aligned} \quad (\text{A.117})$$

The delta functions can then be expanded as sums

$$\begin{aligned} \mathfrak{s}_{\text{SAR}}(\epsilon, t, \chi_R) &= e^{iW_0 t} \sum_{N_1} \frac{1}{2\pi} \int_0^{2\pi} d\Theta_1 \exp \{ iN_1(\Theta_1 - \Omega_R t - \chi_R - \gamma) \} \exp \left\{ i \sum_{m \neq 0} W_m e^{im\Theta_1} \right\} \\ &\quad \times \sum_{N_2} \frac{1}{2\pi} \int_0^{2\pi} d\Theta_2 \exp \{ iN_2(\Theta_2 + \Omega_R \epsilon - \chi_R - \gamma) \} \exp \left\{ -i \sum_{m \neq 0} W_m e^{im\Theta_2} \right\}, \end{aligned} \quad (\text{A.118})$$

and after regrouping, the signal becomes

$$\begin{aligned} \mathfrak{s}_{\text{SAR}}(\epsilon, t, \chi_R) &= e^{iW_0 t} \sum_{N_1} \left[ \frac{1}{2\pi} \int_0^{2\pi} d\Theta_1 \exp \left\{ iN_1\Theta_1 + i \sum_{m \neq 0} W_m e^{im\Theta_1} \right\} \right] \exp \{ -iN_1(\Omega_R t + \chi_R + \gamma) \} \\ &\quad \times \sum_{N_2} \left[ \frac{1}{2\pi} \int_0^{2\pi} d\Theta_2 \exp \left\{ iN_2\Theta_2 - i \sum_{m \neq 0} W_m e^{im\Theta_2} \right\} \right] \exp \{ -iN_2(-\Omega_R \epsilon + \chi_R + \gamma) \}. \end{aligned} \quad (\text{A.119})$$

Now we reverse the summation over  $N_2$ , (i.e.  $N_2 \rightarrow -N_2$ ) and obtain

$$\begin{aligned} \mathfrak{s}_{\text{SAR}}(\epsilon, t, \chi_R) = e^{iW_0 t} \sum_{N_1} \left[ \frac{1}{2\pi} \int_0^{2\pi} d\Theta_1 \exp \left\{ iN_1 \Theta_1 + i \sum_{m \neq 0} W_m e^{im\Theta_1} \right\} \right] \exp \{-iN_1(\Omega_R t + \chi_R + \gamma)\} \\ \times \sum_{N_2} \left[ \frac{1}{2\pi} \int_0^{2\pi} d\Theta_2 \exp \left\{ -iN_2 \Theta_2 - i \sum_{m \neq 0} W_m e^{im\Theta_2} \right\} \right] \exp \{iN_2(-\Omega_R \epsilon + \chi_R + \gamma)\}. \end{aligned} \quad (\text{A.120})$$

If we define

$$A(N) = \frac{1}{2\pi} \int_0^{2\pi} \exp \left\{ i \sum_{m \neq 0} W_m e^{im\Theta} \right\} e^{iN\Theta} d\Theta, \quad (\text{A.121})$$

then we write the signal as

$$\mathfrak{s}_{\text{SAR}}(\epsilon, t, \chi_R) = e^{iW_0 t} \sum_{N_1, N_2} A(N_1) A^*(N_2) e^{-iN_1 \Omega_R t} e^{-iN_2 \Omega_R \epsilon} e^{i(N_2 - N_1)(\chi_R + \gamma)}. \quad (\text{A.122})$$

A partial averaging of the signal over the crystallite Euler angle  $\gamma$  yields

$$\langle \mathfrak{s}_{\text{SAR}}(\epsilon, t) \rangle_\gamma = e^{iW_0 t} \sum_N |A(N)|^2 e^{-iN \Omega_R (t + \epsilon)}. \quad (\text{A.123})$$

## A.6. Hamiltonians

With the definitions of the previous sections in place, we give derivations of various first- and second-order corrections to the NMR frequency.

### A.6.1. Zeeman

The Zeeman Hamiltonian is

$$\hat{\mathcal{H}}_z = -\hat{\boldsymbol{\mu}} \cdot \mathbf{B} = -\hbar \gamma_I \hat{\mathbf{I}} \cdot \mathbf{B}, \quad (\text{A.124})$$

where

$$\boldsymbol{\mu} = \gamma_I \hbar \mathbf{I}. \quad (\text{A.125})$$

Since  $\mathbf{B} = (0, 0, B_0)$ , we have

$$\hat{\mathcal{H}}_z = \hbar \omega_0 \hat{I}_z, \quad (\text{A.126})$$

where  $\omega_0 = -\gamma_I B_0$ .

### A.6.2. Electric quadrupole coupling

The Hamiltonian describing the coupling of the nuclear electric quadrupole moment, associated with a nucleus of spin  $I$ , to its surrounding electric field gradient (efg), is given in irreducible spherical tensor form by

$$\hat{\mathcal{H}}_q = \sum_{m=-2}^2 (-1)^m \mathcal{E}_{2,m} \hat{Q}_{2,-m}, \quad (\text{A.127})$$

where the  $\hat{Q}_{2,m}$  are the elements of the nuclear electric quadrupole moment irreducible spherical tensor operator. The energy states of the nucleus are described by the quantum numbers of the total nuclear angular momentum operator  $\hat{I}$  and its projection  $m_I$  along the  $z$  axis, as well as others, which we will denote by a general index  $\gamma$ . For a given nuclear eigenstate, the charge density, which depends on the quantum numbers  $I$ ,  $m_I$ , and  $\gamma$ , is axially symmetric about the  $z$ -axis. Thus, in the principal axis system, the only nonvanishing element is  $\hat{Q}_{2,0}$ , and a single constant called the nuclear quadrupole moment,  $Q_{\gamma I}$ , is defined as

$$\frac{1}{2} q_e Q_{\gamma I} = \langle \gamma I m_I = I | \hat{Q}_{2,0} | \gamma I m_I = I \rangle, \quad (\text{A.128})$$



where  $q_e$  is the charge on the proton. Using the Wigner-Eckart theorem, one can show that

$$\hat{Q}_{2,m} = \sqrt{\frac{3}{2}} \frac{q_e Q_{\gamma I}}{I(2I-1)} \hat{T}_{2,m}(\mathbf{I}), \quad (\text{A.129})$$

obtaining

$$\hat{\mathcal{H}}_q = \sqrt{\frac{3}{2}} \frac{q_e Q_{\gamma I}}{I(2I-1)} \sum_m (-1)^m \mathcal{E}_{2,-m} \hat{T}_{2,m}(\mathbf{I}). \quad (\text{A.130})$$

The  $\mathcal{E}_{2,m}$  are the expectation values of the electric field gradient,  $\nabla^2 \phi(\mathbf{r})$ , calculated from the ground state wavefunction of the system, and are given by

$$\begin{aligned} \mathcal{E}_{2,0} &= \frac{1}{2} \mathcal{V}_{zz}, \\ \mathcal{E}_{2,\pm 1} &= \mp \frac{1}{\sqrt{6}} (\mathcal{V}_{zx} \pm i \mathcal{V}_{zy}), \\ \mathcal{E}_{2,\pm 2} &= \frac{1}{2\sqrt{6}} (\mathcal{V}_{xx} - \mathcal{V}_{yy} \pm 2i \mathcal{V}_{xy}), \end{aligned} \quad (\text{A.131})$$

where

$$\mathcal{V}_{ik} = \frac{\partial^2 \phi(0)}{\partial \mathbf{r}_i \partial \mathbf{r}_k}. \quad (\text{A.132})$$

Here  $\phi(\mathbf{r})$  is the electrostatic scalar potential produced at the position  $\mathbf{r}$  by surrounding charges with the origin at the nucleus. Using the normalization[94]

$$R_{2,m}^{\{q\}} = \sqrt{6} \mathcal{E}_{2,m}, \quad (\text{A.133})$$

we write the electric quadrupole coupling Hamiltonian in terms of spherical tensor elements as

$$\hat{\mathcal{H}}_q = \frac{q_e Q_{\gamma I}}{2I(2I-1)} \sum_m (-1)^m R_{2,-m}^{\{q\}} \hat{T}_{2,m}(\mathbf{I}), \quad (\text{A.134})$$

and in terms of the Cartesian efg tensor as

$$\hat{\mathcal{H}}_q = \frac{q_e Q_{\gamma I}}{2I(2I-1)} \hat{\mathbf{I}} \cdot \mathbf{V} \cdot \hat{\mathbf{I}}. \quad (\text{A.135})$$

In this form, the relationship between the spherical tensor and second-rank symmetric Cartesian efg tensor is

$$R_{2,0}^{\{q\}} = \sqrt{\frac{3}{2}} \mathcal{V}_{zz}, \quad (\text{A.136})$$

$$R_{2,\pm 1}^{\{q\}} = \mp [\mathcal{V}_{zx} \pm i \mathcal{V}_{zy}], \quad (\text{A.137})$$

$$R_{2,\pm 2}^{\{q\}} = \frac{1}{2} [\mathcal{V}_{xx} - \mathcal{V}_{yy} \pm 2i \mathcal{V}_{xy}]. \quad (\text{A.138})$$

In the principal axis system of the efg tensor, where the principal components of the second-rank symmetric Cartesian efg tensor are  $\lambda_{xx}^{\{q\}}$ ,  $\lambda_{yy}^{\{q\}}$ , and  $\lambda_{zz}^{\{q\}}$ , we define

$$\rho_{2,0}^{\{q\}} = \sqrt{\frac{3}{2}} \zeta_q, \quad \rho_{2,\pm 1}^{\{q\}} = 0, \quad \rho_{2,\pm 2}^{\{q\}} = -\eta_q \zeta_q / 2, \quad (\text{A.139})$$

where the second-rank symmetric efg tensor anisotropy,  $\zeta_q$ , is defined as

$$\zeta_q = \lambda_{zz}^{\{q\}}, \quad (\text{A.140})$$

and the second-rank symmetric efg tensor asymmetry parameter is defined as

$$\eta_q = \frac{\lambda_{yy}^{\{q\}} - \lambda_{xx}^{\{q\}}}{\zeta_q}. \quad (\text{A.141})$$

The quadrupolar coupling constant is given by  $C_q = q_e Q_{\gamma I} \zeta_q / h$  (or  $q_e Q_{\gamma I} \zeta_q / (4\pi\epsilon_0 h)$  in S.I. units), and the quadrupolar splitting given by

$$\omega_q = \frac{6\pi C_q}{2I(2I-1)} = \frac{q_e Q_{\gamma I}}{2I(2I-1)} \cdot \frac{3\zeta_q}{h}. \quad (\text{A.142})$$

For convenience, in the derivations to follow, we express the quadrupole Hamiltonian as

$$\hat{\mathcal{H}}_q = \hbar\omega_q \sum_m (-1)^m \frac{R_{2,-m}^{\{q\}}}{3\zeta_q} \hat{T}_{2,m}(\mathbf{I}). \quad (\text{A.143})$$

*First-order electric quadrupole coupling correction.* Using static perturbation theory and Eq. (A.58), we obtain the quadrupolar first-order correction to the eigenvalues

$$E_{q,i}^{(1)} = \hbar\omega_q \frac{R_{2,0}^{\{q\}}}{3\zeta_q} \langle i | \hat{T}_{2,0}(\mathbf{I}) | i \rangle, \quad (\text{A.144})$$

which substituted into Eq. (A.52) gives

$$\hat{D}_q^{(1)} = \hbar\omega_q \frac{R_{2,0}^{\{q\}}}{3\zeta_q} \sum_{j=-I}^I |i\rangle \langle i | \hat{T}_{2,0}(\mathbf{I}) | i\rangle \langle i|. \quad (\text{A.145})$$

Since  $\hat{T}_{2,0}(\mathbf{I})$  commutes with the diagonal projector  $|i\rangle \langle i|$  we obtain the first-order contribution of the quadrupolar Hamiltonian in the tilted rotating frame

$$\hat{D}_q^{(1)} = \hbar\omega_q \frac{R_{2,0}^{\{q\}}}{3\zeta_q} \hat{T}_{2,0}(\mathbf{I}). \quad (\text{A.146})$$

The first-order contribution to the transition frequency between levels  $j$  and  $i$  is given by

$$\Omega_q^{(1)}(\Theta_q, m_i, m_j) = \omega_q \mathbb{D}^{\{q\}}(\Theta_q) \mathfrak{d}_I(m_i, m_j), \quad (\text{A.147})$$

where

$$\mathbb{D}^{\{q\}}(\Theta_q) = \frac{R_{2,0}^{\{q\}}(\Theta_q)}{3\zeta_q}, \quad (\text{A.148})$$

and

$$\mathfrak{d}_I(m_i, m_j) = \langle I, m_j | \hat{T}_{2,0}(\mathbf{I}) | I, m_j \rangle - \langle I, m_i | \hat{T}_{2,0}(\mathbf{I}) | I, m_i \rangle = \sqrt{\frac{3}{2}}(m_j^2 - m_i^2). \quad (\text{A.149})$$

*Second-order electric quadrupole coupling correction.* To obtain the second-order contribution we expand  $E^{(2)}$  in the eigenbasis  $|i\rangle$ :

$$E_{q,q,i}^{(2)} = \frac{1}{\hbar\omega_0} \sum_{\substack{j=-I \\ j \neq i}}^I \frac{\langle i | \hat{\mathcal{H}}_q | j \rangle \langle j | \hat{\mathcal{H}}_q | i \rangle}{i - j}. \quad (\text{A.150})$$

Using the expression for  $\hat{\mathcal{H}}_q$  in Eq. (A.143), we obtain

$$E_{q,q,i}^{(2)} = \frac{\hbar\omega_q^2}{\omega_0} \sum_{m=-2}^2 \sum_{m'=-2}^2 (-1)^{m+m'} \frac{R_{2,-m}^{\{q\}} R_{2,-m'}^{\{q\}}}{9\zeta_q^2} \times \sum_{\substack{j=-I \\ j \neq i}}^I \frac{\langle i | \hat{T}_{2,m}(\mathbf{I}) | j \rangle \langle j | \hat{T}_{2,m'}(\mathbf{I}) | i \rangle}{i - j}. \quad (\text{A.151})$$

Applying the general selection rule for irreducible tensors restricts the sum over  $j$  in Eq. (A.151) to the cases where  $j = i + m'$  and  $j = i - m$ . The sum over  $m$  and  $m'$  is thus also restricted to  $m + m' = 0$  (with  $m \neq 0$ ) giving

$$E_{q,q,i}^{(2)} = \frac{\hbar\omega_q^2}{\omega_0} \sum_{\substack{m=-2 \\ m \neq 0}}^2 \frac{R_{2,-m}^{\{q\}} R_{2,m}^{\{q\}}}{9\zeta_q^2} \frac{\langle i | \hat{T}_{2,m}(\mathbf{I}) | i - m \rangle \langle i - m | \hat{T}_{2,-m}(\mathbf{I}) | i \rangle}{m}. \quad (\text{A.152})$$

$\pi_{L,J}^{\{2,2\}}$	J=1	J=3
L=0	$\frac{4}{\sqrt{125}} [I(I+1) - 3/4]$	$\sqrt{18/25}$
L=2	$\sqrt{\frac{2}{175}} [I(I+1) - 3/4]$	$-6/\sqrt{35}$
L=4	$-\sqrt{\frac{18}{875}} [I(I+1) - 3/4]$	$-17/\sqrt{175}$

Table A.13:  $\pi_{L,J}^{\{2,2\}}$  coefficients in second-order electric quadrupole coupling Hamiltonian.

Using  $|i-m\rangle\langle i-m| = \mathbf{1} - \sum_{j \neq i-m} |j\rangle\langle j|$ , we obtain

$$E_{q,q,i}^{(2)} = \frac{\hbar\omega_q^2}{\omega_0} \sum_{\substack{m=-2 \\ m \neq 0}}^2 \frac{R_{2,-m}^{\{q\}} R_{2,m}^{\{q\}}}{9\zeta_q^2} \frac{\langle i | \hat{T}_{2,m}(\mathbf{I}) \hat{T}_{2,-m}(\mathbf{I}) | i \rangle}{m}. \quad (\text{A.153})$$

Substituting this expression into Eq. (A.52) and noting that  $\hat{T}_{2,m}(\mathbf{I})\hat{T}_{2,-m}(\mathbf{I})$  also commutes with the diagonal projector  $|i\rangle\langle i|$  (*vide infra*), we obtain

$$\hat{D}_{q,q}^{(2)} = \frac{\hbar\omega_q^2}{\omega_0} \sum_{\substack{m=-2 \\ m \neq 0}}^2 \frac{R_{2,-m}^{\{q\}} R_{2,m}^{\{q\}}}{9\zeta_q^2} \cdot \frac{\hat{T}_{2,m}(\mathbf{I}) \hat{T}_{2,-m}(\mathbf{I})}{m}. \quad (\text{A.154})$$

Splitting the sum over  $m$  into two equal parts and regrouping terms of opposite  $m$  into commutators, we finally obtain

$$\hat{D}_{q,q}^{(2)} = \frac{\hbar\omega_q^2}{\omega_0} \sum_{m=1}^2 \frac{R_{2,m}^{\{q\}} R_{2,-m}^{\{q\}}}{9\zeta_q^2} \frac{[\hat{T}_{2,m}(\mathbf{I}), \hat{T}_{2,-m}(\mathbf{I})]}{m}. \quad (\text{A.155})$$

Within the second-order quadrupole Hamiltonian in Eq. (A.155), we find the product of two second-rank spherical tensors, i.e.,  $R_{2,m}^{\{q\}} R_{2,-m}^{\{q\}}$  and the commutator of two second-rank spherical tensor operators, i.e.,  $[\hat{T}_{2,m}(\mathbf{I}), \hat{T}_{2,-m}(\mathbf{I})]$ . Using the results of Section A.4, we can write the second-order quadrupolar Hamiltonian in the rotating tilted frame:

$$\hat{D}_{q,q}^{(2)} = \frac{\hbar\omega_q^2}{\omega_0} \sum_{L=0,2,4} \frac{\mathcal{R}_{L,0}^{\{qq\}}}{9\zeta_q^2} \sum_{J=1,3} \pi_{L,J}^{\{2,2\}} \hat{T}_{J,0}^{\circ}(\mathbf{I}), \quad (\text{A.156})$$

where

$$\pi_{L,J}^{\{2,2\}} = 2 B(2, 2, J) \sum_{m=1}^2 \frac{\langle L 0 | 2 2 m - m \rangle \langle J 0 | 2 2 m - m \rangle}{m}. \quad (\text{A.157})$$

Values of the  $\pi_{L,J}^{\{2,2\}}$  are given in Table A.13.

The tensor  $\mathcal{R}_{L,0}^{\{qq\}}$  is related to the tensor elements in the sample holder frame,  $\mathcal{R}_{L,n}^{\{qq\}}$ , using Eq. (A.77). The tensor  $\mathcal{R}_{L,n}^{\{qq\}}$  is related to the principal values of the  $R_{2,m}^{\{q\}}$  tensor by

$$\mathcal{R}_{L,n}^{\{qq\}} = \sum_{n'=-L}^L \mathcal{D}_{n',n}^{(L)}(\Theta_q) \sigma_{L,n'}^{\{qq\}}, \quad (\text{A.158})$$

where

$$\sigma_{L,n}^{\{qq\}} = \sum_{m=-2}^2 \langle L n | 2 2 m n - m \rangle \rho_{2,m}^{\{q\}} \rho_{2,n-m}^{\{q\}}. \quad (\text{A.159})$$

From Eq. (A.159) we obtain the relationships:

$$\sigma_{0,0}^{\{qq\}} = \frac{9\zeta_q^2}{6\sqrt{5}} \left( \frac{\eta_q^2}{3} + 1 \right), \quad (\text{A.160})$$

$$\sigma_{2,0}^{\{qq\}} = \frac{9\zeta_q^2}{6} \sqrt{\frac{2}{7}} \left( \frac{\eta_q^2}{3} - 1 \right), \quad (\text{A.161})$$

$$\sigma_{2,\pm 2}^{\{qq\}} = -\frac{9\zeta_q^2 \eta_q}{3\sqrt{21}}, \quad (\text{A.162})$$

$$\sigma_{4,0}^{\{qq\}} = \frac{9\zeta_q^2}{\sqrt{70}} \left( \frac{\eta_q^2}{18} + 1 \right), \quad (\text{A.163})$$

$$\sigma_{4,\pm 2}^{\{qq\}} = -\frac{9\zeta_q^2 \eta_q}{6\sqrt{7}}, \quad (\text{A.164})$$

$$\sigma_{4,\pm 4}^{\{qq\}} = \frac{9\zeta_q^2 \eta_q^2}{36}. \quad (\text{A.165})$$

There are several advantages to writing the second-order quadrupole Hamiltonian in the form of Eq. (A.156). First, we see that the even rank (i.e.,  $J = 0, 2$ , and  $4$ ) terms vanish in the reduction of the commutator  $[\hat{T}_{2,m}(\mathbf{I}), \hat{T}_{2,-m}(\mathbf{I})]$ , with only the odd  $J = 1$  and  $3$  rank terms surviving. We also find that all odd rank values of  $L$  vanish in the reduction of the product  $R_{2,m}^{\{q\}} R_{2,-m}^{\{q\}}$  and only the even  $L = 0, 2$ , and  $4$  rank terms remain. The  $L = 0$  term describes a scalar or isotropic shift, which adds to the isotropic nuclear shielding, while the  $L = 2$  and  $4$  terms contain all the anisotropy in the second-order quadrupolar correction. It is the presence of the fourth-rank orientation dependence,  $\mathcal{R}_{4,0}^{\{qq\}}$ , which is not shared by any of the first-order Hamiltonians in solid-state NMR, however, that lies at the heart of the resolution problem in the solid-state NMR of quadrupolar nuclei. This is because conventional MAS, which can eliminate second-rank orientation broadenings, lacks the proper symmetry in its reorientation trajectory to average away fourth-rank anisotropies. When MAS is applied to a quadrupolar nucleus whose spectrum is broadened by second-order quadrupolar effects, there exists a residual anisotropic broadening due to the fourth-rank anisotropy that, more often than not, prevents site resolution.

The second-order contribution to the transition frequency between levels  $|j\rangle$  and  $|i\rangle$  obtained from Eq. (A.156) is

$$\Omega_{q,q}^{(2)}(\Theta_q, m_i, m_j) = \frac{\omega_q^2}{\omega_0} \mathbb{S}^{\{qq\}} \mathbb{C}_0(m_i, m_j) + \frac{\omega_q^2}{\omega_0} \mathbb{D}^{\{qq\}}(\Theta_q) \mathbb{C}_2(m_i, m_j) + \frac{\omega_q^2}{\omega_0} \mathbb{G}^{\{qq\}}(\Theta_q) \mathbb{C}_4(m_i, m_j), \quad (\text{A.166})$$

where

$$\mathbb{S}^{\{qq\}} = \frac{\mathcal{R}_{0,0}^{\{qq\}}}{9\zeta_q^2} = \frac{1}{6\sqrt{5}} \left( \frac{\eta_q^2}{3} + 1 \right), \quad (\text{A.167})$$

$$\mathbb{D}^{\{qq\}}(\Theta_q) = \frac{\mathcal{R}_{2,0}^{\{qq\}}(\Theta_q)}{9\zeta_q^2}, \quad (\text{A.168})$$

$$\mathbb{G}^{\{qq\}}(\Theta_q) = \frac{\mathcal{R}_{4,0}^{\{qq\}}(\Theta_q)}{9\zeta_q^2}, \quad (\text{A.169})$$

and using  $\mathbb{C}_L(i, j)$  values calculated from

$$\mathbb{C}_L(m_i, m_j) = \sum_{J=1,3} \pi_{L,J}^{\{2,2\}} \left\{ \langle I, m_j | \hat{T}_{J,0}^\circ | I, m_j \rangle - \langle I, m_i | \hat{T}_{J,0}^\circ | I, m_i \rangle \right\} = \sum_{J=1,3} \pi_{L,J}^{\{2,2\}} \xi_J(m_i, m_j). \quad (\text{A.170})$$

### A.6.3. Nuclear shielding

The nuclear shielding Hamiltonian is

$$\hat{\mathcal{H}}_\sigma = \hat{\boldsymbol{\mu}} \cdot \boldsymbol{\sigma} \cdot \mathbf{B} = \hbar\gamma_I \hat{\mathbf{I}} \cdot \boldsymbol{\sigma} \cdot \mathbf{B}, \quad (\text{A.171})$$

and written in terms of irreducible spherical tensors is

$$\hat{\mathcal{H}}_\sigma = \hbar\gamma_I \sum_{L=0}^2 \sum_{m=-L}^L (-1)^m R_{L,-m}^{\{\sigma\}} \hat{T}_{L,m}(\mathbf{I}, \mathbf{B}). \quad (\text{A.172})$$

Here  $\hat{T}_{L,m}(\mathbf{I}, \mathbf{B})$  is formed from the spin angular momentum vector  $\mathbf{I}$  and the magnetic field vector  $\mathbf{B}$ . Using the Clebsch-Gordon coefficients we expand  $\hat{T}_{L,m}(\mathbf{I}, \mathbf{B})$  in Eq. (A.172) to obtain

$$\hat{T}_{L,m}(\mathbf{I}, \mathbf{B}) = \sum_{n=-1}^1 \langle L \ m | 1 \ 1 \ n+m \ -n \rangle \hat{T}_{1,n+m}(\mathbf{I}) B_{1,-n}, \quad (\text{A.173})$$

and since we normally define  $B_{1,0} = B_0$  and  $B_{1,\pm 1} = 0$ , this becomes

$$\hat{T}_{L,m}(\mathbf{I}, \mathbf{B}) = \langle L \ m | 1 \ 1 \ m \ 0 \rangle \hat{T}_{1,m}(\mathbf{I}) B_{1,0}, \quad (\text{A.174})$$

giving us

$$\hat{\mathcal{H}}_\sigma = -\hbar\omega_0 \sum_{L=0}^2 \sum_{m=-1}^1 (-1)^m R_{L,-m}^{\{\sigma\}} \langle L \ m | 1 \ 1 \ m \ 0 \rangle \hat{T}_{1,m}(\mathbf{I}), \quad (\text{A.175})$$

where

$$R_{0,0}^{\{\sigma\}} = -\sqrt{3} \sigma_{\text{iso}}, \quad (\text{A.176})$$

$$R_{1,0}^{\{\sigma\}} = -(i/\sqrt{2})[\sigma_{xy} - \sigma_{yx}], \quad (\text{A.177})$$

$$R_{1,\pm 1}^{\{\sigma\}} = -\frac{1}{2}[\sigma_{zx} - \sigma_{xz} \pm i(\sigma_{zy} - \sigma_{yz})], \quad (\text{A.178})$$

$$R_{2,0}^{\{\sigma\}} = \sqrt{\frac{1}{2}}[\sigma_{zz} - \sigma_{\text{iso}}], \quad (\text{A.179})$$

$$R_{2,\pm 1}^{\{\sigma\}} = \mp \frac{1}{2}[\sigma_{xz} + \sigma_{zx} \pm i(\sigma_{yz} + \sigma_{zy})], \quad (\text{A.180})$$

$$R_{2,\pm 2}^{\{\sigma\}} = \frac{1}{2}[\sigma_{xx} - \sigma_{yy} \pm i(\sigma_{xy} + \sigma_{yx})]. \quad (\text{A.181})$$

Here we follow the IUPAC definitions for the nuclear shielding or nuclear shielding interaction[93]. The isotropic nuclear shielding,  $\sigma_{\text{iso}}$ , is derived from the trace of the shielding tensor,

$$\sigma_{\text{iso}} = \frac{1}{3}(\sigma_{xx} + \sigma_{yy} + \sigma_{zz}). \quad (\text{A.182})$$

In the principal axis system of the antisymmetric shielding tensor, we define

$$\rho_{1,0}^{\{\sigma\}} = -i\sqrt{2} \zeta_\sigma^{(a)}, \quad \rho_{1,\pm 1}^{\{\sigma\}} = 0, \quad (\text{A.183})$$

where

$$\zeta_\sigma^{(a)} = \frac{1}{2} \sqrt{(\sigma_{xy} - \sigma_{yx})^2 + (\sigma_{yz} - \sigma_{zy})^2 + (\sigma_{zx} - \sigma_{xz})^2}. \quad (\text{A.184})$$

In the principal axis system of the second-rank symmetric Cartesian shielding tensor, where  $\lambda_{xx}^{\{\sigma\}}$ ,  $\lambda_{yy}^{\{\sigma\}}$ , and  $\lambda_{zz}^{\{\sigma\}}$  are the principal components of the symmetric part of the shielding tensor, we define

$$\rho_{2,0}^{\{\sigma\}} = \sqrt{\frac{3}{2}} \zeta_\sigma, \quad \rho_{2,\pm 1}^{\{\sigma\}} = 0, \quad \rho_{2,\pm 2}^{\{\sigma\}} = -\eta_\sigma \zeta_\sigma / 2. \quad (\text{A.185})$$

where the second-rank symmetric nuclear shielding tensor anisotropy,  $\zeta_\sigma$ , is defined as

$$\zeta_\sigma = \lambda_{zz}^{\{\sigma\}}, \quad (\text{A.186})$$

the second-rank symmetric nuclear shielding tensor asymmetry parameter is defined as

$$\eta_\sigma = \frac{\lambda_{yy}^{\{\sigma\}} - \lambda_{xx}^{\{\sigma\}}}{\zeta_\sigma}. \quad (\text{A.187})$$

*First-order nuclear shielding correction.* The nuclear shielding is generally orders of magnitude smaller in strength than the Zeeman interaction and therefore can be approximated to high accuracy using first-order perturbation theory as

$$\hat{D}_\sigma^{(1)} = -\hbar\omega_0 \sum_{L=0}^2 R_{L,0}^{\{\sigma\}} \langle L \ 0 | 1 \ 1 \ 0 \ 0 \rangle \hat{T}_{1,0}(\mathbf{I}). \quad (\text{A.188})$$

Since  $\langle 1 \ 0 | 1 \ 1 \ 0 \ 0 \rangle = 0$ , the anti-symmetric ( $L = 1$ ) components do not contribute to the first-order nuclear shielding Hamiltonian[112], and we obtain in the rotating tilted frame

$$\hat{D}_\sigma^{(1)} = -\hbar\omega_0 \left\{ -\sqrt{\frac{1}{3}} R_{0,0}^{\{\sigma\}} + \sqrt{\frac{2}{3}} R_{2,0}^{\{\sigma\}} \right\} \hat{T}_{1,0}^\circ(\mathbf{I}). \quad (\text{A.189})$$

We write the first-order nuclear shielding contribution to the  $|i\rangle \rightarrow |j\rangle$  transition frequency as

$$\Omega_\sigma^{(1)}(\Theta, m_i, m_j) = -\omega_0 \sigma_{\text{iso}} \mathbb{S}^{\{\sigma\}} \mathbb{P}_I(m_i, m_j) - \omega_0 \zeta_\sigma \mathbb{D}^{\{\sigma\}}(\Theta) \mathbb{P}_I(m_i, m_j). \quad (\text{A.190})$$

where

$$\mathbb{S}^{\{\sigma\}} = -\sqrt{\frac{1}{3}} \frac{R_{0,0}^{\{\sigma\}}}{\sigma_{\text{iso}}} = 1, \quad \mathbb{D}^{\{\sigma\}}(\Theta_\sigma) = \sqrt{\frac{2}{3}} \frac{R_{2,0}^{\{\sigma\}}(\Theta_\sigma)}{\zeta_\sigma}, \quad (\text{A.191})$$

and

$$\mathbb{P}_I(m_i, m_j) = \langle I, m_j | \hat{T}_{1,0}^\circ(\mathbf{I}) | I, m_j \rangle - \langle I, m_i | \hat{T}_{1,0}^\circ(\mathbf{I}) | I, m_i \rangle = m_j - m_i. \quad (\text{A.192})$$

*Nuclear Shielding - Electric Quadrupole Cross Term.* To obtain the second-order cross-term contribution between the nuclear shielding and the electric quadrupole coupling, we expand  $E^{(2)}$  in the eigenbasis  $|i\rangle$ :

$$E_{\sigma,q,i}^{(2)} = \frac{1}{\hbar\omega_0} \sum_{\substack{j=-I \\ j \neq i}}^I \frac{\langle i | \hat{\mathcal{H}}_\sigma | j \rangle \langle j | \hat{\mathcal{H}}_q | i \rangle}{i - j} + \frac{1}{\hbar\omega_0} \sum_{\substack{j=-I \\ j \neq i}}^I \frac{\langle i | \hat{\mathcal{H}}_q | j \rangle \langle j | \hat{\mathcal{H}}_\sigma | i \rangle}{i - j}. \quad (\text{A.193})$$

Using the irreducible tensor expansion of  $\hat{\mathcal{H}}_\sigma$  and  $\hat{\mathcal{H}}_q$ , we obtain

$$E_{\sigma,q,i}^{(2)} = -\hbar\omega_q \sum_{L=0}^2 \sum_{\substack{m=-1 \\ m \neq 0}}^1 \frac{\langle L \ m | 1 \ 1 \ m \ 0 \rangle}{m} R_{L,-m}^{\{\sigma\}} \frac{R_{2,m}^{\{q\}}}{3\zeta_q} \times \left\{ \langle i | \hat{T}_{1,m}(\mathbf{I}) \hat{T}_{2,-m}(\mathbf{I}) | i \rangle - \langle i | \hat{T}_{2,-m}(\mathbf{I}) \hat{T}_{1,m}(\mathbf{I}) | i \rangle \right\}. \quad (\text{A.194})$$

Substituting this into Eq. (A.52) and noting again that the operators commute with  $|i\rangle\langle i|$ , we obtain

$$\hat{D}_{\sigma,q}^{(2)}/\hbar = -\omega_q \sum_{L=0}^2 \sum_{\substack{m=-1 \\ m \neq 0}}^1 \frac{\langle L \ m | 1 \ 1 \ m \ 0 \rangle}{m} R_{L,-m}^{\{\sigma\}} \frac{R_{2,m}^{\{q\}}}{3\zeta_q} \left[ \hat{T}_{1,m}(\mathbf{I}), \hat{T}_{2,-m}(\mathbf{I}) \right]. \quad (\text{A.195})$$

Using the results of Section A.4, we simplify this expression to

$$\hat{D}_{\sigma,q}^{(2)}/\hbar = -\omega_q \left[ \pi_{1,1}^{\{1,2\}} \frac{\mathcal{A}_{1,0}^{\{\sigma q\}}}{3\zeta_q} + \pi_{1,3}^{\{1,2\}} \frac{\mathcal{A}_{3,0}^{\{\sigma q\}}}{3\zeta_q} + \pi_{2,0}^{\{1,2\}} \frac{\mathcal{R}_{0,0}^{\{\sigma q\}}}{3\zeta_q} + \pi_{2,2}^{\{1,2\}} \frac{\mathcal{R}_{2,0}^{\{\sigma q\}}}{3\zeta_q} + \pi_{2,4}^{\{1,2\}} \frac{\mathcal{R}_{4,0}^{\{\sigma q\}}}{3\zeta_q} \right] \hat{T}_{2,0}^\circ(\mathbf{I}), \quad (\text{A.196})$$

where the product involving the antisymmetric part of the shielding tensor is given by

$$\mathcal{A}_{L,M}^{\{\sigma q\}} = \sum_{m=-1}^1 \langle L \ M | 1 \ 2 \ m \ M-m \rangle R_{1,m}^{\{\sigma\}} R_{2,M-m}^{\{q\}}, \quad (\text{A.197})$$

and the product involving the symmetric part of the shielding tensor by

$$\mathcal{R}_{L,M}^{\{\sigma q\}} = \sum_{m=-2}^2 \langle L \ M | 2 \ 2 \ m \ M-m \rangle R_{2,m}^{\{\sigma\}} R_{2,M-m}^{\{q\}}. \quad (\text{A.198})$$

The coefficient  $\pi_{L,J}^{\{1,2\}}$  is given by

$$\pi_{L,K}^{\{1,2\}} = \sqrt{6} [\langle L-1 | 1 \ 1 \ -1 \ 0 \rangle \langle 2 \ 0 | 1 \ 2 \ -1 \ 1 \rangle \langle K \ 0 | L \ 2 \ m \ -1 \rangle - \langle L \ 1 | 1 \ 1 \ 1 \ 0 \rangle \langle 2 \ 0 | 1 \ 2 \ 1 \ -1 \rangle \langle K \ 0 | L \ 2 \ -1 \ 1 \rangle] \quad (\text{A.199})$$

Using the symmetry properties of the Clebsch Gordon coefficients, however, one can rearrange Eq. (A.199) to obtain

$$\pi_{L,K}^{\{1,2\}} = \sqrt{6} \langle L-1 | 1 \ 1 \ -1 \ 0 \rangle \langle 2 \ 0 | 1 \ 2 \ -1 \ 1 \rangle \langle K \ 0 | L \ 2 \ 1 \ -1 \rangle [1 + (-1)^K], \quad (\text{A.200})$$

indicating that the  $\pi_{L,K}^{\{1,2\}}$  coefficients with odd  $K$  vanish, whereas the coefficients with even  $K$  are given by

$$\pi_{L,K}^{\{1,2\}} = 2\sqrt{6} \langle L-1 | 1 \ 1 \ -1 \ 0 \rangle \langle 2 \ 0 | 1 \ 2 \ -1 \ 1 \rangle \langle K \ 0 | L \ 2 \ 1 \ -1 \rangle, \quad (\text{A.201})$$

which evaluate to

$$\pi_{2,0}^{\{1,2\}} = \sqrt{\frac{6}{5}}, \quad \pi_{2,2}^{\{1,2\}} = -\sqrt{\frac{3}{7}}, \quad \pi_{2,4}^{\{1,2\}} = -\sqrt{\frac{48}{35}}. \quad (\text{A.202})$$

Thus, the anti-symmetric contributions vanish and leave the second-order correction involving the nuclear shielding tensor as

$$\hat{D}_{\sigma,q}^{(2)}/\hbar = -\omega_q \left( \sum_{K=0,2,4} \pi_{2,K}^{\{1,2\}} \frac{\mathcal{R}_{K,0}^{\{\sigma q\}}}{3\zeta_q} \right) \hat{T}_{2,0}^{\circ}(\mathbf{I}). \quad (\text{A.203})$$

We can write the contribution to the  $|i\rangle \rightarrow |j\rangle$  transition frequency from the second-order cross term between the nuclear shielding and quadrupole coupling as

$$\Omega_{\sigma,q}^{(2)}(\Theta, m_i, m_j) = -\omega_q \zeta_{\sigma} \mathcal{S}^{\{\sigma q\}} \mathfrak{d}_I(m_i, m_j) - \omega_q \zeta_{\sigma} \mathcal{D}^{\{\sigma q\}}(\Theta) \mathfrak{d}_I(m_i, m_j) - \omega_q \zeta_{\sigma} \mathcal{G}^{\{\sigma q\}}(\Theta) \mathfrak{d}_I(m_i, m_j), \quad (\text{A.204})$$

where

$$\mathcal{S}^{\{\sigma q\}} = \sqrt{\frac{6}{5}} \frac{\mathcal{R}_{0,0}^{\{\sigma q\}}}{3\zeta_q \zeta_{\sigma}}, \quad (\text{A.205})$$

$$\mathcal{D}^{\{\sigma q\}}(\Theta) = -\sqrt{\frac{3}{7}} \frac{\mathcal{R}_{2,0}^{\{\sigma q\}}(\Theta)}{3\zeta_q \zeta_{\sigma}}, \quad (\text{A.206})$$

$$\mathcal{G}^{\{\sigma q\}}(\Theta) = -\sqrt{\frac{48}{35}} \frac{\mathcal{R}_{4,0}^{\{\sigma q\}}(\Theta)}{3\zeta_q \zeta_{\sigma}}. \quad (\text{A.207})$$

#### A.6.4. $J$ coupling

The  $J$  Coupling Hamiltonian can be written

$$\hat{\mathcal{H}}_J = \hat{\boldsymbol{\mu}}_1 \cdot \mathcal{K} \cdot \hat{\boldsymbol{\mu}}_2 = \hbar^2 \gamma_1 \gamma_2 \hat{\mathbf{I}}_1 \cdot \mathcal{K} \cdot \hat{\mathbf{I}}_2. \quad (\text{A.208})$$

The convention, however, is to combine the gyromagnetic ratio constants and the *reduced*  $\mathcal{K}$  tensor such that

$$\hat{\mathcal{H}}_J = \hbar \ 2\pi \ \hat{\mathbf{I}}_1 \cdot \mathbf{J} \cdot \hat{\mathbf{I}}_2, \quad (\text{A.209})$$

with

$$\mathbf{J} = \frac{\hbar \gamma_1 \gamma_2}{2\pi} \mathcal{K}. \quad (\text{A.210})$$

This gives a  $\mathbf{J}$  tensor with dimensions of inverse time. Thus, we write the  $J$  coupling Hamiltonian in terms of irreducible spherical tensors

$$\hat{\mathcal{H}}_J = \hbar \ 2\pi \sum_{L=0}^2 \sum_{m=-L}^L (-1)^m R_{L,-m}^{\{J\}} \hat{T}_{L,m}(\mathbf{I}_1, \mathbf{I}_2), \quad (\text{A.211})$$

where the  $\hat{T}_{L,m}(\mathbf{I}_1, \mathbf{I}_2)$  are formed from the spin angular momentum vectors  $\mathbf{I}_1$  and  $\mathbf{I}_2$ , given by the expansion

$$\hat{T}_{L,m}(\mathbf{I}_1, \mathbf{I}_2) = \sum_{n=-1}^1 \langle L \ m | 1 \ 1 \ n+m \ -n \rangle \hat{T}_{1,n+m}(\mathbf{I}_1) \hat{T}_{1,-n}(\mathbf{I}_2), \quad (\text{A.212})$$

and

$$R_{0,0}^{\{J\}} = -\sqrt{3} J_{iso}, \quad (\text{A.213})$$

$$R_{1,0}^{\{J\}} = -(i/\sqrt{2})[J_{xy} - J_{yx}], \quad (\text{A.214})$$

$$R_{1,\pm 1}^{\{J\}} = -\frac{1}{2}[J_{zx} - J_{xz} \pm i(J_{zy} - J_{yz})], \quad (\text{A.215})$$

$$R_{2,0}^{\{J\}} = \sqrt{\frac{1}{2}}[J_{zz} - J_{iso}], \quad (\text{A.216})$$

$$R_{2,\pm 1}^{\{J\}} = \mp \frac{1}{2}[J_{xz} + J_{zx} \pm i(J_{yz} + J_{zy})], \quad (\text{A.217})$$

$$R_{2,\pm 2}^{\{J\}} = \frac{1}{2}[J_{xx} - J_{yy} \pm i(J_{xy} + J_{yx})]. \quad (\text{A.218})$$

The isotropic  $J$  coupling,  $J_{iso}$ , is derived from the trace of the  $J$  coupling tensor,

$$J_{iso} = \frac{1}{3}(J_{xx} + J_{yy} + J_{zz}). \quad (\text{A.219})$$

In the principal axis system of the first-rank antisymmetric  $J$  coupling tensor, we define

$$\rho_{1,0}^{\{J\}} = -i\sqrt{2} \zeta_J^{(a)}, \quad \rho_{1,\pm 1}^{\{J\}} = 0, \quad (\text{A.220})$$

where

$$\zeta_J^{(a)} = \frac{1}{2}\sqrt{(J_{xy} - J_{yx})^2 + (J_{yz} - J_{zy})^2 + (J_{zx} - J_{xz})^2}. \quad (\text{A.221})$$

In the principal axis system of the second-rank symmetric  $J$  coupling Cartesian tensor, where  $\lambda_{xx}^{\{J\}}$ ,  $\lambda_{yy}^{\{J\}}$ , and  $\lambda_{zz}^{\{J\}}$  are principal components, we define

$$\rho_{2,0}^{\{J\}} = \sqrt{\frac{3}{2}}\zeta_J, \quad \rho_{2,\pm 1}^{\{J\}} = 0, \quad \rho_{2,\pm 2}^{\{J\}} = -\eta_J \zeta_J/2. \quad (\text{A.222})$$

where the second-rank symmetric  $J$  coupling tensor anisotropy,  $\zeta_J$ , is defined as

$$\zeta_J = \lambda_{zz}^{\{J\}}, \quad (\text{A.223})$$

the second-rank symmetric  $J$  coupling tensor asymmetry parameter is defined as

$$\eta_J = \frac{\lambda_{yy}^{\{J\}} - \lambda_{xx}^{\{J\}}}{\zeta_J}. \quad (\text{A.224})$$

*First-Order  $J$ -Coupling Correction..* Like nuclear shielding, the  $J$  coupling is orders of magnitude smaller in strength than the Zeeman interaction. Thus, following our earlier approach, the first-order Hamiltonian in the strong coupling limit is obtained by eliminating  $m \neq 0$  terms to obtain

$$\hat{D}_{JI}^{(1)}/\hbar = 2\pi \sum_{L=0}^2 R_{L,0}^{\{J\}} \hat{T}_{L,0}^\circ(\mathbf{I}_1, \mathbf{I}_2). \quad (\text{A.225})$$

The first-order strong  $J$  coupling correction to the transition frequency is

$$\begin{aligned} \Omega_{JI}^{(1)}(\Theta, M_i, M_j) &= 2\pi J_{iso} \mathbb{S}^{\{JI\}} \mathfrak{s}_{II}(M_i, M_j) \\ &+ 2\pi \zeta_J^{(a)} \mathbb{P}^{\{JI\}}(\Theta) \mathbb{p}_{II}(M_i, M_j) + 2\pi \zeta_J \mathbb{D}^{\{JI\}}(\Theta) \mathfrak{d}_{II}(M_i, M_j). \end{aligned} \quad (\text{A.226})$$

where

$$\mathbb{S}^{\{JI\}} = -\frac{R_{0,0}^{\{J\}}}{J_{iso}}, \quad (\text{A.227})$$

$$\mathbb{P}^{\{JI\}}(\Theta) = \frac{R_{1,0}^{\{J\}}(\Theta)}{\zeta_J^{(a)}}, \quad (\text{A.228})$$

$$\mathbb{D}^{\{JI\}}(\Theta) = \frac{R_{2,0}^{\{J\}}(\Theta)}{\zeta_J}, \quad (\text{A.229})$$



and

$$\mathfrak{s}_{II}(M_i, M_j) = \langle I, M_j | \hat{T}_{0,0}^\circ(\mathbf{I}_1, \mathbf{I}_2) | I, M_j \rangle - \langle I, M_i | \hat{T}_{0,0}^\circ(\mathbf{I}_1, \mathbf{I}_2) | I, M_i \rangle, \quad (\text{A.230})$$

$$\mathbb{P}_{II}(M_i, M_j) = \langle I, M_j | \hat{T}_{1,0}^\circ(\mathbf{I}_1, \mathbf{I}_2) | I, M_j \rangle - \langle I, M_i | \hat{T}_{1,0}^\circ(\mathbf{I}_1, \mathbf{I}_2) | I, M_i \rangle, \quad (\text{A.231})$$

$$\mathfrak{d}_{II}(M_i, M_j) = \langle I, M_j | \hat{T}_{2,0}^\circ(\mathbf{I}_1, \mathbf{I}_2) | I, M_j \rangle - \langle I, M_i | \hat{T}_{2,0}^\circ(\mathbf{I}_1, \mathbf{I}_2) | I, M_i \rangle. \quad (\text{A.232})$$

One can show, however, that  $\mathfrak{s}_{II} = 0$ , and thus the first-order strong  $J$  coupling becomes

$$\Omega_{J_{II}}^{(1)}(\Theta, M_i, M_j) = 2\pi\zeta_J^{(a)} \mathbb{P}^{\{J_{II}\}}(\Theta) \mathbb{P}_{II}(M_i, M_j) + 2\pi\zeta_J \mathbb{D}^{\{J_{II}\}}(\Theta) \mathfrak{d}_{II}(M_i, M_j). \quad (\text{A.233})$$

It is interesting to note that the antisymmetric part of the  $J$  tensor is not only observable in the strong coupling case but also has a contribution with  $\mathbb{P}$  spatial symmetry that is not removed by D-MAS[25].

To obtain the first-order Hamiltonian in the weak coupling limit Eq. (A.212) is substituted into Eq. (A.211), replacing  $I_1$  with  $I$  and  $I_2$  with  $S$ , and again eliminating  $m \neq 0$  terms to obtain

$$\hat{D}_{J_{IS}}^{(1)} = \hbar 2\pi \sum_{L=0}^2 \langle L 0 | 1 1 0 0 \rangle R_{L,0}^{\{J\}} \hat{T}_{1,0}(\mathbf{I}_1) \hat{T}_{1,0}(\mathbf{I}_2). \quad (\text{A.234})$$

Since  $\langle L 0 | 1 1 0 0 \rangle = 0$ , the  $L = 1$  term disappears and the first-order energy correction is

$$\hat{D}_{J_{IS}}^{(1)} = \hbar 2\pi \sum_{L=0,2} \langle L 0 | 1 1 0 0 \rangle R_{L,0}^{\{J\}} \hat{T}_{1,0}^\circ(\mathbf{I}_1) \hat{T}_{1,0}^\circ(\mathbf{I}_2). \quad (\text{A.235})$$

The first-order weak  $J$  coupling correction to the transition frequency is,

$$\begin{aligned} \Omega_{J_{IS}}^{(1)}(\Theta, m_{I,i}, m_{S,i}, m_{I,j}, m_{S,j}) &= 2\pi J_{iso} \mathbb{S}^{\{J_{IS}\}} \mathfrak{d}_{IS}(m_{I,i}, m_{S,i}, m_{I,j}, m_{S,j}) \\ &\quad + 2\pi\zeta_J \mathbb{D}^{\{J_{IS}\}}(\Theta) \mathfrak{d}_{IS}(m_{I,i}, m_{S,i}, m_{I,j}, m_{S,j}), \end{aligned} \quad (\text{A.236})$$

where

$$\mathbb{S}^{\{J_{IS}\}} = -\sqrt{\frac{1}{3}} \frac{R_{0,0}^{\{J\}}}{J_{iso}} = 1, \quad (\text{A.237})$$

$$\mathbb{D}^{\{J_{IS}\}}(\Theta) = \sqrt{\frac{2}{3}} \frac{R_{2,0}^{\{J\}}(\Theta)}{\zeta_J}, \quad (\text{A.238})$$

and the  $\mathfrak{d}_{IS}$  are calculated in the weakly coupled basis set,  $|m_I m_S\rangle$ ,

$$\begin{aligned} \mathfrak{d}_{IS}(m_{I,i}, m_{S,i}, m_{I,j}, m_{S,j}) &= \\ \langle m_{I,j}, m_{S,j} | \hat{T}_{1,0}^\circ(\mathbf{I}) \hat{T}_{1,0}^\circ(\mathbf{S}) | m_{I,i}, m_{S,i} \rangle &- \langle m_{I,i}, m_{S,i} | \hat{T}_{1,0}^\circ(\mathbf{I}) \hat{T}_{1,0}^\circ(\mathbf{S}) | m_{I,j}, m_{S,j} \rangle \\ &= m_{I,j} m_{S,j} - m_{I,i} m_{S,i}, \end{aligned} \quad (\text{A.239})$$

*J-Coupling Quadrupolar Cross Term.* Here, we derive the second-order energy cross term between the  $J$  and quadrupole couplings, but only in the weakly  $J$  coupled limit using the  $|m_I m_S\rangle$  basis. Generally, we allow both nuclei to have electric quadrupole moments and separate the second-order energy correction into two terms

$$E_{J,q,m_I m_S}^{(2)} = E_{J,q_I,m_I m_S}^{(2)} + E_{J,q_S,m_I m_S}^{(2)}, \quad (\text{A.240})$$

where

$$\begin{aligned} E_{J,q_I,m_I m_S}^{(2)} &= \sum_{m'_I=-I}^I \sum_{m'_S=-S}^S \frac{\langle m_I m_S | \hat{\mathcal{H}}_J^{\{IS\}} | m'_I m'_S \rangle \langle m'_I m'_S | \hat{\mathcal{H}}_q^{\{I\}} | m_I m_S \rangle}{\hbar(m'_I - m_I)\omega_0^{\{I\}} + \hbar(m'_S - m_S)\omega_0^{\{S\}}} \\ &\quad + \sum_{m'_I=-I}^I \sum_{m'_S=-S}^S \frac{\langle m_I m_S | \hat{\mathcal{H}}_q^{\{I\}} | m'_I m'_S \rangle \langle m'_I m'_S | \hat{\mathcal{H}}_J^{\{IS\}} | m_I m_S \rangle}{\hbar(m'_I - m_I)\omega_0^{\{I\}} + \hbar(m'_S - m_S)\omega_0^{\{S\}}}, \end{aligned} \quad (\text{A.241})$$

and

$$E_{J,qS,m_I m_S}^{(2)} = \sum_{m'_I=-I}^I \sum_{m'_S=-S}^S \frac{\langle m_I m_S | \hat{\mathcal{H}}_J^{\{IS\}} | m'_I m'_S \rangle \langle m'_I m'_S | \hat{\mathcal{H}}_q^{\{S\}} | m_I m_S \rangle}{\hbar(m'_I - m_I)\omega_0^{\{I\}} + \hbar(m'_S - m_S)\omega_0^{\{S\}}} + \sum_{m'_I=-I}^I \sum_{m'_S=-S}^S \frac{\langle m_I m_S | \hat{\mathcal{H}}_q^{\{S\}} | m'_I m'_S \rangle \langle m'_I m'_S | \hat{\mathcal{H}}_J^{\{IS\}} | m_I m_S \rangle}{\hbar(m'_I - m_I)\omega_0^{\{I\}} + \hbar(m'_S - m_S)\omega_0^{\{S\}}}. \quad (\text{A.242})$$

Here,  $E_{J,qI,m_I m_S}^{(2)}$  and  $E_{J,qS,m_I m_S}^{(2)}$  are the cross terms associated with the electric quadrupole moment on nucleus  $I$  and  $S$ , respectively. Although not indicated, values of  $m'_I$  and  $m'_S$  that cause the denominator to go to zero are disallowed in both expressions. We first focus on the  $I$  spin cross term, substituting our expressions for  $\hat{\mathcal{H}}_q$  and  $\hat{\mathcal{H}}_J$  to obtain

$$E_{J,qI,m_I m_S}^{(2)} = 2\pi\hbar\omega_q^{\{I\}} \sum_{L=0}^2 \sum_{n=-1}^1 \sum_{m=-2}^2 \sum_{m'=-2}^2 \langle L \ m | 1 \ 1 \ n+m \ -n \rangle (-1)^{m+m'} R_{L,-m}^{\{J\}} \frac{R_{2,-m'}^{\{qI\}}}{3\zeta_q^{\{I\}}} \times \sum_{m'_I=-I}^I \sum_{m'_S=-S}^S \frac{\langle m_I m_S | \hat{T}_{1,n+m}(\mathbf{I}) \hat{T}_{1,-n}(\mathbf{S}) | m'_I m'_S \rangle \langle m'_I m'_S | \hat{T}_{2,m'}(\mathbf{I}) | m_I m_S \rangle}{(m'_I - m_I)\omega_0^{\{I\}} + (m'_S - m_S)\omega_0^{\{S\}}} + 2\pi\hbar\omega_q^{\{I\}} \sum_{L=0}^2 \sum_{n=-1}^1 \sum_{m=-2}^2 \sum_{m'=-2}^2 \langle L \ m | 1 \ 1 \ n+m \ -n \rangle (-1)^{m+m'} \times \frac{R_{2,-m'}^{\{qI\}}}{3\zeta_q^{\{I\}}} R_{L,-m}^{\{J\}} \times \sum_{m'_I=-I}^I \sum_{m'_S=-S}^S \frac{\langle m_I m_S | \hat{T}_{2,m'}(\mathbf{I}) | m'_I m'_S \rangle \langle m'_I m'_S | \hat{T}_{1,n+m}(\mathbf{I}) \hat{T}_{1,-n}(\mathbf{S}) | m_I m_S \rangle}{(m'_I - m_I)\omega_0^{\{I\}} + (m'_S - m_S)\omega_0^{\{S\}}}. \quad (\text{A.243})$$

Using the general selection rules for irreducible tensor operator matrix elements, the first matrix element gives the constraints  $m_I = m'_I + n + m$  and  $m_S = m'_S - n$ , and the second matrix element gives  $m'_I = m_I + m'$  and  $m'_S = m_S$ . Combining these constraints gives  $n = 0$  and  $m + m' = 0$  in the first term. Similarly, the third matrix element gives the constraints  $m'_S = m_S$  and  $m_I = m'_I + m'$  and the fourth matrix element gives  $m'_I = m_I + n + m$  and  $m'_S = m_S - n$ . Combining these constraints also gives  $n = 0$  and  $m + m' = 0$  in the second term. Thus, we have

$$E_{J,qI,m_I m_S}^{(2)} = -2\pi \frac{\hbar\omega_q^{\{I\}}}{\omega_0^{\{I\}}} \sum_{L=1}^2 \sum_{\substack{m=-1 \\ m \neq 0}}^1 \frac{\langle L \ m | 1 \ 1 \ m \ 0 \rangle}{m} R_{L,-m}^{\{J\}} \frac{R_{2,m}^{\{qI\}}}{3\zeta_q^{\{I\}}} \times \langle m_I m_S | \hat{T}_{1,m}(\mathbf{I}) \hat{T}_{1,0}(\mathbf{S}) | m_I - m \ m_S \rangle \langle m_I - m \ m_S | \hat{T}_{2,-m}(\mathbf{I}) | m_I m_S \rangle + 2\pi \frac{\hbar\omega_q^{\{I\}}}{\omega_0^{\{I\}}} \sum_{L=1}^2 \sum_{\substack{m=-1 \\ m \neq 0}}^1 \frac{\langle L \ m | 1 \ 1 \ m \ 0 \rangle}{m} \frac{R_{2,m}^{\{qI\}}}{3\zeta_q^{\{I\}}} R_{L,-m}^{\{J\}} \times \langle m_I m_S | \hat{T}_{2,-m}(\mathbf{I}) | m_I + m \ m_S \rangle \langle m_I + m \ m_S | \hat{T}_{1,m}(\mathbf{I}) \hat{T}_{1,0}(\mathbf{S}) | m_I m_S \rangle. \quad (\text{A.244})$$

Using the projection operator of Eq. (A.282) and substituting into Eq. (A.52), we obtain

$$\hat{D}_{J,qI}^{(2)}/\hbar = 2\pi \left( \frac{\omega_q^{\{I\}}}{\omega_0^{\{I\}}} \right) \sum_{L=1}^2 \sum_{\substack{m=-1 \\ m \neq 0}}^1 \frac{\langle L \ m | 1 \ 1 \ m \ 0 \rangle}{m} R_{L,-m}^{\{J\}} \frac{R_{2,m}^{\{qI\}}}{3\zeta_q^{\{I\}}} \left[ \hat{T}_{1,m}(\mathbf{I}), \hat{T}_{2,-m}(\mathbf{I}) \right] \hat{T}_{1,0}(\mathbf{S}). \quad (\text{A.245})$$

Using the results of Section A.4, we can simplify this expression to

$$\begin{aligned} \hat{D}_{J,q_I}^{(2)}/\hbar = 2\pi \left( \frac{\omega_q^{\{I\}}}{\omega_0^{\{I\}}} \right) & \left[ \pi_{1,1}^{\{1,2\}} \frac{\mathcal{A}_{1,0}^{\{Jq_I\}}}{3\zeta_q^{\{I\}}} \hat{T}_{2,0}(\mathbf{I}) \hat{T}_{1,0}(\mathbf{S}) + \pi_{1,3}^{\{1,2\}} \frac{\mathcal{A}_{3,0}^{\{Jq_I\}}}{3\zeta_q^{\{I\}}} \hat{T}_{2,0}(\mathbf{I}) \hat{T}_{1,0}(\mathbf{S}) \right. \\ & + \pi_{2,0}^{\{1,2\}} \frac{\mathcal{R}_{0,0}^{\{Jq_I\}}}{3\zeta_q^{\{I\}}} \hat{T}_{2,0}(\mathbf{I}) \hat{T}_{1,0}(\mathbf{S}) + \pi_{2,2}^{\{1,2\}} \frac{\mathcal{R}_{2,0}^{\{Jq_I\}}}{3\zeta_q^{\{I\}}} \hat{T}_{2,0}(\mathbf{I}) \hat{T}_{1,0}(\mathbf{S}) \\ & \left. + \pi_{2,4}^{\{1,2\}} \frac{\mathcal{R}_{4,0}^{\{Jq_I\}}}{3\zeta_q^{\{I\}}} \hat{T}_{2,0}(\mathbf{I}) \hat{T}_{1,0}(\mathbf{S}) \right], \quad (\text{A.246}) \end{aligned}$$

where the product involving the antisymmetric part of the  $J$  tensor is given by

$$\mathcal{A}_{L,M}^{\{Jq_I\}} = \sum_{m=-1}^1 \langle L M | 1 2 m M-m \rangle R_{1,m}^{\{J\}} R_{2,M-m}^{\{q_I\}}, \quad (\text{A.247})$$

and the product involving the symmetric part of the  $J$  tensor by

$$\mathcal{R}_{L,M}^{\{Jq_I\}} = \sum_{m=-2}^2 \langle L M | 2 2 m M-m \rangle R_{2,m}^{\{J\}} R_{2,M-m}^{\{q_I\}}. \quad (\text{A.248})$$

As noted earlier, the  $\pi_{L,J}^{\{1,2\}}$  coefficients vanish for odd values of  $J$ , leaving only the symmetric tensor contributions

$$\hat{D}_{J,q_I}^{(2)}/\hbar = 2\pi \left( \frac{\omega_q^{\{I\}}}{\omega_0^{\{I\}}} \right) \left( \sum_{K=0,2,4} \pi_{2,K}^{\{1,2\}} \frac{\mathcal{R}_{K,0}^{\{Jq_I\}}}{3\zeta_q^{\{I\}}} \right) \hat{T}_{2,0}^\circ(\mathbf{I}) \hat{T}_{1,0}(\mathbf{S}). \quad (\text{A.249})$$

Using Eq. (A.156), the second-order contribution to the transition frequency between levels  $|m_I m_S\rangle$  and  $|m'_I m'_S\rangle$  is obtained

$$\begin{aligned} \Omega_{J,q_I}^{(2)}(\Theta, m_{I,i}, m_{S,i}, m_{I,j}, m_{S,j}) &= 2\pi\zeta_J \left( \frac{\omega_q^{\{I\}}}{\omega_0^{\{I\}}} \right) \mathbb{S}^{\{Jq_I\}}(\mathbb{d}\mathbb{p})_{IS}(m_{I,i}, m_{S,i}, m_{I,j}, m_{S,j}) \\ &+ 2\pi\zeta_J \left( \frac{\omega_q^{\{I\}}}{\omega_0^{\{I\}}} \right) \mathbb{D}^{\{Jq_I\}}(\Theta) (\mathbb{d}\mathbb{p})_{IS}(m_{I,i}, m_{S,i}, m_{I,j}, m_{S,j}) \\ &+ 2\pi\zeta_J \left( \frac{\omega_q^{\{I\}}}{\omega_0^{\{I\}}} \right) \mathbb{G}^{\{Jq_I\}}(\Theta) (\mathbb{d}\mathbb{p})_{IS}(m_{I,i}, m_{S,i}, m_{I,j}, m_{S,j}), \quad (\text{A.250}) \end{aligned}$$

where

$$\mathbb{S}^{\{Jq_I\}} = \sqrt{\frac{6}{5}} \frac{\mathcal{R}_{0,0}^{\{Jq_I\}}}{3\zeta_q^{\{I\}} \zeta_J}, \quad (\text{A.251})$$

$$\mathbb{D}^{\{Jq_I\}}(\Theta) = -\sqrt{\frac{3}{7}} \frac{\mathcal{R}_{2,0}^{\{Jq_I\}}(\Theta)}{3\zeta_q^{\{I\}} \zeta_J}, \quad (\text{A.252})$$

$$\mathbb{G}^{\{Jq_I\}}(\Theta) = -\sqrt{\frac{48}{35}} \frac{\mathcal{R}_{4,0}^{\{Jq_I\}}(\Theta)}{3\zeta_q^{\{I\}} \zeta_J}. \quad (\text{A.253})$$

and the  $\mathbb{d}\mathbb{p}_S(m_{I,i}, m_{S,i}, m_{I,j}, m_{S,j})$  are calculated in the weakly coupled basis set,  $|m_I m_S\rangle$ ,

$$\begin{aligned} \mathbb{d}\mathbb{p}_S(m_{I,i}, m_{S,i}, m_{I,j}, m_{S,j}) &= \langle m_{I,j}, m_{S,j} | \hat{T}_{2,0}^\circ(\mathbf{I}) \hat{T}_{1,0}^\circ(\mathbf{S}) | m_{I,j}, m_{S,j} \rangle - \langle m_{I,i}, m_{S,i} | \hat{T}_{2,0}^\circ(\mathbf{I}) \hat{T}_{1,0}^\circ(\mathbf{S}) | m_{I,i}, m_{S,i} \rangle \\ &= \sqrt{\frac{3}{2}} (m_{I,j}^2 m_{S,j} - m_{I,i}^2 m_{S,i}) - \frac{1}{\sqrt{6}} I(I+1)(m_{S,j} - m_{S,i}). \quad (\text{A.254}) \end{aligned}$$

Similarly, one obtains

$$\begin{aligned}\Omega_{J,q_S}^{(2)}(\Theta, m_{I,i}, m_{S,i}, m_{I,j}, m_{S,j}) &= 2\pi\zeta_J \left( \frac{\omega_q^{\{S\}}}{\omega_0^{\{S\}}} \right) \mathbb{S}^{\{Jq_S\}}(\mathbb{pd})_{IS}(m_{I,i}, m_{S,i}, m_{I,j}, m_{S,j}) \\ &+ 2\pi\zeta_J \left( \frac{\omega_q^{\{S\}}}{\omega_0^{\{S\}}} \right) \mathbb{D}^{\{Jq_S\}}(\Theta) (\mathbb{pd})_{IS}(m_{I,i}, m_{S,i}, m_{I,j}, m_{S,j}) \\ &+ 2\pi\zeta_J \left( \frac{\omega_q^{\{S\}}}{\omega_0^{\{S\}}} \right) \mathbb{G}^{\{Jq_S\}}(\Theta) (\mathbb{pd})_{IS}(m_{I,i}, m_{S,i}, m_{I,j}, m_{S,j}),\end{aligned}\quad (\text{A.255})$$

where

$$\mathbb{S}^{\{Jq_S\}} = \sqrt{\frac{6}{5}} \frac{\mathcal{R}_{0,0}^{\{Jq_S\}}}{3\zeta_q^{\{S\}}\zeta_J}, \quad (\text{A.256})$$

$$\mathbb{D}^{\{Jq_S\}}(\Theta) = -\sqrt{\frac{3}{7}} \frac{\mathcal{R}_{2,0}^{\{Jq_S\}}(\Theta)}{3\zeta_q^{\{S\}}\zeta_J}, \quad (\text{A.257})$$

$$\mathbb{G}^{\{Jq_S\}}(\Theta) = -\sqrt{\frac{48}{35}} \frac{\mathcal{R}_{4,0}^{\{Jq_S\}}(\Theta)}{3\zeta_q^{\{S\}}\zeta_J}, \quad (\text{A.258})$$

and the  $(\mathbb{pd})_{IS}$  are calculated in the weakly coupled basis set,  $|m_I m_S\rangle$ ,

$$\begin{aligned}(\mathbb{pd})_{IS}(m_{I,i}, m_{S,i}, m_{I,j}, m_{S,j}) &= \langle m_{I,j}, m_{S,j} | \hat{T}_{1,0}^\circ(\mathbf{I}) \hat{T}_{2,0}^\circ(\mathbf{S}) | m_{I,i}, m_{S,i} \rangle - \langle m_{I,i}, m_{S,i} | \hat{T}_{1,0}^\circ(\mathbf{I}) \hat{T}_{2,0}^\circ(\mathbf{S}) | m_{I,i}, m_{S,i} \rangle \\ &= \sqrt{\frac{3}{2}} (m_{S,j}^2 m_{I,j} - m_{S,i}^2 m_{I,i}) - \frac{1}{\sqrt{6}} S(S+1)(m_{I,j} - m_{I,i}).\end{aligned}\quad (\text{A.259})$$

#### A.6.5. Magnetic dipole coupling

The through-space magnetic dipole coupling Hamiltonian can be written

$$\hat{\mathcal{H}}_d = -\frac{\mu_0}{4\pi} \hat{\boldsymbol{\mu}}_1 \cdot \mathbf{D} \cdot \hat{\boldsymbol{\mu}}_2 = -\frac{\mu_0}{4\pi} \hbar^2 \gamma_1 \gamma_2 \hat{\mathbf{I}}_1 \cdot \mathbf{D} \cdot \hat{\mathbf{I}}_2, \quad (\text{A.260})$$

where  $\mu_0$  is the permeability constant ( $4\pi \times 10^{-7} \text{ kg}\cdot\text{m}/(\text{s}^2\cdot\text{A}^2)$ ) and  $\mathbf{D}$  is defined in a coordinate system with  $\boldsymbol{\mu}_1$  at the origin and  $\boldsymbol{\mu}_2$  at  $(x, y, z)$  and  $r$  as the distance between  $\boldsymbol{\mu}_1$  and  $\boldsymbol{\mu}_2$  and given by

$$D_{ik} = \frac{1}{r^3} \left( \frac{3r_i r_k}{r^2} - \delta_{ik} \right), \quad \text{where } (r_i, r_k = x, y, z). \quad (\text{A.261})$$

The dipolar coupling tensor,  $\mathbf{D}$ , is traceless and axially symmetric. The principal components of the  $\mathbf{D}$  tensor are

$$\lambda_{xx}^{\{d\}} = -\frac{1}{r^3}, \quad \lambda_{yy}^{\{d\}} = -\frac{1}{r^3}, \quad \lambda_{zz}^{\{d\}} = \frac{2}{r^3}. \quad (\text{A.262})$$

Writing the dipole coupling Hamiltonian in terms of irreducible spherical tensors, we have

$$\hat{\mathcal{H}}_d = -\frac{\mu_0}{4\pi} \hbar^2 \gamma_1 \gamma_2 \sum_{m=-2}^2 (-1)^m R_{2,-m}^{\{d\}} \hat{T}_{2,m}(\mathbf{I}_1, \mathbf{I}_2), \quad (\text{A.263})$$

where

$$R_{2,0}^{\{d\}} = \sqrt{\frac{3}{2}} D_{zz}, \quad (\text{A.264})$$

$$R_{2,\pm 1}^{\{d\}} = \mp (D_{zx} \pm i(D_{zy})), \quad (\text{A.265})$$

$$R_{2,\pm 2}^{\{d\}} = \frac{1}{2} [D_{xx} - D_{yy} \pm i2D_{xy}]. \quad (\text{A.266})$$

In the principal axis system of the dipolar coupling tensor, we define

$$\rho_{2,0}^{\{d\}} = \sqrt{\frac{3}{2}} \zeta_d, \quad \rho_{2,\pm 1}^{\{d\}} = 0, \quad \rho_{2,\pm 2}^{\{d\}} = 0. \quad (\text{A.267})$$

where the second-rank symmetric dipolar coupling tensor anisotropy,  $\zeta_d$ , is defined as

$$\zeta_d = \lambda_{zz}^{\{d\}} = \frac{2}{r^3}, \quad (\text{A.268})$$

The dipolar splitting is given by

$$\omega_d = -\frac{\mu_0}{4\pi} \frac{\gamma_1 \gamma_2 \hbar}{r^3} = -\frac{\mu_0}{8\pi} \zeta_d \gamma_1 \gamma_2 \hbar \quad (\text{A.269})$$

For convenience, in the derivations to follow, we express the dipole coupling Hamiltonian as

$$\hat{\mathcal{H}}_d/\hbar = \omega_d \sum_{m=-2}^2 (-1)^m \frac{R_{2,-m}^{\{d\}}}{\zeta_d/2} \hat{T}_{2,m}(\mathbf{I}_1, \mathbf{I}_2). \quad (\text{A.270})$$

*First-Order Magnetic Dipole Coupling Correction.* Like nuclear shielding, the dipolar coupling is generally orders of magnitude smaller in strength than the Zeeman interaction. Thus, following our earlier approach, the first-order Hamiltonian in the strong coupling limit is obtained by eliminating  $m \neq 0$  terms to obtain

$$\hat{D}_{d_{II}}^{(1)}/\hbar = \omega_d \frac{R_{2,0}^{\{d\}}}{\zeta_d/2} \hat{T}_{2,0}(\mathbf{I}_1, \mathbf{I}_2). \quad (\text{A.271})$$

The first-order strong dipolar coupling correction to the transition frequency is,

$$\Omega_{d_{II}}^{(1)}(\Theta, M_i, M_j) = \omega_d \mathbb{D}^{\{d_{II}\}}(\Theta) \mathfrak{d}_{II}(M_i, M_j), \quad (\text{A.272})$$

where

$$\mathbb{D}^{\{d_{II}\}}(\Theta) = \frac{R_{2,0}^{\{d\}}(\Theta)}{\zeta_d/2}, \quad (\text{A.273})$$

and the  $\mathfrak{d}_{II}$  are calculated in the strongly coupled basis set.

To obtain the first-order Hamiltonian in the weak coupling limit, Eq. (A.212) is substituted into Eq. (A.263), replacing  $I_1$  with  $I$  and  $I_2$  with  $S$ , and again eliminating  $m \neq 0$  terms to obtain

$$\hat{D}_{d_{IS}}^{(1)}/\hbar = \omega_d \sqrt{\frac{2}{3}} \frac{A_{2,0}^{\{d\}}}{\zeta_d/2} \hat{T}_{1,0}^\circ(\mathbf{I}) \hat{T}_{1,0}^\circ(\mathbf{S}). \quad (\text{A.274})$$

The first-order weak dipolar coupling correction to the transition frequency is,

$$\Omega_{d_{IS}}^{(1)}(\Theta, m_{I,i}, m_{S,i}, m_{I,j}, m_{S,j}) = \omega_d \mathbb{D}^{\{d_{IS}\}}(\Theta) \mathfrak{d}_{IS}(m_{I,i}, m_{S,i}, m_{I,j}, m_{S,j}), \quad (\text{A.275})$$

where

$$\mathbb{D}^{\{d_{IS}\}}(\Theta) = \sqrt{\frac{2}{3}} \frac{R_{2,0}^{\{d\}}(\Theta)}{\zeta_d/2}, \quad (\text{A.276})$$

and the  $\mathfrak{d}_{IS}(m_{I,i}, m_{S,i}, m_{I,j}, m_{S,j})$  are calculated in the weakly coupled basis set,  $|m_I m_S\rangle$ .

*Magnetic Dipole-Electric Quadrupole Coupling Cross Term in the Weak Dipole Coupling Limit.* Here, we derive the second-order energy cross term between the dipolar and quadrupole couplings, but only in the weakly dipolar coupled limit using the  $|m_I m_S\rangle$  basis. Generally, we allow both nuclei to have electric quadrupole moments and separate the second-order energy correction into two terms

$$E_{d,q,m_I m_S}^{(2)} = E_{d,q_I,m_I m_S}^{(2)} + E_{d,q_S,m_I m_S}^{(2)}, \quad (\text{A.277})$$

where

$$E_{d,qI,mIm_S}^{(2)} = \sum_{m'_I=-I}^I \sum_{m'_S=-S}^S \frac{\langle m_I m_S | \hat{\mathcal{H}}_d^{\{IS\}} | m'_I m'_S \rangle \langle m'_I m'_S | \hat{\mathcal{H}}_q^{\{I\}} | m_I m_S \rangle}{\hbar(m'_I - m_I)\omega_0^{\{I\}} + \hbar(m'_S - m_S)\omega_0^{\{S\}}} + \sum_{m'_I=-I}^I \sum_{m'_S=-S}^S \frac{\langle m_I m_S | \hat{\mathcal{H}}_q^{\{I\}} | m'_I m'_S \rangle \langle m'_I m'_S | \hat{\mathcal{H}}_d^{\{IS\}} | m_I m_S \rangle}{\hbar(m'_I - m_I)\omega_0^{\{I\}} + \hbar(m'_S - m_S)\omega_0^{\{S\}}}, \quad (\text{A.278})$$

and

$$E_{d,qS,mIm_S}^{(2)} = \sum_{m'_I=-I}^I \sum_{m'_S=-S}^S \frac{\langle m_I m_S | \hat{\mathcal{H}}_d^{\{IS\}} | m'_I m'_S \rangle \langle m'_I m'_S | \hat{\mathcal{H}}_q^{\{S\}} | m_I m_S \rangle}{\hbar(m'_I - m_I)\omega_0^{\{I\}} + \hbar(m'_S - m_S)\omega_0^{\{S\}}} + \sum_{m'_I=-I}^I \sum_{m'_S=-S}^S \frac{\langle m_I m_S | \hat{\mathcal{H}}_q^{\{S\}} | m'_I m'_S \rangle \langle m'_I m'_S | \hat{\mathcal{H}}_d^{\{IS\}} | m_I m_S \rangle}{\hbar(m'_I - m_I)\omega_0^{\{I\}} + \hbar(m'_S - m_S)\omega_0^{\{S\}}}. \quad (\text{A.279})$$

Here,  $E_{d,qI,mIm_S}^{(2)}$  and  $E_{d,qS,mIm_S}^{(2)}$  are the cross terms associated with the electric quadrupole moment on nucleus  $I$  and  $S$ , respectively. Although not indicated, values of  $m'_I$  and  $m'_S$  that cause the denominator to go to zero are disallowed in both expressions. We first focus on the  $I$  spin cross term, substituting our expressions for  $\hat{\mathcal{H}}_q$  and  $\hat{\mathcal{H}}_d$  to obtain

$$E_{d,qI,mIm_S}^{(2)} = \hbar\omega_d \left( \frac{\omega_q^{\{I\}}}{\omega_0^{\{I\}}} \right) \sum_{n=-1}^1 \sum_{m=-2}^2 \sum_{m'=-2}^2 \langle 2 \ m | 1 \ 1 \ n+m \ -n \rangle (-1)^{m+m'} \frac{R_{2,-m}^{\{d\}}}{\zeta_d/2} \frac{R_{2,-m'}^{\{qI\}}}{3\zeta_q^{\{I\}}} \times \sum_{m'_I=-I}^I \sum_{m'_S=-S}^S \frac{\langle m_I m_S | \hat{T}_{1,n+m}(\mathbf{I}) \hat{T}_{1,-n}(\mathbf{S}) | m'_I m'_S \rangle \langle m'_I m'_S | \hat{T}_{2,m'}(\mathbf{I}) | m_I m_S \rangle}{(m'_I - m_I)\omega_0^{\{I\}} + (m'_S - m_S)\omega_0^{\{S\}}} + \hbar\omega_d \left( \frac{\omega_q^{\{I\}}}{\omega_0^{\{I\}}} \right) \sum_{n=-1}^1 \sum_{m=-2}^2 \sum_{m'=-2}^2 \langle 2 \ m | 1 \ 1 \ n+m \ -n \rangle (-1)^{m+m'} \frac{R_{2,-m'}^{\{qI\}}}{3\zeta_q^{\{I\}}} \frac{R_{2,-m}^{\{d\}}}{\zeta_d/2} \times \sum_{m'_I=-I}^I \sum_{m'_S=-S}^S \frac{\langle m_I m_S | \hat{T}_{2,m'}(\mathbf{I}) | m'_I m'_S \rangle \langle m'_I m'_S | \hat{T}_{1,n+m}(\mathbf{I}) \hat{T}_{1,-n}(\mathbf{S}) | m_I m_S \rangle}{(m'_I - m_I)\omega_0^{\{I\}} + (m'_S - m_S)\omega_0^{\{S\}}}. \quad (\text{A.280})$$

Using the general selection rules for irreducible tensor operator matrix elements, the first matrix element gives the constraints  $m_I = m'_I + n + m$  and  $m_S = m'_S - n$ , and the second matrix element gives  $m'_I = m_I + m'$  and  $m'_S = m_S$ . Combining these constraints gives  $n = 0$  and  $m + m' = 0$  in the first term. Similarly, third matrix element gives the constraints  $m'_S = m_S$  and  $m_I = m'_I + m'$  and the fourth matrix element gives  $m'_I = m_I + n + m$  and  $m'_S = m_S - n$ . Combining these constraints also gives  $n = 0$  and  $m + m' = 0$  in the second term. Thus, we have

$$E_{d,qI,mIm_S}^{(2)} = -\hbar\omega_d \left( \frac{\omega_q^{\{I\}}}{\omega_0^{\{I\}}} \right) \sum_{\substack{m=-1 \\ m \neq 0}}^1 \frac{\langle 2 \ m | 1 \ 1 \ m \ 0 \rangle}{m} \frac{R_{2,-m}^{\{d\}}}{\zeta_d/2} \frac{R_{2,m}^{\{qI\}}}{3\zeta_q^{\{I\}}} \times \langle m_I m_S | \hat{T}_{1,m}(\mathbf{I}) \hat{T}_{1,0}(\mathbf{S}) | m_I - m \ m_S \rangle \langle m_I - m \ m_S | \hat{T}_{2,-m}(\mathbf{I}) | m_I m_S \rangle + \hbar\omega_d \left( \frac{\omega_q^{\{I\}}}{\omega_0^{\{I\}}} \right) \sum_{\substack{m=-1 \\ m \neq 0}}^1 \frac{\langle 2 \ m | 1 \ 1 \ m \ 0 \rangle}{m} \frac{R_{2,-m}^{\{d\}}}{\zeta_d/2} \frac{R_{2,m}^{\{qI\}}}{3\zeta_q^{\{I\}}} \times \langle m_I m_S | \hat{T}_{2,-m}(\mathbf{I}) | m_I + m \ m_S \rangle \langle m_I + m \ m_S | \hat{T}_{1,m}(\mathbf{I}) \hat{T}_{1,0}(\mathbf{S}) | m_I m_S \rangle. \quad (\text{A.281})$$

Since  $\langle m_I | \hat{T}_{1,\pm 2}(\mathbf{I}) | m_I \rangle = 0$  the sum over  $m$  is restricted to  $m = \pm 1$  and the Clebsch-Gordon coefficient becomes  $\langle 2 \ \pm 1 | 1 \ 1 \ \pm 1 \ 0 \rangle = 1/\sqrt{2}$ . By using the projection operator

$$|m_I \pm m \ m_S \rangle \langle m_I \pm m \ m_S| = \mathbf{1} - \sum_{m'_I=-I}^I \sum_{m'_S=-S}^S |m'_I m'_S \rangle \langle m'_I m'_S|, \quad (\text{A.282})$$

we obtain

$$E_{d,q_I,m_I m_S}^{(2)} = \hbar \omega_d \left( \frac{\omega_q^{\{I\}}}{\omega_0^{\{I\}}} \right) \sum_{\substack{m=-1 \\ m \neq 0}}^1 \frac{\langle 2 \ m | 1 \ 1 \ m \ 0 \rangle}{m} \frac{R_{2,-m}^{\{d\}}}{\zeta_d/2} \frac{R_{2,m}^{\{q_I\}}}{3\zeta_q^{\{I\}}} \langle m_I m_S | [\hat{T}_{1,m}(\mathbf{I}), \hat{T}_{2,-m}(\mathbf{I})] \hat{T}_{1,0}(\mathbf{S}) | m_I m_S \rangle. \quad (\text{A.283})$$

Substituting this into Eq. (A.52) and noting again that the outer product commutes with the operators, we obtain

$$\hat{D}_{d,q_I}^{(2)}/\hbar = \omega_d \left( \frac{\omega_q^{\{I\}}}{\omega_0^{\{I\}}} \right) \sum_{\substack{m=-1 \\ m \neq 0}}^1 \frac{\langle 2 \ m | 1 \ 1 \ m \ 0 \rangle}{m} \frac{R_{2,-m}^{\{d\}}}{\zeta_d/2} \frac{R_{2,m}^{\{q_I\}}}{3\zeta_q^{\{I\}}} [\hat{T}_{1,m}(\mathbf{I}), \hat{T}_{2,-m}(\mathbf{I})] \hat{T}_{1,0}(\mathbf{S}). \quad (\text{A.284})$$

Using the results of Section A.4 we can simplify  $\hat{D}_{d,q_I}^{(2)}$  to

$$\hat{D}_{d,q_I}^{(2)}/\hbar = \omega_d \left( \frac{\omega_q^{\{I\}}}{\omega_0^{\{I\}}} \right) \left( \sum_{K=0,2,4} \pi_{2,K}^{\{1,2\}} \frac{\mathcal{R}_{K,0}^{\{dq_I\}}}{3\zeta_q^{\{I\}} \zeta_d/2} \right) \hat{T}_{2,0}(\mathbf{I}) \hat{T}_{1,0}(\mathbf{S}), \quad (\text{A.285})$$

where

$$\pi_{2,0}^{\{1,2\}} = \sqrt{\frac{6}{5}}, \quad \pi_{2,2}^{\{1,2\}} = -\sqrt{\frac{3}{7}}, \quad \pi_{2,4}^{\{1,2\}} = \sqrt{\frac{48}{35}}, \quad (\text{A.286})$$

to obtain

$$\hat{D}_{d,q_I}^{(2)}/\hbar = \omega_d \left( \frac{\omega_q^{\{I\}}}{\omega_0^{\{I\}}} \right) \left( \sqrt{\frac{6}{5}} \frac{\mathcal{R}_{0,0}^{\{dq_I\}}}{3\zeta_q^{\{I\}} \zeta_d/2} - \sqrt{\frac{3}{7}} \frac{\mathcal{R}_{2,0}^{\{dq_I\}}}{3\zeta_q^{\{I\}} \zeta_d/2} - \sqrt{\frac{48}{35}} \frac{\mathcal{R}_{4,0}^{\{dq_I\}}}{3\zeta_q^{\{I\}} \zeta_d/2} \right) \hat{T}_{2,0}(\mathbf{I}) \hat{T}_{1,0}(\mathbf{S}).$$

Using Eq. (A.156) the second-order contribution to the transition frequency between levels  $|m_I m_S\rangle$  and  $|m'_I m'_S\rangle$  is obtained

$$\begin{aligned} \Omega_{d,q_I}^{(2)}(\Theta, m_{I,i}, m_{S,i}, m_{I,j}, m_{S,j}) &= \omega_d \left( \frac{\omega_q^{\{I\}}}{\omega_0^{\{I\}}} \right) \mathbb{S}^{\{dq_I\}}(\mathbb{dp})_{IS}(m_{I,i}, m_{S,i}, m_{I,j}, m_{S,j}) \\ &+ \omega_d \left( \frac{\omega_q^{\{I\}}}{\omega_0^{\{I\}}} \right) \mathbb{D}^{\{dq_I\}}(\Theta)(\mathbb{dp})_{IS}(m_{I,i}, m_{S,i}, m_{I,j}, m_{S,j}) \\ &+ \omega_d \left( \frac{\omega_q^{\{I\}}}{\omega_0^{\{I\}}} \right) \mathbb{G}^{\{dq_I\}}(\Theta)(\mathbb{dp})_{IS}(m_{I,i}, m_{S,i}, m_{I,j}, m_{S,j}), \end{aligned} \quad (\text{A.287})$$

where

$$\mathbb{S}^{\{dq_I\}} = \sqrt{\frac{6}{5}} \frac{\mathcal{R}_{0,0}^{\{dq_I\}}}{3\zeta_q^{\{I\}} \zeta_d/2}, \quad (\text{A.288})$$

$$\mathbb{D}^{\{dq_I\}}(\Theta) = -\sqrt{\frac{3}{7}} \frac{\mathcal{R}_{2,0}^{\{dq_I\}}(\Theta)}{3\zeta_q^{\{I\}} \zeta_d/2}, \quad (\text{A.289})$$

$$\mathbb{G}^{\{dq_I\}}(\Theta) = -\sqrt{\frac{48}{35}} \frac{\mathcal{R}_{4,0}^{\{dq_I\}}(\Theta)}{3\zeta_q^{\{I\}} \zeta_d/2}. \quad (\text{A.290})$$

Similarly, one obtains

$$\begin{aligned} \Omega_{d,q_S}^{(2)}(\Theta, m_{I,i}, m_{S,i}, m_{I,j}, m_{S,j}) &= \omega_d \left( \frac{\omega_q^{\{S\}}}{\omega_0^{\{S\}}} \right) \mathbb{S}^{\{dq_S\}}(\mathbb{pd})_{IS}(m_{I,i}, m_{S,i}, m_{I,j}, m_{S,j}) \\ &+ \omega_d \left( \frac{\omega_q^{\{S\}}}{\omega_0^{\{S\}}} \right) \mathbb{D}^{\{dq_S\}}(\Theta)(\mathbb{pd})_{IS}(m_{I,i}, m_{S,i}, m_{I,j}, m_{S,j}) \\ &+ \omega_d \left( \frac{\omega_q^{\{S\}}}{\omega_0^{\{S\}}} \right) \mathbb{G}^{\{dq_S\}}(\Theta)(\mathbb{pd})_{IS}(m_{I,i}, m_{S,i}, m_{I,j}, m_{S,j}), \end{aligned} \quad (\text{A.291})$$

where

$$\mathbb{S}^{\{dqs\}} = \sqrt{\frac{6}{5}} \frac{\mathcal{R}_{0,0}^{\{dqs\}}}{3\zeta_q^{\{S\}}\zeta_d/2}, \quad (\text{A.292})$$

$$\mathbb{D}^{\{dqs\}}(\Theta) = -\sqrt{\frac{3}{7}} \frac{\mathcal{R}_{2,0}^{\{dqs\}}(\Theta)}{3\zeta_q^{\{S\}}\zeta_d/2}, \quad (\text{A.293})$$

$$\mathbb{G}^{\{dqs\}}(\Theta) = -\sqrt{\frac{48}{35}} \frac{\mathcal{R}_{4,0}^{\{dqs\}}(\Theta)}{3\zeta_q^{\{S\}}\zeta_d/2}. \quad (\text{A.294})$$



## References

## References

- [1] A. Abragam, Principles of Nuclear Magnetism, Oxford University Press, Oxford, 1961.
- [2] M. Mehring, High Resolution NMR Spectroscopy in Solids, Vol. 11, Springer-Verlag, Berlin, 1983.
- [3] A. Samoson, B. Q. Sun, A. Pines, New Angles in Motional Averaging, Clarendon Press, Oxford, 1992, pp. 80–94.
- [4] M. H. Levitt, Symmetry in the design of NMR multiple-pulse sequences, J. Chem. Phys. 128 (5) (2008) 052205.
- [5] E. L. Hahn, Spin echoes, Phys. Rev. 80 (4) (1950) 580–594.
- [6] J. Powles, A. Hartland, The measurement of indirect (J) coupling between nuclei in liquids in magnetic resonance by the transient method, Proc. Phys. Soc. 77 (2) (1961) 273–277.
- [7] R. Andrew, A. Bradbury, R. G. Eades, Nuclear magnetic resonance spectra from a crystal rotated at high speed, Nature 182 (4650) (1958) 1659.
- [8] I. J. Lowe, Free induction decays of rotating solids, Phys. Rev. Lett. 2 (1959) 285–287.
- [9] U. Haeberlen, J. S. Waugh, Coherent averaging effects in magnetic resonance, Phys. Rev. 175 (1968) 453–467.
- [10] J. S. Waugh, L. M. Huber, U. Haeberlen, Approach to high-resolution NMR in solids, Phys. Rev. Lett. 20 (1968) 180.
- [11] R. R. Ernst, G. Bodenhausen, A. Wokaun, Principles of Nuclear Magnetic Resonance in One and Two Dimensions, Oxford University Press, Oxford, 1987.
- [12] G. Racah, Theory of complex spectra. II, Phys. Rev. 62 (1942) 438–462.
- [13] H. A. Buckmaster, R. Chatterjee, Y. H. Shing, The application of tensor operators in the analysis of EPR and ENDOR spectra, Phys. Stat. Sol. A 13 (1972) 9–50.
- [14] G. Bodenhausen, H. Kogler, R. R. Ernst, Selection of coherence-transfer pathways in NMR pulse experiments, J. Magn. Reson. 58 (1984) 370–388. doi:10.1016/0022-2364(84)90142-2.
- [15] H. T. Kwak, Z. H. Gan, Double-quantum filtered STMAS, J. Magn. Reson. 164 (2) (2003) 369–372. doi:10.1016/S1090-7807(03)00246-5.
- [16] D. J. States, R. A. Haberkorn, D. J. Ruben, A two-dimensional nuclear overhauser experiment with pure absorption phase in four quadrants, J. Magn. Reson. 48 (1982) 286–292.
- [17] P. J. Grandinetti, J. H. Baltisberger, A. Llor, Y. K. Lee, U. Werner, M. A. Eastman, A. Pines, Pure absorption-mode lineshapes and sensitivity in two-dimensional dynamic angle spinning NMR, J. Magn. Reson. A 103 (1993) 72–81. doi:10.1006/jmra.1993.1132.
- [18] S. Vega, Fictitious spin-1/2 operator formalism for multiple quantum NMR, J. Chem. Phys. 68 (1978) 5518–5527.
- [19] A. Wokaun, R. R. Ernst, Selective excitation and detection in multilevel spin systems: Application of single transition operators, J. Chem. Phys. 67 (1977) 1752–1758.
- [20] O. W. Sørensen, G. W. Eich, M. H. Levitt, G. Bodenhausen, R. R. Ernst, Product operator formalism for the description of NMR pulse experiments, Prog. NMR Spect. 16 (1983) 163–192.

- [21] B. F. Chmelka, K. T. Mueller, A. Pines, J. F. Stebbins, Y. Wu, J. W. Zwanziger, Oxygen-17 NMR in solids by dynamic-angle spinning and double rotation, *Nature* 339 (1989) 42–43. doi:10.1038/339042a0.
- [22] A. Samoson, E. Lippmaa, A. Pines, High resolution solid-state NMR. Averaging of second-order effects by means of a double-rotor, *Mol. Phys.* 65 (1988) 1013.
- [23] N. M. Trease, P. J. Grandinetti, Solid-state nuclear magnetic resonance in the rotating tilted frame, *J. Chem. Phys.* 128 (5) (2008) 052318.
- [24] S. Antonijevec, G. Bodenhausen, Quadrupolar transfer pathways, *J. Magn. Reson.* 180 (2006) 297–304.
- [25] E. R. Andrew, L. F. Farnell, The effect of macroscopic rotation on anisotropic bilinear spin interactions in solids, *Molec. Phys.* 15 (2) (1968) 157–165.
- [26] D. L. Bryce, R. E. Wasylshen, Symmetry properties of indirect nuclear spin–spin coupling tensors: First principles results for  $\text{ClF}_3$  and  $\text{OF}_2$ , *J. Am. Chem. Soc.* 122 (2000) 11236–11237.
- [27] A. D. Bain, Coherence levels and coherence pathways in NMR. a simple way to design phase cycling procedures, *J. Magn. Reson.* 56 (1984) 418–427. doi:10.1016/0022-2364(84)90305-6.
- [28] J. G. Powles, P. Mansfield, Double-pulse nuclear-resonance transients in solids, *Phys. Lett.* 2 (1962) 58–59.
- [29] I. Solomon, Multiple echoes in solids, *Phys. Rev.* 61 (1958) 61–65.
- [30] A. Samoson, Two-dimensional isotropic NMR of quadrupole nuclei in solids, *J. Magn. Reson. A* 121 (1996) 209–211.
- [31] J. T. Ash, N. T. Trease, P. J. Grandinetti, Separating chemical shift and quadrupolar anisotropies via multiple-quantum NMR spectroscopy, *J. Am. Chem. Soc.* 130 (2008) 10858–10859. doi:10.1021/ja802865x.
- [32] L. Frydman, J. S. Harwood, Isotropic spectra of half-integer quadrupolar spins from bidimensional magic-angle spinning NMR, *J. Am. Chem. Soc.* 117 (1995) 5367–5369. doi:10.1021/ja00124a023.
- [33] Z. H. Gan, Isotropic NMR spectra of half-integer quadrupolar nuclei using satellite transitions and magic-angle spinning, *J. Am. Chem. Soc.* 122 (2000) 3242–3243. doi:10.1021/ja9939791.
- [34] K. T. Mueller, B. Q. Sun, G. C. Chingas, J. W. Zwanziger, T. Terao, A. Pines, Dynamic-angle spinning of quadrupolar nuclei, *J. Magn. Reson.* 86 (1990) 470. doi:10.1016/0022-2364(90)90025-5.
- [35] D. E. Kaplan, E. L. Hahn, Expériences de double irradiation en résonance magnétique par la méthode d’impulsions, *J. Phys. Radium* 19 (1958) 821–825.
- [36] C. P. Slichter, Principles of Magnetic Resonance, Springer-Verlag, Berlin, 1980. doi:10.1007/978-3-662-09441-9.
- [37] S. Vega, T. W. Shattuck, A. Pines, Fourier-transform double-quantum NMR in solids, *Phys. Rev. Lett.* 37 (1) (1976) 43–46.
- [38] S. Antonijevec, S. Wimperis, Refocussing of chemical and paramagnetic shift anisotropies in  $^2\text{H}$  NMR using the quadrupolar echo experiment, *J. Magn. Reson.* 164 (2003) 343–350.
- [39] S. Antonijevec, S. Wimperis, Separation of quadrupolar and chemical/paramagnetic shift interactions in two-dimensional  $^2\text{H}$  ( $I = 1$ ) nuclear magnetic resonance spectroscopy, *J. Chem. Phys.* 122 (2005) 044312.
- [40] J. Jeener, P. Broekaert, Thermodynamic effect of a pair of rf pulses, *Phys. Rev.* 157 (1967) 232–240.
- [41] J. C. C. Chan, Spin echoes in half-integer quadrupole systems, *Concept Magn. Reson. B* 11 (6) (1999) 363–377.

- [42] A. A. Maudsley, R. R. Ernst, Indirect detection of magnetic resonance by heteronuclear two-dimensional spectroscopy, *Chem. Phys. Lett.* 50 (3) (1977) 368–372.
- [43] N. E. Jacobsen, *NMR Spectroscopy Explained*, Wiley, 2007.
- [44] G. Bodenhausen, D. J. Ruben, Natural abundance nitrogen-15 NMR by enhanced heteronuclear spectroscopy, *Chem. Phys. Lett.* 69 (1) (1980) 185–189.
- [45] B. Blümich, P. Blumler, J. Jansen, Presentation of sideband envelopes by two-dimensional one-pulse (TOP) spectroscopy, *Solid State NMR* 1 (1992) 111–113. doi:10.1016/0926-2040(92)90023-3.
- [46] P. Blumler, B. Blümich, J. Jansen, Two-dimensional one-pulse rotational echo spectra, *Solid State NMR* 3 (1994) 237–240.
- [47] D. Massiot, J. Hiet, N. Pellerin, F. Fayon, M. Deschamps, S. Steuernagel, P. J. Grandinetti, Two dimensional one pulse MAS of half-integer quadrupolar nuclei, *J. Magn. Reson.* 181 (2006) 310–315. doi:10.1016/j.jmr.2006.05.007.
- [48] W. T. Dixon, Spinning-sideband-free and spinning-sideband-only NMR spectra in spinning samples, *J. Chem. Phys.* 77 (1982) 1800. doi:10.1063/1.444076.
- [49] O. N. Antzutkin, S. C. Shekar, M. H. Levitt, Two-dimensional sideband separation in magic-angle spinning NMR, *J. Magn. Reson. A* 115 (1995) 7–19. doi:10.1006/jmra.1995.1142.
- [50] T. Terao, T. Fujii, T. Onodera, A. Saika, Switching-angle sample-spinning NMR spectroscopy for obtaining powder-pattern-resolved 2D spectra: Measurements of  $^{13}\text{C}$  chemical-shift anisotropies in powdered 3,4-dimethoxybenzaldehyde., *Chem. Phys. Lett.* 107 (1984) 145.
- [51] Z. H. Gan, High-resolution chemical-shift and chemical-shift anisotropy correlation in solids using slow magic-angle spinning, *J. Am. Chem. Soc.* 114 (21) (1992) 8307–8309.
- [52] P. J. Grandinetti, Y. K. Lee, J. H. Baltisberger, B. Q. Sun, A. Pines, Sideband patterns in dynamic-angle spinning NMR, *J. Magn. Reson. A* 102 (1993) 195.
- [53] J. Z. Hu, D. W. Alderman, C. H. Ye, R. J. Pugmire, D. M. Grant, An isotropic chemical shift-chemical shift anisotropy magic-angle slow-spinning 2D NMR experiment, *J. Magn. Reson. A* 105 (1) (1993) 82–87. doi:10.1006/jmra.1993.1252.
- [54] D. W. Alderman, G. McGeorge, J. Z. Hu, R. J. Pugmire, D. M. Grant, A sensitive, high resolution magic-angle turning experiment for measuring chemical shift tensor principal values, *Molec. Physics* 95 (6) (1998) 1113–1126.
- [55] J. C. C. Chan, R. Tycko, Recoupling of chemical shift anisotropies in solid-state NMR under high-speed magic-angle spinning and in uniformly  $^{13}\text{C}$ -labeled systems, *J. Chem. Phys.* 118 (2003) 8378–8389.
- [56] W. T. Dixon, Spinning-sideband-free NMR-spectra, *J. Magn. Reson.* 44 (1981) 220–223. doi:10.1016/0022-2364(81)90206-7.
- [57] A. Medek, J. S. Harwood, L. Frydman, Multiple-quantum magic-angle spinning NMR: A new method for the study of quadrupolar nuclei in solids, *J. Am. Chem. Soc.* 117 (1995) 12779–12787. doi:10.1021/ja00156a015.
- [58] D. Massiot, B. Touzo, D. Trumeau, J. P. Coutures, J. Virlet, P. Florian, P. J. Grandinetti, Two-dimensional magic-angle spinning isotropic reconstruction sequences for quadrupolar nuclei, *Solid State NMR* 6 (1996) 73–83. doi:10.1016/0926-2040(95)01210-9.

- [59] Z. H. Gan, Satellite transition magic-angle spinning nuclear magnetic resonance spectroscopy of half integer quadrupolar nuclei, *J. Chem. Phys.* 114 (2001) 10845–10853. doi:10.1063/1.1374958.
- [60] B. Q. Sun, J. H. Baltisberger, Y. Wu, A. Samoson, A. Pines, Sidebands in dynamic angle spinning (DAS) and double rotation (DOR) NMR, *Solid State NMR* 1 (1992) 267–295.
- [61] A. Samoson, T. Anupold, Synchronized double rotation 2D NMR, *Solid State NMR* 15 (2000) 217–225.
- [62] A. Samoson, E. Lippmaa, Synchronized double-rotation NMR spectroscopy, *J. Magn. Reson.* 84 (1989) 410.
- [63] A. Wokaun, R. R. Ernst, Selective detection of multiple quantum transitions in NMR by two-dimensional spectroscopy, *Chem. Phys. Lett.* 52 (1977) 407–412.
- [64] S. Vega, Y. Naor, Triple quantum NMR on spin systems with  $I = 3/2$  in solids, *J. Chem. Phys.* 75 (1981) 75. doi:10.1063/1.441857.
- [65] S. E. Ashbrook, S. Wimperis, SCAM-STMAS: satellite-transition MAS NMR of quadrupolar nuclei with self-compensation for magic-angle misset, *J. Magn. Reson.* 162 (2003) 402–416.
- [66] Z. H. Gan, P. Srinivasan, J. R. Quine, S. Steuernagel, B. Knott, Third-order effect in solid-state NMR of quadrupolar nuclei, *Chem. Phys. Lett.* 367 (1-2) (2003) 163–169. doi:10.1016/S0009-2614(02)01681-0.
- [67] C. Huguenard, F. Taulelle, B. Knott, Z. H. Gan, Optimizing STMAS, *J. Magn. Reson.* 156 (2002) 131–137.
- [68] A. Jerschow, J. W. Logan, A. Pines, High-resolution NMR of quadrupolar nuclei using mixed multiple-quantum coherences, *J. Magn. Reson.* 149 (2002) 268–270.
- [69] S. E. Ashbrook, S. Wimperis, Rotor-synchronized acquisition of quadrupolar satellite-transition NMR spectra: practical aspects and double-quantum filtration, *J. Magn. Reson.* 177 (2005) 44–55.
- [70] M. J. Thrippleton, T. J. Ball, S. Steuernagel, S. E. Ashbrook, S. Wimperis, STARTMAS: A MAS-based method for acquiring isotropic nmr spectra of spin  $i = 3/2$  nuclei in real time, *Chem. Phys. Lett.* 431 (2006) 390–396.
- [71] I. Hung, A. Wong, A. P. Howes, T. Anupold, A. Samoson, M. E. Smith, D. Holland, S. P. Brown, R. Dupree, Separation of isotropic chemical and second-order quadrupolar shifts by multiple-quantum double rotation NMR, *J. Magn. Reson.* 197 (2009) 229–236.
- [72] A. Bax, N. M. Szeverenyi, G. E. Maciel, Chemical shift anisotropy in powdered solids studied by 2D FT NMR with flipping of the spinning axis, *J. Magn. Reson.* 55 (1983) 494. doi:10.1016/0022-2364(83)90134-8.
- [73] P. Zhang, C. Dunlap, P. Florian, P. J. Grandinetti, I. Farnan, J. F. Stebbins, Silicon site distributions in an alkali silicate glass derived by two-dimensional  $^{29}\text{Si}$  nuclear magnetic resonance, *J. Non. Cryst. Solids* 204 (1996) 294–300. doi:10.1016/S0022-3093(96)00601-1.
- [74] P. Zhang, P. J. Grandinetti, J. F. Stebbins, Anionic species determination in  $\text{CaSiO}_3$  glass using two-dimensional  $^{29}\text{Si}$  NMR, *J. Phys. Chem. B* 101 (20) (1997) 4004–4008. doi:10.1021/jp9700342.
- [75] M. Davis, D. C. Kaseman, S. M. Parvani, K. J. Sanders, P. J. Grandinetti, P. Florian, D. Massiot,  $Q^{(n)}$ -species distribution in  $\text{K}_2\text{O} \cdot 2\text{SiO}_2$  by  $^{29}\text{Si}$  Magic Angle Flipping NMR, *J. Phys. Chem. A* 114 (17) (2010) 5503–5508. doi:10.1021/jp100530m.
- [76] L. Frydman, G. C. Chingas, Y. K. Lee, P. J. Grandinetti, M. A. Eastman, G. A. Barrall, A. Pines, Variable-angle correlation spectroscopy in solid-state nuclear magnetic resonance, *J. Chem. Phys.* 97 (7) (1992) 4800–4808. doi:10.1063/1.463860.

- [77] L. Frydman, G. C. Chingas, Y. K. Lee, P. J. Grandinetti, M. A. Eastman, G. A. Barrall, A. Pines, Correlation of isotropic and anisotropic chemical-shifts in solids by 2-dimensional variable-angle-spinning NMR, *Israel J. Chem.* 161 (2-3) (1992) 161–164.
- [78] Y. K. Lee, R. L. Vold, G. L. Hoatson, Y.-Y. Lin, A. Pines, Linear prediction with singular-value decomposition for removing phase artifacts in 2D VACSY spectra, *J. Magn. Reson. A* 112 (1995) 112–117.
- [79] K. T. Mueller, G. C. Chingas, A. Pines, NMR probe for dynamic-angle spinning, *Rev. Sci. Instr.* 62 (1991) 1445.
- [80] M. A. Eastman, P. J. Grandinetti, Y. K. Lee, A. Pines, Double-tuned hopping-coil probe for dynamic-angle spinning NMR, *J. Magn. Reson.* 98 (1992) 333–341. doi:10.1016/0022-2364(92)90136-U.
- [81] G. P. Drobny, A. Pines, S. Sinton, D. Weitekamp, D. E. Wemmer, Fourier transform multiple quantum nuclear magnetic resonance, *Faraday Symp. Chem. Soc.* 13 (1978) 93. doi:10.1039/FS9781300049.
- [82] J. P. Amoureux, C. Fernandez, S. Steuernagel, Z filtering in MQ-MAS NMR, *J. Magn. Reson. A* 123 (1996) 116–118.
- [83] T. Vosegaard, P. Florian, P. J. Grandinetti, D. Massiot, Pure absorption-mode spectra using a modulated RF mixing period in MQMAS experiments, *J. Magn. Reson.* 143 (2000) 217 – 222. doi:10.1006/jmre.1999.1993.
- [84] T. Vosegaard, D. Massiot, P. J. Grandinetti, Sensitivity enhancements in MQ-MAS NMR of spin-5/2 nuclei using modulated rf mixing pulses, *Chem. Phys. Lett.* 326 (2000) 454–460.
- [85] R. N. Bracewell, K.-Y. Chang, A. K. Jha, Y.-H. Wang, Affine theorem for two-dimensional Fourier transform, *Electron. Lett.* 29 (3) (1993) 304.
- [86] J. P. Elliott, P. G. Dawber, *Symmetry in Physics*, Vol. 1, Macmillan Press Ltd., 1979.
- [87] M. Weissbluth, *Atoms and Molecules*, Academic Press, Inc., San Diego, 1978.
- [88] A. Bax, N. M. Szeverenyi, G. E. Maciel, Correlation of isotropic shifts and chemical shift anisotropies by two-dimensional Fourier-transform magic-angle hopping NMR spectroscopy, *J. Magn. Reson.* 52 (1983) 147.
- [89] S. L. Gann, J. H. Baltisberger, A. Pines, Dynamic-angle spinning without sidebands, *Chem. Phys. Lett.* 210 (1993) 405–410. doi:10.1016/0009-2614(93)87045-5.
- [90] M. Goldman, P. J. Grandinetti, A. Llor, Z. Olejniczak, J. R. Sachleben, J. W. Zwanziger, Theoretical aspects of higher-order truncations in solid-state NMR, *J. Chem. Phys.* 97 (1992) 8947–8960.
- [91] M. H. Levitt, The signs of frequencies and phases in NMR, *J. Magn. Reson.* 126 (1997) 164–182.
- [92] P. J. Grandinetti, Does phase cycling work for nuclei experiencing strong quadrupolar couplings?, *Solid-State NMR* 21 (2003) 1–13.
- [93] R. K. Harris, E. D. Becker, S. M. C. D. Menezes, P. Grangerd, R. E. Hoffman, K. W. Zilm, Further conventions for NMR shielding and chemical shifts, *IUPAC recommendations 2008, Solid State Nucl. Mag.* 3 (2008) 41–56. doi:10.1016/j.ssnmr.2008.02.004.
- [94] R. L. Cook, F. C. DeLucia, Application of the theory of irreducible tensor operators to molecular hyperfine structure, *Am. J. Phys.* 39 (1971) 1433–1454.
- [95] A. Messiah, *Quantum Mechanics*, Vol. 2, Wiley, Amsterdam, 1965.
- [96] D. L. VanderHart, H. S. Gutowsky, T. C. Farrar, Dipole-dipole interactions of a spin-1/2 nucleus with a quadrupole-coupled nucleus, *J. Am. Chem. Soc.* 89 (1967) 5056.

- [97] M. E. Stoll, R. W. Vaughan, R. B. Saillant, T. Cole,  $^{13}\text{C}$  chemical shift tensor in  $\text{K}_2\text{Pt}(\text{CN})_4\text{Br}_{0.3} \cdot 3 \text{H}_2\text{O}$ , J. Chem. Phys. 61 (1974) 2896.
- [98] S. J. Opella, M. H. Frey, T. A. Cross, Detection of individual carbon resonances in solid proteins, J. Am. Chem. Soc. 101 (1979) 5856–5857.
- [99] J. G. Hexem, M. H. Frey, S. J. Opella, Influence  $^{14}\text{N}$  on  $^{13}\text{C}$  NMR spectra of solids, J. Am. Chem. Soc. 103 (1981) 224–226.
- [100] A. Naito, S. Ganapathy, C. A. McDowell, High resolution solid state  $^{13}\text{C}$  NMR spectra of carbons bonded to nitrogen in a sample spinning at the magic angle, J. Chem. Phys. 74 (1981) 5393–5397.
- [101] N. Zumbulyadis, P. M. Henrichs, R. H. Young, Quadrupolar effects in the magic-angle-spinning spectra of spin-1/2 nuclei, J. Chem. Phys. 75 (1981) 1603–1611.
- [102] A. Naito, S. Ganapathy, C. A. McDowell,  $^{14}\text{N}$  quadrupole effects in CP-MAS  $^{13}\text{C}$  NMR spectra of organic compounds in the solid state, J. Magn. Reson. 48 (1982) 367–381.
- [103] J. G. Hexem, M. H. Frey, S. J. Opella, Molecular and structural information from  $^{14}\text{N}$ - $^{13}\text{C}$  dipolar couplings manifested in high resolution  $^{13}\text{C}$  NMR spectra of solids, J. Chem. Phys. 77 (1982) 3847.
- [104] A. C. Olivieri, L. Frydman, L. E. Diaz, A simple approach for relating molecular and structural information to the dipolar coupling  $^{13}\text{C}$ - $^{14}\text{N}$  in  $^{13}\text{C}$  CPMAS NMR, J. Magn. Reson. 75 (1987) 50–62.
- [105] A. C. Olivieri, Quadrupolar effects in the CPMAS NMR spectra of spin-1/2 nuclei, J. Magn. Reson. 81 (1989) 201.
- [106] A. D. Bain, A simple proof that third-order quadrupole perturbations of the NMR central transition of half-integral nuclei are zero, J. Magn. Reson. 179 (2006) 308–310.
- [107] A. R. Edmonds, Angular Momentum in Quantum Mechanics, Princeton University Press, 1960.
- [108] M. E. Rose, Elementary Theory of Angular Momentum, John Wiley and Sons, 1955.
- [109] B. L. Silver, Irreducible Tensor Methods, Academic Press Inc., San Diego, 1976.
- [110] G. J. Bowden, W. D. Hutchison, Tensor operator formalism for multiple-quantum NMR. 1. spin-1 nuclei, J. Magn. Reson 67 (1986) 403–414.
- [111] M. Deschamps, G. Kervin, D. Massiot, G. Pintacuda, L. Emsley, P. J. Grandinetti, Superadiabaticity in magnetic resonance, J. Chem. Phys. 129 (2008) 204100–1–204110–10.
- [112] D. A. Varshalovich, A. N. Moskalev, V. K. Khersonskii, Quantum Theory of Angular Momentum, World Scientific, Teaneck, NJ, 1988. doi:10.1142/0270.